UNIVERSITAT DE BARCELONA

Analysis and modelling of the solar energetic particle radiation environment in the inner heliosphere in preparation for Solar Orbiter

Daniel Pacheco Mateo

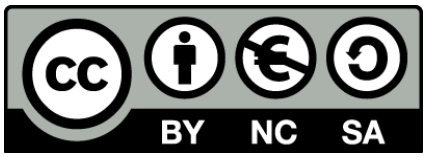

Analysis and modelling of the solar energetic particle radiation environment in the inner heliosphere in preparation for Solar Orbiter

Programa de doctorat en Física

Autor: DANIEL PACHECO MATEO

Directores de tesi:

Dra. M. ÀNGELS ARAN i Dra. NEUS ÀGUEDA

Tutor: Dr. ALBERTO MANRIQUE

UNIVERSITAT DE BARCELONA

"Hasta el último día de la vida hay que estar aprendiendo, y el día que no se aprenda algo nuevo es un día perdido para el ser humano."

Dr. F. A. Castro Ruz

"The first principle is that you must not fool yourself, and you are the easiest person to fool."

Dr. R. P. Feynman

"Ideas are like rabbits. You get a couple and learn how to handle them, and pretty soon you have a dozen."

J. E. Steinbeck

Acknowledgements

Esta tesis doctoral, cuya publicación y defensa culminarán cuatro años de intenso trabajo, no habría sido posible sin la colaboración de multitud de personas y entes, en muchas ocasiones de forma totalmente desinteresada.

Primero de todo, agradecer a aquello que en mayor medida a contribuido a llegar hasta aquí: a la Suerte, que ha acompañado mi vida hasta el momento, por haberme dado la ocasión de dedicarme a aquello que me apasiona, sin la necesidad de temer al hambre o a la guerra. Tales circunstancias privarán al mundo de las que hubieran sido magníficas contribuciones de otros tantos mejores que yo. Simplemente por el hecho de haber nacido en distintas coordenadas.

La pequeña porción que resta, debe repartirse generosamente entre una multitud. Desde los profesores de instituto gracias a los cuales empece a sentir la atracción de la física (gracias Isabel Warner y Toni Sala), hasta todos aquellos, innumerables, que me ilustraron una vez ya en la facultad.

Dar las gracias también a los diferentes estamentos de la Universidad de Barcelona que tanto han contribuido a esquilmar los pocos derechos de estudiantes y trabajadores. Sin su despótico proceder nunca habría aprendido a defender mis derechos. Un efusivo agradecimiento también a los diferentes gobiernos del estado y de Cataluña que nunca han cejado en su empeño de acabar con la universidad pública. Por suerte, uno siempre puede encontrar mágnificas personas que se esfuerzan en hacer su trabajo lo mejor posible, y nos hacen la vida más fácil a los demás. Quiero agradecer a los diferentes decanos de física que han ejercido el cargo durante mis años en la facultad, por su buen hacer. Gracias también a todo el PAS del departamento, especialmente a JR, que siempre me han ayudado ante cualquier problema.

A todos los compañeros junto a los cuales he recorrido este camino de tantísimos años y que me han ayudado a convertirme en lo que soy hoy día en todos los aspectos. A Edu, Nora, Fajula e Ismael, junto a quienes tantas batallas he librado y tanto me han enseñado a luchar por lo que es justo. A todos los JIPIs con los que he compartido y peleado la organización de tres ediciones de este magnífico proyecto. A todos mis compañeros del departamento, por todas esas comidas en buena compañía. A Roi, que pese a ser gallego es un excelente ser humano y amigo. A Toño y Paula, por que... bueno, algo habrá que pueda agradecerles después de tanto tiempo. A mis antiguos compis de piso, Julià, Pau y Lorena, pese a que nunca pasan por casa a recoger sus cartas. A mis nuevo compañeros de piso, Marta y Diego, que no han huido a pesar de mis hachas. A Estef, por darme charla durante tantas horas con un té en la mano (y a veces, chocolate). A María C., que después tanto tiempo casi nada ha cambiado y sigues ahí compartiendo tu comida conmigo. A Mario, por esas interminables discusiones que me obligaban a ser exacto hasta en el más nimio detalle. A Palau, por por sus magnificas venganzas y traiciones, y especialmente por descubrirme libros increíbles; te debo el haber leído a Bradbury y Steinbeck. A Sara, por

tantos años de estar siempre cerca con una sonrisa para compartir el día a día. A Frigola, quizá la persona que más haya influido en mi a lo largo de mi vida, siempre para bien: por tantas y tantas cosas que haría falta un capítulo de esta tesis solo para él. A Diego, el hermano que hubiera elegido tener, por que ha sido de los pocos que siempre ha creído en mi. Y como no, a mis dos hachas, que tanto esfuerzo llevo forjar. Papi os quiere.

Esta tesis ha salido adelante, además, por el cuidadoso esfuerzo de varios notables colaboradores, a los que no puedo más que agradecer su dedicación y ayuda. To Piers, thanks for your kindness when we visited you at ESTEC. A Raúl, Fernando, y el resto del grupo de Alcalá, que hicisteis que mi estancia con vosotros no dejara solo buenos resultados científicos sino también buenos amigos. To Bernd, Nils, Nina and Andreas, many thanks for your hospitality that made my Kiel days much warmer. Gracias César y Ali, por la compañía durante tantas comidas en el Mensa, por todos los cafés que nos tomamos hablando de politiqueces, y los que nos queden.

Per descomptat, he d'expressar el meu profund agraïment a aquells que m'han ajudat i guiat dia a dia durant aquests llargs anys de doctorat. A en Blai, a qui mai li ha faltat un consell que donar-me, i molt especialment a les meves dues mentores, més que caps, Àngels i Neus, ja que sense el seu ajut i dedicació aquest viatge mai hauria arribat enlloc.

Debo dar las gracias también a parte de mi familia. A mis tíos Carlos, Juan y Carmen, de quienes tanto he aprendido. A mis padres, por la paciencia cuando no todo ha ido bien y, sobretodo, por el haberme imbuido el amor por la lectura, el respeto por el conocimiento y una inabarcable curiosidad que aun dista de ser saciada. A mi hermana Laura, por haberme permitido entrenar mi paciencia y obligarme a ser mejor ejemplo en muchas cosas.

Infine voglio ringraziare la persona che ha reso gli ultimi due anni meravigliosi. Senza di lei difficilmente avrei resistito alla tentazione di arrendermi e desistere. Grazie Angelica, per tutto il tuo supporto in questo periodo. And thanks for drawing the wonderful cover for this thesis. Yes, she is the artist who did it.

A aquellos que nunca llegarán hasta aquí
por que una vez prestaron oídos a quien les dijo
"no podrás"

Contents

Resum

El Sol és la principal font de partícules que podem trobar al medi interplanetari del sistema solar, i els esdeveniments de partícules energètiques solars són la principal font de radiació dins de l'heliosfera. L'estudi i predicció d'aquest tipus d'esdeveniments i les seves causes i conseqüències ha esdevingut una àrea d'especial interès per la seva importància enfront dels perills que suposa aquesta radiació per a les telecomunicacions i la salut durant missions espacials tripulades.

Aquesta tesi doctorat s'ha desenvolupat en tres àmbits: i) l'estudi observacional d'esdeveniments de partícules energètiques solars; ii) la simulació d'esdeveniments mitjançant models de transport; iii) el desenvolupament d'eines i models d'instruments de partícules per fer-los servir conjuntament amb els models preexistents per la simulació d'esdeveniments.

Hem portat a terme un estudi observacional d'esdeveni-ments graduals de partícules on hem estudiat la dependència de les distàncies longitudinal i radial sobre la porció de la fluència mesurada després del pas del xoc associat a l'esdeveniment (post xoc) sobre la fluència de la duració total, fent servir dades del catàleg SEPEM (basat en dades de la missió GOES) i de les missions espacials ACE, STEREO i Helios. Primer hem expandit el catàleg d'esdeveniments contingut a SEPEM, estudiant els vint-i-cinc esdeveniments ocorreguts entre 2010 i 2013. Hem comparat els esdeveniments vistos des de la posició de la Terra amb les deteccions de les dues sondes STEREO, que es trobaren a diferents heliolongituds. Aquest anàlisi ens ha permès establir una dependència de la proporció post xoc de la fluència mesurada amb la longitud relativa entre la sonda i la fulguració solar que dóna origen a l'esdeveniment de partícules. Hem trobat que els esdeveniments observats a l'est presenten major proporció de fluència post xoc que els observats a l'oest, extraient una relació per tot el rang de longituds. Seguidament, hem estès l'estudi a aquells esdeveniments observats per la missió Helios, composta de 2 sondes que van orbitar a l'heliosfera interior als anys 70, arribant a un periheli de 0.29 AU. Hem estudiat els esdeveniments observats per aquesta missió recopilats prèviament pel nostre grup en un catàleg de 125 esdeveniments de protons a diferents longituds relatives a la font i distàncies radials. L'estudi dels esdeveniments d'Helios, tot i que no ha comptat amb prou nombre d'esdeveniments per establir dependències específiques per a cada distància, ha permès comprovar que les tendències observades a 1 UA es segueixen complint i hem extrapolat les dependències obtingues allà a distàncies més petites. Aquestes noves dependències radials s'han implementat posteriorment al model de SEPEM de l'ESA, per millorar el model de predicció de fluències acumulades.

Seguidament, en col·laboració amb el grup d'investigació espacial de la Universitat de Alcalá, hem estudiat les diferències en el transport d'electrons quasi relativistes en dos esdeveniments impulsius observats l'1 d'agost de 2014 per les sondes bessones STEREO (A i B) quan aquestes estaven separades només 34º. En un estudi observacional previ (Klassen et al. 2016)

es feia notar que la sonda amb millor connexió magnètica amb la font de partícules al Sol (STEREO B), a priori, observava menys intensitat d'electrons i un inici de l'esdeveniment posterior, en comparació amb la sonda pitjor connectada (STEREO A). Fent servir l'eina SEPinversion prèviament desenvolupada pel nostre grup, i adaptant-la convenientment per fer-la servir directament amb les dades de l'instrument SEPT d'STEREO hem modelitzat els esdeveniments trobant, per cada esdeveniment i cada observador, els perfils d'injecció al Sol i el recorregut lliure mig radial(λ_r) que millor ajusten les dades. Per STEREO A, aquests són de 0.31 UA i 0.37 UA pel primer i segon esdeveniment respectivament, i per STEREO B, 0.1 UA i 0.06 UA. Igualment, hem trobat perfils d'injecció de partícules curts que concorden amb els temps i la durada de les emissions de ràdio al Sol. Veient que els resultats dels recorreguts lliures mitjos són considerablement inferiors per les observacions d'STEREO B, podem concloure que les partícules arribant a aquesta sonda van patir més difusió al llarg del seu viatge a través del camp magnètic interplanetari. Això explica satisfactòriament les diferències observacionals, fent servir només les diferències en el transport de les partícules.

A continuació, hem estudiat els esdeveniments impulsius d'electrons observats per la missió Helios, composta de dues sondes bessones, fent servir les dades de l'instrument E6, proveïdes pel grup de l'Institut de Física Extraterrestre a la Universitat de Kiel. Hem recopilat els esdeveniments observats durant tota la missió, trobant quinze esdeveniments susceptibles de ser modelats amb tècniques d'inversió com la prèviament mencionada. Un cop extretes les característiques observacionals de cada esdeveniment, hem modelitzat i estudiat la resposta angular de l'instrument així com la seva resposta energètica basada en l'estudi de Bialk et al. (1991). Llavors, hem desenvolupat un conjunt de programes per realitzat la inversió total dels esdeveniments, és a dir, fer la modalització i inversió dels mateixos tenint en compte les respostes angular i energètica de l'instrument, i fent servir les funcions de Green que caracteritzen les condicions de transport de les partícules. Els resultats de la inversió donen valors de λ_r al rang del transport dèbil-enfocat per deu casos i dins del rang del transport enfocat (valors més grans) per quatre casos. Només un cas presenta valors prou petits de λ_r. Respecte als perfils d'injecció, hem obtingut perfils que s'ajusten bé a les emissions de ràdio i raigs X observades. També hem trobat que els perfils d'injecció resultants es separaven en dos grups diferenciats, depenent de la durada de la injecció d'electrons (més o menys de trenta minuts). Hem relacionat els perfils extensos amb la connexió magnètica a la corona, que fa dependre el ritme d'injecció amb la proximitat de la font a línies de camp obertes (connectades amb el medi interplanetari). No hem trobat relació entre λ_r i la distancia entre el Sol i l'observador. També, hem vist que alguns dels esdeveniments estudiats podrien no ser visibles a 1 UA, cosa que pot explicar perquè hi ha molt pocs esdeveniments fortament difusius observats des d'aquesta distància.

A l'última part de la tesi, hem explorat diferents aplicacions dels resultats obtinguts. Primer, hem realitzat un estudi de les dependències radials dels pics de les intensitats i de les anisotropies als pics d'intensitat. Fent servir els perfils d'injecció obtinguts pels esdeveniments d'Helios,

hem convolucionat aquests amb les funcions de Green corresponents a 13 distàncies radials diferents per obtenir els perfils d'intensitat d'electrons a aquestes distàncies per cada esdeveniment. Això ens ha permès ajustar una funció potencial, del tipus $f(r) = br^{\alpha}$, als valors de les intensitats màximes de cada perfil, en funció de la distància radial, i fer el mateix pel valor de l'anisotropia al pic d'intensitat. Trobem que les funcions fiten bé les dades obtingudes per tots els casos dels pics d'intensitat, donant un rang de valors de α entre 2.08±0.03 i 3.47±0.07, i per les anisotropies excepte en el cas de l'esdeveniment del 5 d'abril de 1980 (per una menor resolució de les dades), amb un rang de α entre 0.13±0.02 i 1.0±0.1. També hem buscat una relació entre els paràmetres α obtinguts i els λ_r de cada esdeveniment, trobant molt poca correlació. Finalment hem relacionat aquesta α amb la duració dels episodis d'injecció més intensos, dins de cada perfil, trobant una $r = 0.94$ entre aquestes variables i un pendent de la regressió de -0.024, indicant que la durada de la injecció té un paper important a l'hora d'establir la intensitat màxima dels perfils d'intensitat.

En segon lloc, hem fet l'estudi de la resposta angular de l'instrument EPT que anirà a bord de la sonda Solar Orbiter. Fent servir els resultats previs dels esdeveniments modelats per Helios, hem aplicat la resposta obtinguda per EPT al resultat de la convolució de les funcions de Green amb els perfils d'injecció obtinguts per a cada esdeveniment, obtenint el que hauria observat EPT en el lloc d'E6. Per tots els casos, els resultats de EPT permeten observar els esdeveniments amb intensitats semblants a les observades per E6. Els resultats confirmen, a més a més, que EPT presenta una bona cobertura en general, millorant a la cobertura d'Helios quan el camp magnètic local queda fora del pla de l'eclíptica.

Per tancar l'apartat d'aplicacions, hem fet servir SEPEM per estudiar les diferències en la predicció dels resultats de les fluències per la missió Solar Orbiter d'acord amb l'òrbita amb data de llançament a l'octubre de 2018 (actualment descartada). Fent servir la versió de SEPEM sense actualitzar prèvia al treball realitzat en aquesta tesi i al projecte de l'ESA SOL2UP, i comparant els seus resultats amb els obtinguts amb la versió que conté les noves dependències radials, hem vist que la nova versió corregeix les fluències obtingudes per SEPEM, especialment per energies baixes on la versió anterior presentava problemes, donant fluències acumulades per la missió més baixes que les que proporciona el model ECSS vigent actualment. Això permetria abaratir els costos relacionats amb el blindatge de les naus i satèl·lits en viatges interplanetaris. A més a més, hem comparat la fluència obtinguda per Solar Orbiter per l'actualment vigent òrbita amb llançament el febrer de 2020. Hem trobat que les fluències acumulades i els espectres d'ambdues òrbites presenten una variació inapreciable.

Chapter 1

Introduction

1.1 Solar energetic particles and solar eruptive phenomena

The Sun is the main source of all kind of Solar Energetic Particles (SEPs) in the Solar System, electrons, protons and ions with energies from few keV to several GeV. These particles are released from the solar corona and spread through the interplanetary space, the heliosphere, influenced by the interplanetary magnetic field and arriving to the Earth and interacting with the terrestrial magnetosphere. The effects of SEP interactions with space-based devices, manned missions and the Earth atmosphere are encompassed by what is known as space weather.

1.1.1 Particle populations in the heliosphere

The solar wind is a collisionless plasma flow originated in the external part of the solar atmosphere, the corona, which extends until the heliopause filling the whole solar system. It is mainly formed by protons, electrons and ionised Helium within $1.5 - 10$ keV. That plasma stream has embedded the solar magnetic field frozen-in while travelling through the heliosphere.

Together with the solar wind particles, we can find in the interplanetary medium several other particle populations known as cosmic rays. It is known that particles in the heliosphere are produced in a wide variety of different sources, not only the Sun but also we find particles accelerated by planets or coming from the interstellar or intergalactic medium.

Depending on their origin, each particle population has characteristic properties which tell us information about how and where they were produced, i.e. their source and the acceleration mechanism that triggers them into the interplanetary medium. Figure 1.1 shows how the different heliospheric populations of oxygen ion organise in terms of intensity vs. energy. Their general characteristics are (Kallenrode, 1998):

i) Galactic Cosmic Rays: high energetic particles (up to 10^{11}GeV) arriving isotropically and uniformly from beyond the solar system and modulated by the solar cycle.

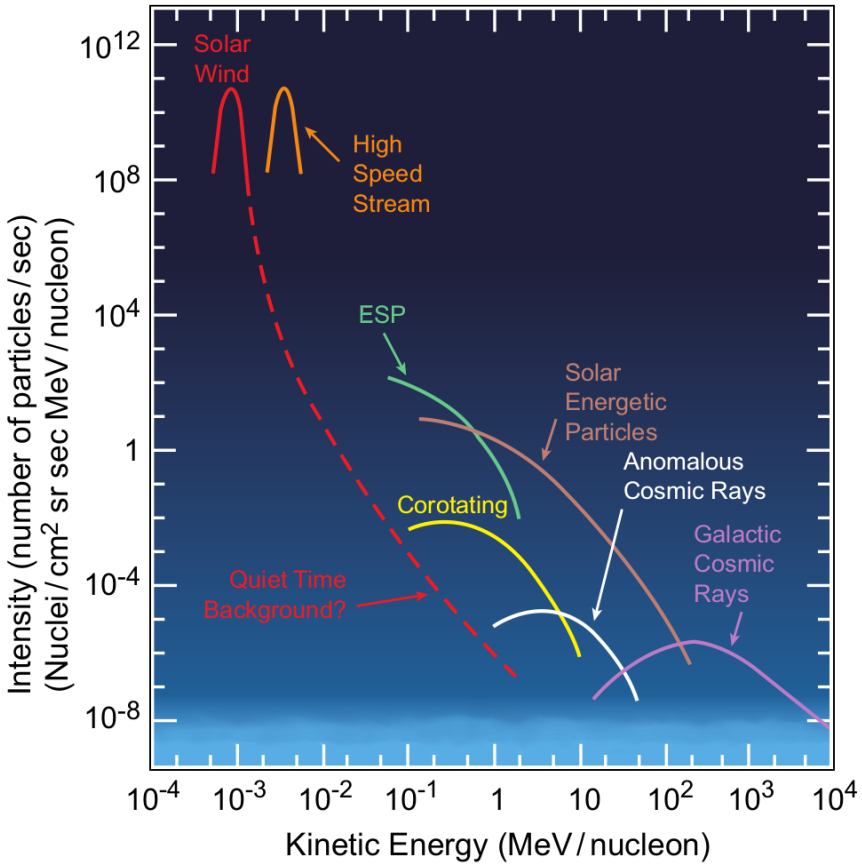

FIGURE 1.1: Differential intensity energy spectra for oxygen ions in the heliosphere regarding their source. Adapted from Lee et al. (2012)

ii) Anomalous Cosmic Rays: neutral particles from the interstellar medium that become ionised travelling through the heliosphere towards the Sun.

iii) Solar Energetic Particles (SEPs): particles coming from the Sun which are released and accelerated by solar flares or Coronal Mass Ejections (CMEs). These are the main topic of this thesis and are further treated below.

iv) Energetic Storm Particles (ESPs): this name is used to refer specifically to SEPs accelerated by interplanetary shocks, but they share most of the SEP's properties except the ion composition ratios, which vary depending on the origin of the particles and the acceleration process they suffered. Although originally considered a different population, nowadays ESPs are know as SEPs as they generally share the same triggering phenomena.

v) Corotating: these particles are accelerated at Corotating Interaction Regions (CIRs) which are the turbulent regions formed when fast solar wind overtakes western slow solar wind streams resulting in the compression of the magnetic field and the acceleration of the particles trapped there. This accelerated particles show a typical energy of about 10 MeV.

We define SEPs as high energetic particles, i.e., electrons, protons and ions, which constitute a type of cosmic rays whose origin is related to the Sun. The typical SEP energies can vary

from few tens of keV up to GeV. They are accelerated at the Sun, from the lower corona into the heliosphere by several mechanisms like current sheet reconnection in form of flares or erupting filaments. Furthermore, these particles can also find acceleration processes in interplanetary shocks arising from CMEs that are originated in the solar corona. Particles suffer the intense magnetic field fluctuations at the interplanetary shocks driven by CMEs which are a well known acceleration-driven mechanism to accelerate particles away from the Sun. The events caused by these shocks are known as ESP events, when crossing the observer.

1.1.2 Solar eruptive phenomena

Solar phenomena are the most powerful natural accelerators of particles in our solar system. We find several types of occurrences triggered by the Sun, related with magnetic disturbances, that cause energy outbursts which release great amounts of energy and particles from all the spectra into the heliosphere.

Solar flares are eruptive phenomena characterised by a sudden outburst of energy observed as a gleam of brightness across a very broad spectrum accompanied by a narrow jet of ionised plasma. They are usually associated with active regions and sunspots, and with the emission of energetic particles. Electrons up to several hundreds of MeV are accelerated during solar flares and it is possible to observe their source regions due to the collisions of these energetic electrons with the ambient plasma they go through. When colliding, electrons produce X-ray and γ-ray electromagnetic emissions, depending on the plasma density, by the bremsstrahlung mechanism. Solar flares are typically classified regarding their intensity in two of their usually most characteristic emissions, H_α and X-rays, although their spectra can encompass from the radio range to hard X-rays or even γ-rays in lower proportion.

From the observational point of view, a CME can be described as an extended bubble of ionised plasma emission (mostly protons and electrons) confined within a complex magnetic field structure and travelling outwards the solar corona. With a wide span of observed speeds, CMEs move with speeds between few tens of km s^{-1} to a maximum above 3000 km s^{-1} (Gopalswamy et al., 2005, Lario et al., 2008) on the sky-plane, based on SOHO/LASCO (Brueckner et al., 1995) measurements. They are called solar prominences when their initial speed does not allow them to leave the corona. If they have enough speed to travel through the heliosphere, then they are known as Interplanetary CMEs (ICMEs). Even in the interplanetary medium, ICMEs are dominated by the magnetic field structures from the source filament and it is possible to distinguish three different parts in a typical ICME, namely i) a bright nucleus containing the hot-ionised ejected material, ii) a dark hollow space of low-density plasma that is embedding the nucleus, probably formed by the ejected flux rope, and iii) an external front bright region which is a strong source of radio emission. They form a closed magnetic cloud in space with clearly different signatures from the surrounding medium (Klein, 2018).

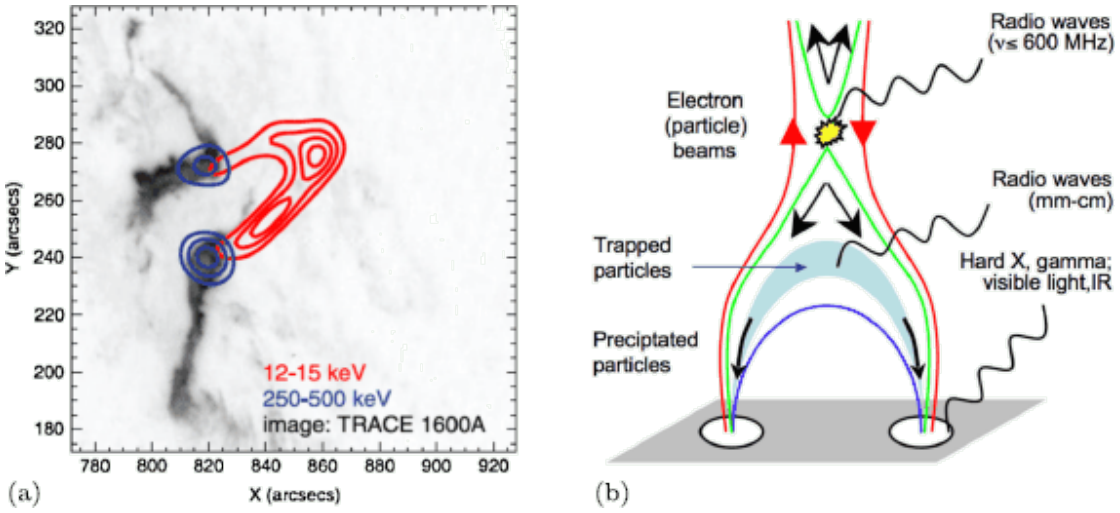

FIGURE 1.2: (a) γ-ray peak image of the 2005 January 20 flare ribbons where TRACE 1600 Å is shown together with hard X-ray emission in two spectral bands from RHESSI, 12 – 15 keV in red contours and 250 – 500 keV in blue contours (Krucker et al., 2008). (b) Sketch showing the origin of electromagnetic emission and particle population release during a flare (Klein and Dalla, 2017).

Interplanetary shocks are disturbances related to ICMEs that propagate outwards the Sun through the solar wind, and arise when a CME is travelling faster that the Alvén/sound speed of the solar wind. Interplanetary shocks can be identified by in-situ measurements owing to discontinuities observed in the plasma and magnetic field parameters. Shocks are characterised by an increase in the solar wind density, speed and temperature, as well as a rise of the magnetic field strength. Interplanetary shocks are the main accelerators of SEPs during the largest solar events (Cane et al., 1988).

Furthermore, we find a sharp boundary between solar wind streams with slow and fast speeds as the IMF of the fast stream is less curved than the slow stream one. This sudden change of speed in the stream borders remains, mixing and slowly blurring while the solar wind propagates outwards into the heliosphere. This fact makes that the IMF inside these borders gets compressed and rotated with the solar wind forming the CIRs. These regions of compressed plasma can develop shocks propagating into both streams which are able to accelerate particles outwards the Sun as well as towards it (e.g., Wijsen et al., 2019, , and references therein).

1.2 Particle events observed in the heliosphere

1.2.1 SEP intensity-time profiles

SEP events are sudden intensity enhancements of particles accelerated at flares or CMEs shocks measured in the heliosphere. These events can persist from a few hours up to several days. We can classify them into three major groups (Reames, 1999, 2013, Vainio et al., 2007):

i) impulsive events, often attributed to flares. They last few hours (see Fig. 1.3), and they are rich in electrons, ^{3}He and heavy ions. These events are typically limited to an spread range of about an angle of 30° in longitude with respect the footpoint of the magnetic field line connecting the observer with the source;

ii) gradual events that can last from several hours to few days (see Fig. 1.4). They are associated with a CME-driven shock which is accelerating the particles as it moves. These events are generally proton rich, and present ion abundances that are consistent with typical coronal composition. Moreover, these events present electron poor profiles but have generally higher intensities and fluences. They can also present a wider dispersion in longitude as a result of being prompt by a broad interplanetary shock that can magnetically connect with a larger longitudinal range in the heliosphere (see Fig. 1.5).

iii) hybrid events (Kocharov and Torsti, 2002), which are events that present characteristics of both former types, pointing to the fact that they are related to the two acceleration processes, i.e., flares and ICMEs. Generally, shock accelerated particles will dominate the fluence with a contribution of a concomitant flare, i.e., the flare that is associated in time with the lift off of the CME.

It is interesting to note that, even though most of the observed CMEs present an associated flare taking place at the same time, not all events occurred under these circumstances present any of the typical impulsive characteristics, so they cannot be considered as hybrid.

For the in-situ observations of the particle intensity profiles, it is very important to take into account the flux tube connecting the spacecraft with the acceleration source. For impulsive events, particle acceleration will occur at the active region that produced the flare, so only observers magnetically well-connected to it will measure the SEP event. The resulting profiles at the spacecraft location will be consequence of the particle injection into the flux tube and the transport conditions that particles will find along the IMF. The large scale of the IMF presents an Archimedean spiral configuration, the Parker spiral, due to the magnetic field frozen in the solar wind together with the solar rotation (e.g., Aran et al., 2018). Therefore, solar eruptive events observed at the western hemisphere of the Sun tend to present a better connection and hence, a faster intensity rising as well as a higher peak intensity and fluence, due to the fact that particles can reach the observer directly following the magnetic field lines. On the other hand, particles arriving from eastern solar eruptive events are those which underwent scattering processes which brought them far from their nominal connection field lines, which implies a smaller mean free path and more time to get to the observer. These events show lower intensities and a delayed onset time, as no particles accelerated in the solar source will make it directly to the observer (e.g., Dröge et al., 2016).

On the other hand, for gradual events we find that the intensity-time profiles is mainly related with the evolution of the magnetic connection of the observer to the particle-accelerating shock.

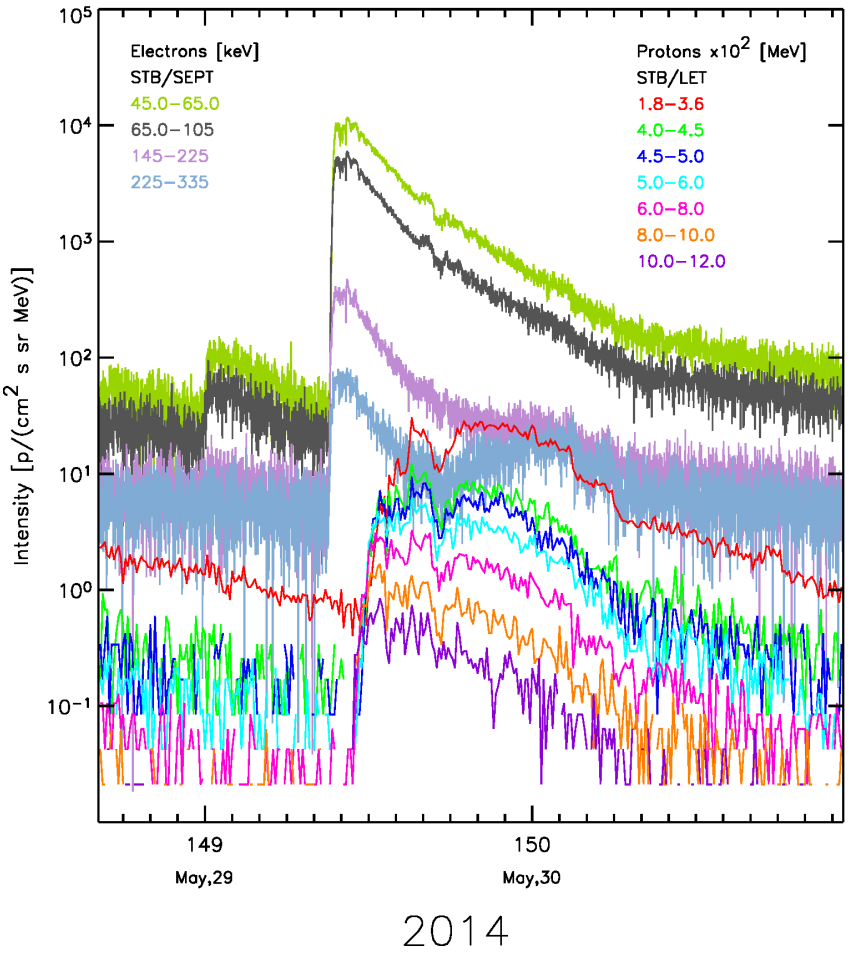

FIGURE 1.3: SEP impulsive event on 2014 May 29 observed by STEREO B. Coloured curves depict intensity-time profiles and for different energy channels from SEPT (electrons) and LET (protons, multiplied per 100) instruments.

This connection point, known as cobpoint (Heras et al., 1995), is from where particles are assumed to be injected by the shock in a different way depending on if it is located in the center of the shock, the "nose", where the efficiency will be higher as it is the most acceleration efficient part, or the flanks (or wings) of the shock, where the particle density and the shock acceleration power is be lower, triggering less particles towards the observer (Lario et al., 1998, Reames, 2013). Of course, particles accelerated at the shock will also suffer from the transport processes along the IMF so, as a consequence, they can suffer from turbulence causing diffusion along the flux tube.

As shown in Figure 1.4, we can distinguish two parts in the behaviour of a gradual event profile. Before the shock arrives to the observer position (upstream), the observer is connected to the front shock and observing the particles that this is accelerating into the connecting flux tube. Once the shock arrives at the observer, the observer generally detects a strong peak, especially at lower energies, due to the measurement of the pool of particles trapped inside the shock, and once passed (downstream), the intensity decays as there is no magnetic connection with any particle source. This asymmetry of the profiles due to the acceleration mechanisms at

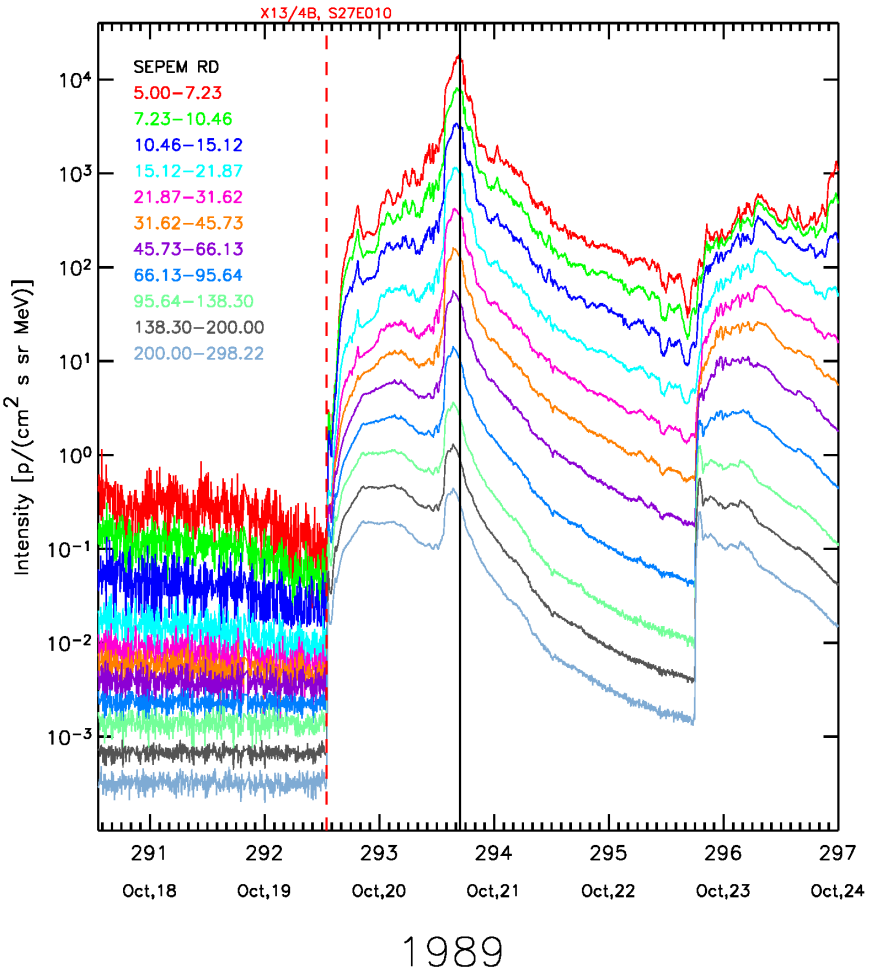

FIGURE 1.4: SEP gradual event on 1989 October 19 from the SEPEM RDS catalogue. Coloured curves depict proton intensity-time profiles for different energy channels. The red vertical dashed line shows the flare time and on the top it is indicated the flare intensity and location. The vertical solid black line shows the shock passage time at the spacecraft position.

the shock-front is highly dependent on the relative longitude between the observer and the shock nose, which will yield very different intensity-time profiles if the shock nose is crossing close to the observer, where most particles are accelerated, or if the latter is just connected to a wing of the shock, which implies a smaller jump in the plasma parameters and less injection of particles towards the observer (Lario et al., 1998).

However, the analysis of these events needs to take into consideration several aspects about how the data is gathered. When interpreting the time-intensity particle profiles, we should be aware that, generally, instruments can have low sensitivity and be limited to a certain range of the energy spectra. Having a high noisy signal can also make it difficult to distinguish clearly some of the traits of the events and introduce an error factor in the measurements. Furthermore, we can also have deviations from the ideal measurements due to instrumental effects that can induce uncertainties in the results. On the other hand, there are other known causes of uncertainties and errors such as poor determination of the measurement parameters as the magnetic field structure along where particles are propagating, the interplanetary transport conditions or the

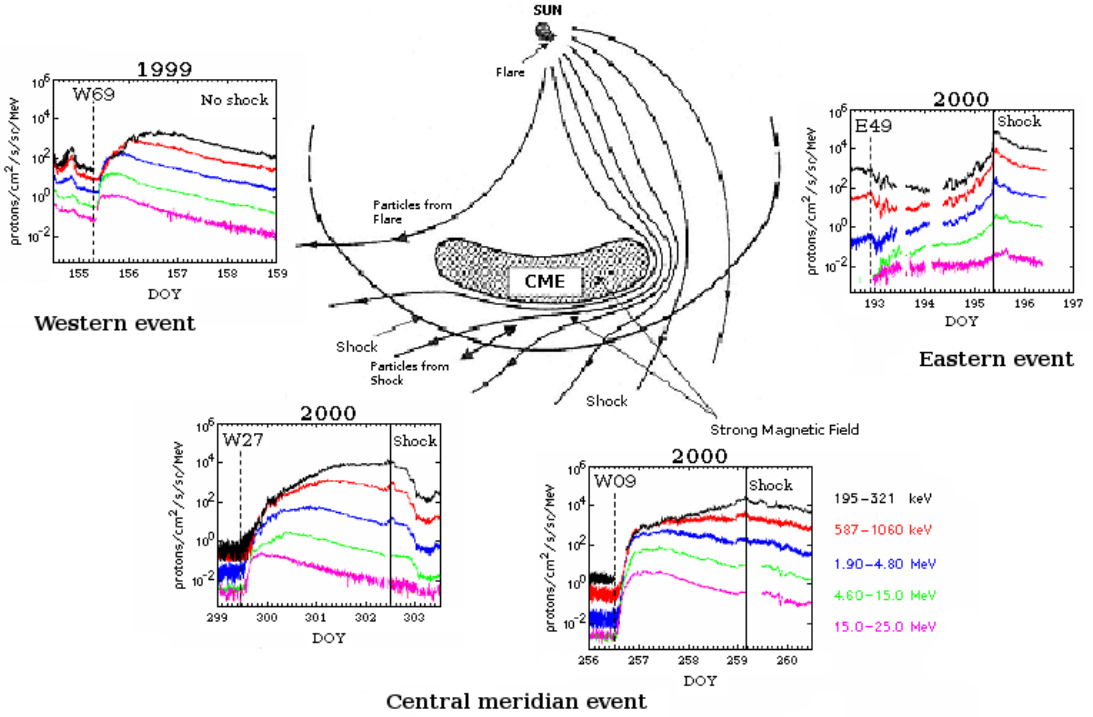

FIGURE 1.5: Sketch showing the configuration of a CME travelling through the heliosphere and the typical observational profiles as seen at different longitudinal distances from the source. The plots, corresponding to events occurred in the years 1999 and 2000, show the ion intensity profiles measured by ACE/EPAM (Gold et al., 1998) and IMP-8 (Sarris et al., 1976), with energies between 195 keV and 25.0 MeV. The relative longitude with respect to the source is indicated in the upper left corner. Dashed lines indicate the event starting time and the solid ones indicates the pass of the shock. Adapted from: Radiation and the International Space Station, National Academy of Sciences, USA, and Lario and Simnett (2004)

determination of the angular position of the solar source and the observer footpoint. Finally, we need to note that even if we can reduce all these errors, our in-situ observations will still be restricted to a certain position in space, so if we want to extract the general characteristics of an event, we could be committing an important error using the local measurements to explain the behaviour of the event in other parts of the heliosphere. Thus, multi-spacecraft analysis, boosted during the last years thanks to the STEREO mission, has become an essential tool to help us understand the difference in spatially separated measurements.

1.2.2 Multi-spacecraft analysis of events

In the study of the event characteristics and their associated transport conditions, the possibility of monitoring the in-situ particle flux from several points in the heliosphere has demonstrated to be a priceless tool. As SEP events show different characteristics regarding the longitude angle between the source and the observer, multi-spacecraft observations allow the comparison of separated measurements related to the same event to infer the different transport and magnetic connection conditions, for impulsive as well as for gradual events. Furthermore, it has been possible to study differences in connectivity and transport conditions regarding the latitude of

the observer (Lario et al., 2004, Agueda et al., 2012a) by using Ulysses mission data (Marsden et al., 1986), a mission whose main characteristic was achieving a high heliographic latitude that allowed also the study of the Sun polar regions.

Many studies have been elaborated about the broad spread of the accelerated particles regarding shock associated events (Beeck et al., 1987, Dresing et al., 2012, Lario et al., 2013, Wiedenbeck et al., 2013, Richardson et al., 2014, Gómez-Herrero et al., 2015, Dröge et al., 2016), which were observed over a wide longitudinal range, even by observers separated 180° in longitude. Lately, taking advantage of the temporal narrow separation between the two STEREO spacecraft, other studies (Klassen et al., 2015, Klassen et al., 2016, Pacheco et al., 2017a) inferred the injection and transport characteristics of short impulsive events. These studies conclude that even contiguous flux tubes can present very different transport conditions, which is only possible to untangle with limited configurations of the spacecraft constellation. This approach is also useful when studying CME properties because providing in-situ measurements from several points allows us to reconstruct the magnetic cloud structure (Al-Haddad et al., 2019). Furthermore, also magnetic structures originated in the solar wind as CIRs have been under the multi-point study scope, finding changes on narrow stream structures and CIRs-associated shocks regarding the observer (Dresing et al., 2009). These results point towards the need of a broad constellation of spacecraft monitoring the Sun and heliosphere from multiple locations allowing 3D studies of the interplanetary space plasma properties.

Luckily, a new era for multi-spacecraft studies is about to start, since Parker Solar Probe was launched in August 2018 and Solar Orbiter will be launched in February 2020. These two missions orbiting the inner heliosphere together with the pre-existing ones orbiting at 1 AU will allow multiple kind of approximations to study radial, longitudinal, or even latitudinal dependences of SEP and plasma parameters. The new data expected from these missions will fill the gap in the observations that is needed to test most of the current heliospheric models.

1.3 Interplanetary Transport Processes

Space based observatories as the Solar & Heliospheric Observatory (SOHO; Domingo et al., 1995), the Geostationary Operational Environmental Satellite (GOES; Space-Systems-Loral, 1996), or the Solar Dynamics Observatory (SDO; Schwer et al., 2002), detect SEP events quite frequently. As most of current space missions are at a radial distance of ∼1 AU either orbiting around the Sun or the Earth, part of the information about the source of the SEP at the Sun is veiled by the effects that these particles suffer during their travel through the inner heliosphere. SEPs travel faster than the solar wind following the magnetic field lines frozen in it, being the typical speed of the solar wind ∼400 km s^{-1}. The solar magnetic field in the heliosphere expands radially and, as a first approximation, is ideally shaped as an Archimedean spiral, called Parker spiral, consequence of the Sun's rotation. That expansion also makes the magnetic field to

diverge and it decreases outwards the heliosphere, which produces a focusing effect over the charged particles travelling along the IMF. The magnetic field curvature forming the Parker spiral will depend on the solar wind speed, the faster the smaller the bending of the field lines. Particles are accelerated during CMEs, either in the corona or at ICMEs at their front shock, and at flares, and propagate along the IMF lines. Of course, ideal conditions are commonly vanished by turbulent phenomena in the IMF, as passing shocks from ICMEs or CIRs formed between different solar wind streams. Thus, the principal processes affecting SEPs during their travel along the IMF are the streaming effect along the magnetic field lines, the aforementioned adiabatic focusing due to the divergent smooth IMF, and the pitch-angle scattering caused by the turbulences the particles find in the IMF. Hence, the particle transport in the heliosphere is the result of the competition of these effects. The efficiency in the acceleration of particles at source, the magnetic connectivity, the transport effects and the solar wind conditions are the main considerations to understand what is influencing the characteristics of the intensity time profiles of SEP events, such as the peak intensity and the fluence, and the dependence of these quantities with the radial distance between the solar source and the observer. For that reason, transport processes have been widely studied to understand their role on the development of the SEP events along the IMF.

Scattering of SEPs has been proved to be a major effect on shaping SEP event profiles (Wibberenz and Cane, 2006, Agueda and Lario, 2016, Pacheco et al., 2019a) dimming the initial characteristics of the event. The seed particle population with energies below ~200 keV suffers also from significant cooling effects and the adiabatic deceleration plays an important role in the SEP transport which diminishes towards higher energies (Mason et al., 2012) being negligible for relativistic particles.

SEPs travelling along the IMF being under the influence of several effects allow us to extract clues about the IMF structure that these particles have travelled along. The angular distribution of particles regarding the local magnetic field is known as pitch-angle distribution (PAD), and is used to analyse the effects of the solar source and the transport processes in the interplanetary space. The pitch-angle scattering is due to small irregularities at a non-ideal Parker spiral (Aran et al., 2018) given by transient magnetic structures. It is related to the mean free path of the particles and can be described by the pitch-angle diffusion coefficient, $D_{\mu\mu}$, knowing the turbulence power spectrum. The dependence of the turbulence and the evolution in time strongly depends on the local properties of the IMF and, given that we usually obtain the turbulence power spectra at 1 AU, it is necessary to go under several assumptions that introduce significant uncertainties to any conclusion about the SEP transport we could achieve.

Observing these events from closer distances is, then, a crucial opportunity to disclose their characteristics and few previous missions, as Helios, have allowed that. Solar Orbiter and Parker Solar Probe are expected to yield very useful measurements in a near future which will test the current transport SEP models. Also researches studying the longitudinal variation of SEP events

have been carried out finding an strong dependence of their characteristics in longitude (e.g., Lario et al., 2006, 2013, Gómez-Herrero et al., 2015). Different connection points with the Sun, even from observers nearby, can give totally different intensity-time profiles, due to distinct different transport conditions (Pacheco et al., 2017a). Particles crossing the heliospheric current sheet (Agueda et al., 2013) or turbulences in the magnetic field are able to spread particles in a wide span of longitudes making an event observable from distant locations, as well as transport perpendicular to the IMF by particle drifts or cross field diffusion.

There are several mechanisms that cause perpendicular transport of particles in the heliosphere. Turbulence in the IMF can produce cross field motion (Dröge et al., 2010, Wijsen et al., 2019) and magnetic field meandering which can result in a wide-longitudinal release for SEPs close to the Sun. Moreover, particles crossing the heliospheric current sheet (Agueda et al., 2013) and charged particle drifts, which directly affects to the plasma composition due to be charge-to-mass ratio dependent (Dalla et al., 2017), may also result in an enhancement of the perpendicular transport. For these reasons, it is important a careful selection of the events taking into account IMF conditions when applying models that do not include perpendicular transport processes. Several studies (Strauss et al., 2017, Dröge et al., 2016) treat the modelling of the physical processes leading to the perpendicular transport. Strauss et al. (2017) point towards the fact that perpendicular transport processes are not efficient over high-energy electrons, which are the ones considered in our studies. Also, they found that for distances close to the Sun the transport of SEPs is dominated by focusing, and hence SEPs propagate ballistically to the spacecraft, especially in cases where there is a good magnetic connection.

1.4 Space Weather and Radiation Environment

Space weather research aims at understanding and forecasting, whenever possible, the physical and phenomenological state of the space environment. The domain of space weather includes the Sun and its activity, the heliosphere, especially the interplanetary space, and planetary environments, particularly the Earth's magnetosphere and ionosphere, as well as the effects on ground such as induced geomagnetic currents. As a part of this thesis work, we focus on describing the particle radiation environment in the inner heliosphere, and more concisely, on depicting the fluence (i.e., the time integral of the particle intensity) spectra of SEP events.

Due to the SEP energy spectra and high intensities, SEP radiation constitutes the principal hazard in the heliospheric environment regarding not only the maximum intensities that can eventually be reached during a given SEP event, but also the accumulated fluence during the total operative life of space missions. While Galactic Cosmic Rays are the main contributors to the radiation dose at high energies (specially during solar minima), SEPs dominate the spectra below some hundreds of MeV. The most energetic part of the SEP spectra can be observed by

neutron monitors at ground level when arriving to the Earth. Those detections are called ground-level events (GLEs). In addition anomalous cosmic rays contribute substantially to the fluence at the low-energy spectrum of galactic cosmic rays during a solar cycle minimum. Finally, the main planetary magnetospheres are known to accelerate high-energy particles (mainly electrons) towards the inner heliosphere. For instance, jovian electrons dominate the electron lower ~MeV spectrum in the heliosphere and have been detected routinely at the near Earth environment by for example the ISEE3 and SOHO missions (e.g., Vogt et al., 2018, and references therein) .

Several studies (e.g., Kunow, 1994, Daly et al., 1996, Zeitlin et al., 2013, Heynderickx et al., 2014, Jiggens et al., 2014a,b, McKenna-Lawlor et al., 2015, Quinn et al., 2017, Cucinotta et al., 2017) have been developed to analyse the impact of the SEP radiation over electronics and living tissues. These studies aimed at understanding the real behaviour of electronic components under different SEP environment conditions as well as at evaluating the potential risks for prolonged interplanetary manned missions. In this regard, protons with energies above 30 MeV can cause damage to humans in space. Also, ions > 1 MeV/nuc may traverse typical shielding conditions and contribute to radiation doses. Heavy ions are the particle species more penetrative, but > 10 MeV protons are the main contributors to radiation doses (e.g., Aran and Vainio, 2013). For a detailed list of the effects and sources of the different SEP species and energies see Feynman and Gabriel (2000).

At the near-Earth space, SEP events have been routinely measured since the early 1970s. From the past five solar cycles, we know that SEP events occurrence is highly variable in frequency and that about 100 events with > 10 MeV protons are measured per solar cycle. From these events, on average, only < 10 are large SEP events with individual fluences accounting for a significant fraction of the total fluence accumulated over a solar cycle (see e.g., Aran and Vainio, 2013, and references therein). Although the occurrence of SEP events may not be completely random (Jiggens and Gabriel, 2009), the current lack of understanding on the underlying physics and the fact that SEP events may not be predictable over long periods of time (see Aminalragia-Giamini et al., 2018, and references therein), makes it necessary the use of probabilistic models for the description of the cumulative fluence and maximum intensity that could be attained during the duration a given space mission. Such radiation estimates are needed for spacecraft and payload design. A summary of recent modelling and data analysis work for estimating different radiation risks and for enabling reliable cost-effective spacecraft design can be found in Mishev and Jiggens (2019) and Jiggens et al. (2018a).

1.5 SEP environment models at 1 AU

Probabilistic SEP fluence or peak flux models are based on the wealth of SEP data collected in the vicinity of the Earth, and provide the probability that a specified fluence (or peak flux) level is exceeded for different confidence levels, as required by the user. As defined by the European

Cooperation for Space Standardization (ECSS) E-10-04C document (April 2008), the current standard model is the Prediction of Solar particle Yields for Characterizing Integrated Circuits (PSYCHIC) model (Xapsos et al., 2000, 2004, 2007). This model, initially called Emission of Solar Protons (ESP) model, provided peak flux and worst case fluence estimates for any mission duration based on the selection of the best probability distribution from the maximum entropy principle. Such probability distribution was a truncated power-law for these magnitudes. For the cumulative fluence this best distribution resulted to be the lognormal distribution, and the ESP model was extended to describe the cumulative fluence over different years based on fitted annual lognormal distributions (Xapsos et al., 2000).

A comparison among different probability distribution functions performed by Jiggens et al. (2012) showed that the lognormal distribution, as used in the previous wide-used JPL model (Feynman et al., 1993, 2002), over-predicted the possibility of very high fluence (and peak flux) events. Also they showed that the truncated power-law distribution (Xapsos et al., 1998, 1999) yielded a maximum event fluence very close to the highest event fluence in the data set; thus, preventing the prediction of larger events than those measured during the last ~35 years. This may be an optimistic constrain since the *Carrington Event* in 1859 September 1 is thought to exceed the largest SEP event in the event list used, as well as other historical events like 1960 November 12 and 1946 July 25, which showed the largest > 30 MeV fluences among the events occurred over the 18 – 23 solar cycles (Smart et al., 2006). According to Jiggens et al. (2012), the cut-off power-law distribution employed by the Moscow State University (MSU) model (Nymmik, 2007, 2011) provides the best fits to data for fluence distributions, since the results are similar to the truncated power-law, but it allows the possibility of larger events than those in the data set (1973 – 2009). Furthermore, the JPL, PSYCHIC and MSU models make use of Poisson distributions to model the event occurrence, and hence assume that SEP events are random. However, this is not the case as shown by Jiggens and Gabriel (2009). Hence, under the ESA's Solar Energetic Particle Environment Modelling (SEPEM) project[1], a new model for protons was developed. This model is based on a new statistical method named, Virtual Timelines Method (VTM). VTM takes into account both the time lapse between events (waiting times) and the duration of the events. Also, the size of the SEP events (that is, either their peak intensity or their event fluence) is linked to their duration; thus creating a time-line of events (Jiggens et al., 2012). The waiting times probability density is then fitted with a Lévy distribution for active year periods and by a time-dependent Poisson distribution for the solar minimum phases (see a detailed discussion in Jiggens et al., 2012). An upgrade to this model, the 'Solar Accumulated and Peak Proton and Heavy Ion Radiation Environment' (SAPPHIRE) has been developed by Jiggens et al. (2018a,b) very recently, after the work related to SEPEM in this dissertation was completed.

[1] http://sepem.eu

1.6 Modelling of the radiation environment in the inner heliosphere

The scarce amount of SEP data measured at heliocentric radial distances < 1.0 AU from the centre of the Sun prevents the development of statistical models based solely on SEP observations, in order to describe the radiation environment in the inner heliosphere. Instead, power-law dependences with the heliocentric radial distance, r, are used to extrapolate the fluence and peak intensities for spacecraft orbiting away from 1 AU. The standard ECSS recommendation for fluence extrapolations is to assume the following dependences: r^{-2} for $r < 1$ AU and r^0 for $r > 1$ AU. These extrapolations are mainly based in the old paradigm that SEP events are produced by fixed sources at the Sun, i.e., by flares, and hence they do not take into account the continuous acceleration of particles by interplanetary shocks driven by CMEs (see e.g., Daly et al., 2005). Further, an observational study using 72 simultaneous measurements of SEP events by spacecraft located at 1 AU and by the Helios spacecraft (that orbited the Sun from 0.31 AU to 0.98 AU) showed that less steep radial dependences than the inverse squared law might be expected, and that these dependences are highly variable from event to event (Lario et al., 2006).

First attempts to incorporate more variability in the radial dependences for SEP fluence models allow the inclusion of different prescribed power-law dependences with the heliocentric radial distance of the spacecraft. Jun et al. (2007) extended the JPL model with such capability and applied it to a short duration orbit for Parker Solar Probe. Lario and Decker (2011a) present a different SEP probabilistic model that uses daily proton fluence averages for estimating mission integrated fluences and hourly averages for the peak intensity. The model is applied to an orbit of the Parker Solar Probe mission (see also Lario and Decker, 2011b) by assuming several power-law dependences with the heliocentric radial distance of the spacecraft. The radial distance extrapolations used in this model yielded larger SEP fluence predictions than the JPL-based model, especially for low-energy protons. However, these two models use the same radial distance extrapolation for all events in their event lists and for all proton energies considered.

In order to include the effect of coronal/interplanetary shocks as sources of SEPs in the radial variations of the peak intensities and fluences of SEP events, a physics-based model, the Shock-and-Particle (SaP) model (Aran et al., 2011a, Pomoell et al., 2015), was developed during the ESA's SEPEM project. From this model, a new tool, the SOLar Particle Engineering COde-2 (SOLPENCO2) was developed (Aran et al., 2011b, Crosby et al., 2015). This tool was used to simulate the proton intensity-time profiles of six SEP events observed at 1 AU in the 5 – 200 MeV range. These reference events describe different SEP event categories discriminated by (Aran et al., 2011b, Crosby et al., 2015): (i) the observation of an interplanetary shock at 1 AU; (ii) the longitudinal position of the parent solar eruptive event and (iii) the intensity level reached at the 7.8 – 10.26 MeV channel of the SEPEM Reference data set (RDSv1) as described in Jiggens et al. (2012). For each of these reference events, proton intensity-time profiles were simulated for virtual spacecraft located at radial distances of 0.2, 0.4, 0.6 0.8,

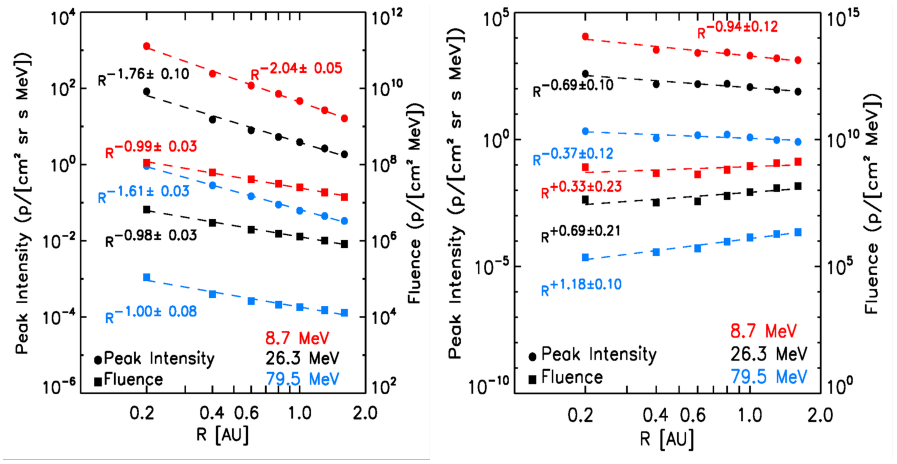

FIGURE 1.6: Results from the SEPEM/SOLPENCO2 tool for the 2012 March 13 SEP event (left) and for the 2001 September 24 SEP event (right). Peak intensity (circles) and fluence (squares) variations with the heliocentric radial distance of the simulated virtual spacecraft for three different proton energy channels (as indicated by different colours). The power-law fits (dashed lines) and indices are also shown. Adapted from Aran et al. (2017a).

1.0, 1.3 and 1.6 AU along the same nominal IMF line as the 1.0 AU-observer. The synthetic profiles are computed from the onset of the event until the shock passage by each spacecraft (i.e., the upstream portion of the SEP intensity profile). From these simulations, different power-law radial dependences were derived for peak intensities and event fluences for each reference case. As an example, Fig. 1.6 shows the radial dependences obtained for two of the reference events modelled. The power-law indices obtained vary also with the energy channel (Aran et al., 2011b). These radial dependences derived from SOLPENCO2 are implemented into the SEP statistical VTM of SEPEM (Jiggens et al., 2012, Crosby et al., 2015), by assigning each SEP event in the SEPEM reference event list at 1 AU to one of the event categories defined by the reference events. In this way, different radial dependences are considered in the same model run for mission trajectories in the inner heliosphere (Crosby et al., 2015). In the recent ESA's 'Updating SOLPENCO2 and New Analysis on Downstream Fluence' (SOL2UP) Project Aran et al. (2017a), the reference cases were extended to ten cases; thus providing more variety to the radial dependences considered in the SEPEM statistical model for interplanetary missions. A description of the modelled reference cases and the implementing method into the statistical modelling of the radial dependencies can be found in Aran and Pacheco (2017), Aran et al. (2017b,a) and in the SEPEM help pages[2].

[2] http://sepem.eu/help/solpenco2_intro.html

1.7 Objectives, methodology and outline of the thesis

The main objective of this Ph.D. thesis is to progress in the understanding and modelling of the SEP radiation environment that the ESA's mission Solar Orbiter will encounter. This objective comprehends three main research lines: i) the analysis of observations in order to improve prediction tools, such as the SEPEM/SOLPENCO2 tool, focusing on the characterisation of the SEP radiation conditions in the inner heliosphere, where Solar Orbiter will travel through (0.28 AU to 1.1 AU); ii) the development of new tools for the study of SEP directional intensities to be applied to the Solar Orbiter instruments, and iii) the study and modelling of particle radiation in the inner heliosphere, including both the description of individual SEP events and the statistical modelling of SEP fluences for long periods of time (years).

In order to accomplish with this main objective, the specific goals of this work have been:

i) to study the contribution to the fluence of the post-shock portion of the proton differential intensity-time profiles (hereafter termed as 'downstream fluence') of gradual events to improve the predictions of the SEPEM/SOLPENCO2 modelling tool;
ii) to model multi-spacecraft SEP events measured by particle detectors of similar characteristics to those of the Solar Orbiter payload, both to better interpret the future observations by this mission and to further understand the effects of the solar wind on the transport of energetic particles;
iii) to model the angular response of detectors to improve the interpretation of the observed particle directional intensities;
iv) to model SEP events measured in the inner heliosphere, at different heliocentric radial distances < 1 AU, to deepen on how the interplanetary transport conditions will affect the evolution of the SEP intensity and anisotropy (or of the PADs) of the events detected by spacecraft travelling to the Sun.

To fulfil these objectives, we used different approaches such as observational studies, modelling of the instrumentation response to the incident particle intensities and the application of inverse modelling techniques to characterise SEP events. Summarising, the work carried out during this thesis can be divided into three different methodological blocks:

1. Observational studies based on the analysis of the data measured by several interplanetary spacecraft. We worked with both proton and electron measurements and with solar wind plasma and interplanetary magnetic field data provided by the corresponding 'in-situ' instruments on board GOES, STEREO, Helios, ACE and the Wind spacecraft. We performed the characterisation of the SEP events, including the study of the solar eruptions generating the particle events by using remote sensing observations. We also performed an identification and classification of events showing common traits and analysed the consequent sample.

2. Development of tools for data analysis of observational SEP events. We developed these tools using IDL programming language and used them to study the maximum (peak) intensity and the downstream fluence variation with the heliocentric radial distance. We performed the analysis of synthetic events for the future interpretation of the particle intensities and PADs derived from the Solar Orbiter measurements.
3. Development of models to interpret SEP events. We modelled the angular response of instruments on-board Helios (E6) and Solar Orbiter (EPT) missions and coupled it with the Monte-Carlo particle transport model previously developed by our group, in order to simulate SEP events observed in the inner heliosphere and to infer how these events would have been seen by the Solar Orbiter EPT instrument. In addition we modelled the energy response to electrons of the Helios E6 experiment and coupled it with the results of the particle transport model. We also adapted SEPinversion code developed by our group in order to use data directly from the STEREO spacecraft, performing an analysis of multi-spacecraft SEP events.

The structure of this dissertation is divided into 6 chapters. Chapter 1, provides a general introduction of the field, aims and methodology of the work. Chapter 2 presents an observational study on the variation of the downstream fluence of SEP events with the longitudinal separation of the spacecraft with respect to the solar source generating the particle event. This study includes SEP events observed by Helios to infer the longitudinal variation of the downstream fluence with the heliocentric radial distance. Further, the analysis of the peak intensities and fluences of these SEP events is presented and we provide the guide-lines for the inclusion of these results into the SEPEM/SOLPENCO2 tool. In Chapter 3 we present a multi-spacecraft study of two particular events observed by both STEREO probes on 2014 August 1 when these two spacecraft were separated by only $\sim 30^{\circ}$ but exhibited differences in the observed SEP profiles. Chapter 4 describes the modelling of the angular and energetic response of the E6 Helios instrument and the subsequent use of this model to study a sample of 15 electron events observed by this mission by performing a full inversion analysis. In Chapter 5 we briefly introduce the Solar Orbiter mission and apply the results obtained in the previous chapters to infer the characteristics of the SEP events that this mission will potentially observe, as well as the SEP environment it will encounter. We present the analysis of the dependence of the peak intensities and anisotropies with the heliocentric radial distance (between 0.3 AU and 1.0 AU) derived from the events studied in Chapter 4. Further, we present the modelling of the angular response of the EPT detector of Solar Orbiter and its application to three modelled events. Next, we use the SEPEM statistical model for interplanetary missions, in which the results of the work performed in Chapter 2 are implemented, to perform the analysis of the expected proton fluence over the total Solar Orbiter operational mission, as a function of the energy. Finally, in Chapter 6 we present a summary and future perspectives of this thesis work.

Finally, this work was developed under the MINECO predoctoral grants BES-2014-067894 and EEBB-I-17-12302, co-funded by the European Social Fund and partly supported by the Spanish MINECO under the projects AYA2013-42614-P and AYA2016-77939-P, this latter with support from the European Regional Development Fund (ERDF/FEDER). In addition, further support for attending to research meetings and workshops was provided by the ESA Contract No: 4000114116/15/NL/HK, the Institute for Space Studies of Catalonia (IEEC) and the Faculty of Physics of Universitat de Barcelona.

Chapter 2

Analysis of the downstream fluence of gradual SEP events

2.1 Introduction

The statistical SEP environment model for interplanetary missions of the SEPEM project of ESA is based on the heliocentric radial distance dependences (hereafter shortened to 'radial dependences') of peak intensities and fluences of SEP events derived from the SOLPENCO2 tool (Aran et al., 2011b, Crosby et al., 2015). At present, SOLPENCO2 provides the proton synthetic intensity-time profiles for a set of ten reference SEP events, from the onset of the particle event up to the interplanetary shock crossing by near-Earth spacecraft. SOLPENCO2 is built from the Shock-and-Particle (SaP) model (Aran et al., 2011a, Pomoell et al., 2015). The SaP model uses a two-dimensional magnetohydrodynamic model to simulate the propagation of interplanetary shocks driven by CMEs, from 4 $R_\odot$ to 1.6 AU. From this MHD model, the position on the shock front of the point magnetically connecting with a given observer (i.e., 'the cobpoint', after Heras et al., 1995) in the ecliptic plane is extracted. The evolution of the cobpoint up to the position of that observer is then used as input to the particle transport model by Lario et al. (1998). In this way, the SaP model, and consequently, the SOLPENCO2 tool, provide the simulation of proton differential intensity-time profiles for the pre-shock (upstream) portion of the SEP event profiles. As it can be seen in three of the events in Figure 1.5, the upstream region extends from the dashed to the solid vertical lines. For the remainder case, the shock associated with the CME was not observed at 1 AU. For the ten modelled events, the synthetic proton intensity profiles were calibrated with 1 AU data using the SEPEM Reference Data Set (RDS) version 2.0 (RDSv2) by Sandberg (2014), Sandberg et al. (2014) and Heynderickx et al. (2017). For each of the modelled events, the synthetic profiles for observers away from 1 AU are calculated for a set of seven virtual spacecraft located at different radial distances but along the same IMF line as the actual spacecraft at 1 AU that gathers the SEP observations. In this way,

the virtual observers share the same time-history of particle injection at the shock, and hence, proper radial dependences are derived for the peak intensities and the event fluences since the source longitudinal-dependence variations are minimised.

The post-shock or downstream portion of the intensity-time profiles is not provided by the SaP model, nor by other models such as the iPATH model (Hu et al., 2017, 2018), due to the inherent difficulties of (i) shock propagation models to correctly reproduce the magnetic structure behind the shock front, and (ii) particle acceleration and transport models to reproduce the observed intensity-time profiles downstream of the interplanetary shock. In SOLPENCO2, the downstream fluence of the modelled events at 1 AU is calculated from the observed post-shock time profile. The total fluence, or event-fluence, of an event is then the addition of the upstream and downstream fluences. For the virtual spacecraft located away from 1 AU, between 0.2 AU and 1.6 AU, and for the eleven energy channels provided by the RDSv2 data, the portion of the event-fluence corresponding to the post-shock region is added to the fluence of the simulated upstream profile by assuming the same ratio of the total-fluence to the upstream-fluence as that of the observed event at 1 AU. This assumption was taken to keep the radial extrapolations simple, as explained in Aran et al. (2011b) and Crosby et al. (2015). However, several works (e.g., Cane et al., 1988, Reames et al., 1996, Lario and Simnett, 2004) have shown that the shape of the proton intensity-time profiles of SEP events associated with interplanetary shocks depends, among other factors (see e.g., Cane and Lario, 2006), on the relative longitudinal distance of the spacecraft with respect to the direction towards the leading edge of the shock-front (a.k.a. 'the nose') of the interplanetary shock[1]. Accordingly, Eastern events tend to show higher intensities in the downstream (post-shock) portion of their profiles than Central Meridian and Western events (see also Appendix I in Lario, 1997). However, this dependence is difficult to characterise and quantify, given the existing large variety of profiles observed in gradual SEP events. This is relevant for the SOLPENCO2 predictions because the observers located along the same IMF line have different relative longitudes with respect to the nose of the travelling shock.

Moreover, Reames et al. (1996) show the 1978 September 23 event observed by the IMP-8 spacecraft at 1 AU and by the Helios 1 and 2 spacecraft at 0.70 AU and 0.72 AU. In these SEP events, the 3 – 6 MeV proton time profiles have the same duration despite that the upstream duration is shorter for the events seen by the two Helios spacecraft, while later they were similar at the three spacecraft. This suggests that the assumption taken in SOLPENCO2 may not hold in some cases. Fortunately, at present and during the last two solar cycles, the STEREO mission

[1]Historically, the main direction of propagation of interplanetary shocks was assumed to be the direction given by the location of the concomitant flare, because of the lack of stereoscopic information about the propagation of the shocks. According to the observational study by Ontiveros and Vourlidas (2009), a CME-driven shock wave could be easily directed $10° - 20°$ off of the flare site, in addition to other possible deviations due to non-nominal interplanetary IMF connections between the source and the spacecraft. STEREO observations help to ease this situation. In the multi-spacecraft analysis presented in this chapter, we have checked if approximately the shock direction coincides with the flare direction, and checked our associations against those provided by other authors (e.g., Lario et al., 2013, Richardson et al., 2014). The task of reconstructing in detail the direction of the propagating shock by using white-light high quality images provided by STEREO has not been undertaken in this work.

provides us with the opportunity to study the same event measured at very similar heliocentric radial distances (at ~1 AU) but at very different heliolongitudinal positions with respect to the parent source of particles (i.e., the direction of the associated shock nose). This permits us to study, with improved instrumentation than in the 1970s, whether there is a dependence of the fluence of the events, and in particular, of the contribution of the downstream fluence to the total fluence of the event, with the relative longitudinal position between the source site and the Sun-spacecraft line (i.e., the heliolongitude). To accomplish this, we used the SEPEM RDSv2 gathered by spacecraft at the near-Earth space and data from the STEREO-A and B spacecraft. We also further exploited observations by the Helios spacecraft in order to determine, if possible, any radial dependence for the downstream fluences. The way of how the obtained results are implemented in the SOLPENCO2 tool is also discussed. The work presented in this Chapter was developed from May 2015 to July 2016 as part of the SOL2UP project, and it is detailed in the Technical Note by Pacheco et al. (2017b) and summarised in the final report of the project (Aran et al., 2017a).

2.2 Event selection and fluence computation

2.2.1 Data and Event lists

We extended the SEPEM Radial dependent Event List (REL), that consisted of 147 SEP events from 1986 to 2007, to include the SEP events observed in the period from August 2010 to March 2013. In the time interval from January 2007 to August 2010, there was no event complying with the selection criteria established for the SEPEM event list (Jiggens et al., 2012, Crosby et al., 2015) but there were 25 events in the period from August 2010 to March 2013. These latter are the events we analysed in order to find their parent solar sources and to split multiple SEP events into individual SEP enhancements (i.e., SEP events). Furthermore, we used data gathered by the STEREO twin spacecraft (Russell, 2008) during the same period of time to study multi-spacecraft SEP events. Finally, in order to draw conclusions on the radial dependence of the downstream fluence, we used proton omnidirectional intensity observations measured by the two Helios spacecraft (Porsche, 1975), covering the heliocentric radial distances from 0.29 AU to 0.85 AU.

2.2.1.1 Events at 1 AU

One of the main aims of the SEPEM project was to provide the community with a standard data set covering the longest possible time-span, as allowed by the current data samples, in order to develop a useful statistical tool to analyse SEP events. For that reason, it was also important to assure that such data set keeps the highest levels of uniformity and continuity considering the

fact that the low quality of the previous SEP data sources used in previous SEP fluence models, such as the JPL model, were substantially limiting the modelling capacities (Rosenqvist and Hilgers, 2003, Rosenqvist et al., 2005, Glover et al., 2008). Consequently, the SEPEM reference proton data set (SEPEM RDSv1) (Jiggens et al., 2012, Crosby et al., 2015) was constructed on base of GOES 5-11/Space Environment Monitor (SEM) data (Onsager et al., 1996, Sellers and Hanser, 1996), GOES 13/Energetic Particles Sensor (EPS) data (Rodriguez et al., 2014), and Interplanetary Monitoring Platform 8 (IMP 8)/Goddard Medium Energy (GME) data (McGuire et al., 1986). We used a newer version of this data set, the SEPEM RDSv2 proton data set, available at the beginning of the SOL2UP project (Sandberg, 2014, Sandberg et al., 2014). The SEPEM RDSv2[2] comprehends proton omnidirectional differential intensities collected from 1973 to 2013 and divided in 11 reference differential energy channels, logarithmically-equally spaced from 5 MeV to 298.22 MeV. This data is based on the data measured by GOES/SEM and cross calibrated with IMP8/GME data (Sandberg, 2014) and it was processed by removing spikes or periods with contamination and saturation. Therefore, data gaps were introduced on periods of time where bad data was found. Also, in GOES data a small number of data gaps during events were found and filled with linear interpolation between closest flux values (e.g., Crosby et al., 2015). Once the data was cleaned, the individual data point spectra was re-binned into the reference energy spectrum, and merged of the individual GOES data sets into an overlapped sample (Sandberg et al., 2014).

Further, in order to ease the identification process of individual SEP events in the period from 2010 to 2013, we utilised low-energy proton data from the LEMS120 telescope of the EPAM instrument (Gold et al., 1998), on-board the ACE spacecraft. In particular, we used 5-minute averages of spin-averaged intensities of the 0.31 – 0.58, 0.587 – 1.060,1.060 – 1.90,1.9 – 4.8 MeV channels, publicly available at `http://www.srl.caltech.edu/ACE/ASC/level2/lvl2DATA_EPAM.html`. We also used 175 – 315 keV electron intensities from the ACE/ EPAM/ LEMS30 telescope, to better determine the start time of the proton event.

In the case of solar wind data, we used merged 64-second averaged data from the SWEPAM (McComas et al., 1998) and MAG (Smith et al., 1998) experiments on board ACE, available at the ACE Science Center web site `http://www.srl.caltech.edu/ACE/ASC/level2/lvl2DATA_MAG-SWEPAM.html`. Specifically we used solar wind ion data for proton density, solar wind speed and proton temperature, as well as the magnetic field components in the GSE reference system. In order to confirm the interplanetary shock detections, we used the ACE and *Wind* spacecraft shock data base available at `https://www.cfa.harvard.edu/shocks/`, as well as the SOHO shock list (`http://umtof.umd.edu/pm/FIGS.HTML`).

[2]Recently, an updated SEPEM RDSv2 has been released (Heynderickx et al., 2017). This proton data covers the period from 1974 to 2016 and its obtention is reviewed in Jiggens et al. (2018a).

Starting with the 25 events identified in the period from 2010 to 2013 in the REL, we looked for SEP events observed by STEREO-A and STEREO-B in the same time periods. To carry out this analysis, we used different data sets from the IMPACT investigation (Luhmann et al., 2008) on board the twin STEREO spacecraft. Particularly, we used:

- Level 1 low-energy proton 10-minute averages differential intensities from the LET instrument (Mewaldt et al., 2008): 1.8 – 3.6 MeV (from the 'summed' data set), 4.0 – 4.5, 4.5 – 5.0, 5.0 – 6.0, 6.0 – 8.0, 8.0 – 10.0 and 10.0 – 12.0 MeV 'standard' energy channels (`http://www.srl.caltech.edu/STEREO/Public/LET_public.html`).
- High-energy proton 15-minute averages differential intensities from the HET instrument (von Rosenvinge et al., 2008): 13.6 – 15.1, 14.9 – 17.1, 17.0 – 19.3, 20.8 – 23.8, 23.8 – 26.4, 26.3 – 29.7, 29.5 – 33.4, 33.4 – 35.8, 35.5 – 40.5, 40.0 – 60.0 and 60.0 – 100.0 MeV. This data is available at `http://www.srl.caltech.edu/STEREO/Public/HET_public.html`
- 0.7 – 1.4 MeV electron 15-minute averages differential intensities from HET to better determine the onset time of the SEP event.

We utilised 10-minute resolution level-2 data to study the magnetic field (magnetic field components and intensity) and the solar wind plasma (proton speed, density and temperature), from the IMPACT MAG (Acuña et al., 2008) and PLASTIC (Galvin et al., 2008) experiments, respectively. This data is available at `http://aten.igpp.ucla.edu/forms/stereo/level2_plasma_and_magnetic_field.html`. We compared the plasma data with the STEREO/IMPACT shock list (`http://www-ssc.igpp.ucla.edu/~jlan/STEREO/Level3/STEREO_Level3_Shock.pdf`) to determine if there was an interplanetary shock associated with the particle event and its crossing time by the spacecraft.

In order to determine the main solar sources generating each SEP enhancement, flares and CMEs, we used different catalogues. To look for the parent CMEs, we consulted the SOHO/LASCO catalogue (`http://cdaw.gsfc.nasa.gov/CME_list/`), the CACTus catalogues (`http://sidc.be/cactus/`) and the STEREO CME catalogue (`https://cor1.gsfc.nasa.gov/catalog/`) from COR-1 observations. For solar flares, we used the SolarSoft catalogue to determine the associated flares (`http://www.lmsal.com/solarsoft/latest_events_archive.html`), and the EUVI list of events from STEREO (`http://secchi.lmsal.com/EUVI/euvi_events.txt`). We also employed on-line GOES X-ray flare catalogues (`ftp://ftp.ngdc.noaa.gov/STP/space-weather/solar-data/solar-features/solar-flares/x-rays/goes/xrs/`). Further, we revised the splitting of the events, of the whole REL, into particle enhancements; for events prior to the SOHO era, we consulted the Solar Geophysical Data (SGD) reports to determine the parent solar sources.

The final event list compiled consists of 25 SEP event episodes divided into 35 SEP events detected simultaneously at the near Earth space and by the two STEREO spacecraft. These events are listed in Appendix A, in Tables A.1, A.2 and A.3, for the near Earth space, STEREO-A and STEREO-B respectively. The SEP events start and end times are listed together with the information of their parent solar source (start time, location and class of the X-ray flare) and the time of the shock crossing at the ACE or the STEREO spacecraft, as well as the solar wind type. In order to determine the solar wind type, we computed the mean value of the solar wind over the duration of the upstream (pre-shock) portion of the SEP event. That is, from the start of the X-ray flare up to the shock arrival at 1 AU. According to this mean solar wind speed, v_{sw}, the solar wind is classified as 'slow' if $v_{sw} \leq 480$ km s^{-1}, otherwise it is classified as 'fast'. We also compared our parent solar source associations against available literature (Lario et al., 2013, Richardson et al., 2014, Rouillard et al., 2012, Gómez-Herrero et al., 2015).

After this study, the REL list, that we renamed as the SOL2UP REL (SREL) list, consists of 172 events, from 1988 January 1 to 2013 March 15, with a total of 263 individual SEP events (or SEP enhancements). The complete SREL is shown in Appendix A in Table A.4. This table lists the same information as in Tables A.1 but for the 172 events in SREL and with the addition of the events classification according to the ten reference cases of SOLPENCO2 (Aran et al., 2017a). This classification is described in Appendix B.

2.2.1.2 Events seen by Helios

For the study of SEP events measured between 0.29 AU and 0.85 AU we used data from the Helios 1 and 2 spacecraft (Porsche, 1975). For the particle intensities, we used hourly averages proton omnidirectional intensities measured by the Helios/E6 experiment (Kunow et al., 1975). This data is publicly available at the NASA's OMNIweb site (`https://omniweb.gsfc.nasa.gov/ftpbrowser/flux_spectr_m.html`) or at the European Union's 7th Frame Program SEPserver project site (`http://server.sepserver.eu`). We used the same data set as presently available in SEPserver but with updated nominal geometric factors provided by the group of Kiel (Müller-Mellin, private communication, 2009; B. Heber, private communication, 2014). Proton differential intensity channels used are: 3.77 – 12.81 MeV, 12.81 – 26.76 MeV, 26.76 – 36.63 MeV and 36.63 – 50.70 MeV for H1 and 3.68 – 12.73 MeV, 12.73 – 27.36 MeV, 27.36 – 37.34 MeV and 37.34 – 51.00 MeV for H2. Hereafter, each energy channel, $E_i - E_e$, is represented by its mean energy value, $E = \sqrt{E_i \cdot E_e}$.

For the solar wind, we used 40 seconds merged solar wind plasma data and interplanetary magnetic field data from the SPDF server of NASA for the two Helios spacecraft (at `ftp://spdf.gsfc.nasa.gov/pub/data/helios/helios1/merged/he1_40sec/`, and at `ftp://spdf.gsfc.nasa.gov/pub/data/helios/helios2/merged/he2_40s`

ec/). These data sets were provided to NASA by R. Schwenn from the HELIOS/E1 experiment (Schwenn et al., 1975) for the solar wind data, and by F. Neubauer from the HELIOS/E2 experiment (Musmann et al., 1975) for the magnetic field data. We used these data sets to compute the mean solar wind speed in the pre-shock region and to identify the interplanetary shock passages by the spacecraft. We further checked these identifications with the interplanetary shock list compiled by A. de Lucas (de Lucas et al., 2011a,b) and publicly available at http://www.dge.inpe.br/maghel/EN/index.html.

The list of SEP events was compiled by our group in the scope of the Spanish Research Project AYA2013-42614-P. There are a total of 125 SEP events detected by Helios-1, from 1974 to 1985, and 47 events by Helios-2, from 1976 to March 1980, when Helios-2 stopped transmissions. We have determined one by one the start and end times of the SEP events, their interplanetary shock associations, and compiled the spacecraft heliocentric radial distance from the Sun as well as the relative source location of the Helios spacecraft with respect to the longitude of the solar source. The event list is presented in Appendix A in Table A.5 for Helios-1 events and in Table A.6 for Helios-2 events.

2.2.2 Selection of the events for the downstream analysis

We selected from the lists mentioned above, the SREL (Table A.4), STEREO-A (Table A.2), STEREO-B (Table A.3) and Helios (Table A.6), the events that fulfil with the following criteria:

1. The SEP events are clearly associated with one main solar source.
2. An interplanetary shock is detected in the in-situ plasma data.
3. For the energy channels showing a proton enhancement, the intensity-time profiles permit a clear identification of the upstream and downstream portions of the SEP events.

In those cases where the downstream part of the intensity-time profiles of an event is interrupted by the onset of a new proton enhancement, the event was selected for the downstream analysis only if the intensities have significantly decreased from their value at the shock crossing. Figure 2.1 illustrates such an instance, for the event on 2003 October 28 (event 128b in Table A.4). In the case of SEP events for which two-to-three shocks are detected, we did select the event and we chose as the main shock the strongest, after inspecting that the other shocks only influenced the intensity-time profiles slightly. We also checked that the resulting transit time of the shock[3] is feasible. In the next section, Figure 2.2 shows two examples of such cases. During the event on 1977 November 22 (right panel in Figure 2.2), two interplanetary shocks (indicated by black solid vertical lines) crossed by the Helios-2 spacecraft at 0.59 AU. The two

[3]We define the transit time of the shock as the time elapsed from the first appearance of the CME in the coronagraphs (i.e., SOHO/LASCO C2 or STEREO/COR-1) up to the time of the shock detection at the spacecraft. When the CME information is not available, we take instead the start time of the associated flare.

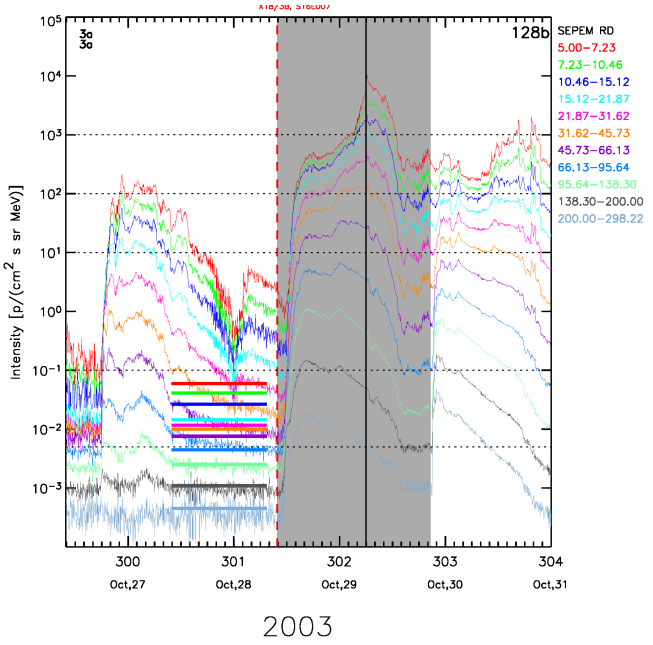

FIGURE 2.1: Proton differential intensities from the SEPEM RDSv2 for the 2003 October 28 SEP event. The dashed red vertical line marks the start time of the flare and the black vertical line the time of the interplanetary shock passage. The grey shaded zone of the proton intensity-time profiles marks the event's upstream region (from the onset to the shock) and the downstream region (from the shock to the onset of the new event on day 29).

TABLE 2.1: Number of events selected for the downstream fluence analysis

Event list	**SREL**	**STEREOs**	**Helios**
No. Events	156	13	42

shocks show similar jumps in the plasma parameters but the second is affecting more the shape of the intensity profiles, while the first only slightly modifies them. Hence, in this case, the second shock is used to determine the upstream and downstream regions. In the case of the event on 1976 March 28 (left panel in Figure 2.2), the first shock shows higher jumps in solar wind density and magnetic field, and the particle intensities decrease fast after the shock crosses the Helios-2 spacecraft (at 0.49 AU). The second shock, however, does not modify the shape of the SEP profiles. Hence, we took the first shock in this case to determine the downstream region.

For the study of the downstream fluence, the number of selected events from near-Earth observations, from the STEREO-A and STEREO-B spacecraft and from the two Helios spacecraft are listed in Table 2.1. The selected events are marked with a 'Y' for 'yes' in the corresponding 'Downstream Analysis' column in Tables A.4, A.2, A.3 and A.6.

2.2.3 Fluences

In this analysis, we refer to 'fluence' as a short name for the differential fluence; that is, to the time-integral of proton differential intensities (in units of [MeV cm^2 sr s]$^{-1}$) over a given period of time. In order to convert the time-integrated intensities to units of differential fluence, [MeV cm^2]$^{-1}$, we assume that intensities are gathered from all directions and multiply the resulting

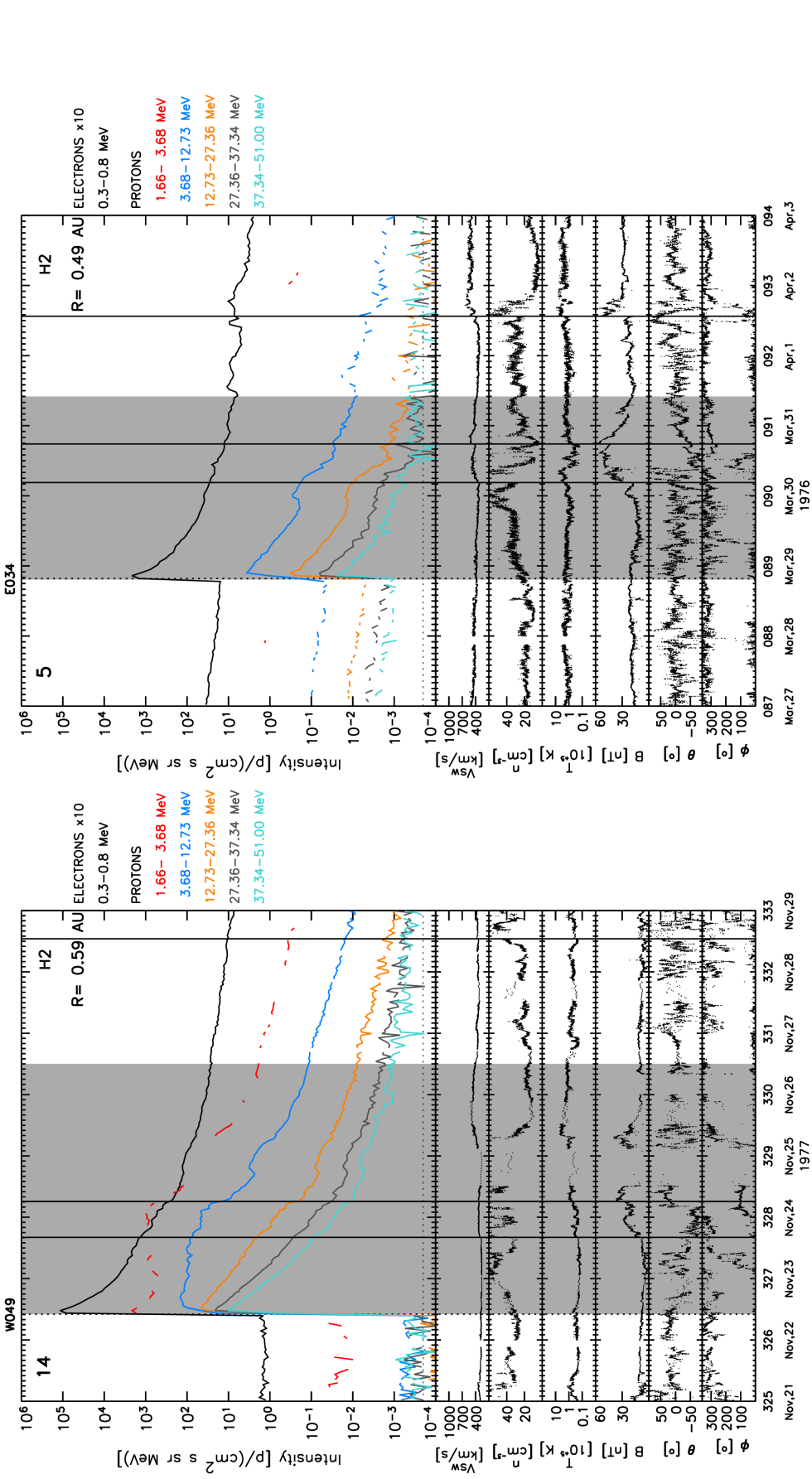

FIGURE 2.2: Examples of SEP events observed by the Helios spacecraft. The left panel shows Helios-2 measurements during the event on 1977 November 22 and the right panel, for the event on 1976 March 28. The horizontal dashed line marks the background level set.

values by 4π sr. In this section we describe the tasks performed to calculate the upstream fluence (hereafter, UF), the downstream fluence (hereafter, DF) and total fluence (hereafter, TF) of the selected SEP events, in the case of STEREO and Helios, and for all events in the SREL. We only calculate the fluences for the selected events of the STEREO and the Helios events list because we use these data for the downstream analysis. In the case of SREL, all events are needed for the implementation of the results to the SEPEM statistical model for interplanetary missions (Pacheco et al., 2017b, Aran et al., 2017a). Finally, we point out that in the following the number of an SEP event refers to the number of the event in the SREL list (Table A.4).

2.2.3.1 Background Subtraction

For the calculation of the fluence of a given event, it is necessary to remove the background (pre-event) intensity level of a given energy channel, in order to account correctly for the fluence of the SEP event at that energy. This is especially important for those profiles that reach low levels of intensity above the background, since then most of the time-integrated intensity would be accountable to the background.

In the case of the SEPEM RDSv2, we scanned the background intensity levels for the eleven reference energies from 1988 to 2013. We determined that the background levels varied in different periods of time, irrespectively whether the same GOES spacecraft was operating or not. Therefore, we decided to compute the background intensities prior to the following set of events: '001', '003', '006a', '008', '010a', '012', '017', '019', '020', '027', '032', '043', '046', '053', '056a', '060', '061', '062', '064', '073', '077', '081a', '083', '084a', '086', '089', '093', '097', '106a', '116', '121', '125a', '130', '132a', '134', '135', '139a', '145a', '147a', '150', '157', '158', '161', '164' and '169'. Figure 2.3 shows two examples of the background levels (i.e., pre-event intensities) computed, indicated by horizontal coloured lines. For each energy, the background intensity is computed as the mean value of the intensity over the 24 hours prior to the onset of the SEP event.

In several cases, we found that the intensity background levels after the end of the SEP event were lower than those prior to the onset of the event. In these cases, the mean value of the intensity was computed over 24 hours centred at the end time of the event; then, the lowest value of the two computed background levels was chosen for that event and energy. Figure 2.4 shows two examples for which the > 45 MeV intensity levels at the end of the event are smaller than those computed prior to the onset of the event on 1989 March 6 (event 6a, the first enhancement in the event number 6). As can be appreciated for the blue and purple energy channels in the right panel of Figure 2.4, this correction might not work if another event starts right after the end time of the next event. The events slightly affected by this issue are events 41e and 162b (in the three higher energy channels) and events 128c and 139c (in the two higher energy channels). To solve such situations, only the 12 hours prior to the end of the event should have been considered

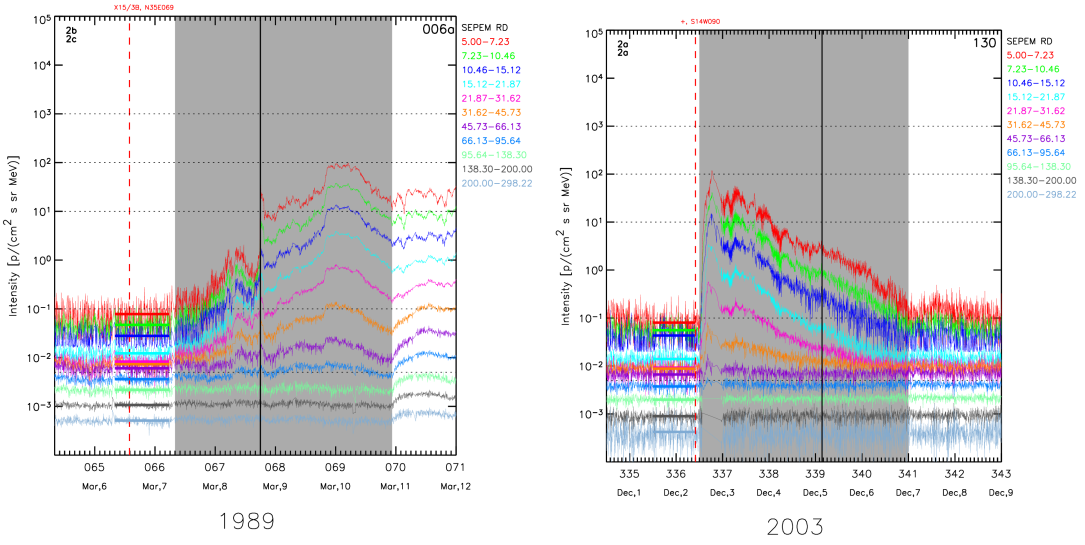

FIGURE 2.3: Proton differential intensities from the SEPEM RDSv2 for the 1989 March 6 and 2011 March SEP 7 events. The dashed red vertical line marks the start time of the flare and the black vertical line the time of the interplanetary shock passage. The grey shaded zone of the proton intensity-time profiles marks the event's upstream region (from the onset to the shock) and the downstream region (from the shock to the end of the SEP enhancement).

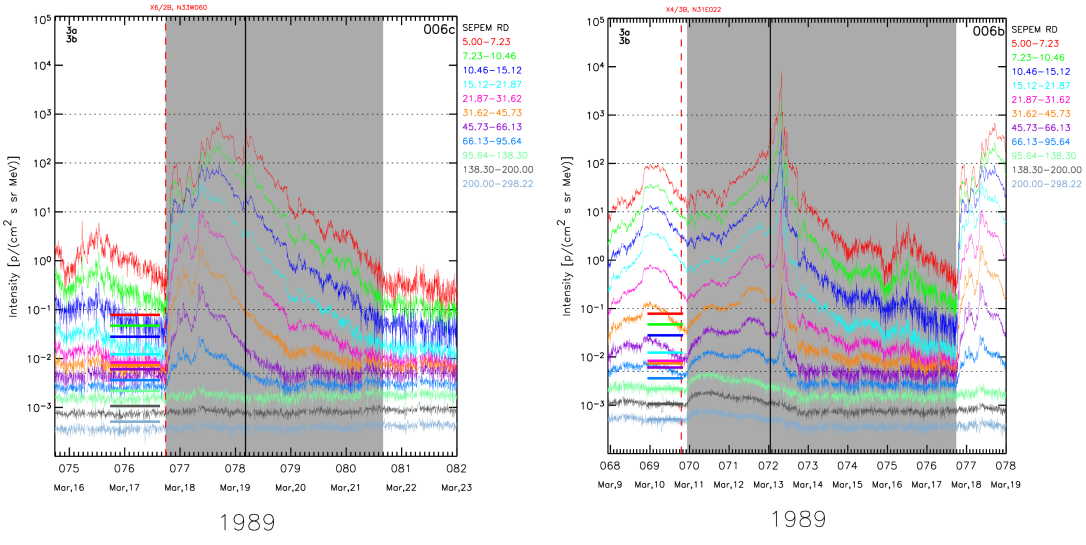

FIGURE 2.4: Proton differential intensities from the SEPEM RDSv2 for the 1989 March 17 (right) and 10 (left) SEP events. Examples of different intensity levels prior to and after the event.

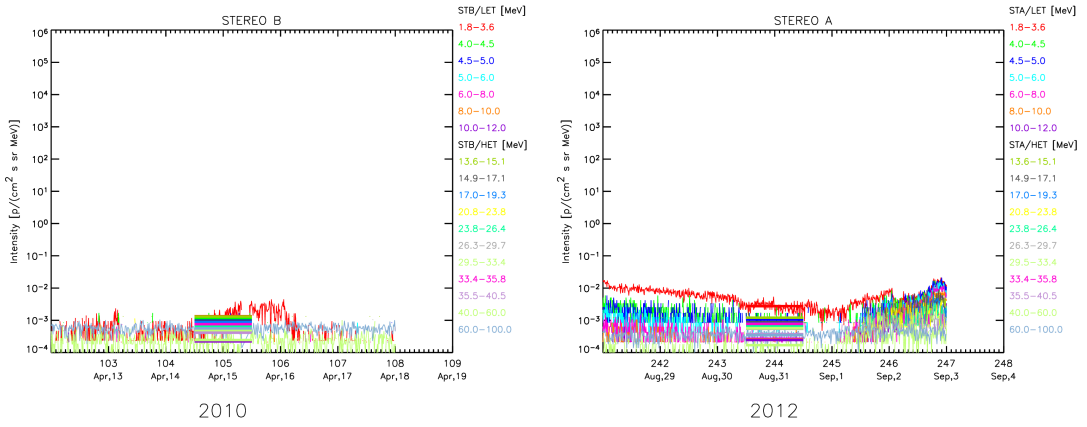

FIGURE 2.5: Examples of the level of intensities measured by the twin STEREO spacecraft during quiet or low-activity periods. The left panel corresponds to STEREO-B observations in April 2010 and the right panel to STEREO-A observations in August 2012. The horizontal lines are the mean intensity values calculated over a day. The energy channels are coloured coded as shown in the legends.

when computing the mean value. We left this for a further improvement of the algorithm due to the tiny impact in computing the fluences of these events.

In the case of the STEREO and Helios data we proceeded differently when computing the background levels due to the intensities observed. Figure 2.5 shows STEREO-B (left panel) and STEREO-A (right) observations during quiet or low-activity periods in 2010 and 2012, respectively. The left panel shows that, for some periods, the background levels coincide independently of the energy of the particles, and/or that data presents gaps for extended periods of time. The right panel shows a higher background level for 4.0 – 6.0 MeV protons prior to the September 1, but similar values for the energy range of the SEPEM data. Note also that, for example, the background level of the 60 – 100 MeV channel is higher than that of the 40 – 60 MeV channel; this could be due to the contribution of galactic cosmic rays not totally removed from the highest differential channel. Considering the behaviour of the background levels over energies, and that the smallest background level is approximately 10^{-4} [MeV cm^2 sr s]$^{-1}$ we took a conservative approach[4] by setting this value as a fixed background level, for all energies and for all analysed events measured by the STEREO spacecraft.

We found a similar behaviour for the Helios observations. Proton intensities show numerous data gaps in no-event times. For example, prior to the onset of the event on 1978 September 23 (not shown here), and the intensities show data gaps that prevent the calculation of the background level for this event. In other cases, the background levels coincide for protons in the 3.6 – 51 MeV range. Figure 2.2 shows two examples of events analysed. For the event on 1977 November 22 (left panel), there are no data gaps prior to the onset of the event and intensity values coincide. At the end of the event on 1976 March 28 (right panel), the intensity levels

[4]The lowest values in the data set are $> 9.0 \times 10^{-5}$ [MeV cm^2 sr s]$^{-1}$.

coincide for the three higher energy channels. The corresponding average value is marked by the dashed horizontal line shown in these plots. We used this value, 2.0×10^{-4} [MeV cm^2 sr s]$^{-1}$, as the fixed background intensity value for all the selected Helios events (that occurred between March 1976 and December 1982).

2.2.3.2 Filling of data gaps

In the three data sets, we found two kind of data gaps: (i) discontinuities in the temporal arrays and (ii) 0 values, NaN values, or values denoting bad data in the intensity arrays. In order to proceed to the calculation of the fluences, we first solved the (i) case, by enlarging the affected temporal arrays with the same time step as the data set used. For example, in the case of the SEPEM data, we added a point in the temporal array every 5 minutes, and filled the corresponding value in the intensity arrays with NaNs, in order to facilitate the computation of the background level.

Next, we treated the NaN values in the intensity arrays. When a NaN value was found, the program kept the value of the intensity in the previous point and searched for the next finite value. Then the program performed a linear interpolation with the logarithms of the intensity values at the two limits of the NaN zone, and saved the interpolated intensity values in the corresponding array. An example of the application of this algorithm is shown in the right panel of Figure 2.3 for the higher energy intensities.

2.2.4 Computation of fluences

After the background subtraction and the construction of continuous arrays (in time and differential intensities), we proceed with the calculation of the fluences (UF, DF,TF). The integration over time was performed in two ways: (i) a simple multiplication of the value of the intensity by the temporal step of the data set used (in seconds) and (ii) by applying a 5-point Newton-Cotes numerical integration algorithm. For this latter, we used the 'int_tabulated.pro' routine provided by the IDL programming and visualisation data package. Since both computing methods lead to similar values, we decided to continue further calculations with the second method. We want to point out that for those events in SREL for which an interplanetary shock was not identified, the UF and the TF coincide. Hence for these events, $DF = 0$.

2.2.5 Energy spectrum

STEREO and Helios proton data present energy channels different than the SEPEM RDSv2 energy channels. In order to compare the fluences derived from the various data sets, we fitted the energy spectra of the fluences (TF, UF and DF) from the selected events observed by STEREO and Helios spacecraft and extracted (or extrapolated) from the fittings the values corresponding

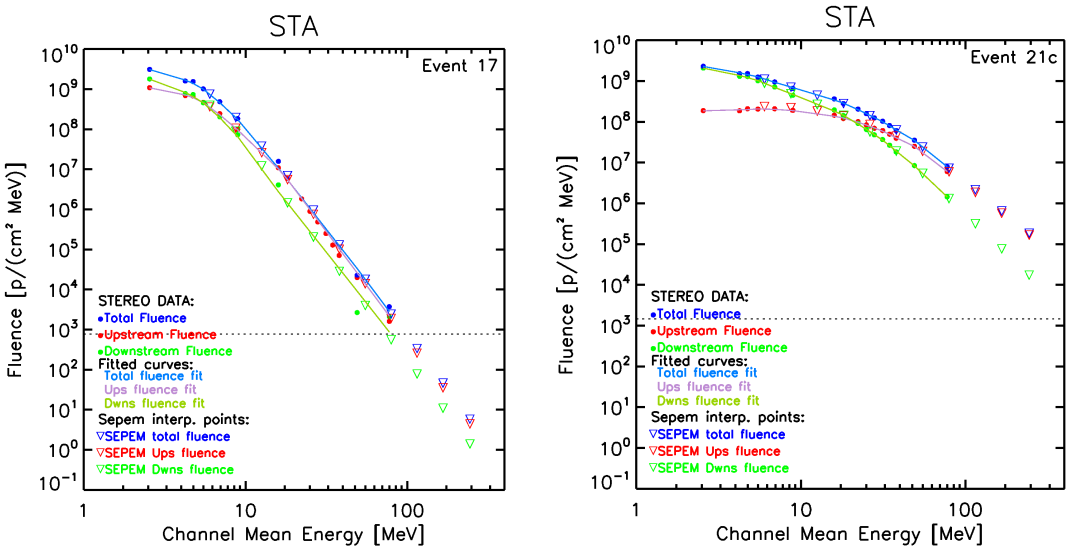

FIGURE 2.6: Examples of the energy spectra fitting for the total fluence (blue), upstream fluence (red) and downstream fluence (green). Left panel shows the 2012 May 26 SEP event and the right panel the 2012 July 23 SEP event observed both by STEREO-A. Small circles mark the fluence computed from observations and triangles mark the interpolated (solid symbols) and extrapolated (empty symbols) values for the SEPEM reference energy channels. Lines show the fittings performed for the total fluence (light blue), upstream fluence (mauve) and downstream fluence (olive green). For additional information, the horizontal dashed lines mark the fluence of background level set computed over the duration of the event.

to the mean energies of the SEPEM reference energy channels. Several methods to compute the energy spectra were tested: power-law, exponential roll-over and Weibull functions. None of them was applicable to all events in the analysis. Moreover, the Helios data presents only three or four points at most for the fitting, which introduces clear uncertainties in deriving the most appropriate spectrum shape. Note, that the Helios energy channels are wide, which renders difficult the identification of any roll-over energy. Therefore, we decided to the use two- or three-points interpolation method to derive the values of the three fluences for each event.

Figure 2.6 shows the energy spectra of the 2012 May 26 SEP event (left) and the 2012 July 23 SEP event (right) observed both by STEREO-A. The TF, UF and DF values are marked in blue, red and green, respectively. Small circles mark the fluence computed from observations and triangles mark the interpolated and extrapolated values for the SEPEM reference energy channels. Lines show the fittings performed for the TF (light blue), UF (mauve) and DF (olive green). These two events show a different evolution of the energy spectra that differ from other events, like the 2012 March 7 SEP event whose energy spectra follows a single power-law. For both events, the UF is smaller than the DF at low energy, whereas at higher energies, the UF is larger. Since the fittings are performed independently for the three fluences, we inspected the events one by one and imposed that $TF = UF + DF$, for each energy, both for STEREO and Helios observations.

2.2.6 Downstream contribution and description of the analysis tool

Once the previous steps were performed, we quantified the relative contribution of DF to the TF of an event as the Downstream-to-Total Fluence Ratio (hereafter, DTFR), $DTFR = DF/TF$.

In view of future extensions of the SREL, we developed a programme, named 'sepem.pro' that provides the fluences for all events in a given input SREL. Figure 2.7 shows the flow diagram of this programme that comprehends all the steps described in the previous sections. The programmes used for the STEREO and Helios data are similar to this one, but adapted to the corresponding input data sets, and to the specific caveats of the data sets (i.e., in order to treat the different types of the data gaps encountered).

The input files to the programs are two: (1) the 'events.txt' file, which is the SREL list, in ascii format and (2) the file, 'data_sepem.sav', containing the provided version of the SEPEM RDSv2. The main program calls several routines, that we outline here:

- 'read_events.pro' and 'read_sepem_data.pro' that read data from the 'event.txt' and the 'data_sepem.sav', respectively
- 'fill_temporalgaps.pro' that enlarges the arrays in case of missing time steps in the data.
- 'backgroundmean.pro', for each event computes the corresponding background intensity levels to be subtracted.
- 'fillnans.pro', replaces NaN-values in the intensity arrays by interpolated intensity values.
- 'set_time.pro', provides the temporal array in string format 'dd/mm/yyyy hh:mm' for the output file 'input_for_radial_dependence_analysis.txt'.

The output files are two: 'output_sepem.txt' and 'input_for_radial_dependence_analysis.txt'. The first file is the input file used for the next analysis of the DTFRs as a function of the heliolongitude of the parent event. It is an ascii file with columns that contain: the event/enhancement number, the ratio of downstream-time duration over the total event duration, the energy channel, the mean energy of the channel, the peak flux intensity, the TF, the UF, and the DF, the event type (as shown in App. B), the DTFR, the background intensity, the longitude of the parent source, the acceptance for the analysis and the type of solar wind. The second file contains similar information but for all events in the SREL and with the addition of the start date and end date of the event. Finally, the 'sepem.pro' program has the option of writing, in the two output files, the information only for the events of the SREL selected for the downstream analysis.

2.3 Multi-spacecraft analysis

In this section we analyse those SEP events from the SREL and STEREO event lists, Tables A.1, A.2, A.3, that (i) are observed simultaneously at least by one of the STEREO spacecraft

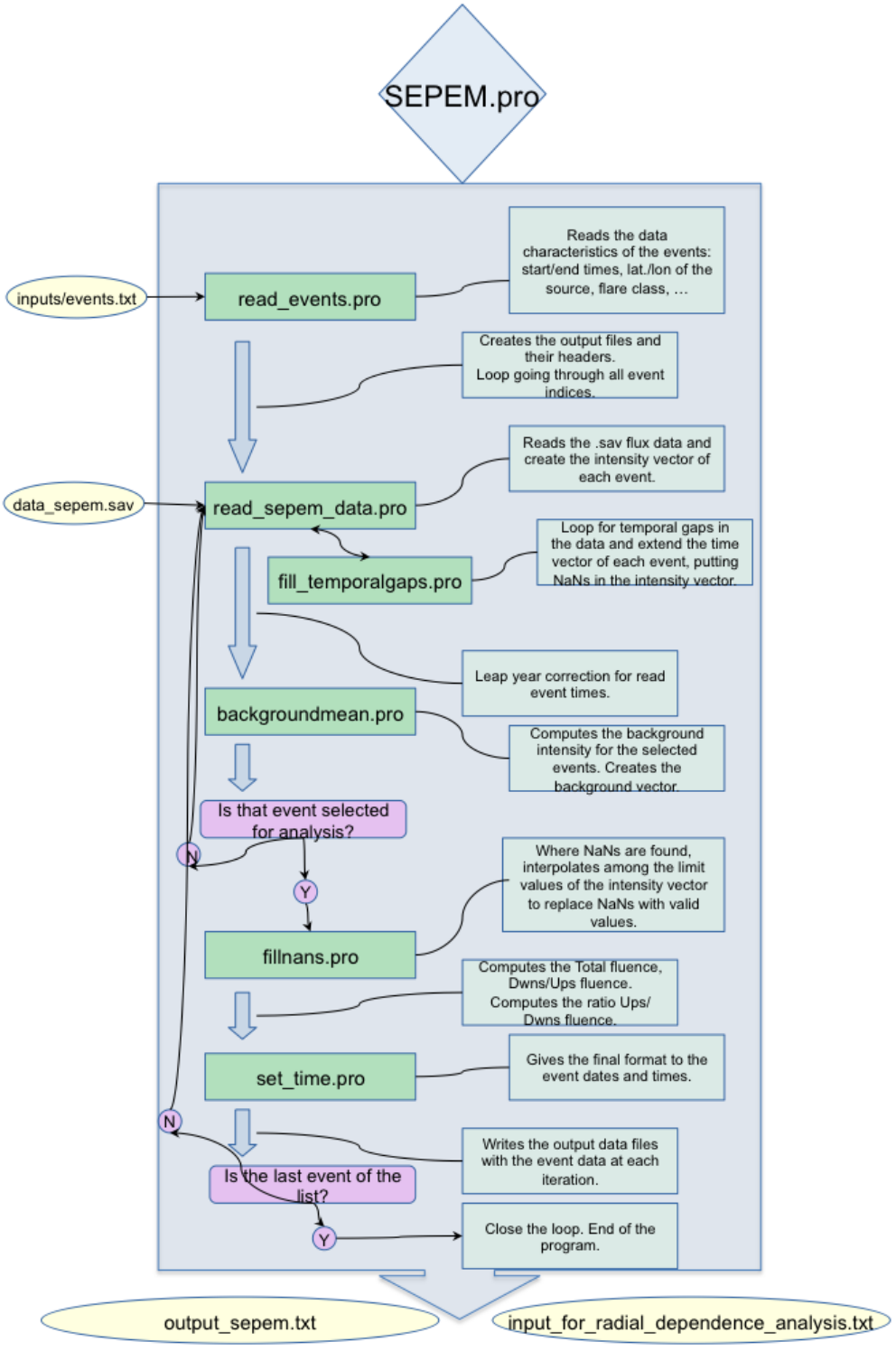

FIGURE 2.7: Flux diagram of the programme used to compute the fluences of the SEP events contained in the SREL list.

TABLE 2.2: List of the eight selected pairs of SEP events for the multi-spacecraft study (top rows: near-Earth observations; middle rows: STEREO-A observations; bottom rows: STEREO-B observations). We numbered the events from 1 to 25, and used letters to distinguish between different episodes inside the same event. We show, from left to right: the event number; the start and end times of the enhancement; the latitude of the solar parent source related to the SEP enhancement, being positive (negative) for northern (southern) latitudes; the heliolongitude of this solar source, being positive (negative) for western (eastern) longitudes; the observed flare start time (X-ray emission); the shock arrival time to the spacecraft; the solar wind type, termed as 'fast' if $v_{sw} > 480$ km s^{-1}, and as 'slow' otherwise; and the flare class according to the peak of the X-ray emission.

Event	Start time (date & UT)	End time (date & UT)	Solar origin Lat.	Long.	Solar Event time (X-ray)	Shock arrival time	Solar wind type	X-ray flare class
			Near-Earth observations - SEPEM data					
Event 3	07/03/2011 20:10	13/03/2011 18:00	30	48	07/03/2011 19:43	10/03/2011 05:45	slow	M3.7
Event 6	04/08/2011 04:34	08/08/2011 16:00	16	38	04/08/2011 03:40	05/08/2011 18:40	slow	M9.3
Event 10	22/10/2011 10:30	26/10/2011 16:00	27	87	22/10/2011 10:00	24/10/2011 17:49	slow	M1.3
Event 12	26/11/2011 07:30	30/11/2011 15:00	11	47	26/11/2011 06:09	28/11/2011 21:00	slow	C1.2
Event 13-c	27/01/2012 18:00	03/02/2012 03:54	33	85	27/01/2012 17:37	30/01/2012 15:43	slow	X1.7
Event 16	17/05/2012 02:05	21/05/2012 17:00	7	88	17/05/2012 01:25	20/05/2012 01:20	slow	M5.1
Event 15-b	06/03/2012 23:30	13/03/2012 16:30	18	-31	07/03/2012 00:02	08/03/2012 10:53	slow	X5.4
Event 22	01/09/2012 00:00	06/09/2012 16:00	-19	-42	31/08/2012 19:59	03/09/2012 11:21	slow	C8.4
			STEREO A					
Event 3	07/03/2011 20:10	12/03/2011 07:20	23	-40	07/03/2011 19:43	09/03/2011 06:47	slow	M3.7
Event 6	04/08/2011 04:34	09/08/2011 11:30	19	-63	04/08/2011 03:40	06/08/2011 12:42	slow	M9.3
Event 10	22/10/2011 16:20	25/10/2011 18:45	39	-18	22/10/2011 10:00	25/10/2011 04:50	slow	M1.3
Event 12	26/11/2011 07:30	30/11/2011 00:20	20	-59	26/11/2011 06:09	28/11/2011 14:50	slow	C1.2
Event 13-c	27/01/2012 18:00	09/02/2012 07:59	30	-23	27/01/2012 17:37	29/01/2012 13:03	slow	X1.7
Event 16	17/05/2012 02:05	22/05/2012 15:15	-3	-27	17/05/2012 01:25	18/05/2012 12:42	fast	M5.1
			STEREO B					
Event 15-b	06/03/2012 23:30	13/03/2012 16:30	7	87	07/03/2012 00:02	08/03/2012 13:36	slow	X5.4
Event 22	31/08/2012 20:30	08/09/2012 07:39	-8	74	31/08/2012 19:59	03/09/2012 07:11	slow	C8.4

and in the SEPEM RDSv2 data, and (ii) for which the *DF* could be determined. The fact that the events in the STEREO event list were initially selected from the SEPEM event list, and hence, restricted to the period between January 2010 and March 2013, caused that in the spacecraft configuration during the more active period studied, 2011-2012, STEREO-B was located too eastward from the Earth to detect a relevant SEP enhancement in most of the events. Also, the longitudinal separation between the two STEREO spacecraft was ~180° in 2011 to ~230° in June 2012. These two facts establish a bias in favour of pairs of events simultaneously seen at near-Earth and by one of the STEREO spacecraft (usually STEREO-A) to the detriment of those events that might have been observed by the two STEREO spacecraft solely.

2.3.1 Event selection

Table 2.2 lists the eight pair of events fulfilling the above criteria. We found 6 events simultaneously detected by near-Earth spacecraft and STEREO-A and 2 by near-Earth spacecraft and STEREO B. The numbering of the events and the information listed in Table 2.2 is the same as in Tables A.1, A.2, A.3.

In Figure 2.8 and in Figure 2.9, we respectively show an example of a discarded and of a selected event. In the discarded instance, the SEP event detected at the near-Earth space on 2012 September 28 started on the 28th at 00:20 UT, as can be seen in the SEPEM data (left panel in Fig. 2.8). At the same time, STEREO-A detected an SEP enhancement that was preceded by another enhancement associated by a previous CME on September 27 at 09:55 UT, observed by the COR-1 coronagraph. This CME was accompanied with extreme ultraviolet emission detected by EUVI of the SECCHI package (Howard et al., 2008) on board of the STEREO spacecraft. This latter event was better connected to STEREO-A (W21) than to the Earth (W146). The overlapping of the intensities from both SEP enhancements at STEREO-A prevented from satisfactorily separate their contributions to the UF (see also Richardson et al., 2014).

Figure 2.9 shows the SEP events on the 2012 January 27 observed by STEREO-A (left panel) and near-Earth (right panel) that were selected for this multi-spacecraft study. The top middle panel of Figure 2.9 presents the spacecraft configuration. As seen from the Sun, the shock was directed slightly to the East of STEREO-A (E23), whereas for the near-Earth spacecraft, the event was a west limb event (W85). The bottom middle panel shows the TF, UF and DF energy spectra of the STEREO SEP event (see Sect. 2.2.5). At both spacecraft, the rising phase of the profiles is clearly seen for $E > 5$ MeV, despite the event is preceded by high intensities, for $E < 40$ MeV, due to the event on January 23. In the case of the near-Earth space, the upstream and downstream regions are clean of other interplanetary structures. For the STEREO-A event, there is another interplanetary shock (first vertical line in the left panel of Figure 2.9) prior to the arrival of the main shock (second vertical line). This first shock does not modify the intensity-time profiles of the particles at its crossing by STEREO-A, and the jumps registered in the plasma data are small. For this reason, we kept the event in the present analysis and consider the second as the main shock, to compute the UF and the DF. However, it is possible that this shock may have acted as a barrier for the main interplanetary shock, enhancing the SEP event.

2.3.2 Fluence Analysis

For the selected eight pairs of events, we studied the variation of the TF and of the downstream-to-total fluence ratios, DTFRs, with the heliolongitude of the events as seen from each spacecraft. In Figure 2.10, we show the total fluence [p/(cm^2 MeV)], for two of the SEPEM reference energies, 8.70 MeV (top) and 54.99 MeV (bottom), respectively, as a function of the heliolongitude of the parent source with respect to the Sun-spacecraft line, in degrees. Eastern (western) locations are negative (positive). Each pair of events are plotted with the same colour and labelled following the event numbers listed in Table 2.2. Fluences computed from STEREO observations are indicated with inverted triangles and fluences computed using SEPEM data with diamonds. In this way, it is easy to compare the fluences for the two SEP events generated by the same eruptive phenomena, but registered from spacecraft widely separated in longitude; thus,

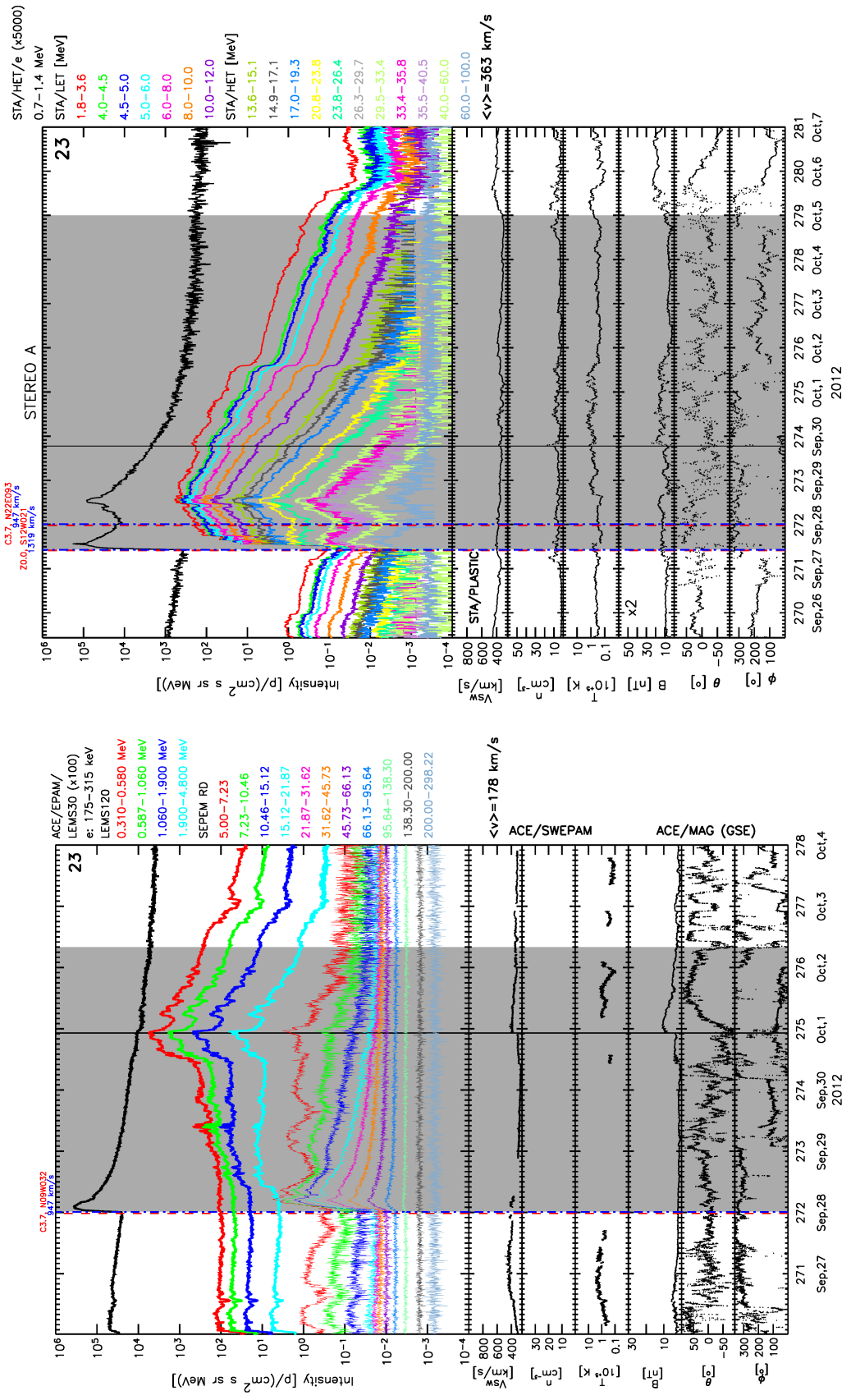

FIGURE 2.8: SEP event on 2012 September 28. Left: SEPEM and ACE data. Right: STEREO-A data. This event was not selected for the study because two events contributed to the SEP enhancement detected at STEREO-A.

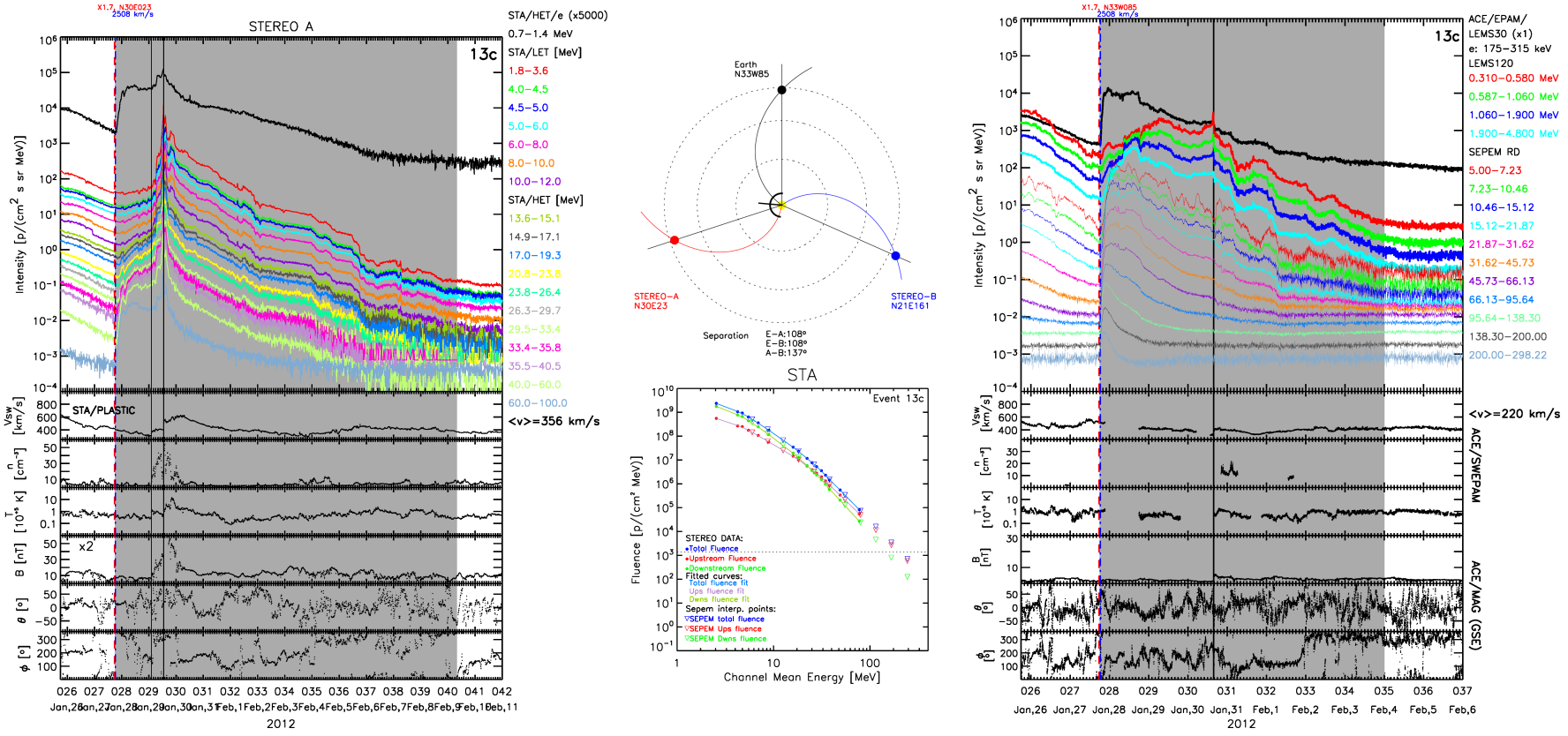

FIGURE 2.9: 2012 January 27 SEP event. The left panel shows STEREO-A observations and the right panel shows near-Earth observations (SEPEM and ACE data). The times of the associated flare onsets and CME first detection times are marked with red and blue vertical dashed lines, respectively, in the SEP event plots. At the top of each plot, the flare location and the flare soft X-ray peak intensity level are indicated (red) as well as the projected CME speed (blue). The times of the associated interplanetary shock passage by each spacecraft are indicated by black vertical solid lines. The top middle panels display the spacecraft configuration on January 27. Red, black and blue circles mark the location of STEREO-A, the Earth and STEREO-B, respectively. Nominal IMF lines connecting the spacecraft to the Sun are computed for the observed solar wind speed, following the same colour code. The relative angular separation in longitude between the origin of the flare and each spacecraft is indicated. In the panel displaying the spacecraft configuration, the relative separation between the origin of the flare and each spacecraft are shown. Further, we plot the direction (small black line) of the CME-driven shock (small arc), centred at the flare heliolongitude. The bottom middle panel shows the fluence spectra (small circles) of the SEP event measured by STEREO-A, the fits (curves) and the extrapolated values for the SEPEM reference energies (triangles) as explained in Section 2.2.5.

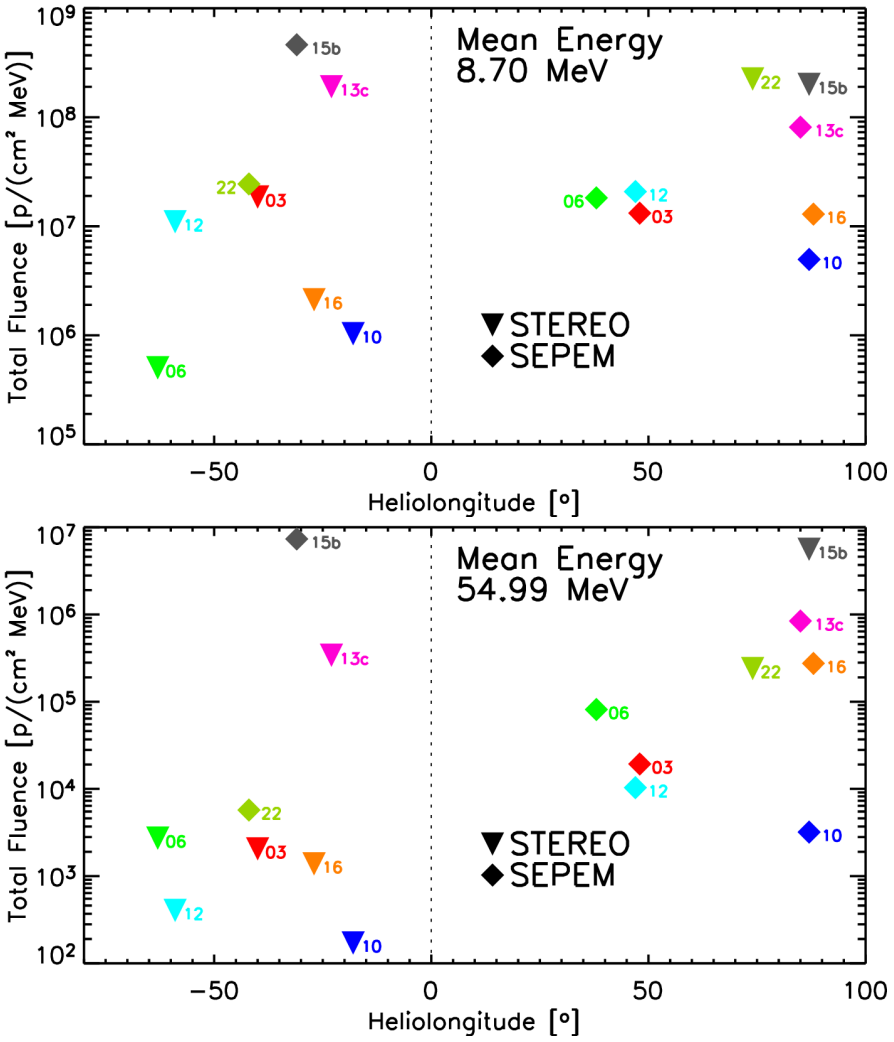

FIGURE 2.10: Total Fluence variation with the heliolongitude for 8.7 MeV protons (top panel) and for 54.99 MeV (bottom panel) protons. Diamonds indicate Total Fluence values derived from SEPEM data, and inverted triangles from STEREO data. Events detected simultaneously are indicated with the same colour.

meaning, that the magnetic connection to the particles source is established under different conditions. As can be seen in Figure 2.10, there is not a clear trend of the total fluence as a function of the heliolongitude of the solar parent event at the lower energies. At high-energies, in 6 out of 8 cases, the eastern events show fluences significantly smaller than their western counterparts.

Next, we analysed the contribution of the DF to the TF of each event. Figure 2.11 shows, for the same energies and with the same format as the previous two figures, the derived DTFRs as a function of the heliolongitude. In both cases, we can clearly see that the DTFRs are smaller for the western events (positive values of the heliolongitude) than the DTFRs derived from the eastern events (negative heliolongitude values). In order to quantify this variation, we computed the mean DTFRs for the two groups of events that show their western counterparts clustered around W45 (events 3, 6, and 12) and around W85 (events 13c, 15b and 16).

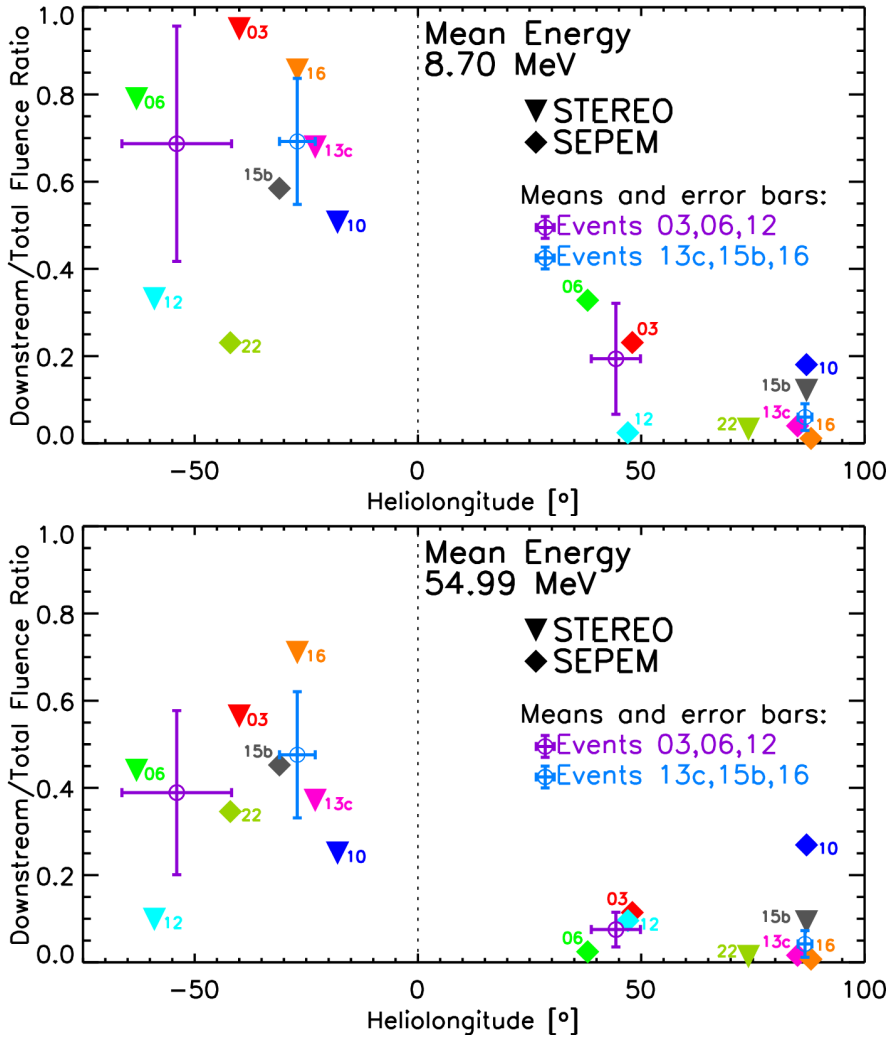

FIGURE 2.11: Downstream-to-Total fluence ratio (DTFR) variation with the heliolongitude for 8.7 MeV protons (top panel) and for 54.99 MeV protons (bottom panel). Diamonds indicate Total Fluence values derived from SEPEM data, and inverted triangles, from STEREO data. Events detected simultaneously are indicated with the same colour. The mean DTFR values of each group of events are marked by open circles. Vertical error bars mark the standard deviation of the DTFRs. Horizontal bars indicate the angular separation of the grouped events.

Note that we discarded event 10 (2011 October 22) because the SEP event seen at STEREO-A only shows an SEP enhancement for $E < 26.3$ MeV and in SEPEM data, for $E < 31.62$ MeV; which prevents the analysis for all energies. In addition, we discarded event 22 (2012 August 31) because the heliolongitude for STEREO-B was W74, slightly separated from the three other western limb events and because the SEPEM data shows only an enhancement for $E <$ 31.62 MeV with very irregular shape in the low-energy profiles. In their ICME list (`http://www.srl.caltech.edu/ACE/ASC/DATA/level3/icmetable2.htm`), Richardson and Cane identify signatures of an ICME passage from the 2012 September 1 at 06:00 UT to 2012 September 3 15:00 UT. A rotation in the polar angle of the magnetic field, indicates the presence of such interplanetary structure, although its solar counterpart (the CME) is not

identified. Hence, the upstream region of this event is affected by the presence of this ICME, and consequently, we decided not to include the event in the DTFRs analysis.

In order to compute the mean DTFRs values and their standard deviation, we used the logarithm of the total fluence of the events as a weighting factor. The total fluence of the events is a measure of the size of SEP events. In statistical fluence models, like those available in the SEPEM web server, larger events have a greater impact on the final results. Hence, in order to be more accurate when implementing our study of the downstream region in the SEPEM statistical SEP model for interplanetary missions, we biassed the mean values obtained toward larger events. Note that although we give a higher weight to the larger events (which have less uncertainty in their fluence values because intensities are well above background levels), by taking the logarithm of the total fluence, we still consider the contribution of smaller events. Figure 2.11 shows the mean DTFRs values (open circles) obtained for the West-limb group (blue) and the W45 group (cyan). Vertical error bars mark the standard deviation of the fluence ratios and the horizontal bars indicate the angular separation of the three events in each group.

Owing to the small number of valid events found in our study, we faced a rather large dispersion in the DTFR values, especially for the eastern events. Figure 2.12 shows the weighted mean DTFRs (solid circles) for 6 – 115 MeV protons. Energies are typified by colours and linked by dashed lines, which indicate the general trend of the studied ratios: western observations yield a lower DTFR than their eastern counterparts. That trend is shown by all studied energies and we also find that the weighted mean DTFRs decrease with increasing proton energy. For the group of events 3, 6, and 12 we do not show the average DTFRs for $E > 54.99$ MeV because the events measured by STEREO-A do not show any particle enhancement in the highest energy channel (60 – 100 MeV). Between the two eastern groups we find no significant difference in the mean values of the fluence ratios. The same is true for the western groups with the exception of the two lower energy channels, which show increasing DTFRs towards central meridian longitudes.

2.3.3 Summary

In this multi-spacecraft study we identified eight SEP events simultaneously detected by near-Earth spacecraft and by one of the STEREO spacecraft and analysed the heliolongitudinal dependence of the downstream contributions to the total fluence of the SEP events. For each pair of events, we find that the western event has a smaller DTFR than its eastern counterpart. Also, we find that the DTFRs decrease with the energy of the particles. For the two groups of events established, the dependence of the DTFR with the heliolongitude varies from event to event, within events of similar heliolongitude. For the two groups of events, we find no significant difference in the mean values of the DTFRs between the two eastern groups as well as between the two western groups.

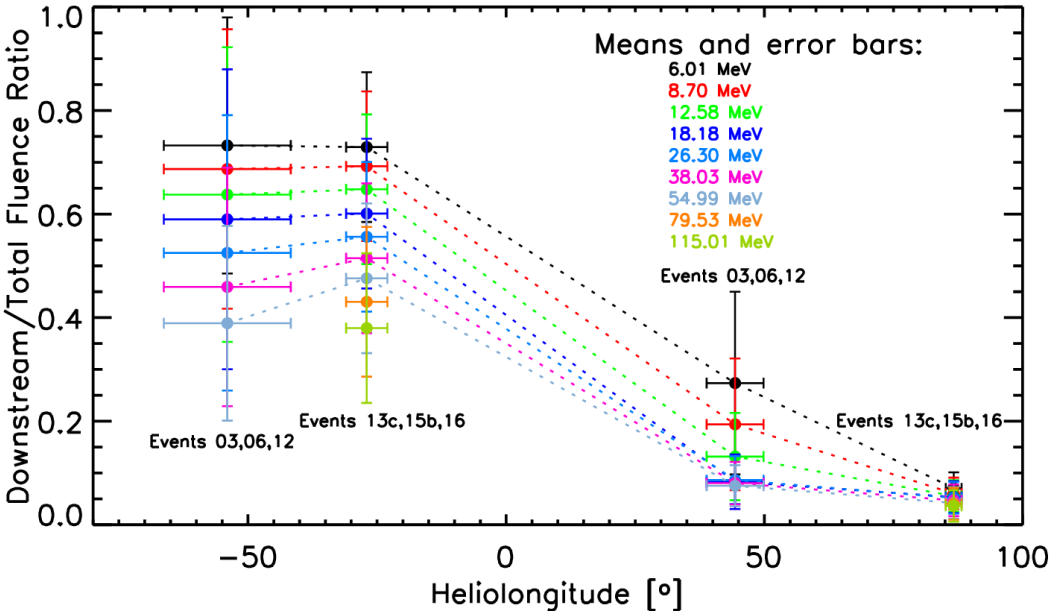

FIGURE 2.12: Weighted mean DTFRs and tendencies as a function of the energy. Mean DTFRs derived for each group of events (solid circles) and for all energies (colour coded). Error bars indicate the same as in previous figures.

The main conclusion of this multi-spacecraft study is that in the case of events originated by the same solar activity, there is a variation of the DTFRs with the heliolongitude of the parent event. The contribution of the downstream region fluence to the total fluence of the events is larger for eastern cases than for western events.

2.4 Analysis of the Downstream-to-Total Fluence Ratios

After confirming that there exists a variation of the DTFRs with the heliolongitude of the parent solar source in SEP events measured simultaneously by spacecraft located at different positions in the heliosphere, we extended the study to the whole set of events observed at 1 AU and at other radial distances from the Sun.

2.4.1 Longitudinal and radial variation

We started with the analysis of the distribution of the DTFRs as a function of the heliolongitude for all events available at ~1 AU. Figure 2.13 shows the DTFRs for 8.7 MeV protons; all events shown are labelled with the event number indicated in the SREL (Table A.4), and in the STEREO event lists (Tables A.2 and A.3). The events in SREL are indicated by using different colours and symbols corresponding to the seven categories of events associated with shocks, following the SOLPENCO2 reference cases (see App. B). The DTFRs corresponding to STEREO observations are indicated by red diamonds.

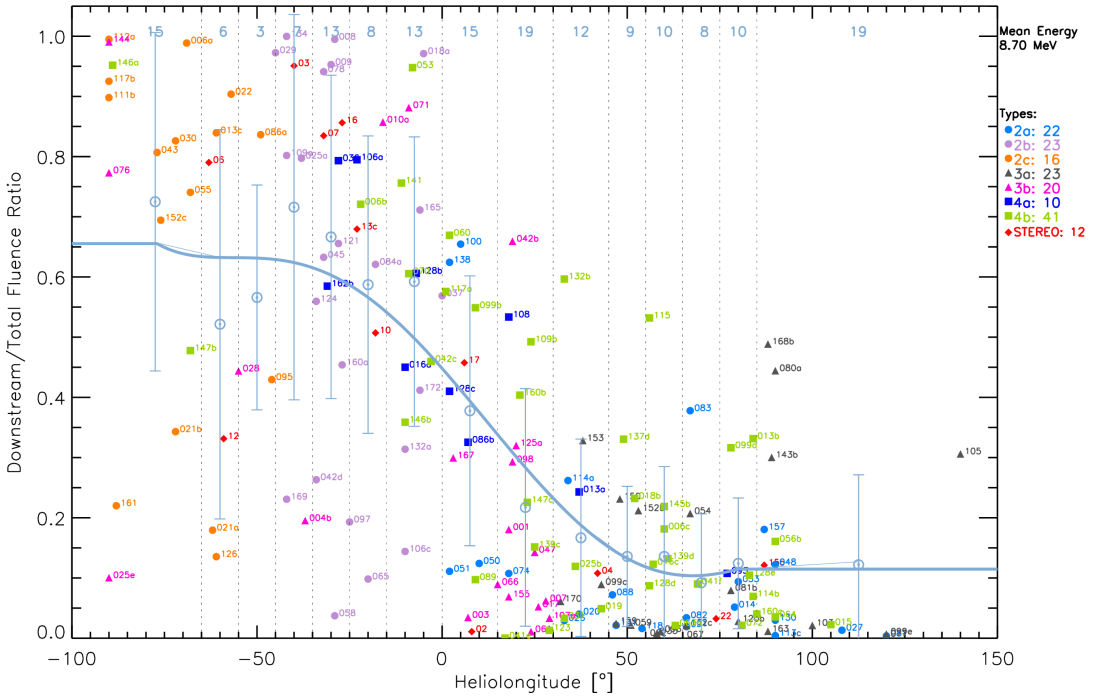

FIGURE 2.13: Downstream-to-total Fluence Ratios for 1 AU SEP events and for 8.7 MeV protons of SEP as a function of the heliolongitude of the associated main solar particle source. Events in SREL are labelled with the corresponding event number and marked with different symbols and colours according to SOLPENCO2 different event types (as indicated in the legend). Events detected by the STEREO spacecraft are indicated by red diamonds and numbered as in Tables A.2 and A.3. Sky blue open circles mark the weighted averaged ratios for the longitude sectors delimited by black dashed vertical lines. The error bars mark the standard deviations. The sky blue line is a polynomial fit to the average values, in order to show the tendency followed by the DTFRs as a function of the heliolongitude.

The total number of events in this study is 168: 156 events from the SREL and 12 events from the STEREO event list[5].

The SOLPENCO2 model uses a grid of virtual observers placed at fourteen longitudinal positions with respect to the simulated interplanetary shock nose (Aran et al., 2011a). Since the final objective is to include the results from this study into the radial dependences predicted by SOLPENCO2, we initially considered longitudinal sectors limited by the fourteen angular positions of the model. The black dashed vertical lines in Figure 2.13 mark the limits of the angular sectors considered (also indicated in Figure 2.14). The sky blue open circles are the weighted mean DTFRs calculated as described in Section 2.3.2 and the vertical error bars indicate the

[5]After performing the whole analysis, we realised that the event 21c observed by STEREO-A was not included in the analysis. This is the SEP event starting on 23 July 2012, associated with a central meridian source (W04). Although this event is one of the largest in terms of fluence and peak intensity in the analysed period, given the dispersion in the DTFRs around central meridian, its inclusion would not have changed the final results significantly (see next section with the moving mean analysis). Note that for 8.7 MeV protons the DTFR for this event is 0.69, close to events 60 and 100. This would imply that the mean ratio would have been higher, but only slightly because in this set of events between W00 and W15, there are other large events, like the 128c (2003 October 29) and 86b (2000 July 14) with lower DTFRs, 0.41 and 0.33, respectively.

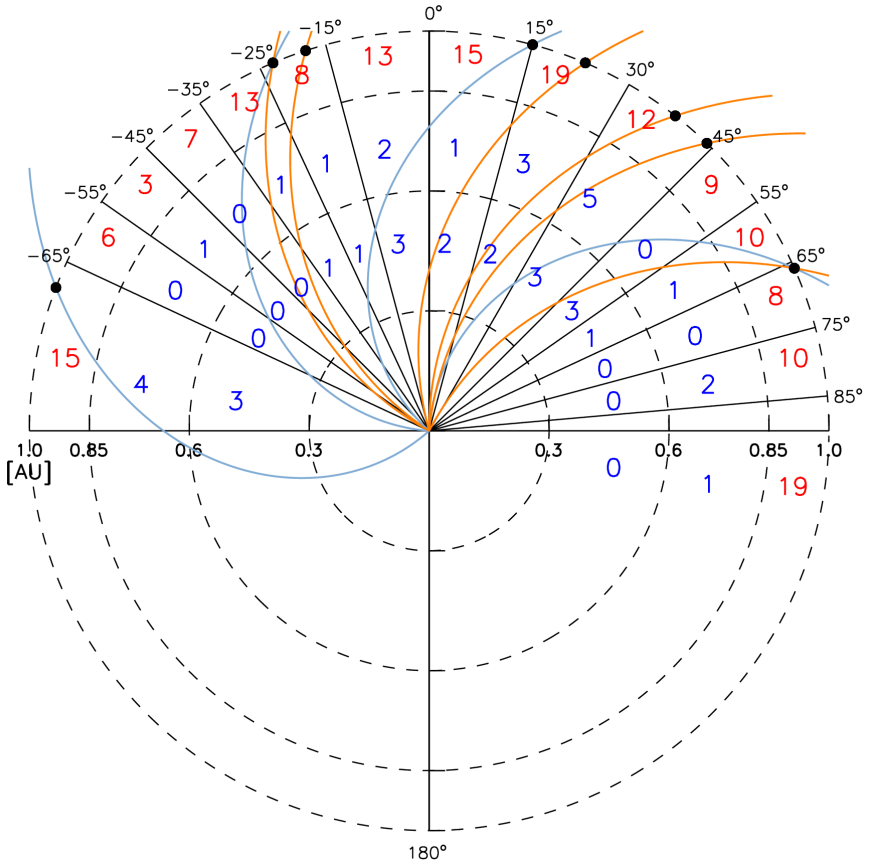

FIGURE 2.14: Number of events per longitudinal and heliocentric radial distance bins. External red numbers correspond to events observed by spacecraft at ~1 AU and the internal to events measured by the Helios spacecraft from 0.3 – 0.6 AU. Blue numbers correspond to events observed by the Helios spacecraft when located in the intermediate region. Black solid circles mark the angular position of the near-Earth spacecraft with respect to the solar source for the reference events simulated with SOLPENCO2. The IMF lines connecting these observers with the Sun, following a Archimedean spiral geometry, are shown in sky blue(orange) for slow(fast) solar wind conditions.

standard deviation of the mean values. Owing to the large spread of the values of the DTFRs, the error bars are large, especially for SEP events with sources originating from central meridian and eastern solar sites. The number of events used to obtain the mean value for each sector is indicated at the top of Figure 2.13. In order to show the tendency of the DTFRs with the heliolongitude, we fitted a polynomial to the mean values the angular sectors, between ~E78 and W80 longitudes (solid sky blue line in Fig. 2.13). In addition, instead of using the angular bins of SOLPENCO2, we computed the average values of the DTFRs by constructing angular bins with equal number of events. Both methods yielded similar results.

Figure 2.14 shows the longitudinal sectors into which we divided the ecliptic plane. We shifted the heliolongitude positions to a reference frame where the spacecraft is positioned at different longitudes with respect to the flare or the direction of the shock-nose, which is fixed at 0°. In this way, eastern events are seen by spacecraft placed in the top left quadrant of

Figure 2.14, and western events are seen by spacecraft in the right quadrants. Concentric dashed circles mark the heliocentric distance boundaries that we established to study the DTFRs of events measured at different radial distances, 0.3 – 0.6 AU, 0.6 – 0.85 AU and ~1 AU (i.e., 0.96 – 1.09 AU). The number of events found for each longitudinal sector and radial ring are indicated in the plot (in blue for events observed by Helios between 0.6 – 0.85 AU and in red for events observed at the other heliocentric radial distances)[6]. The most eastern sector covers from −65° to −180° and the last sector in the western heliolongitudes spans from 85° to 180°. From this figure, one can easily notice that there is a scarce number of events between 0.3 – 0.85 AU for eastern longitudes between −15° and −65°, and for > 55° in the west. We want to point out that the number of events shown in Figure 2.14 corresponds to the largest number possible (corresponding to 8.7 MeV protons); the situation worsens for higher energy channels, since the number of events showing particle enhancements decreases with the energy of the particles.

The DTFRs corresponding to the events observed by the Helios spacecraft, at 8.7 MeV, are listed in Tables 2.3 and 2.4 together with the corresponding DTFRs derived from 1 AU observations. DTFRs are shown for the first seven SEPEM standard energy channels which encompass the actual energy range of the E6 particle experiment of the Helios spacecraft. Due to the small number of events seen by Helios that could be selected for the analysis of the *DF*, we used wider longitudinal bins than in the case of 1 AU observations. As can be seen, standard deviations are large for most of the longitudinal bins (or sectors) and for the two regions (in radial distance) because of the small number of events in each bin; some of these sectors contain less than 2 events. In spite of the reduced number of events, that prevents the inference of any statistical meaningful quantification of the variation of the DTFRs, it is found, qualitatively, that the eastern events tend to show larger DTFRs than western events also for distances < 0.85 AU. Moreover, note that DTFRs are roughly constant with the radial distance for the majority of angular sectors and energies.

The left graph of Figure 2.15 shows the values of the mean DTFRs derived from all studied events, per longitudinal sector and for 8.7 MeV protons. The corresponding standard deviations are shown in the right panel. Owing to the values of the associated standard deviations, the mean DTFRs found show a roughly constant value with the radial distance, specially in the case of western events. For eastern events between 0° to 55° the mean values of the DTFRs show a slight increase with the heliocentric radial distance of the observers. In the case of far eastern events, the DTFR mean ratios show a slight increase for decreasing radial distances, at this energy.

In Figure 2.14 and Figure 2.15, we also show the position of the near-Earth spacecraft for the reference SEP events modelled with SOLPENCO2 (see App. B and Aran et al., 2017a, for further details) marked by black solid circles along the dashed circumference at 1 AU. The blue

[6]We added the event 94 to the study; thus, in the 1 AU W00 to W15 sector, we have 16 events instead of the 15 indicated in Figure 2.14.

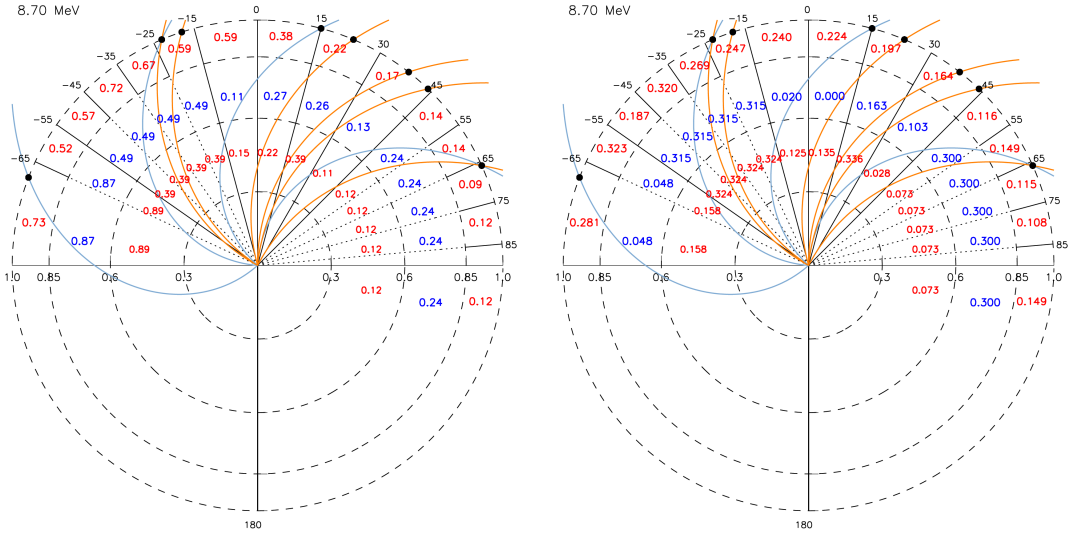

FIGURE 2.15: Sector-averaged DTFRs for 8.7 MeV protons (left graph) and corresponding standard deviations (right graph). Format is the same as in Figure 2.14.

TABLE 2.3: Downstream-to-total fluence mean ratios and standard deviations as a function of the heliolongitude (in degrees) and proton energy.

Energy	**Distance**	**Downstream-to-total fluence ratios per longitudinal sector**							
[MeV]	**[AU]**	**[-180,-65)**	**[-65,-55)**	**[-55,-45)**	**[-45,-35)**	**[-35,-25)**	**[-25,-15)**	**[-15,0)**	**[0,15)**
6.01	1	0.74 ± 0.27	0.58 ± 0.31	0.63 ± 0.17	0.74 ± 0.31	0.72 ± 0.26	0.63 ± 0.26	0.64 ± 0.23	0.45 ± 0.25
	0.6 – 0.85	0.92 ± 0.02		0.51 ± 0.31				0.16 ± 0.06	0.40 ± 0.00
	0.3 – 0.6	0.90 ± 0.13		0.44 ± 0.36				0.17 ± 0.15	0.23 ± 0.14
8.70	1	0.73 ± 0.28	0.52 ± 0.32	0.57 ± 0.19	0.72 ± 0.32	0.67 ± 0.27	0.59 ± 0.25	0.59 ± 0.24	0.38 ± 0.22
	0.6 – 0.85	0.87 ± 0.05		0.49 ± 0.32				0.11 ± 0.02	0.27 ± 0.00
	0.3 – 0.6	0.89 ± 0.16		0.39 ± 0.32				0.15 ± 0.13	0.22 ± 0.14
12.58	1	0.71 ± 0.28	0.47 ± 0.32	0.49 ± 0.19	0.68 ± 0.32	0.61 ± 0.28	0.54 ± 0.23	0.54 ± 0.25	0.30 ± 0.20
	0.6 – 0.85	0.81 ± 0.08		0.48 ± 0.32				0.09 ± 0.00	0.19 ± 0.00
	0.3 – 0.6	0.87 ± 0.19		0.35 ± 0.29				0.13 ± 0.10	0.22 ± 0.13
18.18	1	0.71 ± 0.28	0.41 ± 0.31	0.39 ± 0.15	0.64 ± 0.32	0.55 ± 0.28	0.48 ± 0.22	0.49 ± 0.25	0.24 ± 0.18
	0.6 – 0.85	0.74 ± 0.14		0.47 ± 0.32				0.07 ± 0.02	0.13 ± 0.00
	0.3 – 0.6	0.86 ± 0.23		0.31 ± 0.25				0.11 ± 0.09	0.22 ± 0.13
26.30	1	0.72 ± 0.26	0.38 ± 0.28	0.35 ± 0.13	0.61 ± 0.30	0.52 ± 0.27	0.46 ± 0.18	0.43 ± 0.24	0.23 ± 0.16
	0.6 – 0.85	0.65 ± 0.21		0.47 ± 0.32				0.05 ± 0.02	0.09 ± 0.00
	0.3 – 0.6	0.84 ± 0.28		0.28 ± 0.23				0.09 ± 0.07	0.22 ± 0.12
38.03	1	0.70 ± 0.27	0.41 ± 0.23	0.24 ± 0.08	0.57 ± 0.28	0.48 ± 0.27	0.44 ± 0.11	0.42 ± 0.24	0.21 ± 0.15
	0.6 – 0.85	0.56 ± 0.25		0.40 ± 0.26				0.06 ± 0.03	0.05 ± 0.00
	0.3 – 0.6	0.84 ± 0.26		0.18 ± 0.13				0.08 ± 0.07	0.26 ± 0.14
54.99	1	0.60 ± 0.28	0.29 ± 0.17	0.07 ± 0.00	0.52 ± 0.31	0.38 ± 0.16	0.36 ± 0.07	0.36 ± 0.24	0.20 ± 0.16
	0.6 – 0.85	0.51 ± 0.25		0.29 ± 0.19				0.07 ± 0.04	0.03 ± 0.00
	0.3 – 0.6	0.85 ± 0.23		0.11 ± 0.05				0.07 ± 0.07	0.26 ± 0.14

TABLE 2.4: Downstream-to-total fluence mean ratios and standard deviations as a function of the heliolongitude (in degrees) and proton energy.

Energy	**Distance**	**Downstream-to-total fluence ratios per longitudinal sector**						
[MeV]	**[AU]**	**[15,30)**	**[30,45)**	**[45,55)**	**[55,65)**	**[65,75)**	**[75,85)**	**[85,180)**
6.01	1	0.26 ± 0.23	0.22 ± 0.20	0.15 ± 0.13	0.18 ± 0.17	0.12 ± 0.12	0.16 ± 0.14	0.15 ± 0.17
	0.6 – 0.85	0.30 ± 0.20	0.19 ± 0.16			0.27 ± 0.32		
	0.3 – 0.6	0.44 ± 0.38	0.12 ± 0.03			0.15 ± 0.09		
8.70	1	0.22 ± 0.20	0.17 ± 0.16	0.14 ± 0.12	0.14 ± 0.15	0.09 ± 0.11	0.12 ± 0.11	0.12 ± 0.15
	0.6 – 0.85	0.26 ± 0.16	0.13 ± 0.10			0.24 ± 0.30		
	0.3 – 0.6	0.39 ± 0.34	0.11 ± 0.03			0.12 ± 0.07		
12.58	1	0.18 ± 0.18	0.12 ± 0.13	0.12 ± 0.11	0.10 ± 0.14	0.07 ± 0.11	0.10 ± 0.09	0.10 ± 0.13
	0.6 – 0.85	0.21 ± 0.13	0.09 ± 0.07			0.21 ± 0.28		
	0.3 – 0.6	0.35 ± 0.30	0.11 ± 0.03			0.10 ± 0.07		
18.18	1	0.15 ± 0.16	0.09 ± 0.11	0.19 ± 0.22	0.09 ± 0.14	0.03 ± 0.04	0.09 ± 0.08	0.09 ± 0.11
	0.6 – 0.85	0.17 ± 0.10	0.06 ± 0.05			0.19 ± 0.25		
	0.3 – 0.6	0.31 ± 0.26	0.10 ± 0.03			0.09 ± 0.08		
26.30	1	0.14 ± 0.15	0.08 ± 0.09	0.19 ± 0.20	0.08 ± 0.15	0.03 ± 0.03	0.09 ± 0.08	0.09 ± 0.10
	0.6 – 0.85	0.14 ± 0.07	0.05 ± 0.04			0.16 ± 0.22		
	0.3 – 0.6	0.28 ± 0.23	0.10 ± 0.03			0.08 ± 0.08		
38.03	1	0.12 ± 0.14	0.06 ± 0.08	0.20 ± 0.18	0.08 ± 0.16	0.03 ± 0.03	0.09 ± 0.08	0.08 ± 0.09
	0.6 – 0.85	0.12 ± 0.06	0.06 ± 0.07			0.15 ± 0.22		
	0.3 – 0.6	0.23 ± 0.19	0.11 ± 0.04			0.07 ± 0.08		
54.99	1	0.12 ± 0.14	0.05 ± 0.06	0.22 ± 0.16	0.08 ± 0.17	0.03 ± 0.02	0.08 ± 0.08	0.07 ± 0.06
	0.6 – 0.85	0.11 ± 0.07	0.09 ± 0.12			0.15 ± 0.22		
	0.3 – 0.6	0.18 ± 0.13	0.12 ± 0.04			0.07 ± 0.09		

(orange) lines indicate the magnetic connection of the spacecraft with the Sun for a nominal IMF configuration, for the slow (fast) solar wind conditions[7]. The synthetic intensity-time profiles of these reference events are provided by SOLPENCO2 for virtual observers located at 0.2, 0.4, 0.6, 0.8, 1.0, 1.3 and 1.6 AU along the IMF lines connecting the 1 AU observer with the Sun, i.e. along the IMF lines plotted in Figure 2.14. Note, that as we move inwards starting from 1 AU along the IMF lines, the heliolongitude of the observers changes towards eastern locations because of the IMF curvature. For instance, in the case of the E23 event on 24 September 2001, the blue IMF line starts at the (−15°,−25°) sector at 1 AU and ends, at 0.2 AU, in the last eastern sector, that shows a larger value of the DTFRs, which in turn is roughly the same as if the observer had kept moving at 1 AU towards the last eastern sector; and hence, the longitudinal movement along 1 AU is similar to the radial movement along the IMF line (within error bars).

Then, from this first evaluation, we obtain the same tendency of the variation of the DTFRs with the longitude and the energy as for the six SEP events of the multi-spacecraft study in the previous section (Sect. 2.3.2). For the events in the SREL and STEREO lists, we obtain that the mean values of the DTFRs, when grouping the events into 15 intervals in longitude, increase towards eastern heliolongitudes and decrease with the energy of the protons, in spite that the standard deviations found are large. On the other hand, for the events detected by the HELIOS

[7]The solar wind speeds used to calculate the magnetic connection are v_{sw} = 365 km s^{-1} for the slow solar wind and v_{sw} = 595 km s^{-1} for the fast solar wind (Aran et al., 2011a).

spacecraft (19 events within 0.3 – 0.6 AU and 22 events within 0.6 – 0.85 AU), the small number of events prevents us from drawing significant quantitative conclusions, but indicates that the DTFRs increase with heliolongitude and keep roughly constant (that is, approximately within error bars) with the heliocentric radial distance.

In conclusion, given that Helios data only permits us to extract qualitative information on how the DTFRs vary with the heliolongitude and with the radial distance, and that the qualitative variation derived coincides with the tendency shown by the 1 AU data, we finally decided to use the tendency in heliolongitude inferred from 1 AU data, which is based on a larger number of events, to describe the radial dependence of the downstream fluence of the events in the SREL.

This decision is based on: (i) The DTFRs variation with the radial distance is meant to be used in the predictions of the dependence of the TF of the events with the radial distance provided by SOLPENCO2. (ii) This model provides the radial dependences for virtual spacecraft located at different radial distances but along the same IMF line; thus, sharing the same nominal magnetic connection with the shock front, as it propagates away from the Sun, and consequently, sharing the same particle source injection function for the accelerated protons escaping from the shock front. And (iii), our study clearly indicates that the relative contribution of the downstream portion of the proton intensity-time profiles to the total fluence of SEP events mainly depends on the longitudinal separation of the spacecraft with respect to the direction of the propagation of the associated interplanetary shock.

For instance, for the reference event of Type 2c (see App. B), the 6 March 1989 SEP event (represented by the black solid circle located in the most eastern sector in Figure 2.14), the radial dependence of the total fluence (equal to the radial dependence of the UF in the first version of SOLPENCO2) was $R^{+1.26}$ and $R^{+1.87}$ for 8.7 MeV and 26.3 MeV, respectively. With the proposed method and following the polynomial fit shown in Figure 2.13 (i.e., translating the decreasing heliocentric distance of the virtual observers with the longitudinal translation along the IMF line towards eastern locations), the radial dependence of the TF for this event would be, $R^{+0.70}$ and $R^{+0.44}$ for 8.7 MeV and 26.3 MeV, respectively.

2.4.2 Results: longitudinal variation of the DTFRs for SOL2UP

Following the main conclusion of the analysis performed in the previous section, we further investigated the variation of the DTFRs with the heliolongitude of the particle source for the SEP events at 1 AU.

By considering the large dispersion of points in each angular sector (see, e.g., Fig. 2.13), we changed the methodology employed to obtain the mean DTFR values. We applied a moving mean technique in which the lowest and the highest values of the selected sub-set (or moving window) of data are discarded in the calculation of the mean DTFR value. As in previous sections, the mean values are weighted considering the total fluence of the events. We tested

moving windows of 3, 5, 7, 9 and 11 points. The best results for all energies are obtained when using an 11-points moving mean for 1 AU data. Figure 2.16 shows the resulting mean DTFR values (red open circles) and standard deviations (red error bars) for 8.7 MeV proton fluences.

The larger mean DTFR values are obtained for the eastern heliolongitudes. At central meridian, around W05, there is a steep decrease of the values of the mean DTFRs (Fig. 2.16). This feature is observed for $E < 79.53$ MeV and may be related to the efficiency of the interplanetary shock in accelerating, injecting and/or trapping (both in the sheath and the downstream regions) protons up to these energies, that are only measured once the shock has crossed 1 AU.

In order to derive an overall variation with the heliolongitude, we fitted polynomials of different orders (3rd, 4th, 5th, and 8th) to the mean DTFR values. None of them fitted well solely the tendency shown by the mean ratios for all energies. We tried a combination of polynomials instead, and fixed, in heliolongitude, the range of applicability of these polynomials between 90° (west limb) and the most eastern mean heliolongitude (which varies with the particle energy, depending on the available observations). The main reason for choosing such heliolongitude ranges is twofold: (i) Most of the events were detected prior to the STEREO era; hence, the solar source sites determined off the limbs have a larger uncertainty because they were estimated from considering the time elapsed between a given active region disappeared (in the case of the west limb) and the eruptive phenomena occurred, or the time elapsed since the active region appeared (by the eastern limb) after the eruptive phenomena was detected. (ii) To avoid the divergences of the polynomials in the extreme longitudinal values. For far eastern heliolongitudes and for western heliolongitudes > 90°, we assumed for the DTFRs constant values equal to the values obtained from the polynomial fits.

The black line in Figure 2.16 corresponds to a polynomial obtained by adding the 3rd, 4th and 5th polynomial fits and the grey line corresponds to the addition of 3rd and 8th order polynomial fits. The mean DTFRs and the resulting combination of polynomials for 6.01 MeV, 18.18 MeV, 54.99 MeV and 115 MeV protons are shown in the corresponding figures of Section C.1 in Appendix C. The figures for the remainder SEPEM energy references are given in Pacheco et al. (2017b). For $E \geq 54.99$ MeV, both combined polynomials yield similar curves; but for the lower energies, the latter combination reproduces better the behaviour of the DTFRs for the eastern heliolongitudes.

Hence, we conclude that the tendency curves derived from the combination of the 3rd and 8th order polynomial fits better describe the variation of the DTFRs of the SEP events at 1 AU with the heliolongitude, and we finally implement this result into the modelled fluence predictions by SOLPENCO2.

For completeness, we applied the moving mean technique to the DTFRs derived from Helios data. In this case, among the tested options, the 7-points moving window yielded better fits to the mean values. Figure 2.17 displays the moving mean DTFRs (red open circles) and standard deviations (vertical error bars), for 8.7 MeV fluences, and for 0.6 – 0.85 AU (top panel) and for

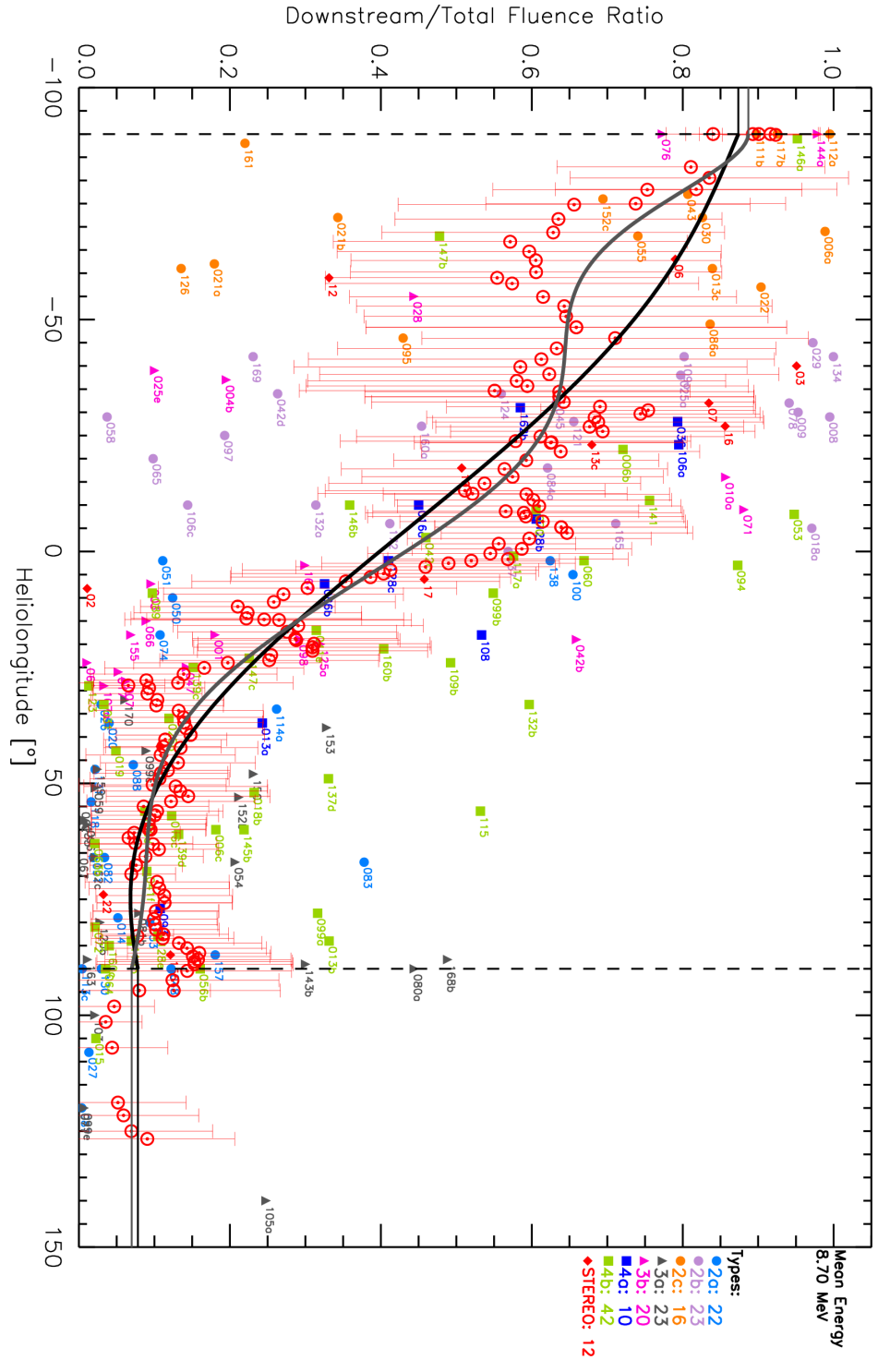

FIGURE 2.16: DTFRs (coloured symbols) for 8.7 MeV of the events analysed at 1 AU (labels indicate the event number) as a function of the heliolongitude. Red open circles and error bars correspond to the moving mean values and standard deviations.The grey and black thick lines between -90° to 90° correspond to two different polynomial fits applied to the mean DTFR values, as explained in the text.

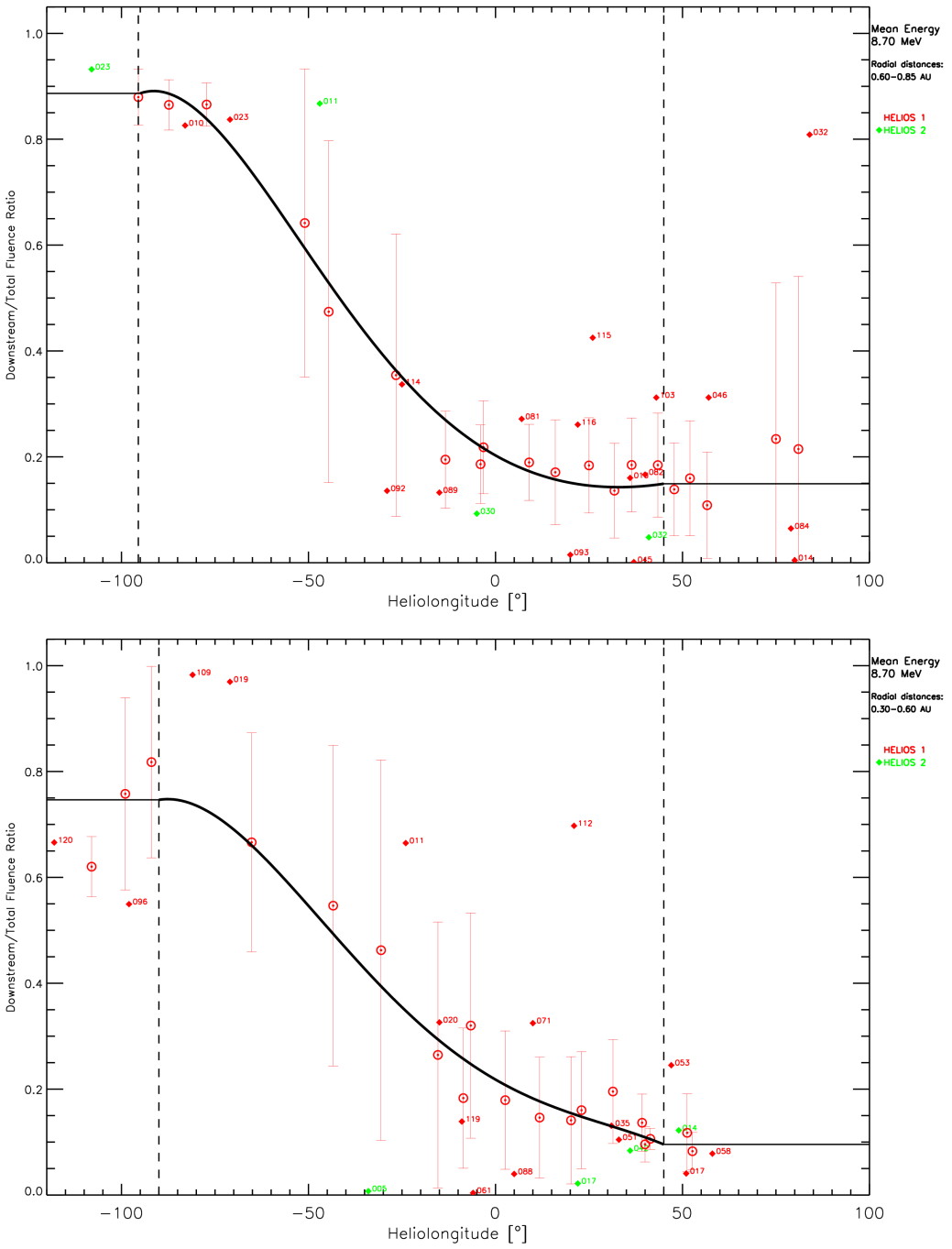

FIGURE 2.17: DTFRs for 8.7 MeV of the events detected at 0.6 – 0.85 AU (top panel) and at 0.3 – 0.6 AU (bottom panel) (labels indicate the event number) as a function of the heliolongitude. Red open circles and error bars correspond to the moving mean values and standard deviations. The black thick line corresponds to the polynomial fit applied to the mean DTFR values, as explained in the text.

0.3 – 0.6 AU (bottom panel). Black thick curves correspond to the addition of a 3rd, 4th and 5th order polynomials fits. In contrast to 1 AU data, the DTFRs of eastern events do not show a 'plateau' after the increase at central meridian locations. For this reason, in this case, we did not show the combination of the 3rd and 8th order polynomial fits. It is likely, however, that the tendency of the DTFRs differs from the 1 AU data due to the scarce number of events measured by Helios that could be considered in the analysis. Similar figures but for 6.01 MeV, 18.18 MeV, 54.99 MeV and 115 MeV protons can be found in Sections C.1.1 and C.1.2 in Appendix C. The figures for the remainder SEPEM reference energies can be found in Pacheco et al. (2017b).

As concluded in the previous section, in order to determine the DTFRs at other radial distances, we used the polynomials derived from data at 1 AU, and assumed therefore that the longitudinal dependence of the DTFRs is more important than the radial dependence.

The virtual observers away from 1 AU used in SOLPENCO2 are placed along the same IMF line as the observer at 1 AU. Therefore, as shown before, it is possible to translate the dependence of the DTFR determined at 1 AU by using the angular separation between a given virtual observer and the observer at 1 AU provided by the bending of the IMF. This separation will depend on the solar wind speed detected for each event. In the SREL (Table A.4), the solar wind is classified as 'fast' or 'slow' or 'not determined', being the threshold value defining the first two categories v_{sw} = 480 km s^{-1}. In order to consider these three solar wind scenarios, we took the same solar wind speeds used to model the interplanetary shocks propagation in the 'slow' and 'fast' cases, v_{sw} = 365 km s^{-1} and v_{sw} = 595 km s^{-1}, respectively (Aran et al., 2011a). For the 'not determined' cases, we have taken the threshold value for the solar wind speed.

Figure 2.18 illustrates, for the 8.7 MeV reference energy, the translation of the 1 AU tendencies to the other radial distances. The mauve, violet and purple lines in Figure 2.18, show the grey 1-AU polynomial fit shown in Figure 2.16, translated to a heliocentric radial distance of r = 0.725 AU (top panel) and of r = 0.45 AU (bottom panel), for the three solar wind options, over-plotted into the corresponding panels of Figure 2.18. Tendency lines derived for the fast solar wind are the curves with the smallest displacement in longitude (mauve curves) and those for the slow solar wind are the lines showing the largest displacement (purple curve). Tendency lines for the intermediate solar wind lie between the other two (violet curves). The comparison for 6.01 MeV, 18.18 MeV, 54.99 MeV and 115 MeV protons is shown in Section C.1.1 for 0.6 – 0.85 AU and Section C.1.2 for 0.3 – 0.6 AU. The comparisons for the remainder energies can be found in Pacheco et al. (2017b).

The 1 AU derived curves are similar to those derived from the Helios data, and reside within the error bars of the mean DTFRs, with the exception of two points residing in the eastern longitudes of the 0.6 – 0.85 AU region (see top panel of Fig. 2.18). The same is true for the remaining energy channels, being better the comparison for the higher energies.

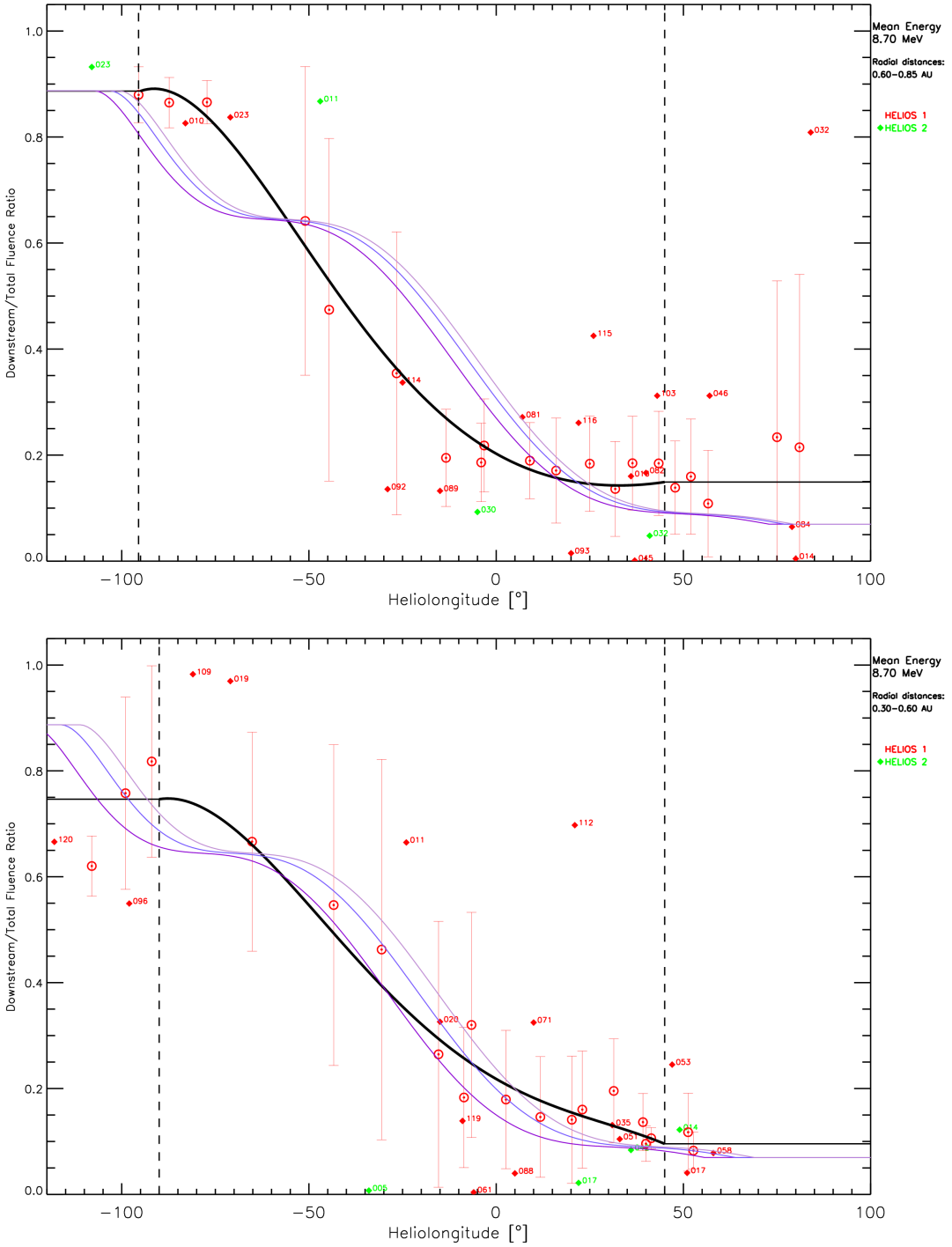

FIGURE 2.18: DTFRs for 8.7 MeV of the events detected at 0.6 – 0.85 AU (top panel) and at 0.3 – 0.6 AU (bottom panel) (labels indicate the event number) as a function of the heliolongitude. Red open circles and error bars correspond to the moving mean values and standard deviations.The black thick lines correspond to the polynomial fits applied to the mean DTFR values, as explained in the text. Tendency lines derived from 1 AU data for the three solar wind speeds are shown for comparison: mauve lines correspond to the fast solar wind case, violet lines to the intermediate solar wind speed, and purple lines to the slow solar wind.

2.4.3 Implementation and impact of the results

In conclusion, we use the polynomial fits (3rd+8th order combination) derived from 1 AU data to characterise the variation of the DTFRs for the virtual observers located away from 1 AU. In order to compute the TF away from 1 AU of a given the SEP event in SREL, we vertically translate the tendency curve found, to match the observed DTFR value at 1 AU at the heliolongitude of the event, and then apply the corresponding angular displacement given by the bending of the IMF line to each of the other radial positions, following the general tendency curves derived. That is, we assume that the polynomial fits represent the "Average Variation" with heliolongitude, and apply the same tendency for all events, starting from the observed DTFR value at the observed heliolongitude. The maximum value allowed for a DTFR is set to 0.99.

This procedure to add the contribution of the DF to obtain the TF of each SEP enhancement in SREL is outlined as follows:

1. For a given SEP event, the heliolongitude of the parent source, the type of solar wind, and the UF and DF for the eleven SEPEM reference energies is specified.

2. Next, the difference between the value of the DTFR obtained from the polynomial fit derived at 1 AU and the observed DTFR value for that particular SEP event, Δ_R, is computed for each reference energy.

3. For the corresponding solar wind type, we compute the longitudinal displacement for each of the seven virtual observers placed along the same IMF line as the observer at 1 AU and located at heliocentric radial distances of 0.2, 0.4, 0.6, 0.8, 1.0, 1.3 and 1.6 AU. With this, we obtain the corresponding DTFR values from the polynomial fits, and in turn, the DTFRs as a function of the heliocentric distance, r.

4. For each energy, we add to the DTFRs(r) found in the previous step the increment Δ_R found in step 2, in order to match the observed and derived DTFR value at 1 AU.

5. Next, we look for DTFRs larger than 0.99 and set those values to 0.99 (this is the largest value allowed, otherwise we could not distinguish between upstream and downstream regions) and in case of finding negative value for any DTFR, this is set to 0.

6. Finally, the $UF(r)$ values for each of the virtual observers are multiplied by the corresponding DTFRs(r) to obtain the total fluence of the event as a function of the heliocentric distance and for each energy. Note that $UF(r)$ values are obtained using the heliocentric radial distance power-laws derived in Aran et al. (2017a) and shown in Appendix B for the corresponding reference event.

This procedure is part of the software developed in the frame of the SOL2UP project that calculates the peak intensity and the total fluence of the SEP events in SREL (Table A.4). The

outputs finally implemented into the SEPEM statistical SEP model for interplanetary missions are the ratios to the observed values at 1 AU of the peak intensities and total fluences, for the seven virtual observers and for the eleven reference proton energies, and for all SEP events classified in SREL.

In order to illustrate the impact of the DTFRs in the radial dependence of the TF of the SEP events, we show here the radial dependences obtained in the scope of the SOL2UP project for some of the events in the SREL.

Figure 2.19 shows the results obtained for the 1989 March 6 SEP event, which is the reference event of low-energy far eastern events in SREL, Type 2c. In the left panel the values of the UF obtained from the simulated intensity-time profiles by SOLPENCO2 (Aran et al., 2017a) for each of the virtual spacecraft located at the selected radial distances, for 6.01 MeV (orange circles), 18.18 MeV (blue circles) and 79.53 MeV (purple circles). The corresponding power-law radial dependences derived are indicated by the dashed lines and the radial indices are provided in the legend, using the colour code.

In the previous version of SOLPENCO2, the DTFR determined at 1 AU was kept constant for all radial distances, and hence the radial dependence of the TF was equal to the radial dependence of the UF. The right panel of Figure 2.19 shows the radial dependence of the TF as derived now, after implementing the DTFRs obtained by the work presented in this dissertation. Since this is an E69 event, and it developed on slow solar wind conditions, the effect of the contribution of the downstream region to the radial dependence of the TF is large. The positive radial index at low-energies for the upstream fluence translates into an almost flat dependence in the total fluence. For higher energies, the radial dependence softens significantly.

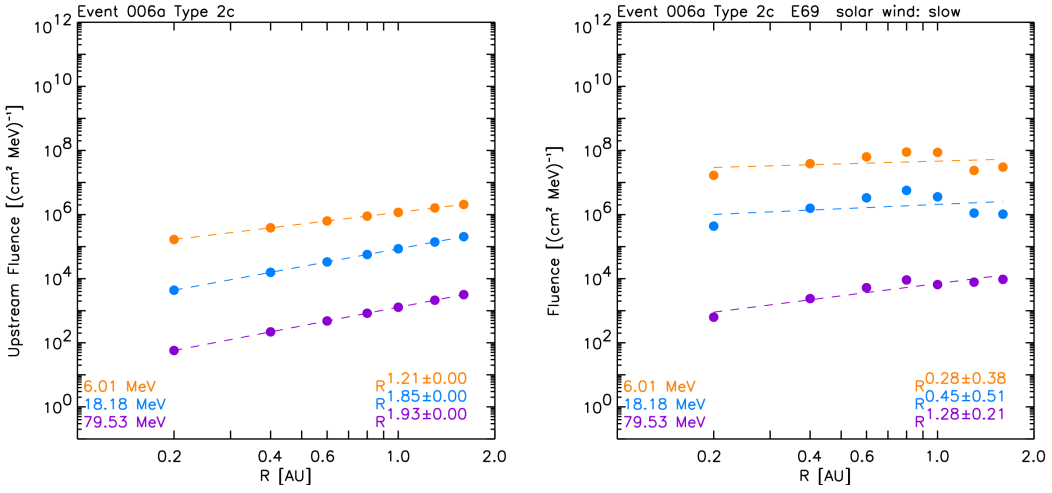

FIGURE 2.19: Type 2c. 1989 March 6 SEP event. Top panels: Radial dependence of the upstream fluence (left) and total fluence (right) for three different proton energies, 6.01 MeV (orange), 18.18 MeV (blue) and 79.53 MeV (purple).

Finally, we show the impact for one of the categories containing the largest events (in terms both of peak intensity and fluence) in SREL, the Type 4a-np events. This category contains the four largest events not showing a prompt component in their high-energy intensity-time profiles. The results for the Type 4a-p events are shown in Appendix D.

For each event shown, the comparison between the left and the right panels highlights the variation of the radial dependences found for the total fluence of the events with respect to the previous results obtained during the SEPEM project. The format of the figures is the same as in Figure 2.19.

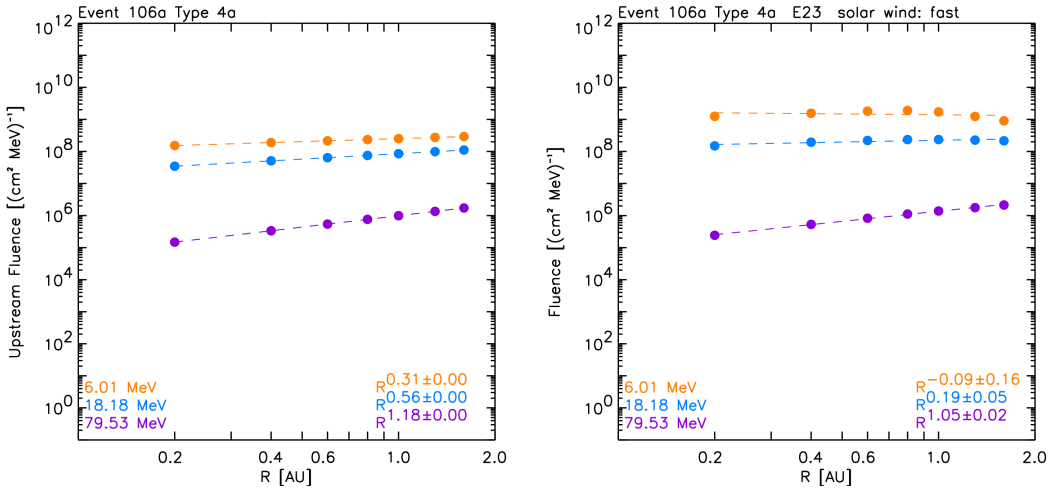

FIGURE 2.20: Type 4a-np reference event. 2001 September 24 SEP event. Radial dependence of the upstream fluence (left) and total fluence (right) for three different proton energies, 6.01 MeV (orange), 18.18 MeV (blue) and 79.53 MeV (purple).

For the reference case, that occurred under fast solar wind conditions, the positive radial dependences obtained for the UF are softened to a flat radial dependence for the low-energies in the case of the TF and kept positive for the higher energies due to the lower contribution of the DF. For the remaining three events the radial dependencies vary as shown in Figures 2.20, 2.21, 2.22 and 2.23.

We want to note that for the events belonging to the same event type, the UF radial dependences are the same. This is the result of the assumption made for the DTFRs in the previous version of SOLPENCO2. In contrast, now, different radial dependences of the TF are obtained for each event, as shown in the right panels of Figures 2.20, 2.21, 2.22 and 2.23.

2.5 Conclusions

In this chapter, we have presented the results from the analysis of the post-shock fluence from selected events observed by near-Earth spacecraft and the STEREO spacecraft at 1 AU, and by the Helios spacecraft at heliocentric radial distances between 0.3 AU and 0.85 AU. We described

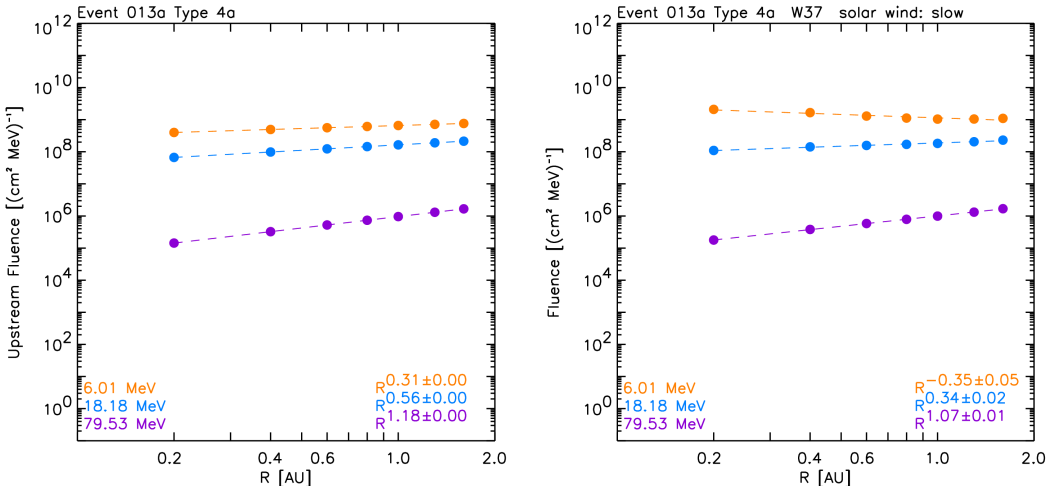

FIGURE 2.21: 1989 August 12 SEP event. Radial dependence of the upstream fluence (left) and total fluence (right) for three different proton energies, 6.01 MeV (orange), 18.18 MeV (blue) and 79.53 MeV (purple).

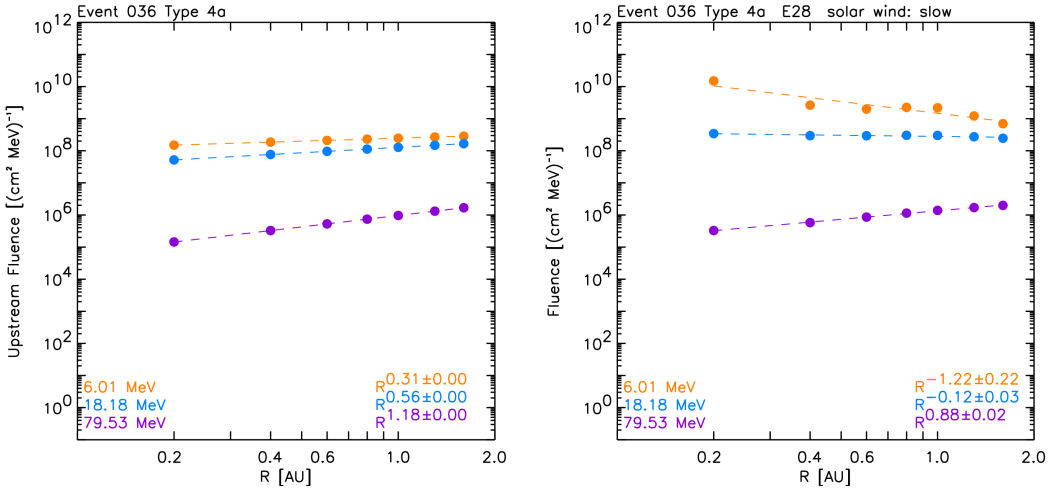

FIGURE 2.22: 1991 March 23 SEP event. Radial dependence of the upstream fluence (left) and total fluence (right) for three different proton energies, 6.01 MeV (orange), 18.18 MeV (blue) and 79.53 MeV (purple).

the various data sets used in the analysis and the three event lists compiled. Next, we have shown the tasks performed for the calculation of the upstream (pre-shock), downstream (post-shock) and total fluences of the events: the selection of the events for the study, the analysis of the pre-event background intensity levels to be subtracted, the treatment of the different data gaps encountered and the energy spectra fits to the STEREO and Helios fluences. Then we described the coded software used to compute the downstream-to-total fluence ratios for the events in the updated reference event list (SREL) of the SEPEM statistical SEP model for interplanetary missions.

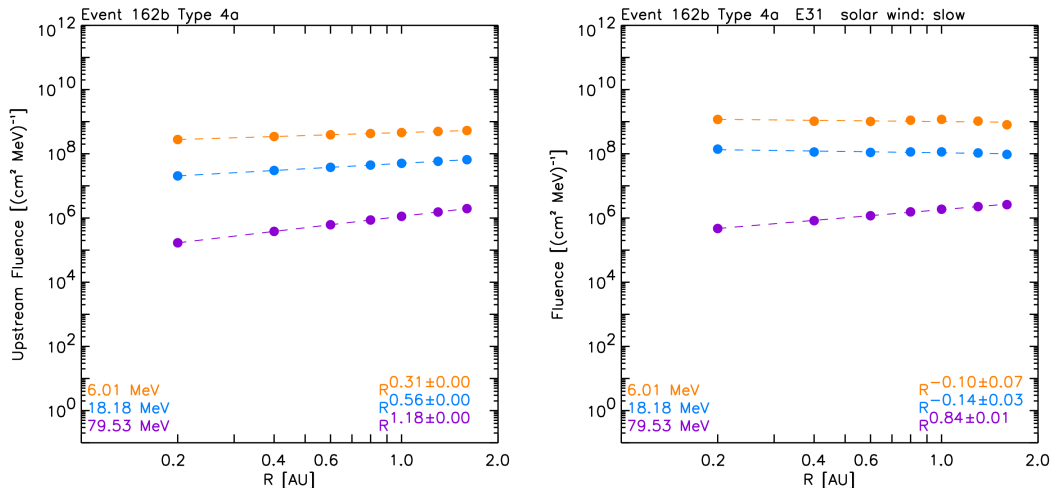

FIGURE 2.23: 2012 March 7 SEP event. Radial dependence of the upstream fluence (left) and total fluence (right) for three different proton energies, 6.01 MeV (orange), 18.18 MeV (blue) and 79.53 MeV (purple).

Afterwards, we performed a multi-spacecraft study of SEP events to determine whether there exists a variation of the downstream fluence of these SEP events with the heliolongitude of their parent solar source. From the eight pairs of events simultaneously detected by near-Earth spacecraft and by one of the STEREO spacecraft, we found that the downstream-to-total fluence ratios do vary with the heliolongitude. Eastern events show higher DTFRs ratios than their western counterparts.

The extension of the study to 168 events observed at 1 AU permitted us to quantify the variation of the DTFRs with the heliolongitude, by fitting polynomials to the moving mean values of these ratios. Moreover, the number of events observed by the Helios spacecraft at heliocentric radial distances between 0.3 AU and 0.85 AU that were suitable for the downstream fluence analysis is small, yielding large uncertainties in the mean values found for the DTFRs. However, the same trend is found as for the 1 AU data: eastern events tend to show higher DTFRs ratios than western events. On the other hand, we find that the mean DTFRs are roughly constant with the heliocentric radial distance (within errors). Consequently, we use the fits obtained from the better statistics gathered from 1 AU observations to determine the evolution of the downstream-to-total fluence ratios with the heliolongitude.

Considering that, for a given event, SOLPENCO2 provides predictions for spacecraft located at different radial distances but along the same IMF line, we can translate the variation in heliolongitude (provided by the curvature of the IMF line) of these spacecraft to a radial variation of the DFTRs. Therefore, we used the polynomial fits (3rd+8th order combination) derived from 1 AU to characterise the variation of the DTFRs for the virtual observers located away from 1 AU. In the implementation of these results into the total fluence computation of the SREL events for distances away from 1 AU, we vertically translated the tendency curve found, to match the

observed DTFR value at 1 AU for each event. Next, we applied the corresponding angular displacement to the radial distances considered, by following the general tendency curves derived. That is, we assumed that the polynomial fits derived represent the "Average Variation" with heliolongitude, and applied the same tendency for all events, starting from the observed DTFR value at the observed heliolongitude.

Finally, our results were implemented into the SEPEM statistical SEP model for interplanetary missions, for all events in the SREL. The resulting radial dependences of the TF vary from event to event thanks to the contribution of the downstream fluence modelled in this work. We have shown that strong positive radial dependences of the TF provided previously by SOLPENCO2 for eastern events are now softened. The same is true for the radial dependence of the TF of the largest events in SREL. In Chapter 5, we illustrate the impact of these results on the SEPEM statistical model by simulating the Solar Orbiter mission orbit.

Chapter 3

Electron events observed over a narrow range of heliolongitudes

3.1 Introduction

We studied two consecutive solar near-relativistic electron events observed by the Solar Electron Proton Telescope (SEPT, Müller-Mellin et al., 2008) on board STEREO A and STEREO B on 2014 August 1, when the longitudinal separation between the two spacecraft was of only ~35° (Klassen et al., 2016). The approach of the STEREO mission to the solar conjunction provided us with the opportunity to study SEP events at 1 AU when the two STEREO spacecraft had nominally nearly the same magnetic connection to the Sun and explore how the interplanetary transport conditions can change over narrow angular intervals.

Despite their close location, the two STEREO spacecraft were embedded in different solar wind streams. The solar eruptions associated with these events were two flares located in the same active region (Klassen et al., 2016) and there were no signatures of shock waves. The particle events observed by STEREO A and STEREO B showed strong differences in terms of onset, peak intensities and evolution of the measured angular distributions. The spacecraft with the better nominal magnetic connection to the flare detected a later arrival of electrons than the worse connected one, and a lower peak intensity by a factor ~5 (Klassen et al., 2016).

Several studies of solar energetic particle (SEP) events have assumed that the longitudinal distribution of particle peak intensities at 1 AU follows a Gaussian distribution with respect to the longitudinal separation between the flare site and the nominal magnetic footpoint of the spacecraft (Wibberenz and Cane, 2006, Lario et al., 2006, 2013, Richardson et al., 2014, Dresing et al., 2014, Gómez-Herrero et al., 2015). This is also predicted by simulations assuming uniform turbulence conditions in the interplanetary medium or, e.g., a symmetric Gaussian distribution of particles released close to the Sun (Dröge et al., 2010, Strauss and Fichtner, 2015).

In two recent studies, Klassen et al. (2015) and Klassen et al. (2016) reported the observation of non-symmetric intensity distributions of electrons at 1 AU for several events examined over relatively narrow angular intervals. The authors hypothesised that the unexpected particle distributions detected at 1 AU could be attributed to a rippled peak intensity distribution at 1 AU formed by narrow peaks ("fingers") superposed on a quasi-uniform Gaussian distribution (Klassen et al., 2016). In this scenario, open magnetic field lines from the flaring region would provide prompt access of SEPs and form the fingers, while large-scale ”closed” magnetic fields around the active region and/or coronal holes with stronger turbulence would inhibit perpendicular diffusion and partially shield the penetration of particles inside these regions, providing the valleys.

In this chapter we study under which circumstances the STEREO observations on 2014 August 1 could be explained by different transport conditions in different solar wind streams connecting each STEREO spacecraft back to the Sun. We review the characteristics of the two consecutive SEP events observed on 2014 August 1, and model them using SEPInversion tool. The main results were presented in Pacheco et al. (2017a).

3.2 Observations

We used particle measurements provided by the SEPT experiment on board the two STEREO spacecraft that measures electrons from 45 to 400 keV. SEPT consists of four identical detectors, i.e., four fields of view, which are pointing to the ecliptic north, to the ecliptic south, along the nominal Parker spiral towards the Sun (named as Sun) and in the opposite direction (Antisun). We complemented this information with IMF measurements by STEREO/MAG (Acuña et al., 2008) to determine the particle pitch-angle distributions and particle anisotropies and with solar wind observations from the PLasma and SupraThermal Ion Composition experiment (PLASTIC, Galvin et al., 2008), to study the in-situ characteristics of the plasma. In addition, we used measurements by the STEREO Radio and Plasma Wave Investigation (SWAVES, Bougeret et al., 2008) to study the radio emission spectra at frequencies lower than 16 MHz.

We studied two consecutive electron events observed with only a few hours of delay by the STEREO twin spacecraft on 2014 August 1. On that date, the longitudinal separation between the spacecraft was of only ∼35° (see the longitudinal positions of STEREO A, STEREO B and Earth and the nominal Parker spiral connecting them to the Sun in Fig. 3.1).

The upper panels of Figure 3.2 show the omni-directional intensities (solid curves) for 45 - 65 keV (top panel) and 65 - 105 keV (second panel) electrons measured by STEREO A (red) and STEREO B (blue). Dotted (dashed) curves correspond to the intensities measured by the Sun (Antisun) fields of view (orange curves for STEREO A and grey curves for STEREO B). The following panels in Figure 3.2 show the solar wind speed, density and temperature, and the IMF intensity, latitude and longitude angles in the RTN reference frame, as measured by STEREO A

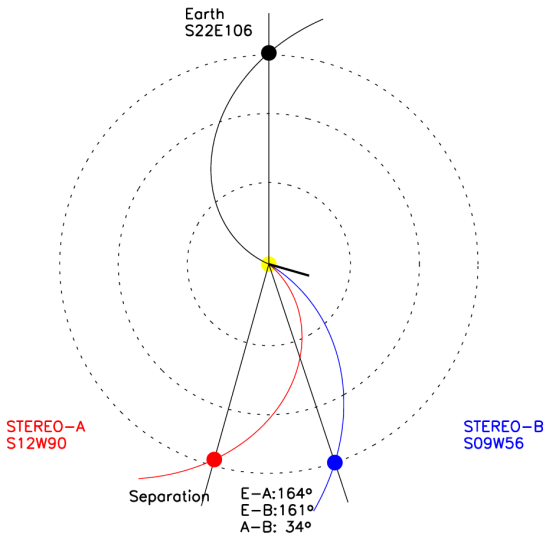

FIGURE 3.1: View from the north ecliptic pole showing the location of the Earth (black symbol), STEREO-A (red symbol) and STEREO-B (blue symbol) on 2014 August 1. Nominal interplanetary magnetic field lines are shown connecting each spacecraft with the Sun (yellow circle, not to scale). The black thick line indicates the longitude of the parent active region (E106 from the Earth, W56 from STEREO-B and W90 from STEREO-A).

(red) and STEREO B (blue). Table 3.1 summarises the main characteristics of the 2014 August 1 electron events. Both particle events showed a significant intensity enhancement, that is, peak intensities were at least one order of magnitude higher than the pre-event background intensities, in the energy ranges 45-65 keV and 65-105 keV electrons.

Despite the close location of the two spacecraft, for both events, the electron intensities observed by STEREO A and STEREO B showed clear differences in terms of onset time, peak intensity and evolution of the pitch-angle distributions. The events observed by STEREO A started to rise up to 20 min earlier than at STEREO B, and the peak intensity was about a factor 5 higher at STEREO A. STEREO B observed more isotropic pitch-angle distributions signalled by the observation of similar profiles by the four fields of view of SEPT (see also the pitch-angle distribution at the bottom panel of Fig. 10 in Klassen et al., 2016). On the other hand, the intensity profiles observed by STEREO A were very different, being the most intense intensities recorded by the Sun field of view, which signals more anisotropic pitch-angle distributions (note the difference between the orange profiles in Figure 3.2).

Interestingly, as can be seen in the third panel of Figure 3.2, on 2014 August 1, STEREO A was embedded in a slow solar wind stream, while STEREO B was inside a fast stream region, due to a coronal hole (Klassen et al., 2016). The mean solar wind speeds, computed during the first hour after the event onset, are given in Table 3.1. Assuming that the large scale interplanetary magnetic field (IMF) was a Parker spiral consistent with the solar wind speed measured in situ by each spacecraft, the longitudinal separation between the nominal footpoints of the two

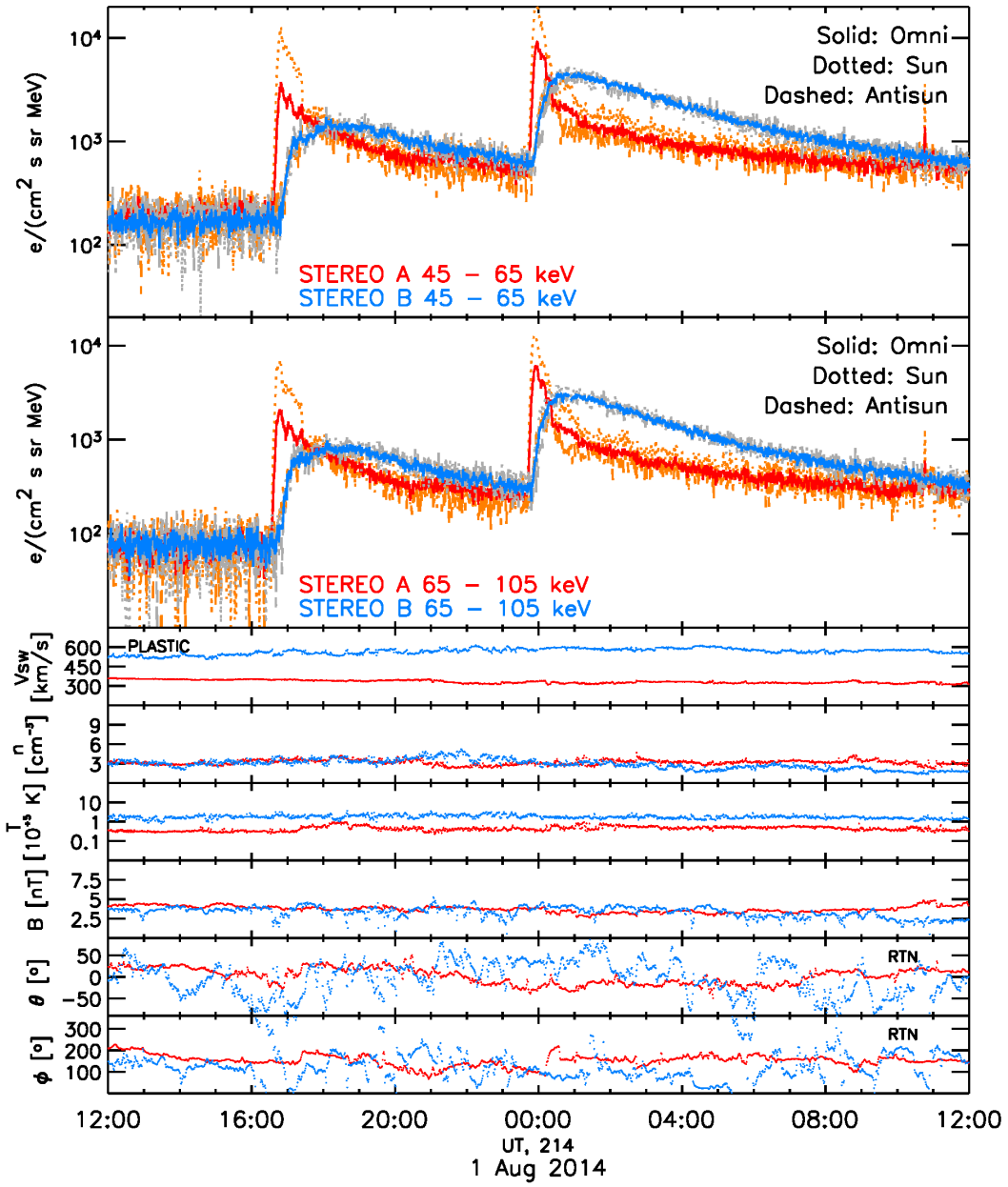

FIGURE 3.2: In-situ measurements by STEREO A (red) and STEREO B (blue). Omni-directional (solid curves) intensities are shown for 45 - 65 keV (top panel), and for 65 - 105 keV (second panel) electrons. Intensities for the Sun (STEREO A orange-dotted, STEREO B grey-dotted) and Antisun (STEREO A orange-dashed, STEREO B grey-dashed) fields of view are also displayed for both spacecraft in these two panels. The solar wind speed, the density and the plasma temperature are shown from the third to the fifth panels, respectively. The last three panels display the magnetic field strength and its direction (latitudinal and azimuthal angles in the RTN reference frame).

spacecraft was very small, of less than 9°. However, given the estimated uncertainties in determining the magnetic connection (i.e., 10° as estimated by Nolte and Roelof, 1973a,b, or even > 20°, depending on the method employed, e.g., Lario et al., 2014, 2016), one could even claim that the footpoints of STEREO A and STEREO B were the same.

According to Klassen et al. (2016), the first electron event was associated with a jet appearing

TABLE 3.1: Main characteristics of the 2014 August 1 electron events (based on Klassen et al., 2016)

Properties		Event I	Event II
Type III burst onset [UT]		16:22	23:24
Type II burst onset [UT]		No	No
CME		No	No
Connection angle [°]	STA-flare	27	26
	STB-flare	18	22
Electrons onset time [UT]	STA	16:34	23:45
	STB	16:54	23:54
Delay STB vs. STA [min]		20	9
Peak intensity ratio, STA/STB		5.5	4.0
V_{sw} [km s^{-1}]	STA	349	328
	STB	557	584

at S22W55, as seen from STEREO B, at 16:13 UT. It was associated with a type III radio burst detected 9 min later, at 16:22 UT. The second electron event, was associated with a solar flare from the same active region occurring at 23:16 UT and followed by a type III radio burst at 23:24 UT. No type II radio burst or coronal mass ejections (CMEs) were observed in association with any of the two events.

The connection angle, defined as the angular difference between the flare source and the spacecraft nominal footpoint, was larger for STEREO A than for STEREO B. The apparently better connected spacecraft, STEREO B, observed a smaller intensity increase and a later event onset time than STEREO A. In the next section, we explore if this can be due to different electron transport conditions along the flux tube connecting each spacecraft back to the Sun.

3.3 Modelling

3.3.1 Interplanetary transport model

SEPServer[1] currently hosts a database of results of a Monte Carlo interplanetary transport model (Agueda et al., 2008) to aid the study of near-relativistic (>50 keV) electron events observed by STEREO/SEPT (Agueda et al., 2012b). The transport model solves the focused transport equation (Roelof, 1969, Ruffolo, 1995), including the effects of particle streaming along the magnetic field lines, adiabatic focusing by the diverging magnetic field (Roelof, 1969), interplanetary scattering by magnetic fluctuations frozen into the solar wind (Jokipii, 1966, Dröge, 2003), convection with scattering fluctuations, and adiabatic deceleration resulting from the interplay of scattering and focusing (Ruffolo, 1995, Kocharov et al., 1998). Diffusion perpendicular to the average magnetic field is neglected.

[1] `http://server.sepserver.eu`

The expression ruling the evolution of the particle distribution function, i.e. the focused transport equation (Roelof, 1969), is given by

$$\frac{\partial f}{\partial t} + v\mu\frac{\partial f}{\partial z} + \frac{1-\mu^2}{2L}v\frac{\partial f}{\partial \mu} = \frac{\partial}{\partial \mu}D_{\mu\mu}\frac{\partial f}{\partial \mu}, \tag{3.1}$$

where $f(z, p, \mu, t)$ is the particle distribution function that depends on the position along the field line (z), momentum (p), pitch-angle (μ) and time; v is the particle velocity, $D_{\mu\mu}$ is the pitch-angle diffusion coefficient and L is the focusing length of the magnetic field which is given by

$$\frac{1}{L(z)} = -\frac{1}{B(z)}\frac{\partial B}{\partial z}. \tag{3.2}$$

The model assumes a static source of particles at two solar radii which energy spectrum follows a power law ($\frac{dN}{dE} \propto E^{-\gamma_s}$) and an Archimedean spiral magnetic flux tube connecting the Sun and the spacecraft. In-situ observations of the solar wind speed and the spectra at the peak intensity help us constrain the curvature of the Archimedean spiral and the source spectrum, respectively.

In Equation 3.1, the pitch-angle diffusion coefficient is given by

$$D_{\mu\mu} = \frac{\nu}{2}(1-\mu^2), \tag{3.3}$$

where the scattering frequency, ν, adopts the form (Agueda et al., 2008)

$$\nu(\mu) = \nu_0\left(\frac{|\mu|}{1+|\mu|} + \epsilon\right), \tag{3.4}$$

that allows us to model a range of scattering conditions, from quasi-isotropic ($\epsilon \gtrsim 1$) to fully pitch-angle dependent ($\epsilon = 0$). The case of isotropic pitch-angle scattering is obtained by taking $\nu(\mu) = \nu_0$ (see details in Agueda et al., 2008 and Agueda and Vainio, 2013 for a comparison of the ϵ-scattering model with the modified standard model).

Once the form of the pitch-angle scattering frequency is fixed, the radial mean free path, λ_r, is the only free parameter that describes the amount of pitch-angle scattering processes undergone by the energetic particles. It is related to the parallel mean free path by

$$\lambda_\parallel = \lambda_r \sec^2\psi, \tag{3.5}$$

where ψ is the angle between the radial direction and the local magnetic field. The expression of the parallel scattering mean free path $\lambda_\parallel$ in terms of the $D_{\mu\mu}$ is given by (Hasselmann and Wibberenz, 1968, 1970)

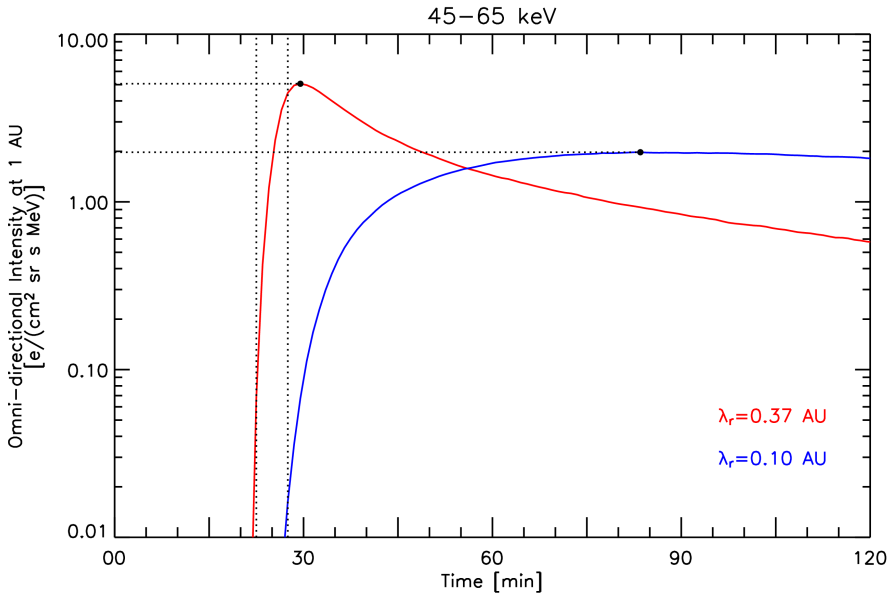

FIGURE 3.3: Omni-directional 45-65 keV electron intensities expected at 1 AU under two interplanetary transport scenarios assuming that $\lambda_r = 0.37$ AU (red) and $\lambda_r = 0.10$ AU (blue). The release of particles was assumed to occur at $t = 0$ for 10^{30} electrons in both cases. The particle event starts later and peaks at lower intensities for small values of the mean free path (more turbulent interplanetary transport conditions).

$$\lambda_{\parallel} = \frac{3v}{8}\int_{-1}^{1}\frac{(1-\mu^2)^2}{D_{\mu\mu}} = \frac{3v}{4}\int_{-1}^{1}\frac{1-\mu^2}{\nu(\mu)}d\mu, \tag{3.6}$$

The results of the model are intensity directional distributions of electrons at 1 AU resulting from an instantaneous release of electrons close to the Sun, i.e., the model provides the Green's functions of interplanetary transport. Figure 3.3 shows the intensities expected at 1 AU under two interplanetary transport scenarios assuming that $\lambda_r = 0.37$ AU and $\lambda_r = 0.10$ AU, and isotropic pitch-angle scattering. It can be seen that for a given injection function at the Sun, the peak intensities expected at 1 AU will be larger for larger values of the radial mean free path, and the pitch-angle distributions more anisotropic (cf. Fig. 2 in Agueda et al., 2012b or Fig. 5 in Strauss et al., 2017 for 2 GV protons). In addition, the event onset time will appear earlier for larger values of the radial mean free path. Another interesting aspect under the assumptions of the focused transport model is that for an injection function at the Sun that scales in helio-longitude following a Gaussian distribution and under the assumption of uniform interplanetary transport conditions (same radial mean free path in contiguous solar wind streams), the peak intensities expected at 1 AU follow a Gaussian distribution.

3.3.2 Fit to observed directional intensities

We used the *SEPinversion* software available in *SEPServer* to infer the release time history and the interplanetary transport conditions of near-relativistic electrons for each event in our

sample. *SEPinversion* makes use of the database of results of an interplanetary transport model (i.e, Agueda et al., 2008) to fit spacecraft observations at 1 AU. The fitting is done using the most direct form of directional data provided by the spacecraft (i.e. intensities recorded in four fields of view for STEREO/SEPT). *SEPinversion* assumes that the particle detector is a conical aperture and integrates the intensities for all the pitch angles in the detector aperture range according to the angular response of the telescope (Agueda et al., 2012b). The software uses an inversion approach to fit the observations (Agueda et al., 2008), that is, it computes the intensities expected at 1 AU for a set of multiple consecutive instantaneous injection episodes (also refereed as Green's functions) and then solves a least-square problem determine the relative weight of each injection episode to best fit the intensities measured at 1 AU.

To find out the best fit scenario for each event, we considered: (i) the two options available in *SEPServer* for the description of the pitch-angle diffusion coefficient (isotropic and pitch-angle dependent with $\epsilon = 0.01$), (ii) a wide range of interplanetary conditions covering 25 values of the radial mean free path, logarithmically spaced between 0.05 to 2.77 AU; and (iii) five values of the spectral index of the electron source (between 2.0 and 4.0, with step intervals of 0.5). Also, from the solar wind speeds list available in the database (covering from 300 k s^{-1} to 750 k s^{-1}, with 50 k s^{-1} steps), we selected the closest to the measured values at the onset of each event, shown in Table 3.1

For each transport scenario, the best possible release time history was obtained. The goodness of the fit for each case was then evaluated by comparing the observations and the modelled data (see Agueda et al., 2009, for more details). Each energy channel was fitted separately.

3.4 Results

We selected the time intervals between 16:20 – 19:00 UT for STEREO A and 16:35 – 20:25 UT for STEREO B to fit Event I, and 23:25 – 01:15 UT for STEREO A and 23:35 – 05:00 UT for STEREO B to fit Event II. The start time of these intervals was chosen to take into account the onset of the particle event, for each spacecraft. The end times for STEREO A correspond to the time when the particle intensity had decreased one order of magnitude from the peak intensity. For STEREO B, with events showing slowly decreasing intensities, we chose the end time in a way that the results of the fits and the inferred parameters did not vary under minor time changes.

In Figure 3.4 the resulting values of the goodness-of-fit estimator are shown for each value of the mean free path tested (between 0.05 and 2.77 AU). We can see that the curves for Event II show a more clear minimum for both STEREO probes than for Event I. This is related with the better pitch-angle coverage for Event II combined with the fact that during Event I both spacecraft, but specially STEREO A, observed changes in the local magnetic field on which they were embedded (see discussion below).

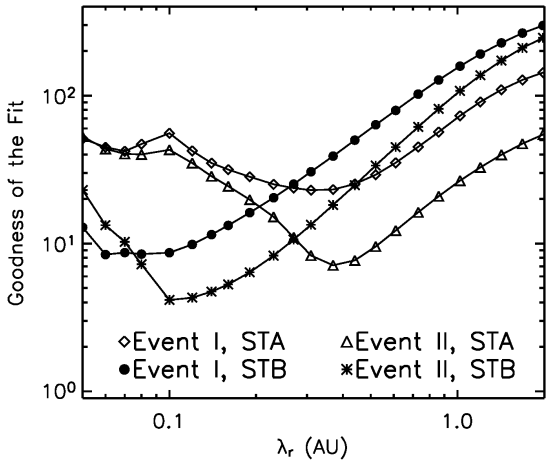

FIGURE 3.4: Goodness of the fit for the two events observed by STEREO A and STEREO B for each value of the mean free path tested.

The two upper panels of Figure 3.5 show for each event (Event I, top row; Event II, bottom row), the 45 – 65 keV electron intensity-time profiles observed by STEREO A (left column) and STEREO B (right column) for the four fields of view (thin coloured lines) of the SEPT instrument. For each field of view, the evolution of the pitch-angle cosine, μ observed at the centre of the telescope is shown in the bottom panels (with the same colour code as the corresponding intensities) together with the pitch-angle range covered (grey area) given the $\sim 50^{\circ}$ aperture of the telescopes.

TABLE 3.2: Best fit radial mean free path inferred for each event and in-situ solar wind speed.

Event	**S/C**	λ_r **[AU]**	$\mathbf{V_{sw}}$ **[km s^{-1}]**
I	STA	0.31	349
	STB	0.06	557
II	STA	0.37	328
	STB	0.10	584

The coloured thick solid lines in the two upper panels of Figure 3.5 show the best fit obtained using *SEPinversion*. We can claim that the model is able to reproduce quite well the observations, except for some disagreements that could be due to, e.g., the passage of local interplanetary magnetic field structures that invalidate the Parker field model, or other effects not included in the model. The results obtained assuming either the isotropic or the pitch-angle dependent scattering diffusion coefficient yield similar fits, being slightly better over all cases the fits derived by assuming isotropic pitch-angle scattering.

The electron radial mean free paths that provide the best fit in each case together with corresponding solar wind speed are listed in Table 3.2. The electron radial mean free paths that provide the best fit for Event I are, λ_r = 0.31 AU for STEREO A and λ_r = 0.1 AU for STEREO B; and for Event II, λ_r = 0.37 AU for STEREO A and λ_r = 0.06 AU for STEREO B.

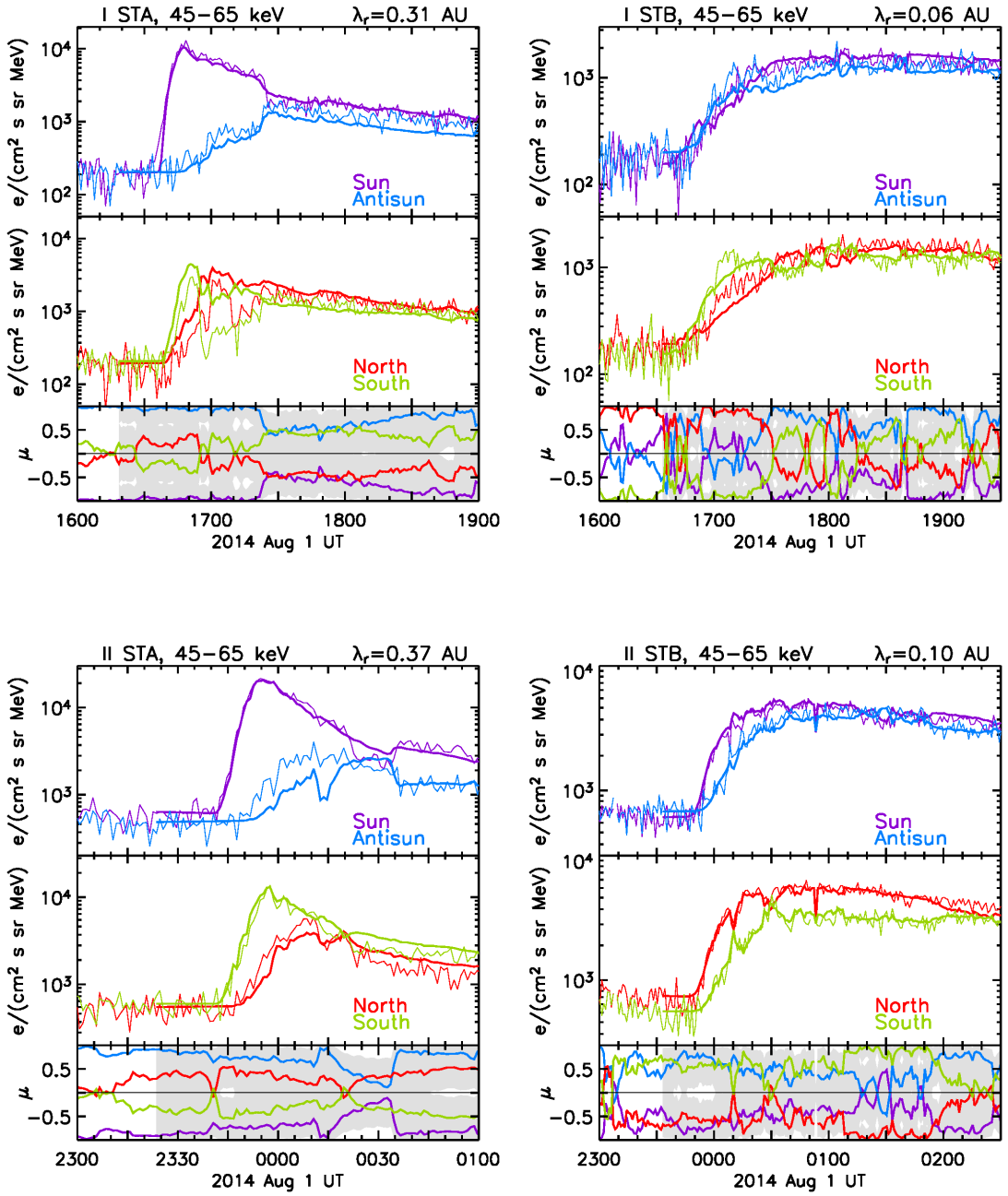

FIGURE 3.5: Two upper panels: Observed (thin curves) directional 45 – 65 keV electron intensities by STEREO A (left column) and STEREO B (right column) for Event I (top row) and Event II (bottom row). The intensity profiles for each field of view are identified by different colours as indicated in the inset (Sun and Antisun fields of view at the top panels; North and South fields of view at the second panels). Thick lines are the corresponding model fits. Bottom panels show the evolution of the pitch-angle cosine measured at the centre of each field of view (colour curves). The grey area shows the pitch-angle range covered by the telescopes.

The inferred value of the mean free path for each case is shown at the top of each plot.

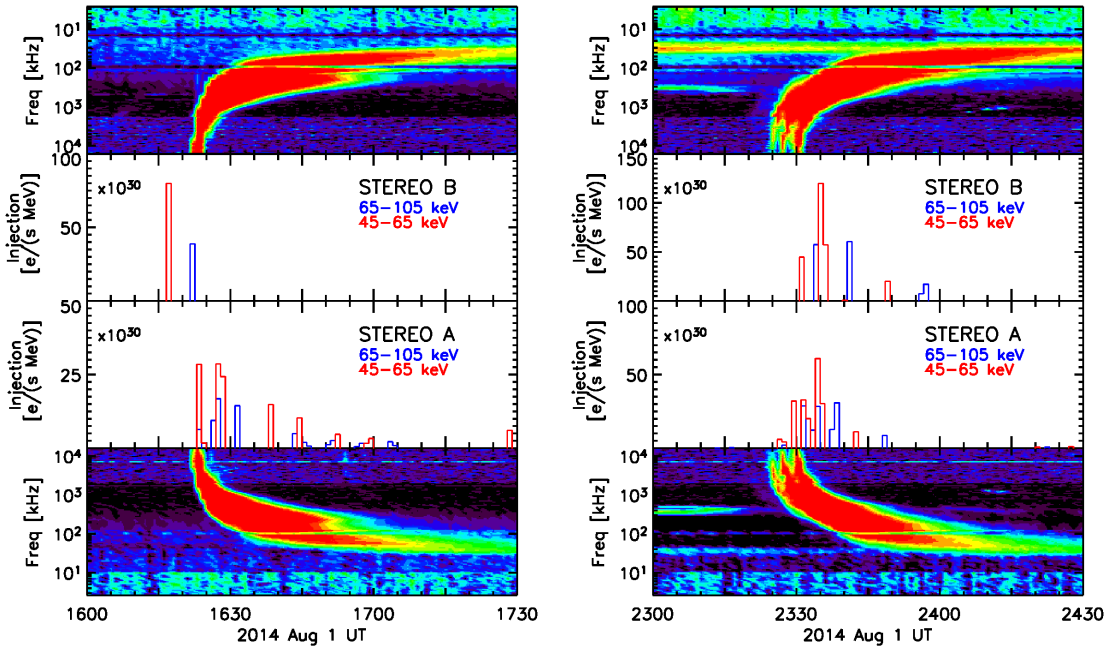

FIGURE 3.6: Release functions inferred for Event I (*left*) and Event II (*right*). For each event, from top to bottom: Radio spectra observed by STEREO B/WAVES mirrored in the y-axis, electron source profile deduced at $2R_{\odot}$ for STEREO A and STEREO B in two energy channels, 45 – 65 keV (red) and 65 – 105 keV (blue), and radio flux observed by STEREO A/WAVES. Injection times are shifted by 500 s for comparison purposes with electromagnetic emissions.

In Figure 3.6, for Event I (left) and Event II (right), the derived injection profiles are shown in the middle panels (STEREO B, upper panel and STEREO A, lower panel) for the two energy channels fitted (45 – 65 keV, red and 65 – 105 keV, blue). For each event, the radio spectra recorded by SWAVES is shown for STEREO B (top panels) and for STEREO A (bottom panels). Note that injection times are shifted by 500 s for comparison purposes with electromagnetic emissions. For the two events and for both STEREOs, we obtain a set of short injection profiles at $2R_{\odot}$ which agree with the timing and duration of the type III radio burst emission by SWAVES (with a 5 min uncertainty). The release of particles is almost simultaneous for both spacecraft and the injection is higher for STEREO B, the better-connected spacecraft, in both cases. Klassen et al. (2016) mentioned that different transport conditions could explain the onset delay and the peak intensity difference between the spacecraft. Our results confirm this idea.

Figure 3.7 shows the electron maximum peak injection at the Sun for Event I (diamonds) and Event II (triangles) as a function of the angular connection distance between the solar source and the spacecraft footpoint. STEREO A injections are shown in red as STEREO B injections are shown in blue for 45 – 65 keV (left panel) and 65 – 105 keV (right panel) electron channels. Note that for each event the injections lay over a Gaussian distribution centred at the source site (dashed and dotted curves for Event I and II, respectively); thus, suggesting a Gaussian distribution of the release of particles at the source, while the observed intensities at 1 AU do not follow this pattern due to the transport conditions. We can see that STEREO B injections

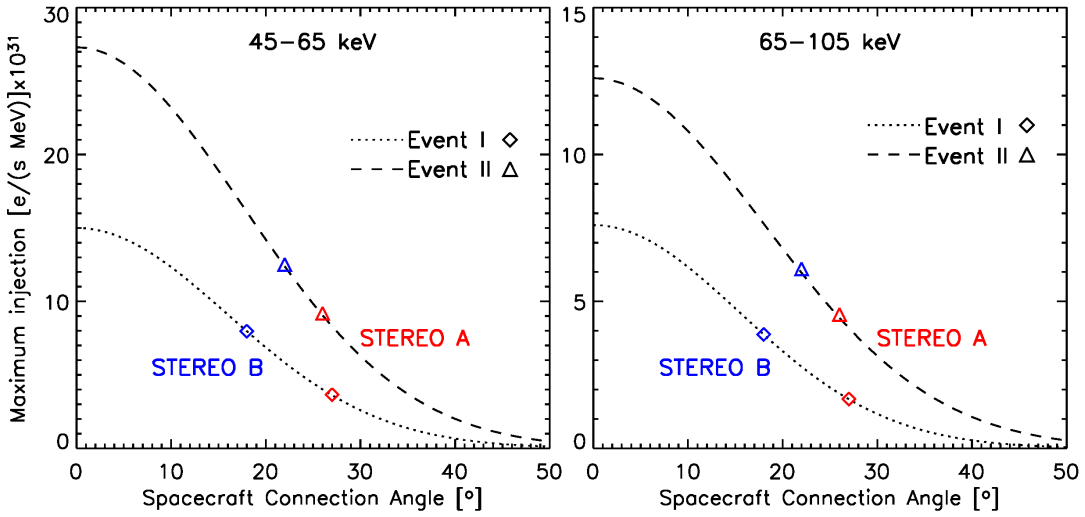

FIGURE 3.7: Maximum injection of electrons at the Sun vs. the spacecraft connection angle with the solar flare location, for 45 – 65 keV (left) and 65 – 105 keV (right) electrons. The inferred values of the maximum injection for STEREO A (red) and STEREO B (blue) are shown with diamonds (Event I) and triangles (Event II). The dotted/dashed curves show Gaussian distributions.

are consistently more intense than STEREO A for both channels and events. Nevertheless, the spacecraft connection angle considered should be taken carefully due to the error associated with their determination. It is clear from Figure 3.7 that under the assumptions of our model, the particle injection from second solar eruption was more intense than the first one.

3.5 Conclusions

In this chapter, we studied two consecutive electron events observed by the STEREO twin spacecraft on 2014 August 1 with only a few hours of delay between the events. Both electron events were associated with an unambiguous type III burst and not accompanied by type II radio bursts or CMEs (Klassen et al., 2016).

On that date, the longitudinal separation between the spacecraft was of only ~35°. Despite the close location of the two spacecraft, STEREO A was embedded in a slow solar wind stream, while STEREO B was inside a fast stream region stemming from a coronal hole.

In addition, for both events, the electron intensities observed by STEREO A and STEREO B showed clear differences in terms of onset time, peak intensity and evolution of the pitch-angle distributions. The events observed by STEREO A started to rise up to 20 min earlier than at STEREO B, and the peak intensity was about a factor 5 higher at STEREO A and more anisotropic. The apparently better connected spacecraft, STEREO B, observed a smaller intensity increase and a later event onset time than the worse connected spacecraft, STEREO A.

We studied if these observations could be explained by different electron transport conditions along the flux tube connecting each spacecraft back to the Sun. We modelled the two events using *SEPinversion* and inferred an almost simultaneous release of electrons for both spacecraft in both events. The release is consistent with the timing and duration of the type III radio burst emission and it is larger for STEREO B, the better connected spacecraft. In addition, we obtained different transport conditions in different solar wind streams, signalled by different solar wind speeds. We found that the stream in which STEREO B was embedded was more diffusive (λ_r = 0.1 AU for Event I and λ_r = 0.06 AU for Event II) than the stream in which STEREO A was embedded (λ_r = 0.31 AU for Event I and λ_r = 0.37 AU for Event II). These different transport regimes are sufficient to explain the early onset and the larger intensities for the worse connected spacecraft, STEREO A, as well as the difference in the observed anisotropies. We conclude that the interplanetary transport conditions can vary drastically between nearby solar wind streams.

Chapter 4

Electron events observed by Helios in the inner (< 1 AU) heliosphere.

4.1 The Helios spacecraft

The Helios mission was launched during the 70's and it was the product of the collaboration between the German Test and Research Institute for Aviation and Space Flight, Deutsche Forschungs- und Versuchsanstalt für Luft- und Raumfahrt (DFVLR, at present, DLR), and the United States National Aeronautics and Space Administration (NASA). The mission consisted of two almost identical solar probes, Helios 1 and Helios 2, orbiting the Sun with a high eccentricity during solar cycle 21. These spacecraft were spin-stabilised satellites with a spin period of 1 s. The mission lasted from December 1974 to March 1985 in the case of Helios 1, and from January 1976 to March 1980 for Helios 2. Both spacecraft reached a heliocentric radial distance from the Sun of ~0.3 AU in the perihelion and of ~0.99 AU in the aphelion with periods of ~190 days, providing the first in-situ study of the inner heliosphere devoted to the interplanetary medium and, at present, Helios is still the mission that has provided the largest data set of SEP events measured in the inner heliosphere. Helios 2 is still the spacecraft that orbited closest to the Sun until now, with a perihelion of 0.29 AU.

Each probe carried 12 experiments aiming at studying the main physical processes in the interplanetary space, from a near-Sun environment, specifically, the study of heliospheric energetic particles, the solar wind plasma, the interplanetary magnetic fields and the cosmic dust. Table 4.1 lists the experiments on board the Helios spacecraft (see Porsche, 1975, Goodwin et al., 1976).

Helios data have been deeply studied since then and have been crucial in the understanding of the interplanetary transport of solar energetic particles (SEPs). SEP events observed by

TABLE 4.1: Description of the instruments on board Helios spacecraft.

Num.	Experiment	Measurements
E1	Plasma Detector Experiment	Flux density, velocity, composition, direction and energy of the charged particles
E2/E3	Flux-Gate Magnetometer	Magnetic field strength and direction in the inner heliosphere.
E4	Search-Coil Magnetometer	Sudden changes in the interplanetary electromagnetic field in the frequency range of 5 Hz to 3 kHz
E5	Solar Wind Plasma and Radio Wave Experiment	Low-frequency radio waves in the inner heliosphere.
E6	Cosmic Ray Experiment	High-energy charged particles in terms of their energy, time, charge, mass and direction of incidence.
E7	Galactic and Solar Cosmic Ray Experiment	High-energy cosmic rays above the range of E6, including the X-ray radiation, with three different particle telescopes for electrons, protons and heavier particles.
E8	High Energy Electron and Proton detector	Using an inhomogeneous magnetic field to deflect the heavy charged particles, it measured protons, electrons and positrons for lower energies than E6.
E9	Zodiacal Light Photometer	Intensity of the zodiacal light in 3 wavebands (UV radiation, blue waveband and entire visual band) using 3 photometers oriented at angles of 15°, 30°, and 90° to the ecliptic.
E10	Micrometeoroid Counter and Analyser	Dust particles and determine their mass and energy with a mass threshold of about 10^{-15} g.
E11	Celestial Mechanics Experiment	Oblateness of the Sun, general relativity with respect to both orbital and signal propagation effects, the mass of the planet Mercury, the Earth-Moon-mass ratio and others.
E12	Faraday Rotation Experiment	The composition of linearly polarised electromagnetic waves that travelled across the solar corona and the interplanetary medium.

Helios permitted to study their characteristics and untangle the influence of the Sun over the interplanetary medium (e.g., Schwenn and Marsch, 1990, 1991, Reames et al., 1996, Lario et al., 2006).

4.1.1 Particle measurements by Helios

The Cosmic Ray Experiment (E6) (Kunow et al., 1975, 1977) was designed at the University of Kiel to study solar energetic particles. It consisted of five semiconductor-layer detectors and a sapphire Čerenkov detector, all surrounded in anticoincidence by a plastic scintillator. The semiconductor detector configuration had a nominal geometrical factor of ~0.48 cm^2 sr and a nominal full opening angle of 55°. Table 4.2 lists the nominal energy ranges of the four electron channels E03, E08 (both sectored), E2 and E3 (both omnidirectional) together with the nominal energies of the five proton differential channels P1, P4, P13, P27, P37 (all sectored except P37,

TABLE 4.2: Nominal energy ranges of electron and proton channels of E6, for Helios 1 and Helios 2.

Electron channel	Energy range (MeV)		Proton channel	Energy range (MeV)	
	Helios 1	Helios 2		Helios 1	Helios 2
E03	0.3 – 0.8	0.3 – 0.8	P1	1.28 – 3.77	1.66 – 3.68
E08	0.8 – 2.0	0.8 – 2.0	P4	3.77 – 12.81	3.68 – 12.73
E2	2.0 – 3.0	2.0 – 3.0	P13	12.81 – 26.76	12.73 – 27.36
E3	3.0 – 4.0	3.0 – 4.0	P27	26.76 – 36.63	27.36 – 37.34
			P37	36.63 – 50.70	37.34 – 51.00
			P51	>50.70	>51.00

which is omnidirectional), and of the integral channel, P51. So far, these measurements are the only source available of particle events detected at the inner heliosphere with sectored data allowing us to reconstruct the PADs.

Bialk et al. (1991) presented a Monte Carlo simulation for the reaction of the detectors which compound E6 to a wide energy-range of protons, γ-rays and electrons, taking into account the geometry, energy resolution and electronics of the detectors. As shown in Figure 4.1a, in a first approach, simulations showed that the response function obtained for protons were in good agreement with the nominal geometrical factors. On the other hand, the electron response function was much wider (see Fig. 4.1b), considerably overlapping the different electron channels and extending up to ~5 MeV for E03. Furthermore, it was found that the response for protons in the electron channels was substantial when exposed to high proton flux levels, as depicted in Figure 4.1c.

The E6 experiment scanned the space in the ecliptic plane, 90° away from the spacecraft Z axis, using the rotation of the spacecraft to measure the particle angular distributions relative to the local direction of the magnetic field (i.e., the PADs) of SEPs in interplanetary space. Measurements of the 360° rotation were divided into eight equally spaced sectors, labelled from 0 to 7 as shown in Figure 4.2, for electrons, protons and alpha particles channels. Helios 1 rotation axis was pointing towards the ecliptic North pole and Helios 2 towards the ecliptic South (e.g., Wibberenz et al., 1989). For further reference, Figure 1c) of Wibberenz et al. (1989) shows a scheme of the field of view scanned by the E6 instrument. Table 4.3 shows, for each spacecraft, the coordinates of the sector centre unit vectors $\hat{s}$, in the spacecraft-centred spherical Spacecraft Solar Ecliptic (SSE)[1] coordinates (e.g., Fränz and Harper, 2002), where θ is the colatitude and φ is the azimuth. The Z axis corresponds to $\theta = 0°$ and it is perpendicular to the ecliptic plane. The azimuth origin is the spacecraft-to-Sun line (see Fig. 4.2).

[1]This coordinate system uses the Earth mean ecliptic plane as XY-plane, being the X axis the projection over XY-plane of the spacecraft-Sun line and takes the Z axis perpendicular to them. Fränz and Harper (2002) mention that this coordinate system points toward the ecliptic South pole. Comparison with magnetic field data provided by the NASA's NSSDCA Archive (see below) in both the SSE and the Radial Tangential Normal (RTN) coordinate system shows that B_N=$B_{Z(\mathrm{SSE})}$, thus indicating that Z_{SSE} points towards the ecliptic North. In any case, this discrepancy does not affect the sector directions, nor the pitch-angle distributions retrieved from data in next sections.

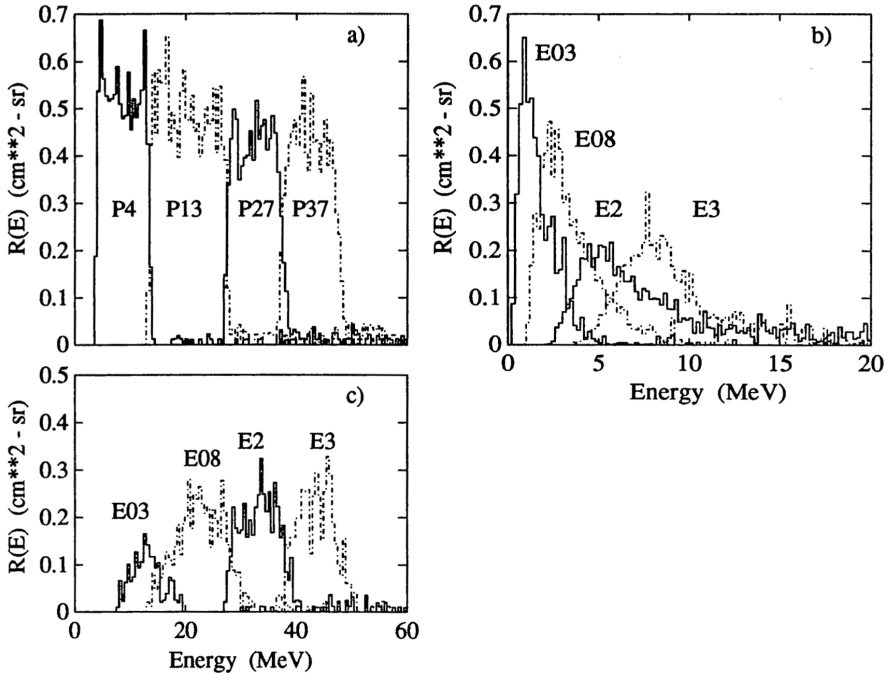

FIGURE 4.1: Response function for the different channels of E6 experiment on board Helios. Panel a) shows protons measured in proton channels, b) electrons detected in electron channels and, as a measure of the cross contamination, c) shows the protons counted in electron channels. From Bialk et al. (1991).

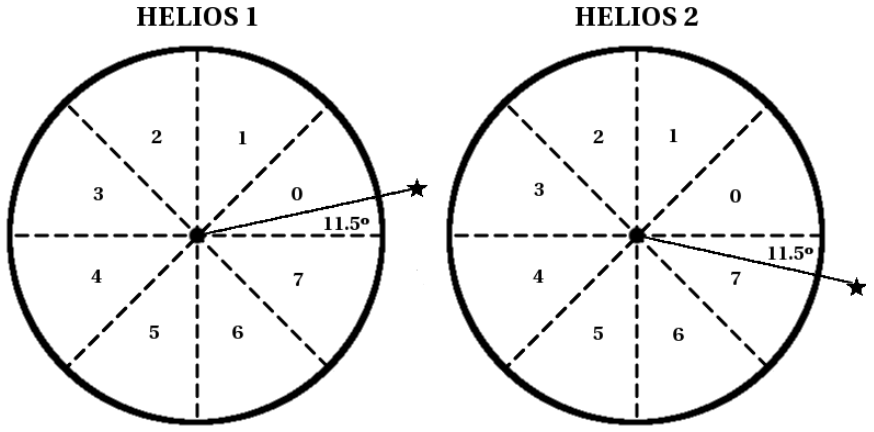

FIGURE 4.2: Configuration of the sectors defined by the E6 experiment. Each sector is identified by a number. The azimuth origin for each spacecraft corresponds to the spacecraft-Sun (star) line.

The E2 experiment (Musmann et al., 1975) was a three axes flux-gate magnetometer on board Helios probes designed by the University of Braunschweig to work over different ranges of magnetic field strength. Its observations were afterwards combined with particle data from E6 by the team at the University of Kiel to create a single data set, with proton, alpha-particles and electron intensities and magnetic field vector data.

E2 data originally presented a very good time resolution, of 8 measurements per second at the highest resolution mode. On the other hand, E6 time resolution was around 40 s in spite of the fact that it presented strong irregularities in the time step. The resolution of the instruments used from each moment depended on the information transmission rate of the probe to the Earth ground-based stations, that unfortunately was often quite small. Magnetic field data is available also at the NASA Space Science Data Coordinated Archive (NSSDCA)[2].

For the present study, data files of the whole mission were provided by the University of Kiel (B. Heber, private communication) in daily files containing both particle sectored data and interplanetary magnetic field strength and direction (in the SSE coordinate system) with the same time resolution. This time resolution varies from 1 min to 15 min although the precise time step is not totally uniform, as the exact values can vary from 40 s to 90 s for the 1 min resolution files. Also data gaps are frequent and they can extend for several days. For the same time period, the time step and the data gaps can be different for different energy channels of the instrument.

Due to this fact, we decided to use a regularly spaced time grid of resolution 1 min (or occasionally 15 min, when 1 min data was unavailable). For that purpose, the data of the E03 electron channel of E6 and the magnetic field data gathered by E2 were linearly-interpolated.

The particle pitch-angle, α, is defined as the angle between the magnetic field vector and the particle velocity. The cosine of α is then given by the scalar product of the magnetic field vector and the unit velocity vector of the particle, $\mu = \hat{B} \cdot \hat{v}$. The average cosine of the particles detected by each sector can be approximated by the product of the magnetic field unit vector and the direction of the pointing vector at the centre of each sector (see Table 4.3), i.e., $\mu = -\hat{B} \cdot \hat{s}$.

In order to analyse the SEP events, we also used the solar wind speed, density and temperature from the Plasma Detector Experiment, E1 (Schwenn et al., 1975), available at NASA's National Space Science Data Center, Space Physics Data Facility.[3]

4.2 Event Selection

We scanned data provided by the E6 experiment designed by the University of Kiel for the whole mission period. We selected relativistic electron events observed in the E03 channel, with

[2] ftp://spdf.gsfc.nasa.gov/pub/data/helios/
[3] ftp://spdf.sci.gsfc.nasa.gov/pub/data/helios

TABLE 4.3: Pointing directions of the sectors of the E6 experiment on board the Helios probes.

Sector	Helios 1 $\hat{\mathbf{s}}$		Helios 2 $\hat{\mathbf{s}}$	
ID	θ	φ	θ	φ
0	90°	11°	90°	34°
1	90°	56°	90°	79°
2	90°	101°	90°	124°
3	90°	146°	90°	169°
4	90°	191°	90°	214°
5	90°	236°	90°	259°
6	90°	281°	90°	304°
7	90°	326°	90°	349°

nominal energy range 0.3 – 0.8 MeV. We found more than 200 hundred electron events during the mission period, detected by at least one of the two spacecraft. However, most of them were discarded for the purposes of our study. The criteria we followed to select the best-observed events for modelling are:

i) no data gaps during the rising phase of the electron event for the instruments used in the study, i.e., the E03 electron channel of E6 and the magnetic field data of E2;
ii) electron event peak intensities at least one order of magnitude above the pre-event background intensities;
iii) IMF as close as possible to an ideal Parker Spiral;
iv) location of the parent solar activity associated with each event documented in the literature;
vi) no significant cross-contamination by protons during the time interval selected for each event.

The first criterion was by far the most restrictive owning to the long periods when the coverage of one of the instruments was lost or presented numerous gaps. In particular, we found several cases showing data gaps just at the peak or during the rising phase of the events, either in the particle intensities or the magnetic field data. Moreover, many other events were discarded as being not intense enough or happening right after a larger event, in such a way that the pre-event intensity level masked the onset of the event of interest. We discarded only few events due to criterion iii), to be sure that magnetic configuration was as close as possible to a Parker Spiral. We checked shock crossing at the spacecraft since a shock between the sun and the spacecraft or beyond the spacecraft could affect the transport conditions of electrons and/or increase the length of the field line. Furthermore, we required that the origin of the SEP events was documented in the literature: published articles, Solar-Geophysical Data (SGD) reports[4]

[4] `ftp://ftp.ngdc.noaa.gov/STP/SOLAR_DATA/SGD_PDFversion/`

TABLE 4.4: Observational characteristics of the list of selected events.

Year	Date	DOY	S/C	Onset [UT]	Rise [min]	Reso. [min]	Distance [AU]	v_{sw} [km s^{-1}]	IMF polarity
1976	Mar 21	81	H1	12:52	18	1	0.36	450	-1
1978	Jan 1	1	H1	22:00	53	1	0.94	434	-1
1978	Dec 11	345	H2	20:00	74	1	0.73	317	-1
1980	Apr 5	96	H1	15:55	28	15	0.85	314	+1
1980	Apr 26	117	H1	13:40	19	1	0.66	389	+1
1980	May 3	124	H1	08:00	20	1	0.58	421	-1
1980	May 12	133	H1	02:51	30	1	0.46	328	-1
1980	May 28 a	149	H1	15:44	5	1	0.31	278	-1
1980	May 28 b	149	H1	17:04	10	1	0.31	278	-1
1980	May 28 c	149	H1	19:38	7	1	0.31	278	-1
1980	May 28 d	149	H1	23:34	7	1	0.31	278	-1
1981	Jan 14	14	H1	21:01	20	1	0.73	309	+1
1981	May 8	128	H1	22:50	86	15	0.69	369	-1
1981	Jun 10	161	H1	06:16	30	1	0.32	245	-1
1982	Jun 2	153	H1	15:44	59	1	0.59	467	-1

and GOES Soft X-ray (SXR) data available online[5]. Finally, in the last selection step we evaluated the cross-contamination of protons in the electron channel E03. We compared the E03 intensities with the proton intensities for channels P4 and P13 and discarded events showing a combined proton flux from both channels (properly corrected using the cross-contamination factors provided by B. Heber) higher than the 10% of the E03 intensity.

The final sample of events is composed by 15 events. In Table 4.4 we list their year, date and DOY, the spacecraft used in the analysis, the onset time and rise time of the event, i.e., the time from the onset to the E03 intensity peak, the time resolution of the data used in the study, the helioradius of the spacecraft, the computed average solar wind speed during the six hours previous to the event, and the modal polarity of the IMF. The polarity of the IMF up to 1 AU can be defined as

$$\text{sign}(\vec{B}) = \text{sign}(B_R - B_T \tan\Psi), \tag{4.1}$$

where B_R and B_T are the R and T components of the magnetic field vector in the Radial Tangencial Normal (RTN) coordinate system, respectively, and Ψ is the angle between the nominal Parker spiral magnetic field vector and the radial vector from the Sun, i.e. $\tan\Psi = \frac{r\Omega}{v_{sw}}$, being r the radial distance to the Sun, Ω the solar rotation rate and v_{sw} the solar wind speed. Note that we are neglecting here the inclination of the ecliptic at the position of the spacecraft with respect to the solar equatorial plane, that can introduce an error up to 1% in RTN components.

At first sight, it is remarkable the difference in numbers for the events observed by Helios 1 (14 events) and Helios 2 (only 1 event). The solar maximum period of Solar Cycle 21 started

[5] ftp://ftp.ngdc.noaa.gov/STP/space-weather/solar-data/solar-features/solar-flares/x-rays/goes/xrs/

on the second half of 1977, being 1980 one of the years with larger number of SEP events. Unfortunately, Helios 2 stopped operating in the early March of that year, explaining the larger number of selected events detected by Helios 1. Also, Helios 2 instruments underwent more problems reflected in numerous data gaps.

The sample is composed by SEP events observed during streams of solar wind speeds between 245 km s^{-1} and 467 km s^{-1}. The whole range of radial distances is well covered, having events observed from 0.31 AU to 0.94 AU. We can divide the locations into three different groups, events observed at radial distances < 0.40 AU (6 events), events observed between 0.40 – 0.70 AU (5 events) and events observed at radial distances > 0.70 AU (4 events). This latter group allows us to directly compare our results with previous results obtained close to the Earth orbit (∼1 AU). It is also important to remark that as a result of the different time-resolutions in the SEP data files, we worked with 1 min resolution data for 13 events, and 15 min for 2 events corresponding to 1980 April 5 and 1981 May 8 (as indicated in Table 4.4).

The sample includes 11 events with rising times shorter than 35 min, and 4 events with longer rising times of up to ∼90 min. The different shape of the intensity-time profiles between these impulsive and gradual groups is also noticeable in the decaying phase, presenting the gradual events a sustained intensity plateau extending for several hours that decreases very slowly, whereas for impulsive events the decay is faster after the peak. A series of typical impulsive events, with a fast and short rise phase is shown as an example in Figure 4.3. Figure 4.4 depicts a gradual event showing the aforementioned plateau.

Table 4.5 lists the location of the parent solar source associated with each event as observed from Earth in Hα (Kallenrode et al., 1992a,b, Lario et al., 2006, Agueda and Lario, 2016, Gardini et al., 2011, Solar-Geophysical Data reports), the longitudinal distance between the Hα source and the spacecraft and the connectivity of the source (Δ), i.e. the longitudinal distance between the solar source and the footpoint of the Archimedean magnetic field line connecting the spacecraft to the Sun, calculated by using the solar wind speed measured in situ. The magnetic connectivity is positive when the footpoint is further West than the solar source, and it is negative if the footpoint is further East.

Most of the selected events are well connected to the solar source, with $\Delta < 20°$. Only three events have larger values of Δ, which correspond to one western event near the limb (1981 Jan 14) and two events associated with central meridian sources located 1° East (1981 June 10) and 5° East (1978 Dec 11). Note that these locations of the solar sources are given as seen by the Helios spacecraft. The fact that most of the events are well connected can be attributed to the event selection criteria of showing intensity peaks of at least one order of magnitude above the pre-event background. Hence, our sample is biased to western events, owing to the large-scale bending of the IMF that favours the magnetic connection of the spacecraft to western solar locations.

TABLE 4.5: Solar electromagnetic emissions detected from Earth associated with the selected events.

Year	Date	Onset	Hα	Hα	Δ	Soft X-rays[a]				Radio[b]				
		[UT]	Earth	observer	[◦]	Start [UT]	Peak [UT]	End [UT]	Class	Start [UT]	Peak [UT]	Duration[c] [min]	Freq [MHz]	Station
1976	Mar 21	12:52	N03W33	W08	-10	13:06	13:10	13:23	M1	12:42	12:51	29.0	2695	SGMR
										12:42	13:00	-	2695	SGMR
										13:11	13:11	15.0	2695	SGMR
1978	Jan 1	22:00	S21E06	W33	-17	21:47	21:58	22:30	M3	21:48	22:07	19.1	9400	HUAN
										22:07	22:20	12.9	9400	HUAN
1978	Dec 11	20:00	S15E14	E05	-57	18:33	19:42	20:18	X1	19:40	19:49	11.0	1420	BOUL
										19:51	19:57	-	1420	BOUL
										19:51	20:32	49.0	1420	BOUL
1980	Apr 5	15:55	N08E22	W64	2	15:32	16:52	16:58	M5	15:46	15:53	21.0	600	UCCL
1980	Apr 26	13:40	S21E23	W59	20	12:50	12:52	13:05	C3	13:40	13:43	11.8	29	UPIC
1980	May 3	08:00	N25E35	W41	9	07:50	08:06	08:13	C9.4	08:00	08:01	4.5	808	ONTR
1980	May 12	02:51	S14E11	W51	18	02:54	02:55	03:03	C4.3	02:54	02:54	11.0	500	HIRA
1980	May 28 a	15:44	S24W28	W23	-3	15:53	15:58	16:19	C9.1	15:45	15:53	35.0	5000	BERN
1980	May 28 b	17:04	S18W35	W30	4	17:05	17:18	17:53	M3.6	17:02	17:17	30.0	930	BORD
1980	May 28 c	19:38	S18W33	W28	2	19:24	19:51	20:53	X1.1	19:47	19:48	21.0	100	HIRA
1980	May 28 d	23:34	S17W39	W34	8	23:32	23:44	24:45	M6.9	23:38	23:42	18.0	500	HIRA
1981	Jan 14	21:01	N12E02	W80	26	20:58	21:33	21:33	C7.2	20:59	21:00	3.3	245	SGMR
1981	May 8	22:50	N09E37	W61	18	22:50	22:51	23:20	M1.7	23:10	23:20	38.6	245	LEAR
1981	Jun 10	06:16	N13E24	E01	-31	06:22	06:24	07:08	M2.2	06:21	06:24	24.0	200	HIRA
										06:21	06:26	-	200	HIRA
										06:21	06:32	-	200	HIRA
1982	Jun 2	15:44	S08E81	W25	-4	15:08	15:48	16:20	M9.9	15:44	15:46	11.5	2800	OTTA

[a] GOES catalogue: `ftp://ftp.ngdc.noaa.gov/STP/space-weather/solar-data/solar-features/solar-flares/x-rays/goes/xrs/`.

[b] Solar-Geophysical Data reports: `ftp://ftp.ngdc.noaa.gov/STP/SOLAR_DATA/SGD_PDFversion/`.

[c] Radio emissions with no duration value indicate different peaks inside a long lasting emission.

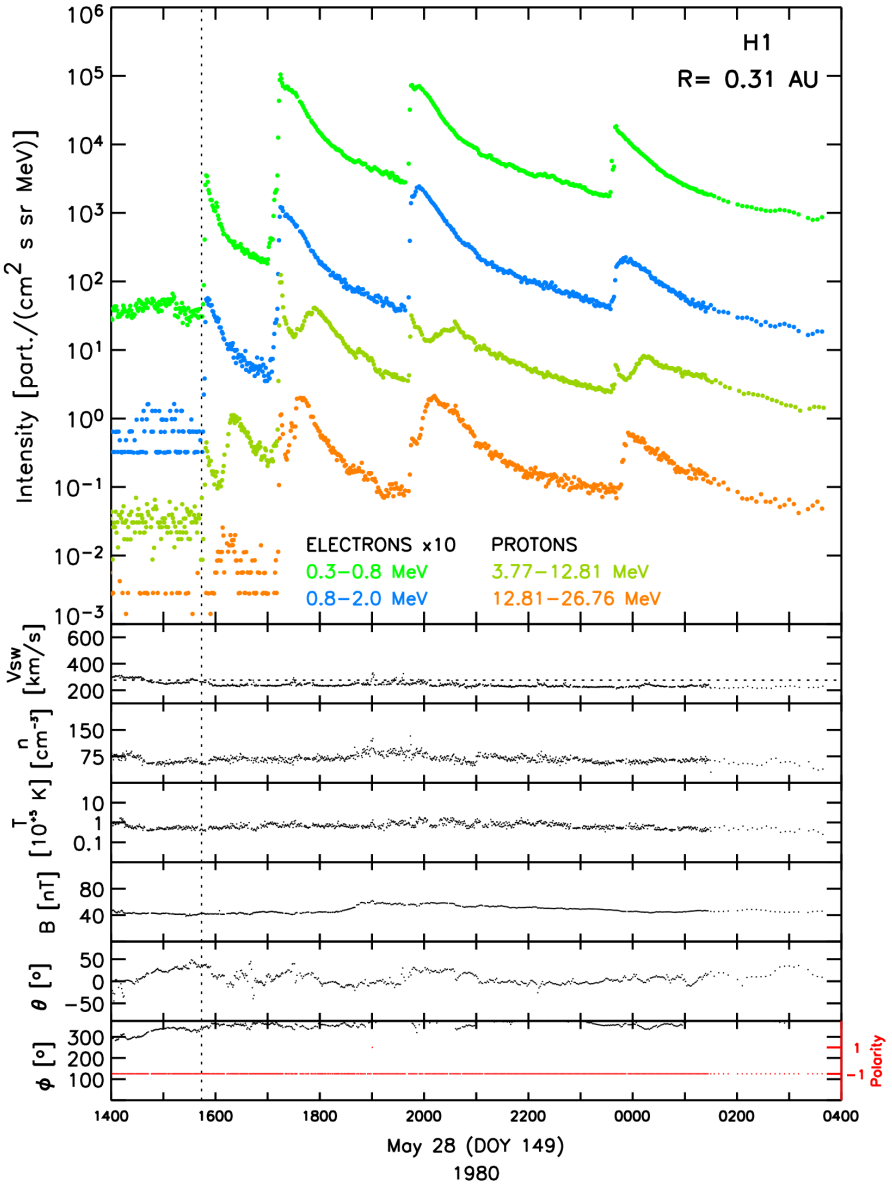

FIGURE 4.3: In-situ measurements on 1980 May 29 by Helios 1. Top panel: particle intensities for electrons (dots, scaled by a factor of 10) from channels E03 (green) and E08 (blue), and protons (curves) from channels P4 (olive) and P13 (orange), measured by E6. Next panels from top to bottom: proton solar wind speed, density and temperature; magnetic field strength and direction (RTN). Red dotted line in the last panel depict the IMF polarity. The vertical dotted line across all panels indicates the event onset.

Figure 4.5 shows the spatial configuration scheme for each event; given the similar configuration of the four events on 1980 May 28, only one plot is shown (top left in Fig. 4.5). In each instance, the black curve represents the IMF line connecting the spacecraft with the Sun, the thick short straight line shows the observed flare position on the Sun surface, the thin straight line shows the Sun-spacecraft line to allow the comparison with the flare direction, and the dashed circles represent the orbits of Mercury (0.4 AU), Venus (0.7 AU) and Earth (1.0 AU). As can be seen in Figure 4.5, 13 out of 15 events in our sample are associated with parent solar activity occurring at longitudes western from the Sun-spacecraft line.

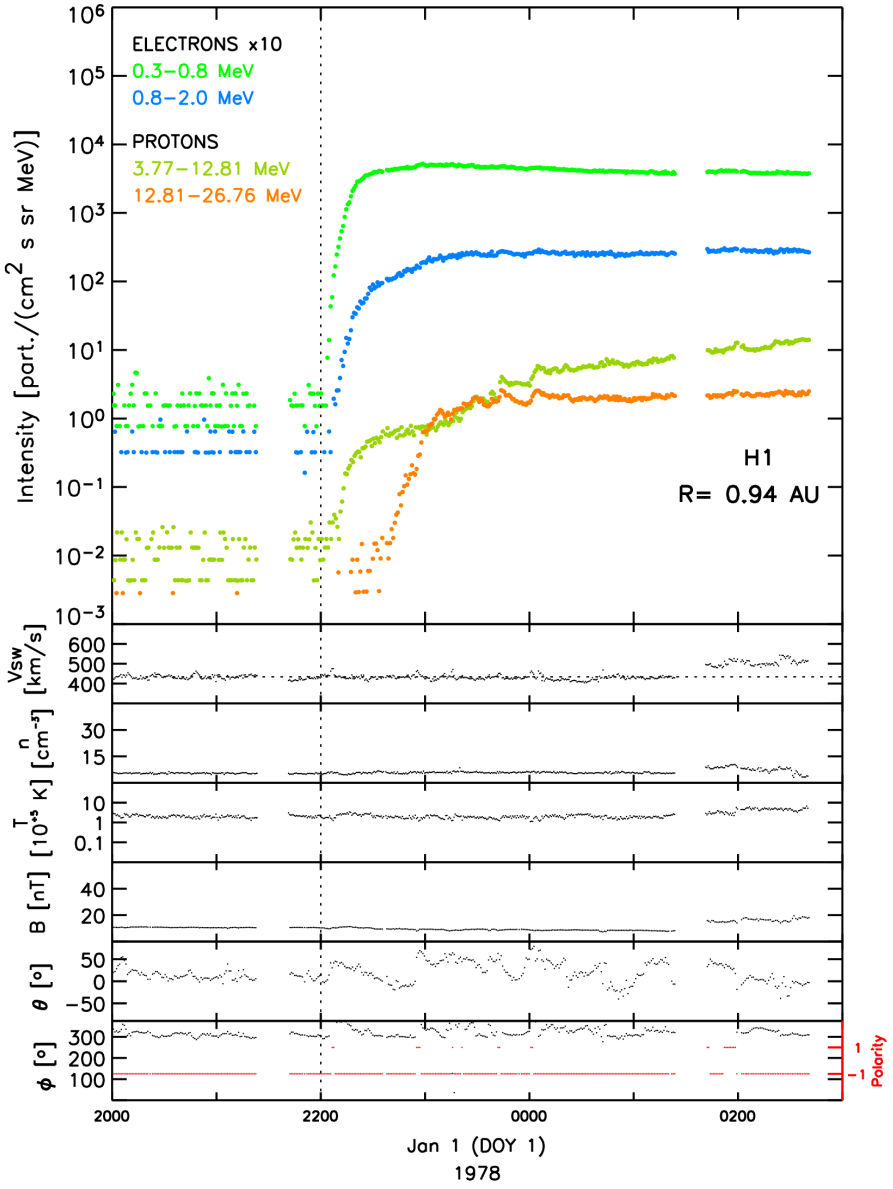

FIGURE 4.4: In-situ measurements on 1978 January 1 by Helios 1. See caption of Figure 4.3 for details.

Table 4.5 also lists the electromagnetic emissions (EMs) associated with each event. It lists the onset, peak and end of the SXR emission observed by GOES, the flare class, and the timing and characteristics (frequency and station) of the solar radio emission listed in the SGD reports. For each event, we identified the SXR emission and the radio emission occurring closer to the onset time of the event. We took into account the travel time of 950 keV electrons from the Sun to the spacecraft along the IMF and the time needed for the EMs to reach 1 AU, where GOES and radio stations are. We found no SXR emission matching precisely the timing for the event on 1980 Apr 26, so we listed the closest SXR emission found in GOES reports, corresponding to a 15 min long C3-class flare. For several events, various stations reported radio emission periods at different frequencies. In these cases we chose the lower radio frequency (always > 29 MHz) and the radio emission available lasting less than 30 min when possible. When the emission

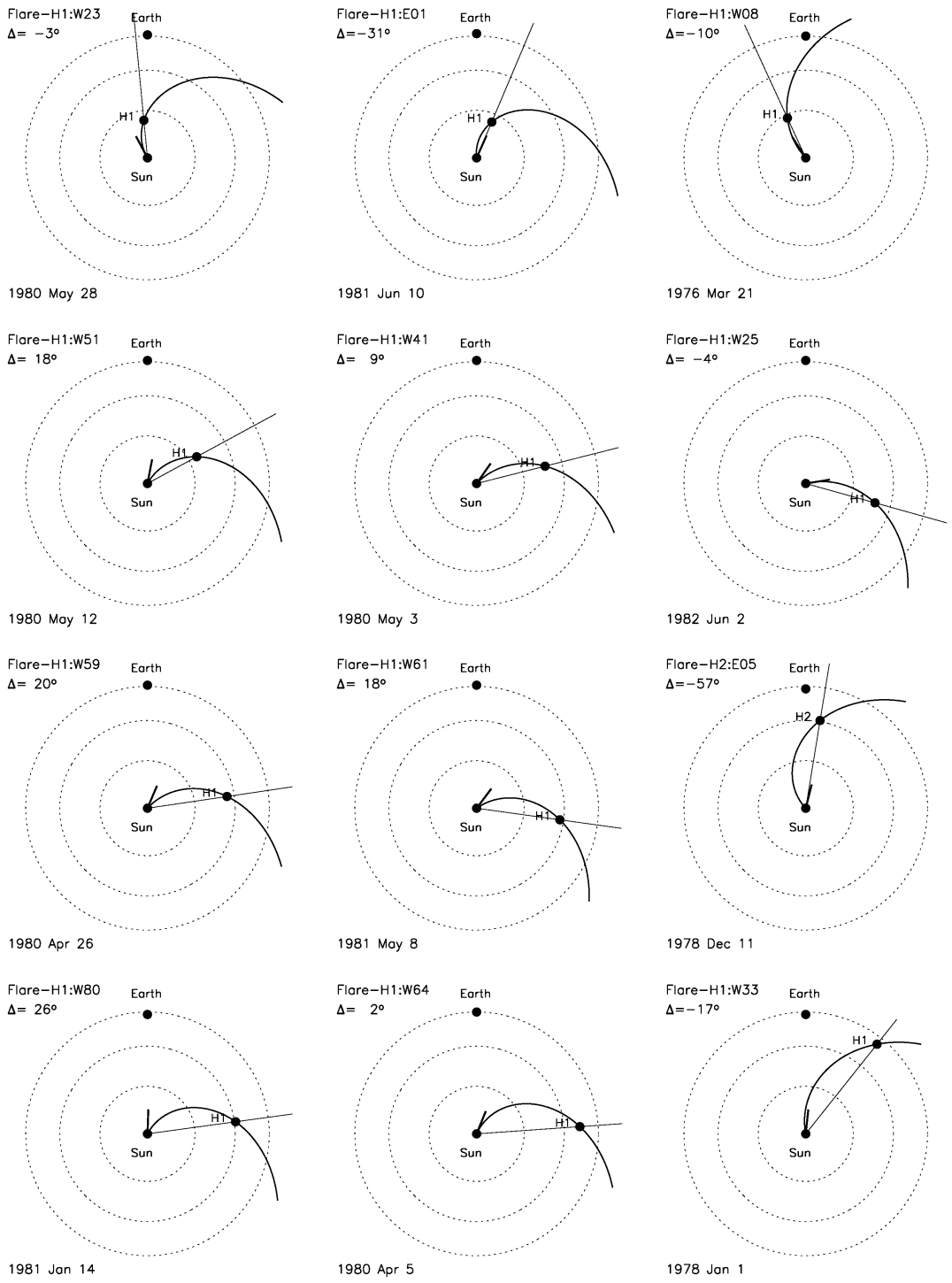

FIGURE 4.5: Longitudinal configurations of spacecraft and source active regions for each of the events in the sample. Events are ordered by increasing distance of the Helios spacecraft from the Sun. The thick line marks the longitude of the flaring source active region, the black spiral is the nominal Parker field line connecting the spacecraft to the Sun according to the solar wind speed measured in situ.

showed several peaks at the same frequency observed by the same station, we understood that they belong to the same radio burst, and we listed them together as an extended emission with several peaks with no duration. The sample includes radio emissions at frequencies larger than 29 MHz and up to 9400 MHz.

The events in our sample were associated mostly with M- and C- class flares. Eight events were associated with M-class flares, five with C-class flares and only 2 events with X-class flares. The duration of the SXR emission was less than 60 min for most of the events, except for the largest 5 flares in the sample (1978 December 11, 1980 April 5, 1980 May 28 c and d, and 1982 June 2) that showed SXR emission lasting up to ~2 h. The rise time of the SXR emission is less than 40 min in most cases (13 events), and only two event are associated with flares with longer rise times. These latter are the 1978 December 11 and 1980 April 5 events. In general, we observe that flares with shorter rise times have shorter durations.

The start of the radio emission is observed within 10 min of the beginning of the SXR emission for most of the events (7 events). For 5 events, the radio emission starts between 10 and 30 min before/after the beginning of the SXR emission. And only for 3 events (1978 December 11, 1980 April 26 and 1982 June 2) the beginning of the radio emission is delayed between 30 and 70 min with respect to the beginning of the SXR emission. The peak in SXR emission appears within 10 min of the radio emission for 10 events, while for 3 events the time of the peak emission differs from 10 to ~30 min. One event of the sample (1980 April 5) shows a long delay of an hour between the peak in radio emission and the peak in SXRs.

For 4 cases, we found complex radio emission consisting on several bursts and showing various peaks for the same frequency. On 1978 January 1, for example, we identified a complex radio emission divided into 2 different bursts of 19-min and ~13 min length at 9400 MHz, showing 2 different peaks 9 and 22 min after the SXR peak. Moreover, on 1978 December 11 event a complex radio emission was detected at 1420 MHz, consisting on a 11 min precursor with a peak 9 min after the onset, and a great burst with 2 different peaks 17 min and 52 min after the initial radio onset. The first 2 peaks fall inside the rising phase of the event while the last one is located in the decaying phase.

4.3 Modelling

In the absence of large-scale disturbances, the IMF can be described as an average field given by an Archimedean spiral with a superposed turbulent component. The propagation of charged particles along the IMF has then two components, adiabatic motion along the smooth field and pitch-angle scattering by magnetic turbulence. The quantitative treatment of the evolution of the particles' phase space density, $f(t, z, \mu, v)$, is described by the focused transport equation

(Roelof, 1969),

$$\frac{\partial f}{\partial t} + \frac{\partial}{\partial z}\,\mu\, v\, f + \frac{\partial}{\partial \mu}\frac{1-\mu^2}{2L} v\, f - \frac{\partial}{\partial \mu}\left(D_{\mu\mu}\frac{\partial f}{\partial \mu}\right) = q(z,\mu,t), \tag{4.2}$$

where t is the time, z is the distance along the magnetic field line, μ is the particle pitch-angle cosine, and v is the particle speed. The focusing effect is characterised by the focusing length, $L(z) = -B(z)/(\partial B/\partial z)$, in the diverging magnetic field, B, while the pitch-angle diffusion coefficient, $D_{\mu\mu}$, describes stochastic processes. The injection of particles close to the Sun is given by $q(z,\mu,t)$.

Equation 4.2 neglects convection and adiabatic deceleration. This approximation is useful for high energy particles. Note also that in this equation the particle speed, v, acts only as a parameter, and it can be removed using an appropriate scaling factor. If instead of f, we consider the differential intensity, $dI/dE = p^2 f$, and multiply Equation 4.2 by p^2/v, we get that the focused transport equation for the scaled quantity $j = Ic/v$ is valid regardless of the speed we use to obtain the solution[6] (e.g., Heber et al., 2018). Therefore Green's functions computed for hypothetical relativistic particles ($v = c$) can be used to obtain the Green's functions for other mono-energetic particles. The Green's function computed for $v = c$, $J(t,z,\mu,c)$, with the time and the intensity variables scaled with the quantity v/c provides the Green's function for mono-energetic particles with speed v, that is,

$$J(t,z,\mu,v) = \frac{v}{c}\, J\left(\frac{v}{c}t, z, \mu, c\right). \tag{4.3}$$

4.3.1 Energy response of the detector

We use the interplanetary transport model by Agueda (2008) to compute the Green's functions of interplanetary transport to be used in the study of Helios E03 electron observations. To obtain the Green's function in the nominal 0.3 – 0.8 MeV energy range, we consider 20 discrete electron energies with a constant logarithmic step within the range. We scale the Green's function obtained for $v = c$ for each electron energy according to Equation 4.3 and then interpolate the results in order to obtain the intensities in a 1 min time resolution grid. Then the intensities are scaled according to the normalised solar spectrum. We assume a power-law dependence $N(E) \propto E^{-\gamma}$, where γ is the spectral index of the solar source.

As an example, Figure 4.6 shows the differential intensities at 0.31 AU for 20 energies between 300 keV and 800 keV (coloured curves), obtained by assuming an instantaneous injection of electrons at two solar radii with spectral index $\gamma = 3.5$ and a radial mean free path of 0.14 AU. At each time, the differential intensity for the nominal 300 – 800 keV energy range (black

[6] http://www.ieap.uni-kiel.de/et/people/heber/summerschoool/GF-scaling.pdf

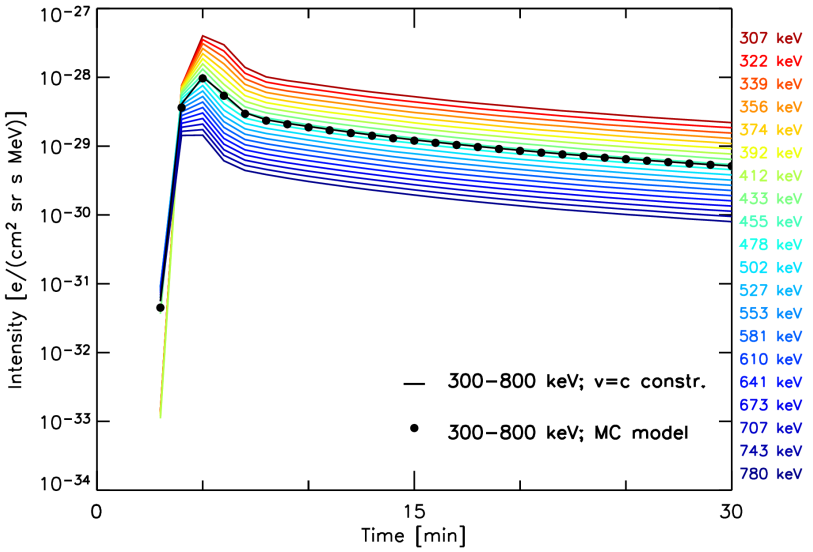

FIGURE 4.6: Green's function of interplanetary transport at 0.31 AU for 0.3 – 0.8 MeV electrons released at the Sun at $t = 0$ assuming a spectral index of $\gamma = 3.5$ and a radial mean free path of $\lambda_r = 0.14$ AU (black dots). Mono-energetic Green's functions (coloured curves) between 300 keV and 800 keV, obtained by scaling the $v = c$ Green's function. Green's function for 0.3 – 0.8 MeV electrons constructed from the mono-energetic Green's functions (black curve).

curve) is obtained according to

$$J_c = \frac{\int_{E_1}^{E_2} J(E)\ dE}{\Delta E}, \tag{4.4}$$

where $J(E)$ are the differential intensities of electrons with kinetic energy E, $E_1 = 0.3$ MeV, $E_2 = 0.8$ MeV, $\Delta E = E_2 - E_1$, and J_c are the differential intensities of the channel. For comparison, Figure 4.6 also shows the differential intensities computed for the same energy range using a Monte Carlo transport model (i.e., not scaling the $v = c$ Green's function). The results (black dots) are identical to the curve constructed based on the $v = c$ Green's function.

The procedure described so far to construct the Green's function of the nominal energy channel based on mono-energetic Green's functions assumes a flat energy response within the energy range under consideration. However, Bialk et al. (1991) showed that the electron channel E03 may respond to electrons of energy higher than its nominal energy range of 0.3 – 0.8 MeV and that the energy response is not flat but similar to a Gaussian, peaking at 950 keV.

A more accurate estimation of the Green's function of the E03 channel can be obtained by taking into account that

$$C_c = \int J(E)\, R(E)\, dE, \tag{4.5}$$

where C_c is the count rates of the channel in [counts/s], $J(E)$ is the differential intensity of electrons with kinetic energy E, and $R(E)$ is the response function in channel E03. Here we assume that the proton contamination in the electron channels is negligible, as we selected for the study only events where this effect was small (see Sect. 4.2).

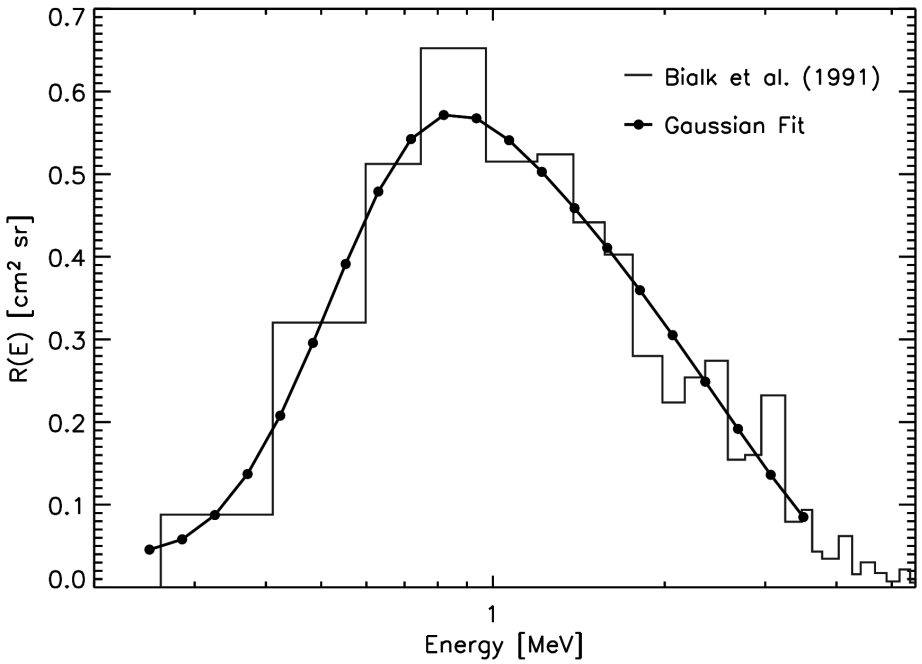

FIGURE 4.7: Energy response for channel E03 of E6 experiment on board Helios. The histogram (grey) shows the energy response computed by Bialk et al. (1991), the black solid curve shows a 6-parameter Gaussian fit, and dots display the response values for a grid of 20 logarithmically spaced energies.

Figure 4.7 shows the E03 energy response computed by Bialk et al. (1991) together with a 6-parameter Gaussian fit. It can be seen that the energy range from 0.25 MeV to 3.5 MeV covers the relevant part of the response. Neglecting energies above 3.5 MeV introduces a small error since the intensities decrease as a power-law (note that the values of γ under consideration range from 2.4 to 4.6. See Table 4.6 in Sect. 4.4 for more details) and the values of the response function are very low (< 0.08). A logarithmic grid of 20 energies within this range (dots) is able to cast the main characteristics of the profile.

For the same example as above (Fig. 4.6), Figure 4.8 shows the Green's function (in units of counts/s) computed by taking into account the energy response of E03 and an energy spectra with $\gamma = 3.5$. For comparison, Figure 4.8 includes the Green's function for the nominal energy channel (0.3 – 0.8 MeV) assuming a constant geometric factor of 0.48 cm^2 sr (Bialk et al., 1991). It can be seen that the timing of the two Green's functions does not differ, i.e. the onset and the time of the peak of the count rate are the same within the 1-min time resolution. On the other hand, the peak is smaller by a factor ~3 when the extended energy response is considered, since the instrument is mostly sensitive to particles with energies higher than the nominal energy range, for which there are lower intensities. The effect depends on the spectral index of the source.

If we assume that the electron mean free path is independent of the energy and that the effects of adiabatic deceleration are negligible, then the energy spectrum of the particles at the Sun is not modified by their interplanetary transport. The estimation of γ from in-situ data is, however, entangled because of two reasons: 1) the large extent of the energy channels, and 2)

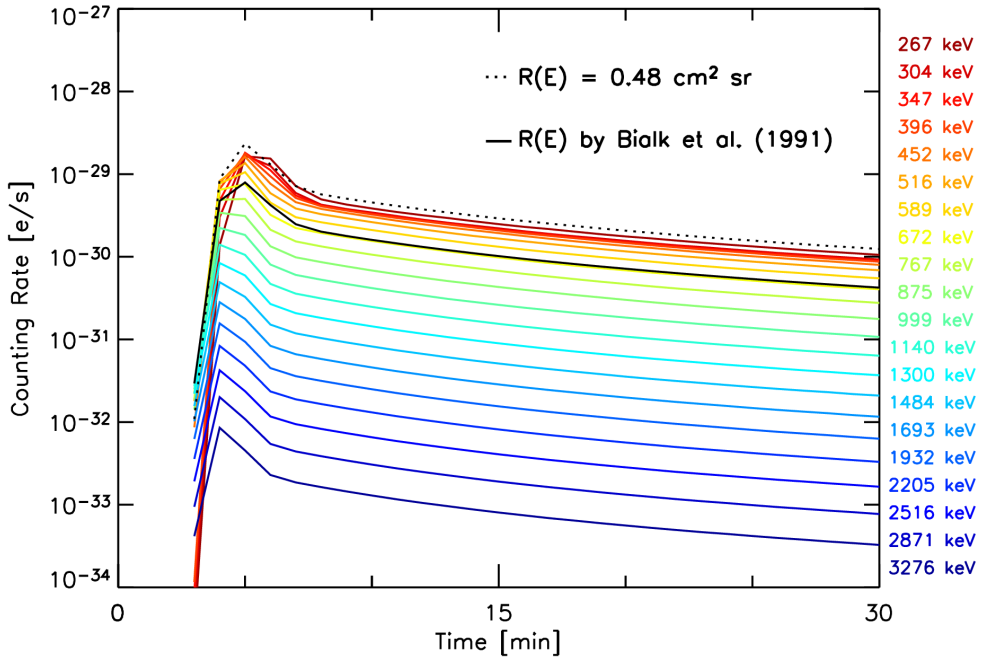

FIGURE 4.8: Mono-energetic Green's functions from 0.25 MeV to 3.5 MeV (coloured curves) released at the Sun at $t = 0$ assuming a spectral index of $\gamma = 3.5$, a radial mean free path of $\lambda_r = 0.14$ AU and taking into account the energy response of E03. The black curve shows the Green's function of the channel in units of counts/s assuming the energy response computed by Bialk et al. (1991). The dotted curve shows the Green's function of the nominal energy channel assuming a geometric factor of 0.48 cm^2 sr.

the differential intensity spectral index is defined in terms of momentum, $dN/dp \propto E^{-\gamma'}$, instead of energy. Figure 4.9 shows the Green's functions of the E03 channel at 0.31 AU and 0.84 AU assuming two values of the solar spectral index, $\gamma = 1.5$ (solid curve) and $\gamma = 3.5$ (dotted curve), for $\lambda_r = 0.05$ AU (top) and $\lambda_r = 0.14$ AU (bottom). The grey dots show the curve for $\gamma = 3.5$ multiplied by a factor ~0.5. It can be seen that a steeper spectrum results in lower intensities at the observer location and a slightly later onset. Thus the value of the spectral index does mainly affect the magnitude of the Green's function and therefore it influences the values of the inferred injection profile. Such a factor in intensity translates into a rather small change in the values of the solar injection, as shown in previous studies (see Agueda et al., 2014, for example). Besides, differences for the onset times of the particle count rates are comparable with the data resolution of 1 min. For simplicity, in this study we assume that the spectral index of the electron source equals the observational value of the spectral index computed from in-situ data. As a first approximation, we computed the spectral index using the intensity measurements at the peak of the four electron channels of E6.

4.3.2 Angular response of the sectors

The E6 experiment on board Helios uses the rotation of the spacecraft to measure the particle angular distributions relative to the local direction of the magnetic field (i.e., the pitch-angle distributions, PADs) of SEPs in interplanetary space. Rotation allows a single detector to scan

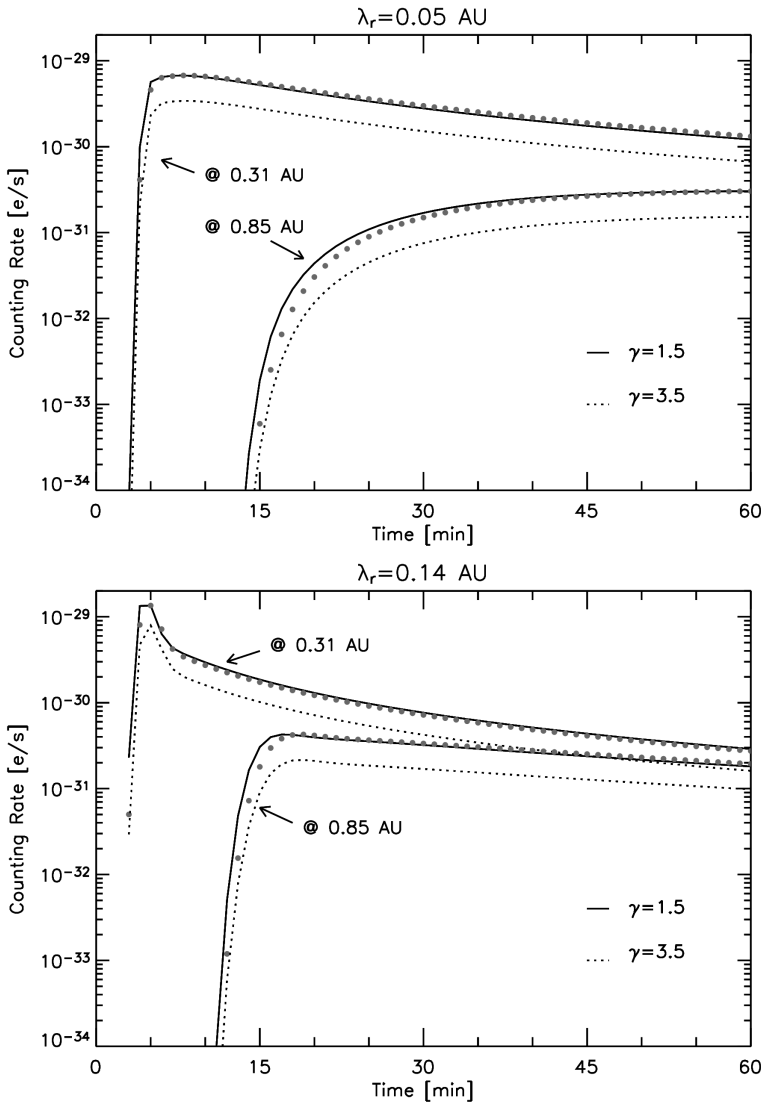

FIGURE 4.9: Green's functions of the E03 channel at 0.31 AU and 0.85 AU assuming two values of the solar spectral index,γ = 1.5 (solid curve) and γ = 3.5 (dotted curve), for λ_r = 0.05 AU (top) and λ_r = 0.14 AU (bottom). The grey dots show the curve for γ = 3.5 normalised to the peak of the profile for γ = 1.5

different directions as it spins. As explained in Section 4.1.1, the region of space swept out by E6 during a spin is divided into eight sectors (see Table 4.3). Our aim is to model these sectors to better understand both the potential and the limits of the observations, as well as to be able to model the electron events selected in Section 4.2.

We modelled the E6 particle detector on board Helios as a conical aperture of half-width 20°. The nominal aperture of the detector was 25° but we assumed a smaller value because the detector response function decays linearly due to edge effects (B. Heber, private communication).

We used the SSE coordinate system, being Z perpendicular to the ecliptic plane, aligned with the Helios spin vector, X the radial direction pointing towards the Sun and Y the tangential direction to the spacecraft trajectory pointing backwards, these latter two in the ecliptic plane. The aperture centre of the detector lays perpendicular to the Z axis, at a constant colatitude

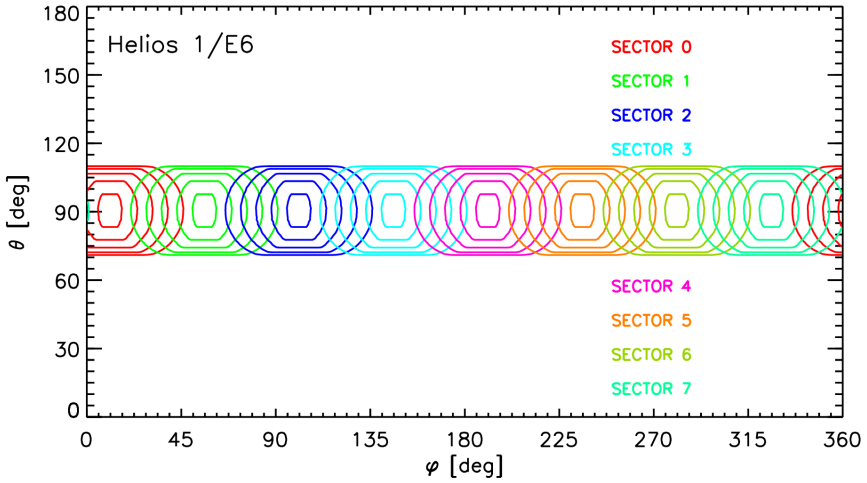

FIGURE 4.10: Angular response of the eight sectors of E6 defined in the SSE coordinate system for the configuration of Helios 1. Helios 2 would present the same result shifted 23°.

$\theta = 90°$, measured from the Z axis towards the ecliptic plane ($X - Y$). The azimuth angle, φ, is measured anticlockwise from the spacecraft-Sun line, i.e., X direction. The detector azimuth changes at constant speed as the spacecraft spins, increasing clock angle by 60 rpm or 360°/s.

We use the Monte Carlo technique to model a set of particle trajectories drawn from an isotropic particle distribution and record how they would be seen by a rotating detector sweeping a 45°-wide clock angle sector. We use the methodology presented by Agueda (2008) and Agueda et al. (2008).

We record the particle trajectories on a bi-directional matrix R_{jk} of 180x360 elements (1° resolution), where the (j,k) elements give the detection probability per square degree that a particle with direction (θ,φ) is detected when the detector zenith axis sweeps a sector of 45°. We normalise the response to unity, $\sum_{jk} R_{jk} = 1$. Figure 4.10 shows the response function of the eight sectors of E6 defined in the SSE coordinate system. Note that it is not a boxcar function, but it peaks at the midpoint clock-angle zenith direction of each sector. It is clear that the eight sectors of E6 are able to scan a wide range of directions around the ecliptic plane. On the other hand, the angular coverage descends ~20° away from the ecliptic, where the coverage at $\theta = 0°$ is almost null.

The resulting coverage in pitch angle depends on the direction of the local magnetic field. We can determine the pitch-angle cosine range scanned by each sector by computing the angle between the incident trajectory of the particles and the direction of the local magnetic field in SSE.

We define a vector with the direction of the magnetic field unit vector in spherical coordinates, $\hat{B} = (1, \theta_B, \varphi_B)$ being θ_B the colatitude angle and φ_B the azimuth. Then, we compute the values of the pitch-angle cosines corresponding to the grid of directions where the sector responses were evaluated, μ_{jk}. By performing an element by element product between the

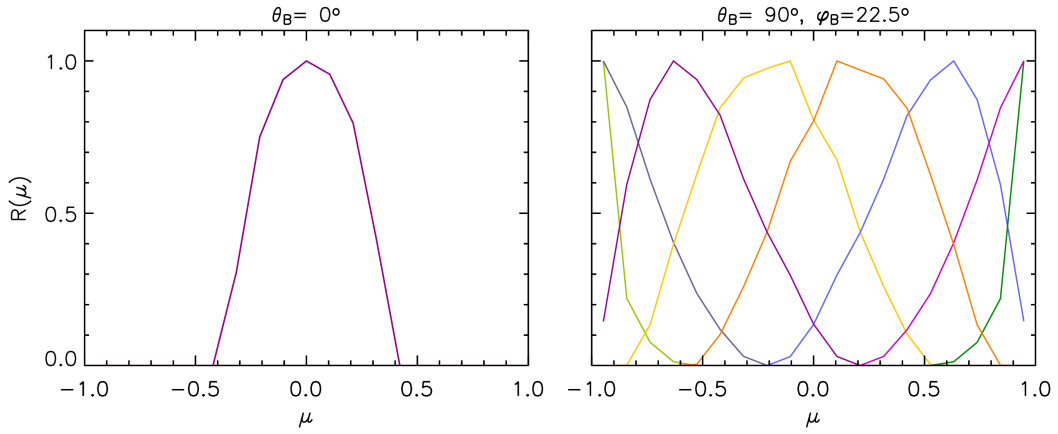

FIGURE 4.11: Normalised angular response of the sectors of Helios 1 assuming two magnetic field configurations: $\theta_B = 0°$ (left panel), and $\theta_B = 90°$ and $\varphi_B = 22.5°$ (right panel).

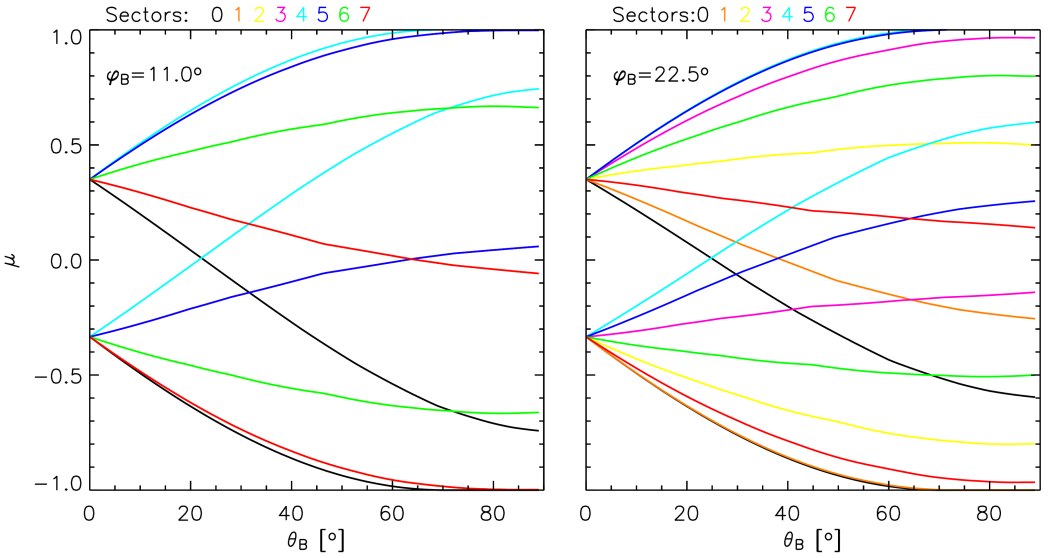

FIGURE 4.12: Pitch-angle cosine coverage of the sectors (for Helios 1 configuration): maximum and minimum pitch-angle cosines detected by each sector as a function of the magnetic field colatitude ($\theta_B = 90°$ means that the magnetic field is on the ecliptic plane). φ_B is the magnetic field azimuth angle: $\varphi_B = 11°$ in the left panel and $\varphi_B = 22.5°$ in the right panel.

obtained pitch-angle matrix with the angular response matrix for each sector, we obtain the pitch-angle response of each sector for a given magnetic field configuration, R^s_{jk}.

Figure 4.11 shows the pitch-angle cosine response function for each sector of Helios 1, assuming two different magnetic field configurations: $\theta_B = 0°$ (left panel), and $\theta_B = 90°$ (right panel). In the first case, independently of the value of φ_B, the magnetic field is aligned with the spacecraft spin axis and the response function is the same for all sectors, minimizing the pitch-angle cosine coverage of the telescope. On the other hand, when $\theta_B = 90°$ and $\varphi_B = 22.5°$, the telescope is able to cover the whole pitch-angle cosine range and we obtain the best possible mapping of the pitch-angle distributions.

Figure 4.12 shows the view boundaries of the sectors for Helios 1, i.e., the minimum and maximum values of μ that each sector is able to scan, as a function of θ_B. For each sector, the

maximum and minimum μ-values are displayed with the same colour. The left panel shows the case for $\varphi_B = 11°$, for which the magnetic field vector is aligned with the mid-point clock angle $\hat{s}$ of sector 0 and we find the maximum overlapping of the sectors due to the symmetric configuration of the telescope sectors with respect to φ_B. Right panel depicts the case for a magnetic field vector close to one edge of sector 0 with $\varphi_B = 22.5°$. That, on the contrary, it is found to result into the most sectored spread configuration of μ coverage. However, also in Figure 4.12, it is possible to observe how the value of φ_B does not change the pitch-angle coverage of the telescope but just the values observed by each sector that overlap more or less depending on the specific alignment of the magnetic field. For both cases then, the total μ coverage of the telescope is the same and it only depends on the value of θ_B. These results apply for Helios 2 as well, as the only difference in Helios 2 sector configuration is the azimuth origin of sector 0 (see Fig. 4.2).

To sum up, with 8 different sectors over the ecliptic plane, we can generally expect a good coverage of pitch angles when $\theta_B \gtrsim 90° \pm 30°$. However the pitch-angle coverage quickly gets worse when the magnetic field moves away from the ecliptic plane. If the magnetic field vector is aligned with the spin axis of the spacecraft, all sectors scan the same pitch-angle range, being the observations worthless for the study of the particle pitch-angle distribution due to the restricted angular information available (just one point).

4.3.2.1 Sectored Green's function

Once we know the angular response function of the sectors of the E6 telescope, it is possible to transform the simulated count rates obtained with the Monte Carlo transport model into modelled sectored count rates which are directly comparable with observations. Simulated pitch-angle distributions are computed with a fine pitch-angle resolution of only 9°.

The simulated count rates observed in sector s are given by

$$G^s(t) = \sum_{jk} R^s_{jk}\, C_c(\mu_{jk}(t), t), \tag{4.6}$$

where $C_c(\mu, t)$ are the pitch-angle distributions given by Equation 4.5, and $G^s(t)$ are the modelled count rates for each sector s as a function of time. In Equation 4.6 the matrix product is performed element by element and the sum extends over all (θ, φ) directions identified by the indices j,k, where j is the azimuthal angle index from 0 to 360 and k is the colatitude index, from 0 to 180. Note that observations of the local magnetic field vector show changes as a function of time, varying the grid of pitch-angle cosines, $\mu_{jk}(t)$, at each time.

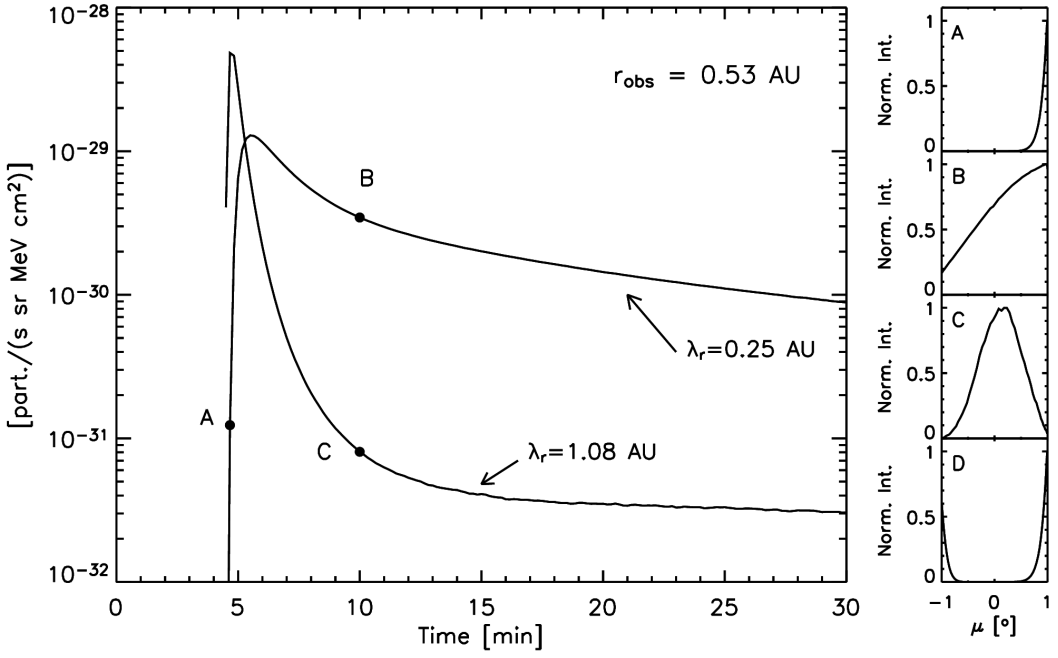

FIGURE 4.13: Mono-energetic omni-directional intensities expected at 0.53 AU assuming two different values of the mean free path (λ_r = 0.25 AU and λ_r = 1.08 AU). The right panels show the PADs (normalised to maximum) corresponding to the three snapshots (A, B and C) plus a bidirectional synthetic PAD (D).

4.3.2.2 Study of synthetic PADs

The focused transport equation (Equation 4.2) predicts that at the onset of an SEP event the PADs are collimated around pitch angle zero degrees for positive IMF polarity (180° for negative IMF polarity). This is due to the fact that the particles arriving first at the observer location suffer few pitch-angle scattering. Later on, the PADs monotonically evolve into isotropic PADs. The isotropisation rate depends on both the value of the radial mean free path and the duration of the solar release processes. Small values of the mean free path imply higher scattering frequencies and shorter isotropisation rates. While a sustained release of particles at the Sun produces episodes of sustained anisotropy and thus longer isotropisation rates.

In this section we study how a given synthetic pitch-angle distribution would be observed by the eight sectors of E6 for different configurations of the local magnetic field vector. Figure 4.13 shows the Green's functions of particle transport at 0.53 AU for two values of the radial mean free path, λ_r = 0.25 AU and λ_r = 1.08 AU. The four panels on the right show the normalised PADs for three selected times (A, B and C) of a typical event. The last PAD (D) was included to study bi-directional PADs.

Figure 4.14 and Figure 4.15 show the normalised synthetic PADs (black curves), the observations at the centre of each sector (coloured crosses) and the observed normalised intensity at the average pitch angle of each sector (coloured diamonds), assuming four different configurations

of the local magnetic field vector given by $\theta_B = 0°, 30°, 60°, 90°$. Figure 4.14 shows the PADs for case A (top) and case B (bottom). Figure 4.14 shows case C (top) and case D (bottom).

First of all, we can clearly notice that for $\theta_B = 0°$ and irrespectively of the case, no reliable information can be extracted from the observations as all the sectors are observing particles with the same pitch angle value and no distribution can be inferred. On the other hand, we can point out that the PADs for all cases are well covered when $\theta_B = 90°$, even though only for case B the PAD can be really well reproduced. For the other 3 cases (A, C and D), we found that the observations at the centre of the sectors would show slightly lower anisotropies than the actual PADs. If we compare the values of the pitch angle of the centre of the sector with the mean pitch angle according to the PAD we can see that the assumption of the sector centre generally underestimates the anisotropy of the actual PAD. On the other hand, the average pitch angle value results into distributions with higher anisotropy when the pitch-angle range is well covered.

Moreover, for very anisotropic cases (A and D), only when the magnetic field shows a $\theta_B =\sim 90°$ we can reliably reconstruct the actual PAD from the observations at the centre. For cases with moderate anisotropy (B and C), even for lower values of θ_B it would be possible to extract useful information.

Our conclusion is that observations should provide a good pitch-angle coverage of the particle distribution in order to properly infer the PAD of the underlying particle fluxes. In the case of the Helios spacecraft, this means that the magnetic field should come as close as possible to the ecliptic plane.

4.3.3 Full inversion of Helios E6 observations

We use an inversion approach (Agueda et al., 2008) to infer the electron injection profile at the Sun, $q(t)$, from sectored particle observations by Helios. For a given fitting time interval $t \in [t_1, t_2]$, we compute the Green's functions of particle transport (assuming a value of the radial mean free path λ_r) expected at the observer location for a set of multiple consecutive instantaneous injection episodes occurring at $t' \in [T_1, T_2]$, where $T_2 = t_2 - \Delta t$ and $T_1 = t_1 - \Delta t$, being Δt the transit time of the first arriving electrons at the observer location.

The modelled sectored intensities, M^s, are given by

$$M^s(t; \lambda_r) = \int_{T_1}^{T_2} G^s(t, t'; \lambda_r)\, q(t')\, dt', \tag{4.7}$$

where $G^s(t, t'; \lambda_r)$ are the sectored Green's functions. If J_k are the observations once the pre-event background has been subtracted, it is possible to determine the n_t components of the vector $\mathbf{q}$ that minimise the distance between the observations ($\mathbf{J}$) and the modelled intensities ($\mathbf{M}$), i.e.,

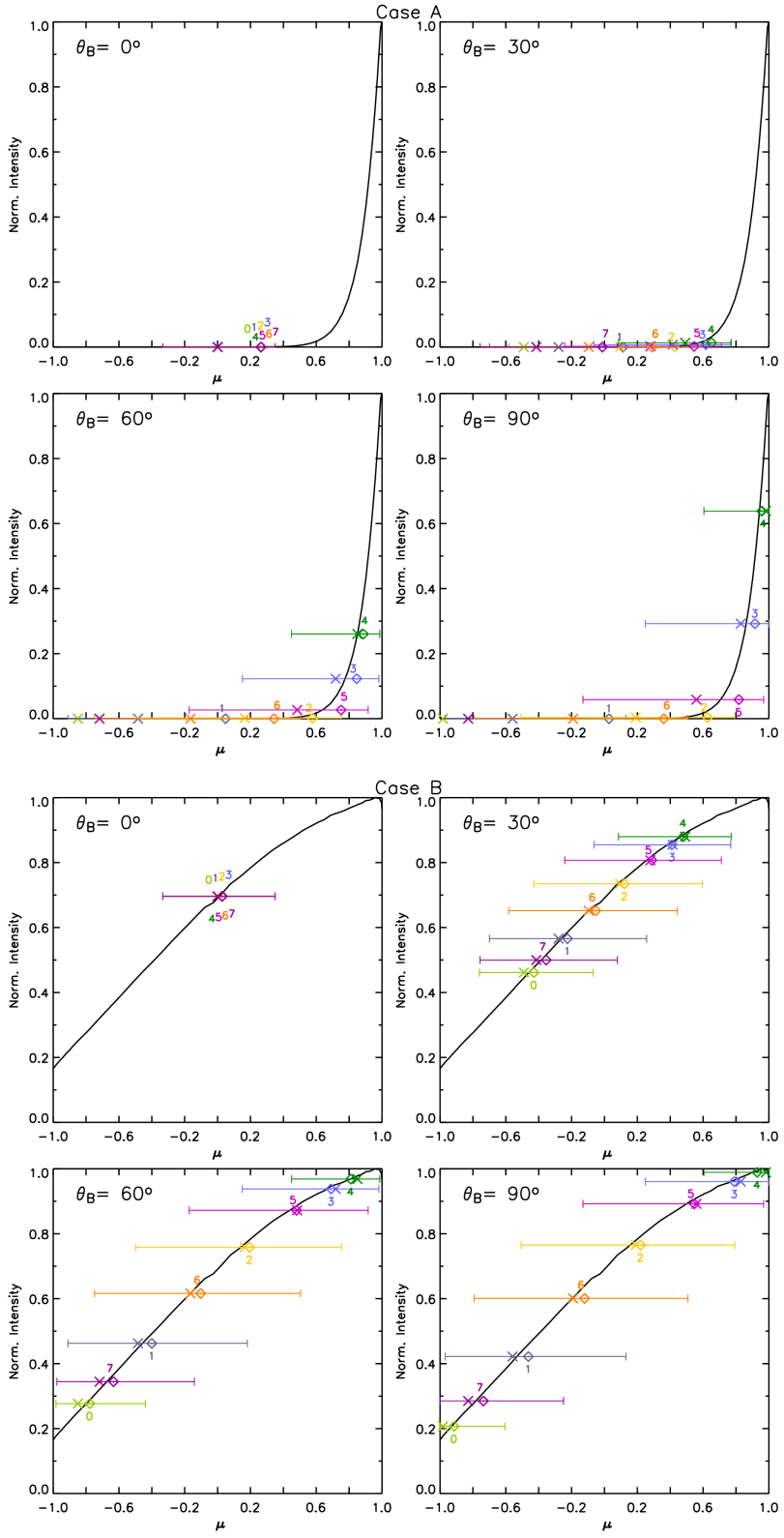

FIGURE 4.14: Intensities observed by the eight E6 sectors for two synthetic PADs (case A and case B) assuming different values of θ_B ($0°, 30°, 60°, 90°$). Sectors and the pitch angle range they observe (horizontal bars) are numbered in different colours. It is also indicated the pitch angle observed by the centre of each sector (crosses) and the average pitch angle measured within the range of each (diamonds).

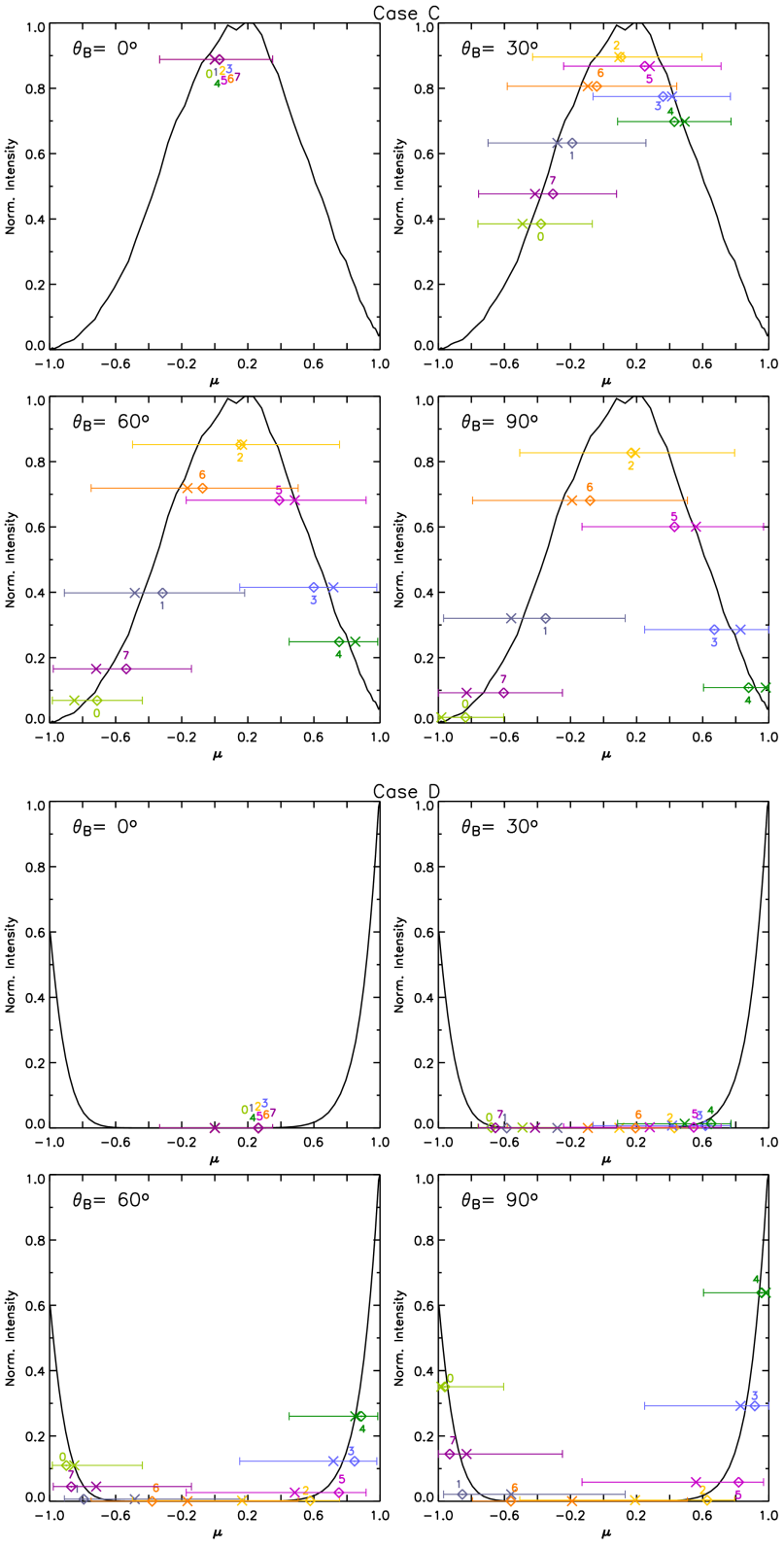

FIGURE 4.15: Same as in Figure 4.14 for case C, and D.

we minimise

$$\| \mathbf{J} - \mathbf{M} \| \equiv \| \mathbf{J} - \mathbf{G} \cdot \mathbf{q} \|, \tag{4.8}$$

under the constraint that $q_k \geq 0 \; \forall l = 1, 2, ..., n_t$. By using the non-negative least-squares method of Lawson and Hanson (1974) that assures the convergence to a solution, we get the injection amplitudes. For a time grid with δt-resolution and no gaps, the number of data points are $n_t = (t_2 - t_1/\delta t + 2)$ in each sector, while the number of unknowns in the injection profile are n_t. In general, since $8n_t \gg n_t$ the problem is well-constrained.

For each transport scenario (see next section for a description), we obtain the best possible release time history. The goodness of the fit is then evaluated by summing the logarithmic differences between the observations and the modelled data.

4.4 Results

We computed the Green's functions of interplanetary transport (Agueda et al., 2008, 2012b) assuming that the solar source is static at two solar radii and that particles are moving at the speed of light ($v = c$) for several interplanetary transport scenarios. These scenarios correspond to different values of the electron radial mean free path, logarithmically spaced between 0.01 AU and ~0.52 AU. We assumed an anisotropic pitch-angle scattering diffusion coefficient with $\epsilon = 0.01$ (Agueda and Vainio, 2013). The Green's functions of interplanetary transport were computed for the E03 electron channel of Helios/E6 taking into account the energy response of the channel given by Bialk et al. (1991) and the angular response of the sectors. Further, to characterise the IMF in the particle transport simulations we used the solar wind speed values listed in Table 4.4 and, as mentioned at the end of Section 4.3.1, the spectral index derived from the peak count rates to characterise the energy dependence of the solar injection.

We selected a fitting period including the onset, the rising phase of the event and a sufficient part of the decaying phase. For this sample, the fitting period ranges from an hour to 3 hours approximately. Table 4.6 lists the fitting parameters and the results for each event in our sample. Columns 1 and 2 show the year and date of the events, column 3 shows the fitting period length, column 4 the source spectral index used to compute the energy spectra at the Sun, column 5 and 6 list the inferred values for the maximum injection at the Sun and the type of injection: short or extended, for durations shorter/longer than 30 min. Columns 7 and 8 list the inferred value of the electron radial mean free path and the ratio between the parallel mean free path and the focusing length, L[7], of the particles along the Archimedean spiral as a simple estimation of focused ($\lambda_\parallel/L \geq 1$), weak-focused ($0.1 < \lambda_\parallel/L < 1$) and diffusive ($\lambda_\parallel/L \leq 0.1$) propagation as suggested by Beeck and Wibberenz (1986).

[7]The focusing length is $L(z) = -B(z)/(\partial B/\partial z)$, that for the Archimedean spiral IMF is given by the expression $L = \frac{r(r^2+R^2)^{3/2}}{R(r^2+2R^2)}$, where r is the radial distance from the observer to the Sun, and $R = u/\Omega$, being v_{sw} the solar wind speed and Ω the solar rotation rate.

TABLE 4.6: Fitting parameters for the selected events.

Year	Date	Fitting period [min]	Spectral index	Max inj. [e (s sr)$^{-1}$]	Injection type	λ_r [AU]	$\lambda_\parallel$/L
1976	Mar 21	55	3.4	1.7×10^{28}	Short	0.040	0.22
1978	Jan 1	100	2.4	2.2×10^{30}	Extended	0.106	0.24
1978	Dec 11	100	3.5	4.6×10^{29}	Extended	0.100	0.29
1980	Apr 5	130	4.6	1.9×10^{29}	Short	0.060	0.15
1980	Apr 26	60	4.0	6.0×10^{29}	Short	0.080	0.28
1980	May 3	150	3.7	7.3×10^{29}	Extended	0.080	0.28
1980	May 12	65	3.3	1.7×10^{29}	Extended	0.120	0.53
1980	May 28 a	72	4.4	1.3×10^{29}	Extended	0.270	1.75
1980	May 28 b	120	4.5	3.9×10^{30}	Extended	0.160	1.04
1980	May 28 c	82	3.9	3.1×10^{30}	Extended	0.207	1.34
1980	May 28 d	63	4.1	6.2×10^{29}	Extended	0.270	1.75
1981	Jan 14	60	2.9	3.0×10^{28}	Short	0.090	0.26
1981	May 8	195	3.1	3.0×10^{30}	Extended	0.070	0.21
1981	Jun 10	85	3.6	3.4×10^{28}	Extended	0.080	0.50
1982	Jun 2	162	2.9	7.7×10^{28}	Short	0.020	0.07

The values of the radial mean free path derived in this study range from $\lambda_r \sim 0.02$ AU to $\lambda_r \sim 0.27$ AU. These values are in general small compared to the distance between the Sun and the spacecraft, suggesting that the transport was not scatter-free for most of the events of the sample. For ten of the events, the electrons propagated in the weak-focused regime, for four of them in the focused and only for one of them the transport was clearly diffusive.

Figure 4.16 shows the values of the goodness-of-fit estimator for each mean free path tested for each event. Different ranges and resolutions of the mean free path have been used depending on where the minimum value of mean free path appeared in the initial tests.

For most of the events we obtain a clear minimum of the goodness-of-fit estimator, which allows us to identify the ranges of λ_r-values providing the best fit. However, there are 5 cases (1978 December 11, 1980 May 3, 1980 May 12, 1981 June 10, 1982 June 2) showing a plateau for low values of the radial mean free path.

For all cases we applied the same method: when different values of the radial mean free path had similar values of the goodness of the fit, we chose the one related to the most simple injection profile that could explain the observations. This was generally resulting in smaller values of the radial mean free path for short injection profiles and larger values for extended injections (see Agueda et al., 2014, for a discussion). In that way, we avoid over-fitting situations where the model is trying to adjust noise adding extra injections in a short profile or on/off injection episodes for extended injection profiles.

The chosen value of the mean free path was in general only 1 position shifted from the minimum value given by the goodness-of-fit estimator except for the event on 1982 June 2

where we took the smaller mean free path value (0.020 AU instead of 0.035 AU given by the minimum of the goodness-of-the-fit).

Figure 4.17 shows the results of the fit for the event on 1982 June 2. The first two panels show the data (dots) and the modelled (solid curve) counts per second in the sectors 0,1,2,3 (top panel) and sectors 4,5,6,7 (middle panel) with different colours. The third panel shows the cosine of the pitch angle for the eight sectors. Figures 4.18, 4.19 and 4.20 show the fits for the other events in our sample. We obtain a good fit for most of the events in the list. However, for short periods of time, few events (e.g. 1978 January 1, 1980 April 26) show clear discrepancies between the observed and the modelled count rates. For the event on 1978 January 1 (left panel of Fig. 4.20), the model is unable to reproduce the data hollow observed around ~22:20 UT coinciding with a local fluctuation of the magnetic field given by a rotation in latitude θ larger than 50°. For the event occurring on 1980 April 26 (see Fig. 4.20), the model underestimates a double peak appearing in those sectors observing antisunward particles with $\mu \sim 1$. On the other hand, the model overestimates the observations for $\mu \sim 0.5$. For this event, we find a sudden change in the latitude of the local magnetic field vector of 20°. For the case of the event on 1980 May 3 (Fig. 4.18), we obtain a very good fit despite the data gap between 08:25 – 09:00 UT. The gap is not affecting the rising phase nor the peak of the event. Therefore it is possible to infer a reliable value of the mean free path and of the injection time-profile. In the selection phase, we discarded two events (1977 November 22 and 1978 April 11) because they presented gaps during the rising phase of the SEP event either in the sectored data or in the magnetic field data.

Figure 4.21 shows the inferred injection profile at the Sun corresponding to the best fit mean free path for the event on 1982 June 2. The bars indicate the rate of released particles per steradian for each 1-min time bin. The profile is shifted 8 min in order to directly compare the timing of the injection profile with the electromagnetic emissions detected from Earth, shown as horizontal thick bars on the top of the plot (the peak time of the EM emissions are indicated by small vertical lines in these bars). For this event, the injection profile is very short and the main release episode occurs between 15:40 UT and 15:45 UT in coincidence with the peak in SXR and radio emission, which suggest that the release for this event was associated with the well-connected M9.9 flare.

Figure 4.22 shows the injection profiles for those events with short (< 30 min) durations. In these cases, the timing of the maximum release is consistent with the timing of the radio emission peak. Also, the 1976 March 21 event shows more than one peak in radio emission which is consistent with several injection episodes. The correspondence between the injection episodes and the SXR emission varies from event to event. For the event on 1980 April 26, as explained in Section 4.2, no SXR emission was reported in association with the onset time of the event, but we show instead the closest SXR emission reported, which clearly appears much earlier than the inferred electron release. Nevertheless, a short radio emission was found matching the injection start time and showing a peak that coincides accurately with the maximum injection.

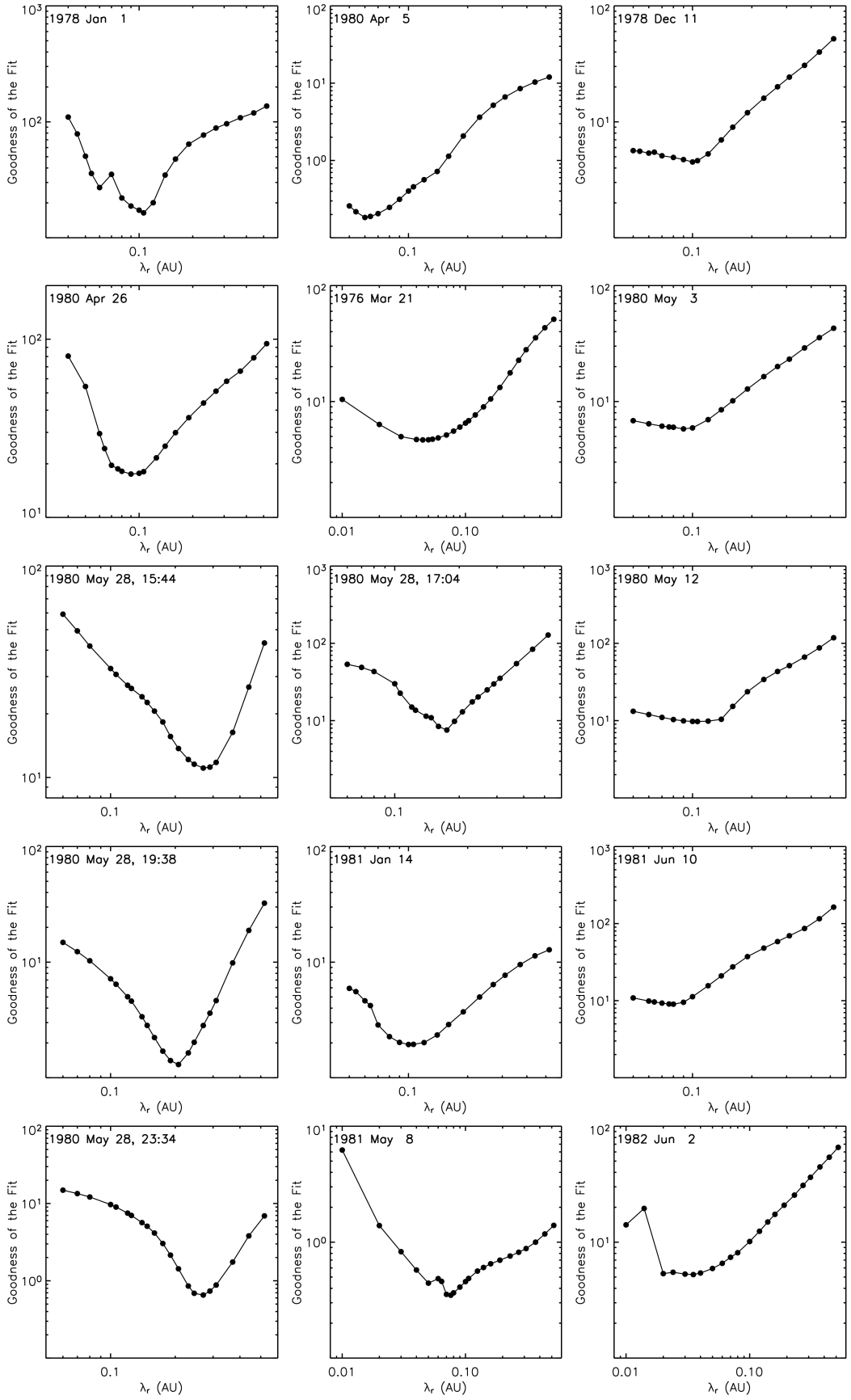

FIGURE 4.16: Goodness of the fit for every value of λ_r tested. Most of the events show a clear minimum around the best fit value. Events in the right column are particular cases (see text for details).

The duration of the electron release for these events seems consistent with flare emission. The associated flares have connection angles < 26°, which indicates that the open magnetic flux tubes cover several tens of degrees in longitude on the source surface. Klein et al. (2008) found that open field lines may connect the parent active region to the footpoint of the nominal Parker spiral, even when the parent active region is as far as 50° away.

Figure 4.23 shows the injection profiles for those events with long (> 30 min) durations. The event on 1980 May 3 shows a ~20-min data gap during the decaying phase of the event. This gap results on an equivalent gap in the injection profile between 08:22 and 08:54 UT and a higher intensity of the injection right before and after the gap. We performed an analysis filling the data gap using simple linear interpolation and found no difference for the inferred value of the best mean free path. However, during the gap the inferred injection was continuous and of smaller intensities.

Most (10) of the events in our sample show extended release episodes lasting at least an hour. In these cases, the beginning of the release appears before or at the peak in SXR emission. The duration of the SXR emission does not seem related to the injection duration as three of the events (1980 May 3, 1980 May 12 and 1981 May 8) have the shortest SXR emission in the sample. Furthermore, the injection extends past the duration of the radio emission. Although the events observed on 1978 January 1 and 1978 December 11 show more than one radio peak consistent with several injection episodes.

We found no correlation between the source flare class and the duration of the inferred injection profile, being intense flares related to short injection profiles (such as the M9.9 flare on 1982 June 2, with ~8 min injection duration) as well as weaker flares being related to extended injection profiles (e.g. the C4.3 flare associated with the event on 1980 May 12, for which we inferred an injection profile lasting more than 45 min). Nevertheless, for the two events associated with the two strongest flares we obtained extended injection profiles lasting at least 1 hour.

4.5 Discussion

4.5.1 Transport conditions and particle injection

The sample of 15 events selected for this study suggests different electron transport conditions in the interplanetary medium with best-fit values of the radial mean free path between 0.02 AU and 0.27 AU. These values are in general small compared with the distance of the spacecraft to the Sun along the Archimedean spiral, which implies that the propagation is not scatter-free, and the $\lambda_{\parallel}/L$ ratios found indicate that the propagation occurred in the focused and weak-focused regimes; therefore the focused-diffusion transport equation that we used is the appropriate framework to model these electron events. Note that 10 of the events in our sample show

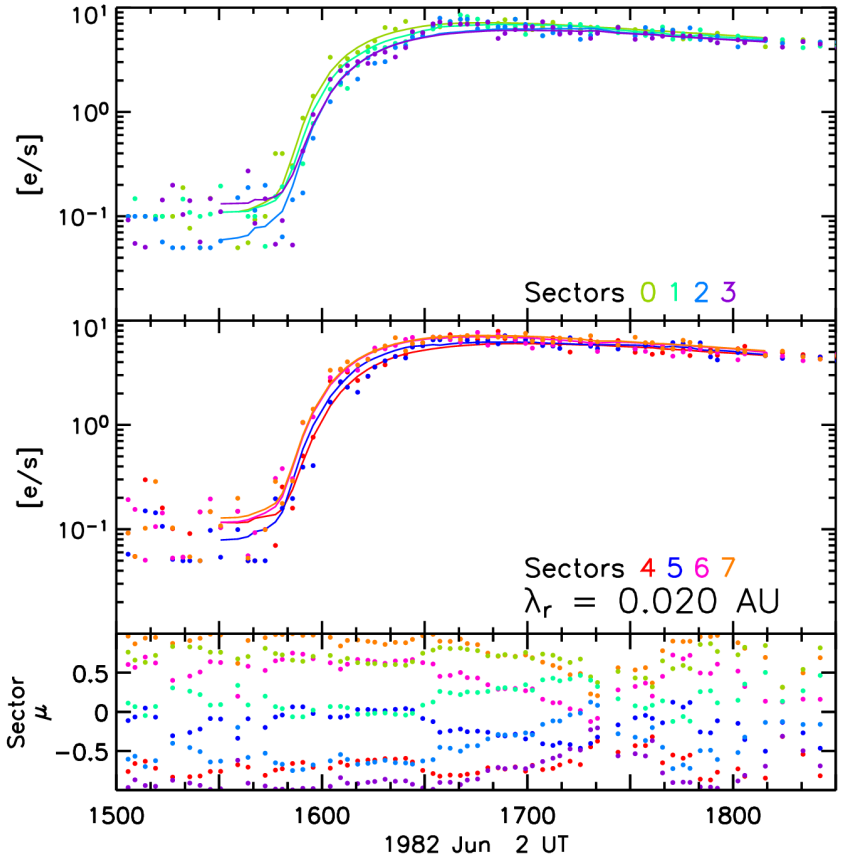

FIGURE 4.17: Top two panels: observational sectored data (dots) and model predictions (coloured curves) on 1982 June 2. Bottom panel: electron pitch-angle cosine observed by each sector using the same colour code.

weak focusing conditions at the observer's position, 4 a transport regime clearly dominated by focusing and 1 event (1982 June 2) evolves under diffusive conditions.

Kallenrode et al. (1992b) studied a sample of 6 events (1978 April 11, 1980 April 26, 1980 May 3, 1980 May 12, 1981 June 10 and 1982 June 2), five of them contained in the sample of the present study. These include all but the 1978 April 11 event, that we discarded because of a gap in the magnetic field data during the rising phase of the event. Kallenrode et al. (1992b) determined the electron transport conditions by fitting the averaged intensity and the anisotropy time profiles with the results of a focused transport model assuming an instantaneous δ-injection or a Reid-Axford injection at the Sun and the nominal energy range of E03 (0.3 – 0.8 MeV). They estimated the uncertainty in the local values of λ_r achieved by their method to be of the order of 50%. They found small values of the radial mean free path, between 0.02 AU (1982 June 2) and 0.15 AU (1980 April 26) where our results show a range of 0.020 – 0.12 AU (for 1982 June 2 and 1980 May 12, respectively). The values of the radial mean free path obtained by Kallenrode et al. (1992b) are summarised in Table 4.7 and compared with the values inferred in this study. It can be seen that the values are consistent within the errors reported by Kallenrode et al. (1992b). Regarding the properties of the injection profile at the Sun, we find that for two of the events (1980 April 26 and 1982 June 2), Kallenrode et al. (1992b) could fit the observations

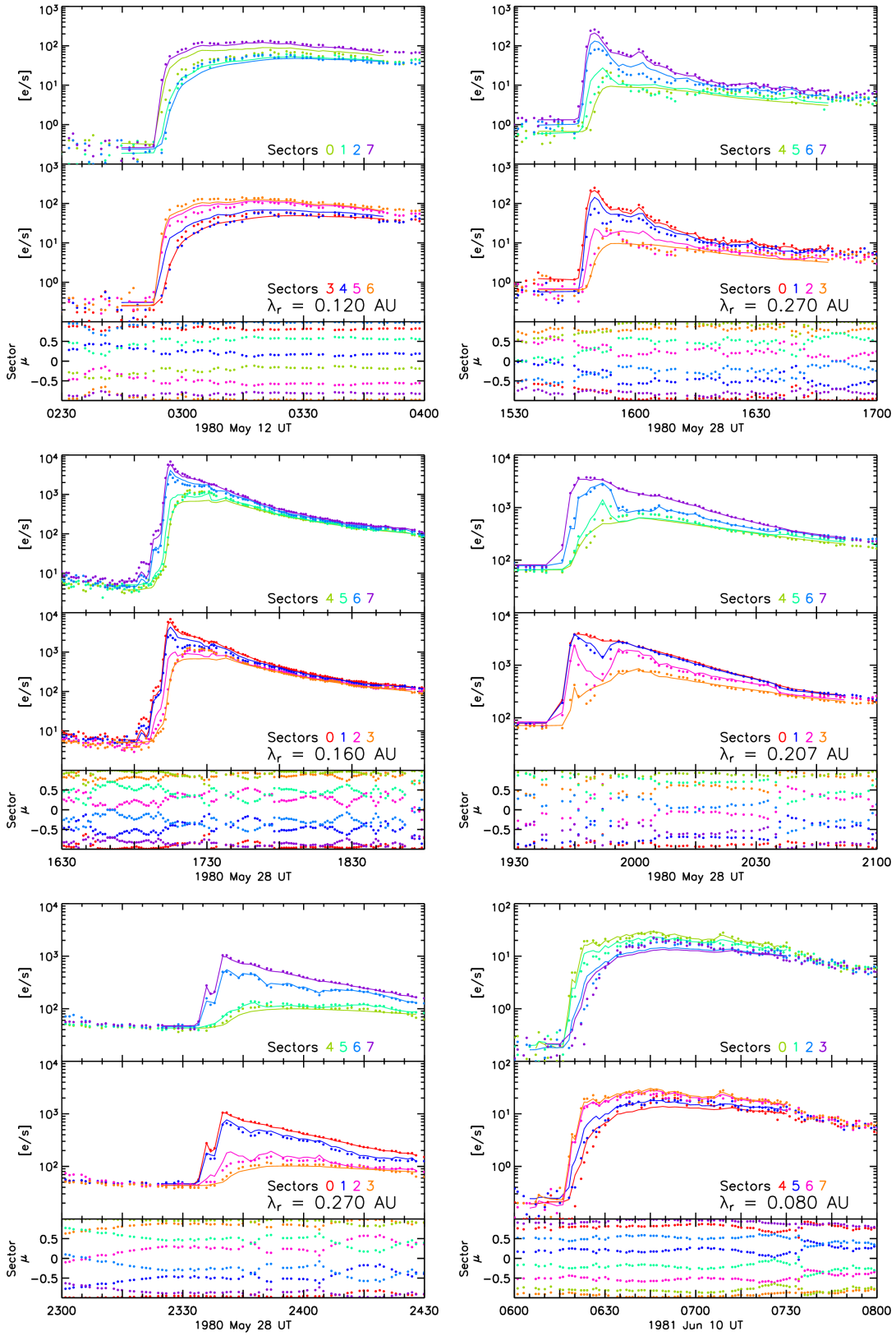

FIGURE 4.18: Results of the fit for the studied events. See caption at Figure 4.17 for detailed explanation.

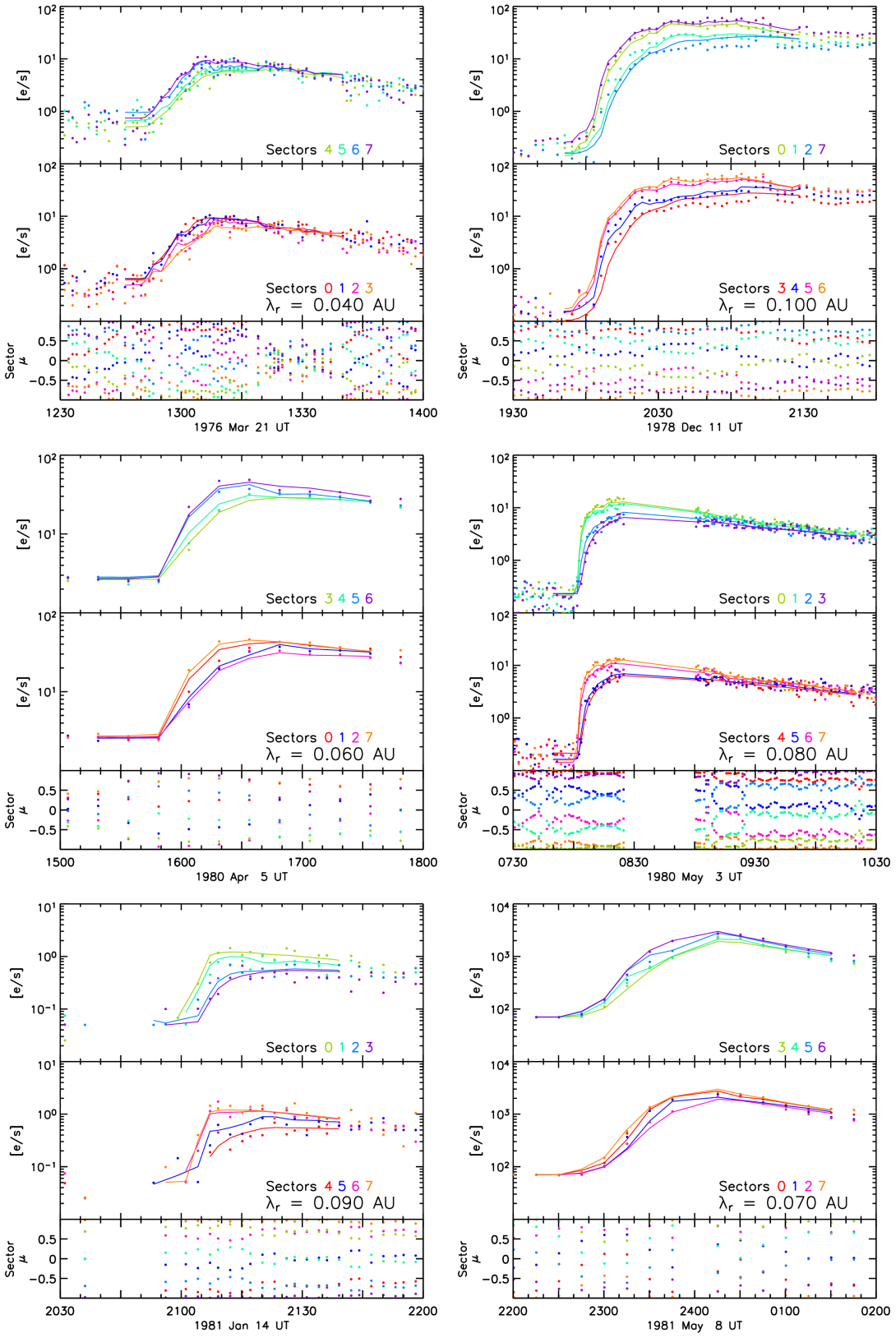

FIGURE 4.19: Same as in Figure 4.17.

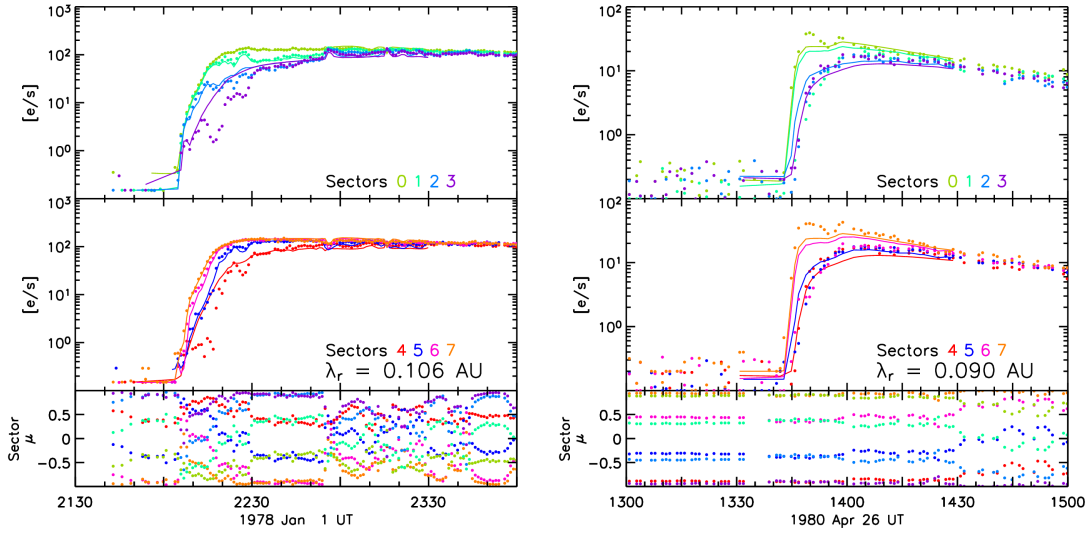

FIGURE 4.20: Same as in Figure 4.17.

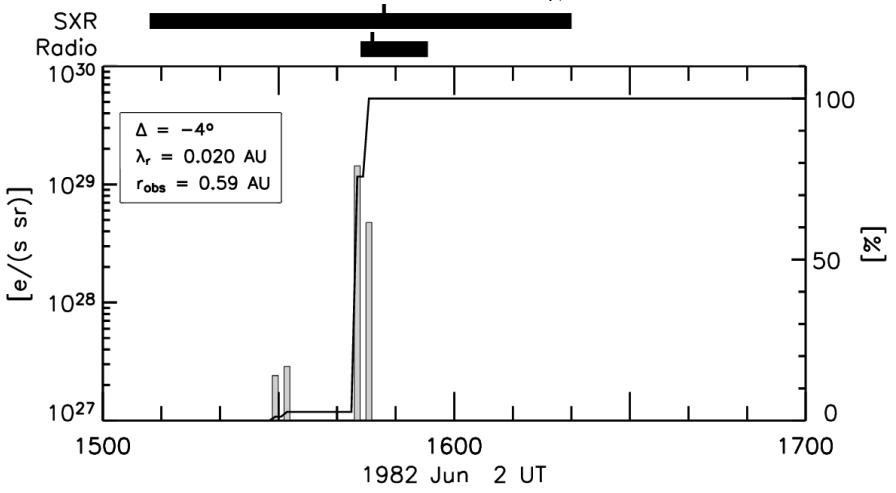

FIGURE 4.21: Release time profile inferred for the event on 1982 June 2. The histogram shows the inversion result with 1-min time resolution; the solid curve shows the total percentage of electrons. The profile has been shifted by +8 min to allow the comparison with EM emissions. Black thick horizontal bars on the top of the panel show the timing of the SXR and radio emissions. The time of the EM peaks are indicated with vertical lines. The legend shows the connectivity of the source (Δ), the inferred radial mean free path and the radial distance of the spacecraft.

assuming a δ-injection and the results of the inversion suggest short episodes as well. On the other hand, two of the events (1980 May 12, 1982 June 10) could not be fitted by a δ-injection by Kallenrode et al. (1992b). In addition, their fit for the 1980 May 3 event failed reproducing the slower anisotropy decay suggesting also a longer injection duration. Consistently, for these three events we inferred extended injection profiles.

Kallenrode (1993b) also studied a sample of 27 proton and electron events observed by the Helios spacecraft. Five of them are part of our sample (1980 April 26, 1980 May 3 and 1980 May 12, already studied by Kallenrode et al. (1992b), and 1981 January 14 and 1981 May 8). Kallenrode (1993b) made use of a combination of the first two electron channels of E6 (0.3 – 2 MeV) and tried to fit the averaged intensity and the anisotropy time profiles with the results

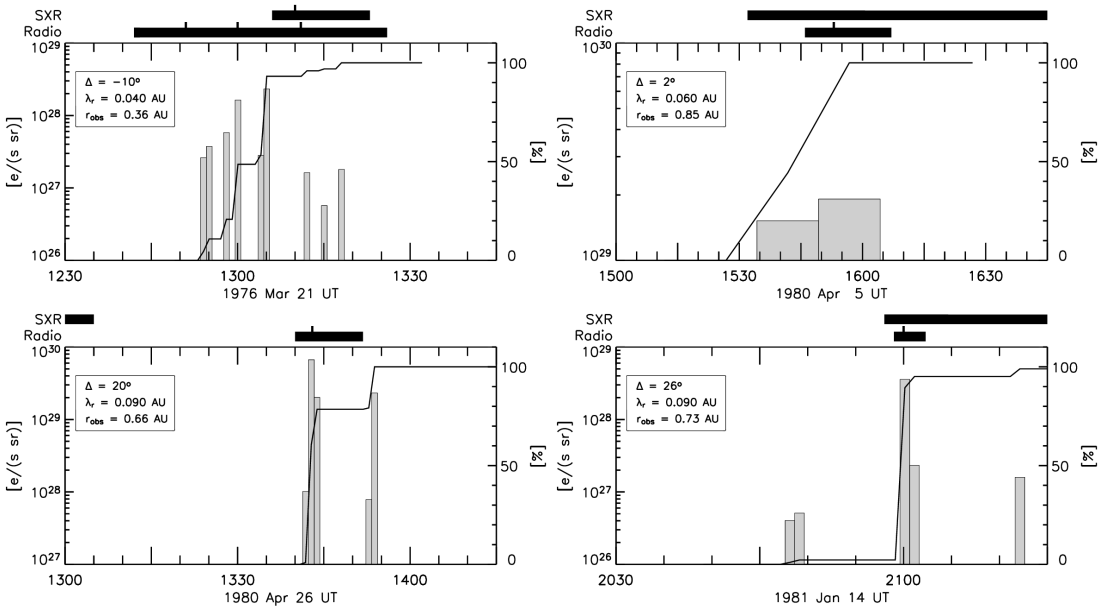

FIGURE 4.22: Same as in Figure 4.21 for those events with short (< 30 min) injection profiles.

TABLE 4.7: Mean free path and injection type inferred by our study, Kallenrode et al. (1992b), Kallenrode (1993b) and Agueda and Lario (2016). Red values indicate discrepancies with our result for the radial mean free path.

			This study		Kallenrode et al. 1992		Kallenrode 1993	Agueda & Lario 2016	
Year	**Date**	**Onset [UT]**	**λ_r [AU]**	**Injection Type**	**λ_r [AU]**	**Injection Type**	**λ_r [AU]**	**λ_r [AU]**	**Injection Type**
1980	Apr 26	13:40	0.080	Short	0.15	δ	0.15		-
1980	May 3	08:00	0.080	Extended	0.05	δ	0.06	-	-
1980	May 12	02:51	0.120	Extended	0.10	Reid Axford	0.15	-	-
1981	Jan 14	21:01	0.090	Short	-	-	0.10	-	-
1981	May 8	22:50	0.070	Extended	-	-	0.20	-	-
1981	Jun 10	06:16	0.080	Extended	0.05	Reid Axford	-	-	-
1982	Jun 2	15:44	0.020	Short	0.02	δ	-	-	-
1980	May 28 a	15:44	0.270	Extended	-	-	-	0.26	Short
1980	May 28 b	17:04	0.160	Extended	-	-	-	0.14	Extended
1980	May 28 c	19:38	0.207	Extended	-	-	-	0.18	Extended
1980	May 28 d	23:34	0.270	Extended	-	-	-	0.20	Extended

of an interplanetary transport model as done by Kallenrode et al. (1992b). They mention that the event on 1980 May 3 suffers from proton contamination in this range of energies, which is mainly due to the contribution of the second channel of E6, E08, with a higher response to protons than E03 (see Fig. 4.1); hence, we can neglect proton cross-contamination in the E03 channel. Furthermore, as there is no energy dependence on the radial mean free path over this range of energies and we also considered in the energy response a similar range (from 0.25 MeV to 3.5 MeV) it is possible the direct comparison of the mean free path values obtained by Kallenrode (1993b) and those obtained in this study. Kallenrode (1993b) found, in general, small values of the radial mean free path, between <0.02 AU and 0.35 AU, except for the event on 1978 April 28, for which they found $\lambda_r \geq 0.5$ AU. For 15 of the events of their sample they found $\lambda_r < 0.2$ AU. The values of the radial mean free path obtained by Kallenrode (1993b) for

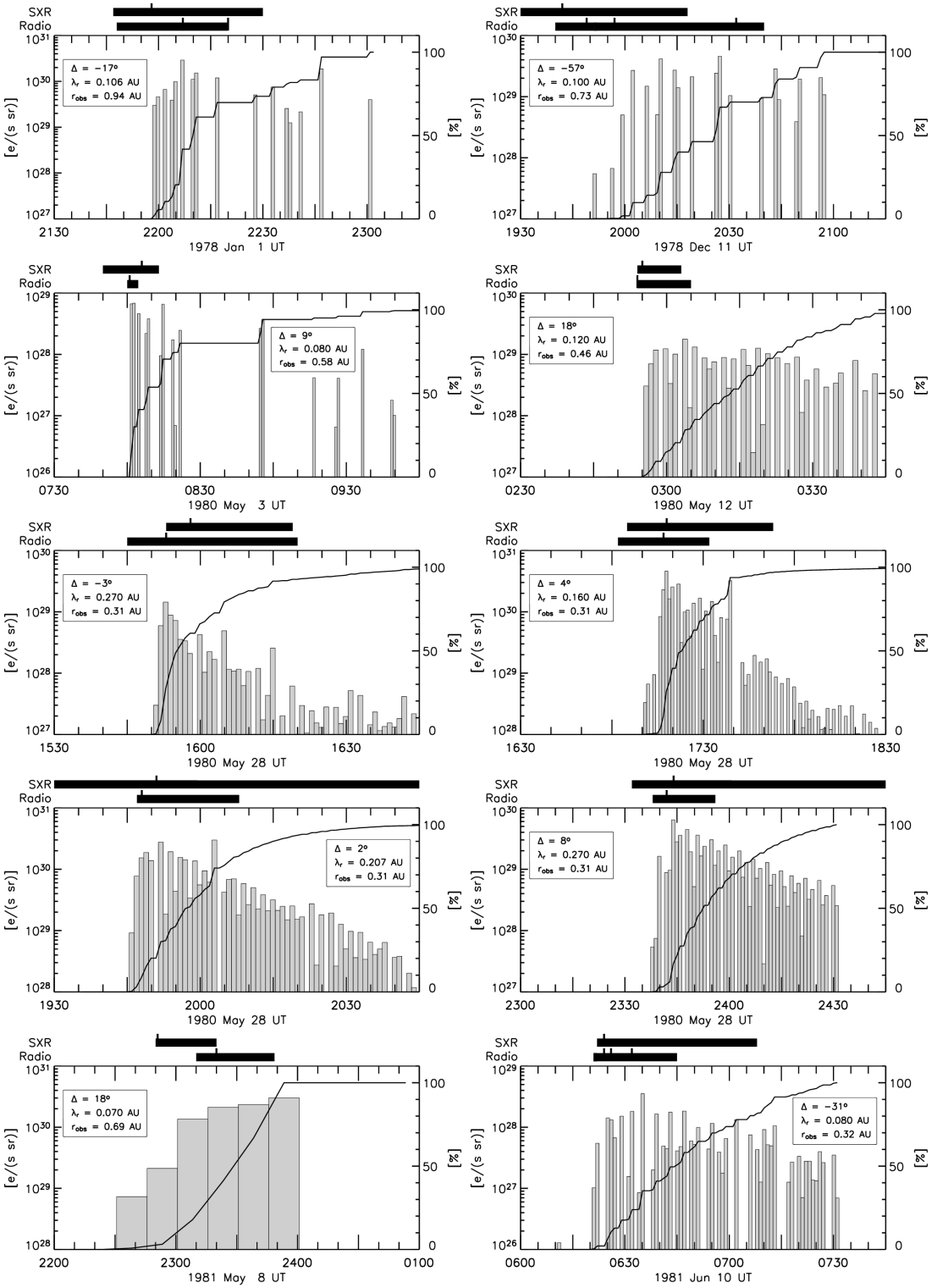

FIGURE 4.23: Same as in Figure 4.21 for those events with extended (> 30 min) injection profiles.

the events present in our sample are compatible with the values we inferred, except for the 1981 May 8 event, for which we found a mean free path a factor ∼3 smaller (0.07 AU). The values are summarised in Table 4.7.

Wibberenz and Cane (2006) studied a sample of impulsive electron events observed by Helios associated with short flares and type III bursts. They took into account the energy response (Bialk et al., 1991) and assumed diffusive transport conditions. These authors determined the radial mean free path by evaluating the time in the profile from the particle onset to the maximum intensity and compared it with the electron flight time between the Sun and the spacecraft. They analysed the event on 1976 March 21, which is included in our sample, and found λ_r = 0.046 AU, which agrees with our inferred value (λ_r = 0.040 AU).

Recent studies have applied inversion techniques to events detected by the Helios mission. Agueda and Lario (2016) presented a study of the four events observed on 1980 May 28, were they fitted the observed PADs with an exponential function in order to infer the electron transport conditions and the injection profile at the Sun by using the transport model by Agueda et al. (2008), assuming the nominal energy range of E03. The main differences between Agueda and Lario (2016) and the present study are the use of the energetic response from Bialk et al. (1991) and the fact that we fit the most direct form of directional data, i.e. the sectored intensities. For the four events on 1980 May 28, the values of λ_r inferred in this study and by Agueda and Lario (2016) (see column 4 and 9 in Table 4.7, respectively) are very similar except for the 4th event, for which we derived a slightly larger value. The tiny differences found are explained by the different grid of λ_r-values tested and due to the difference in the assumed energy spectra. As we mention in Section 4.3.2.2, when the PADs are derived using the pitch-angle cosine of the sector centre instead of the mean pitch-angle cosine taking into account the sector response, the anisotropy of the PADs are generally underestimated, which may partly explain the smaller value of λ_r found by Agueda and Lario (2016) for the fourth event in this series.

The injection profiles inferred by Agueda and Lario (2016) are very similar to the ones inferred in the present study (see their Fig. 8). Since they use a secondary product (i.e., PADs obtained by fitting an exponential function to the sectored intensities) less affected by noise and where data gaps had been interpolated, their injections show smoother profiles. For the first three events (a, b and c in their Fig. 8), with a very similar value of the radial mean free path, we find smaller values of the maximum of the injection per energy unit, where Agueda and Lario (2016) found values of 5×10^{29} e/(s sr MeV), 1×10^{31} e/(s sr MeV), 6×10^{30} e/(s sr MeV), respectively. For event d, they found λ_r = 0.20 AU and a value of the maximum injection of 1×10^{30} e/(s sr MeV). Assuming γ = 2.0, the same spectral index as Agueda and Lario (2016), we obtain 2×10^{28} e/(s sr MeV), 8×10^{29} e/(s sr MeV), 6×10^{29} e/(s sr MeV), 1×10^{29} e/(s sr MeV), respectively for the first to the fourth event. The difference between the peak injection values found by Agueda and Lario (2016) and this study is mainly due to the fact that we take into account the energetic response of the E03 channel and due to the different approach

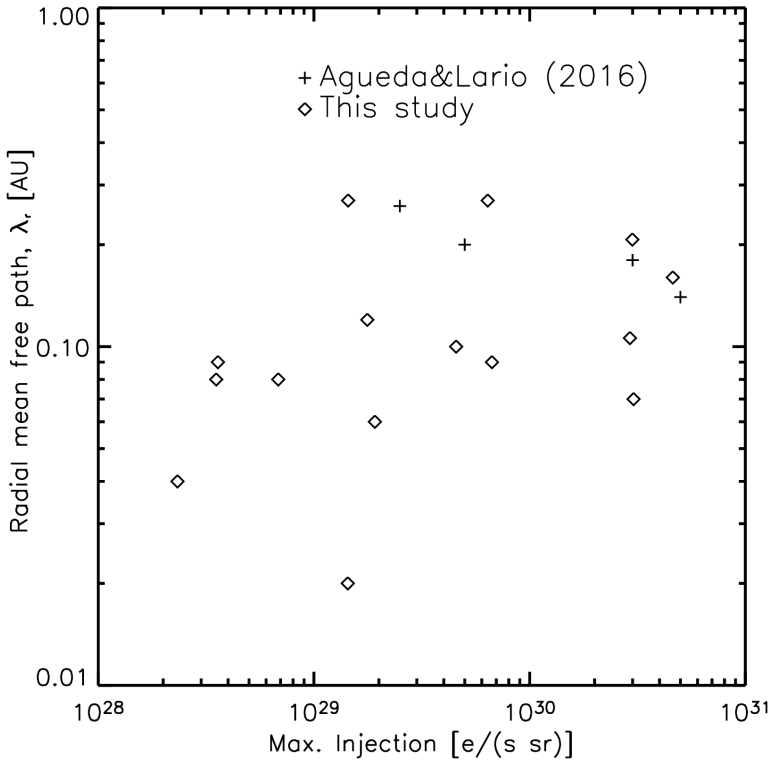

FIGURE 4.24: Radial mean free path vs. maximum electron injection at the Sun. Diamonds: values inferred in this study; crosses: values from Agueda and Lario (2016).

on fitting the intensities. Agueda and Lario (2016) assumed electrons in the energy range of 0.3 – 0.8 MeV, while we assumed 0.25 – 3.5 MeV. This latter energy range makes the injection values in units of e/(s sr MeV) to become smaller, since the considered energy range is a factor 6.5 larger than the nominal energy range. Further, Agueda and Lario (2016) fitted an exponential function to the sectored intensities, which might yield to an overestimation of the intensities for the electrons propagating along the IMF with pitch angle 0°; thus, implying higher inferred injection values.

Figure 4.24 shows the electron radial mean free path versus the maximum electron release at the Sun, where results are depicted from this study (diamonds) as well as from Agueda and Lario (2016) (crosses). Agueda and Lario (2016) report that the amount of interplanetary scattering suffered by the electrons seemed to be related to the amount of electrons released at the Sun for the four events on 1980 May 28, in such a way that λ_r decreases with increasing peak injection. This tendency is also inferred from our study for this subset of events (see the top four diamonds in Fig. 4.24). However, we find no indication of a general relation between the maximum injection at the Sun and the value of the radial mean free path when considering the whole sample, in agreement with the results from Kallenrode et al. (1992b).

4.5.2 Particle release: duration and plausible processes

Regarding the duration of the injection profile, we classified the events in our sample into short (when the release of particles lasts less than 30 min) or extended. Previous studies (Agueda et al., 2012a, Agueda et al., 2013, Agueda et al., 2014, Gómez-Herrero et al., 2015, Pacheco et al., 2017a) found a similar dichotomy from the study of solar near-relativistic electron events observed by ACE, Wind, STEREO and Ulysses, in different regions of the heliosphere. For example, Agueda et al. (2014) studied the duration of the release processes of seven near-relativistic electron events observed at the near-Earth environment by the ACE and Wind spacecraft. They found that the electron release was produced either during short (< 30 min) or long (> 2 h) periods of time, agreeing with the results of our study. Also, Agueda et al. (2012a) and Agueda et al. (2013) studied four multi-spacecraft electron events observed by ACE and Ulysses, the latter being located at high latitudes in the heliosphere and at 2 AU. They found extended periods of particle release, lasting a few hours in 5 of the events, whereas the other 3 events presented long-duration intermittent sparse injection episodes (when the magnetic footpoint of the spacecraft laid at the opposite magnetic sector of the flare site, see Agueda et al., 2013 for further details). Finally, Gómez-Herrero et al. (2015) studied the multi-spacecraft event on 2011 November 3. They modelled the ~62 – 105 keV electron event observed by STEREO-A, ACE and STEREO-B (covering ~ 300° in longitude) and derived an extended injection episode of several hours for the three spacecraft. The observation of a single CME and the observed anisotropies support the direct injection of particles at the three locations by an extended source, but a clear observational evidence of such a wide coronal and/or interplanetary shock was not found.

The fact that 10 out of the 15 events in our list show extended injections points towards some mechanism allowing a continuous electron acceleration or a slow release of the electrons into the interplanetary space. In a previous analysis of near-relativistic electron events observed by the ACE and Wind spacecraft, Agueda et al. (2009) and Agueda et al. (2014) related short (< 15 min) particle release episodes to flare processes, and they indicated as the most plausible scenario for extended injection episodes (> 1 hour) the injection of particles from coronal CME-driven shocks and/or reconnection processes behind the CMEs. In Agueda et al. (2014), they found that only for those events associated with type III radio bursts reaching the plasma line near the spacecraft a short flare-related injection episode was inferred, suggesting that magnetic connectivity plays an important role in space for short injection profiles. This was consistent with a scenario where electrons released during type III radio bursts not reaching the local plasma line never reach the observer due to the lack of magnetic connectivity. In addition, they concluded that the presence of type II radio bursts does not seem to be a discriminator between short and extended injections. These authors found that extended injections are related to different EM signatures of long particle acceleration in the corona (long decay SXR emission, type IV radio bursts, and time-extended microwave emission).

Other mechanisms to explain the observed extended particle injections are proposed by Klein et al. (2010). These authors studied in detail the EM emissions of a sample of 15 CME-less flares. These flares show bright SXR and microwaves bursts which indicate an efficient acceleration of the electrons in the flare. They found that no SEP event was connected to these flares as accelerated particles remained confined in the low corona, because magnetic field lines kept closed over the Sun's surface. The only CME-less flare associated with a weak SEP event near the Earth environment shows type II radio emission, suggesting that a coronal shock (not related to a CME) was the source of the accelerated electrons. In addition, Klein et al. (2010) analysed 3 eruptive flares (i.e., associated with CMEs) occurring few hours after the CME-less flares. These eruptive flares showed SEP events. Klein et al. (2010) point out that an easy conclusion that could be drawn from their analysis is that CMEs are needed to open magnetic field lines in order for the electrons to escape into the interplanetary space. However, Klein et al. (2010) found that this is not the scenario for the three eruptive events in their study. They state that even if the CME had opened the coronal magnetic field to allow particles access to the flux tubes along the interplanetary space, the observed SEP events associated with type III bursts were detected too early, during the impulsive phase of the flares, and thus CMEs did not have still enough time to open the coronal magnetic field around the particle source. Therefore, to explain the origin of these SEPs, they suggest the scenario where both CMEs and type III bursts are triggered from the surroundings of active regions with open magnetic field lines which connect the site with the interplanetary medium.

Dresing et al. (2018) also found that a long-lasting electron injection profile was needed to explain the widespread event on 2013 December 26. They point out that the shock front propagating into the interplanetary medium could play a role explaining that extended injection. They suggest two possible explanations, (i) the extended shock is accelerating the observed electrons when propagating into the interplanetary medium, or (ii) a leakage process coming from a magnetic trap where particles are gradually released giving the same result as a long injection. They point out that the shock will hardly explain the high-energy particles observed, so they propose possible scenarios where particles are early accelerated in the corona into the interplanetary medium and, while some of the electrons are directly injected into open field lines, a fraction of them are trapped by a closed magnetic field region that only allows a slow electron leakage towards the flux tube connecting the trap with the observer. This trap could be suddenly opened by solar activity in the corona, releasing abruptly the trapped particles it contains.

Therefore, the influence of magnetic structures and the importance of the flare sites being connected to open magnetic field lines has been proved to be a relevant factor for the release timing and duration of the electrons towards the interplanetary medium (Klein et al., 2010). Then, alternatively to coronal CME-driven shocks, it is reasonable to suggest that extended electron injections can be due to scenarios where the flare site is not well connected to open

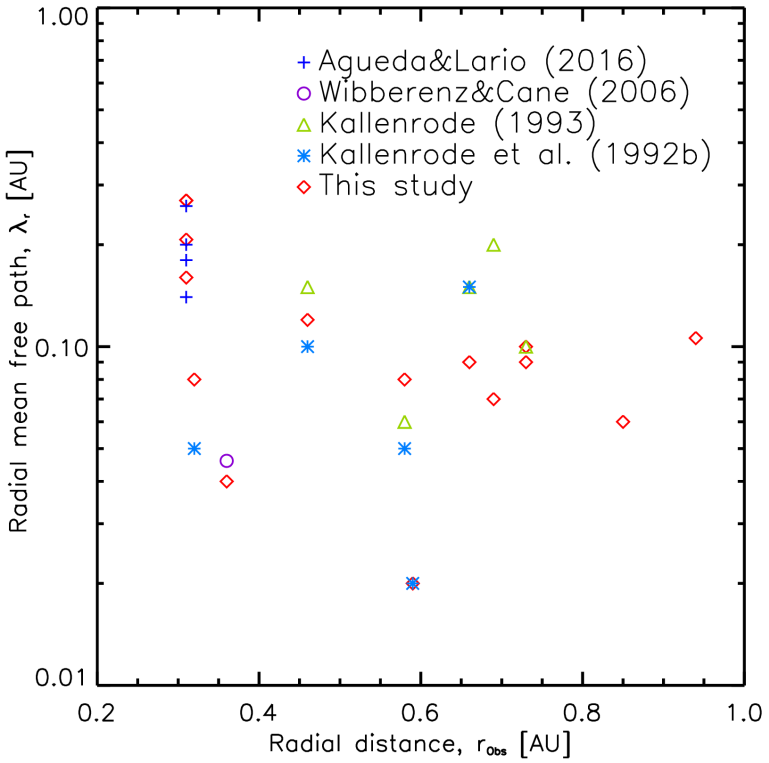

FIGURE 4.25: Radial mean free path vs. radial distance to the Sun. Red diamonds: values inferred in this study; blue crosses: values from Agueda and Lario (2016); purple circle: Wibberenz and Cane (2006); olive green triangles: values from Kallenrode (1993b); light blue asterisks: values from Kallenrode et al. (1992b).

magnetic field structures in the corona. So even if there is a partial escape of the injected particles coinciding in time with the radio emissions, a bulk of electrons is kept magnetically trapped until they reach open field lines and are gradually leaked into the flux tube connecting with the observer.

4.5.3 Intensity profiles and mean free path variation with the heliocentric radial distance

Finally, we analyse the variation of λ_r with the radial distance to the observer location. Figure 4.25 shows this variation for the events in this study (red diamonds), and those obtained by Kallenrode et al. (1992b) (light-blue asterisks), Kallenrode (1993b) (olive green triangles), Wibberenz and Cane (2006) (purple circle) and Agueda and Lario (2016) (blue crosses) for the events in the present list. We find no evidence of a radial dependence of the radial mean free path, which agrees with the conclusions of Kallenrode et al. (1992b). We expect that observers at small heliocentric distances to the Sun will observe events showing any value of the mean free path, at least between 0.03 and 0.27 AU (as seen in Fig. 4.25), when analysing their transport conditions. For this reason, it will be important to have the field-of-view data from missions like Parker Solar Probe and Solar Orbiter available in order to be able to disentangle the PADs.

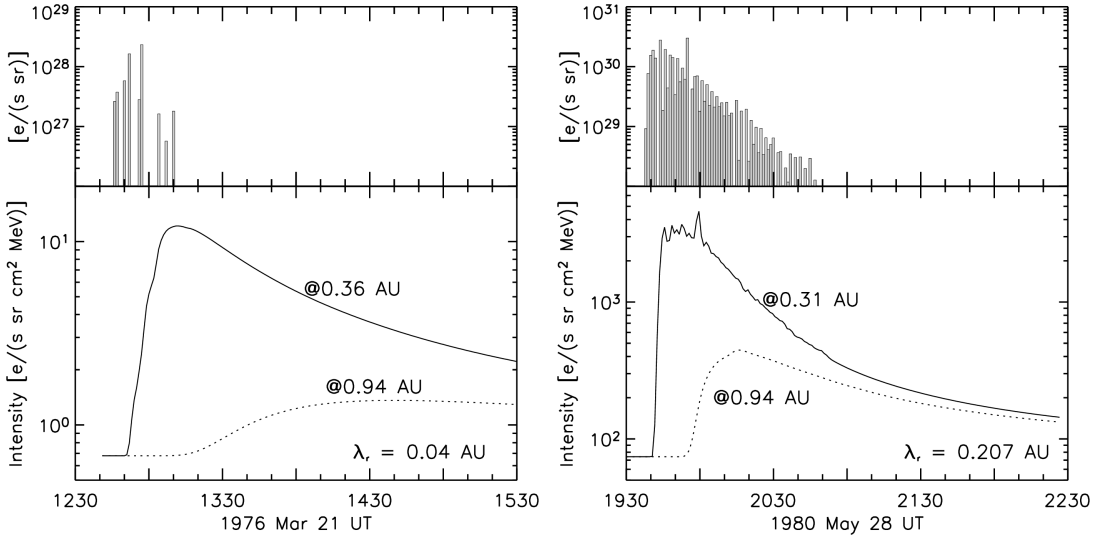

FIGURE 4.26: Events on 1976 Mar 21 (left) and 1980 May 28 c (right) modelled electron intensities at different radial distances. The upper panel shows the injection profile at the Sun. The lower panel shows the omni-directional modelled electron event at the Helios location (solid curve) and at 0.94 AU (dashed curve).

Kallenrode (1993b) found a weak dependence of λ_r with the heliocentric radial distance below 0.5 AU for protons. We do not find such a trend in our sample of electron events (see Fig. 4.25). On the other hand, Kallenrode (1993b) suggests that such radial dependence could stem from a bias in the selection of the events, that hinders from choosing events with a diffusive profile near 1 AU. We have further inspected this point.

Figure 4.26 shows, for the event on 1976 March 21 (left) and the third event on 1980 May 28 c at ~19:30 (right), the inferred electron release profiles at the Sun (top panels) and the electron profiles (lower panels) obtained by convolving the injection profiles with the Green's functions of particle transport for the best fit value of λ_r at the Helios location (solid curves) and at a radial distance of 0.94 AU (dashed curves). The profiles show that these two events, clearly observable in the inner heliosphere, appear barely above the background when observed close to 1 AU, especially in the case of the event on 1976 March 21, due to the diffusive transport conditions in the interplanetary medium characterised by the same λ_r for all helioradii. Therefore, the selection bias may be twofold: (i) some SEP events, especially those evolving under strong diffusive transport conditions, may not be observed at 1 AU because the intensities they show at these distances may remain below the background level and (ii) some SEP events may be instead observed at 1 AU but exhibiting, even under focused transport conditions, low intensity levels that render their modelling difficult given the low statistics of the measurements. Hence, small to middle size (in terms of their peak intensity) SEP events, like those in our sample that are detected at radial distances close to the Sun, might be undetected at larger distances.

4.6 Conclusions

The full inversion approach presented in this study represents a step forward with respect to previous analysis of Helios observations, as for the first time both energy and angular responses have been taken into account in order to develop a more accurate approach to fit the directional distributions of electrons observed in-situ.

We scanned the full Helios mission looking for the best-observed electron events to model and we found a sample of 15 events fulfilling the selection criteria. Then, we modelled the angular and the energetic response of the E6 instrument on board Helios and computed a sample of Green's Functions for the different transport scenarios, given by different values of the mean free path, taking into account several parameters as the solar wind speed, the energy spectrum and the radial distance between the Sun and the spacecraft. For each event in our sample, we inferred the injection profile and the value of the radial mean free path that best fitted the observations.

The results suggest values of the radial mean free path between 0.02 AU and 0.27 AU. When we compared the computed parallel mean free paths to the focusing lengths they agree, in general, with weak-focused transport ($0.1 < \lambda_{\parallel}/L < 1$ for 10 cases). Four events (the 4 consecutive events on 1980 May 28) show higher values of the radial mean free path (0.16 – 0.27 AU), and suggest focused transport ($\lambda_{\parallel}/L \geq 1$). Only one event (1982 June 2) presents diffusive transport results ($\lambda_{\parallel}/L \leq 0.1$) with $\lambda_r = 0.020$ AU.

We compared the obtained values of the radial mean free path and maximum injection with those reported by previous studies (Kallenrode et al., 1992b, Kallenrode, 1993b, Agueda and Lario, 2016) and found that our results were compatible with them for all cases except for the result on 1981 May 8 (Kallenrode, 1993b), which differs a factor ~3 with our inferred mean free path. We also compare the duration of the events studied by Kallenrode et al. (1992b) finding that 2 of them could be fitted by using short episodes of δ-injections and other 3, for which their fit failed adjusting the slow anisotropy decay, we inferred extended injection profiles.

Regarding the injection profiles, we found two separated groups depending on the duration of the injection. We found 5 short injection profiles (lasting less than 30 min) and 10 extended injection profiles (lasting more than 30 min). The value of the maximum injection takes values from 1.7×10^{28} [e (s sr)$^{-1}$] to 3.1×10^{30} [e (s sr)$^{-1}$]. The peak and duration of the inferred electron release histories match, in general, with radio and soft X-ray emissions extracted from the literature. We suggest that extended injection profiles can be explained by either coronal CME-driven shocks or complex magnetic structures trapping the electrons and allowing a slow release over a long time period, as discussed by Klein et al. (2010) and Dresing et al. (2018).

We found no dependence between the radial mean free path and the radial distance between the Sun and the observer. We compared the modelled profiles at small radial distances with those modelled profiles close to 1 AU and concluded that diffusive events associated to relatively small

injection profiles may not be observable at 1 AU. According to this and together with the fact that in our sample we find events observed close to the Sun with a rather wide range of values for λ_r, we might expect that SEP events to be observed by Parker Solar Probe and especially by Solar Orbiter, that will travel to similar heliocentric radial distances to those of the Helios orbit, show a large variety of transport conditions. Hence sectored data as it will be provided by the EPD instrument of Solar Orbiter (Rodríguez-Pacheco et al., 2018) may be important to both infer the transport effects at play in SEP events and particle release histories. Also, in order to improve our understanding of the electron interplanetary transport conditions and the release processes at the Sun, it will be crucial to have multi-spacecraft observations from several radial distances. This will allow us to study differences in the transport conditions over the heliosphere and characterise the angular extent of their solar sources.

Chapter 5

Applications to Solar Orbiter

5.1 Solar Orbiter and its Energetic Particle Detector in brief

Solar Orbiter (Müller et al., 2013) is a coming heliospheric scientific mission developed by ESA in collaboration with NASA and it is planned to be launched in 2020 from Cape Canaveral. The mission aims at studying how the Sun creates and controls the heliosphere from several points of view, using remote sensing instruments as well as in-situ experiments that will allow a deep study on the solar phenomena that shape the heliosphere and control its properties. The main objectives of the mission are to disentangle what triggers the different solar wind and coronal magnetic field, how do solar transients drive heliospheric variability, how and where SEPs are accelerated, the functioning of solar dynamo and the connection between the Sun and the heliosphere.

Solar Orbiter is a three-axis stabilised spacecraft that will orbit the Sun with a very eccentric trajectory with a minimum perihelion of 0.28 AU. This orbit close to the Sun together with the fact of carrying the most complete set of high-resolution instruments up to date (see Table 5.1) will allow Solar Orbiter to study the interface region in the corona where the solar wind is originated and the sites where SEPs are accelerated both by flares and coronal and interplanetary shocks.

The mission will make use of gravitational assistance manoeuvres to achieve a high-inclination orbit that will allow the study of the Sun polar regions. For this purpose, the inclination will raise up to <25° during the nominal phase of the mission, and up to 33.4° during the extended phase, depending on the launch baseline date[1].

Furthermore, Solar Orbiter will allow multi-spacecraft studies together with Parker Solar Probe, STEREO-A and the spacecraft orbiting the near-Earth space, as well as future missions to the fifth Lagrangian point of the Earth-Sun system. These studies will be specially interesting

[1]These latitude values are of the orbit planned for launch in February 2020, according to the SolO CREeMA-SOL-ESC-RP-05500, Issue 4 revision 1 - 2017-06-01 document from ESA.

TABLE 5.1: Instruments on board Solar Orbiter spacecraft.

Type	Instrument	Acronym
In-Situ	Energetic Particle Detector	EPD
	Magnetometer	MAG
	Radio and Plasma Wave analyser	RPW
	Solar Wind Analyser	SWA
Remote-Sensing	Extreme Ultraviolet Imager	EUI
	Multi Element Telescope for Imaging and Spectroscopy (coronagraph)	METIS
	Polarimetric and Helioseismic Imager	PHI
	Solar Orbiter Heliospheric Imager	SoloHI
	Spectral Imaging of the Coronal Environment	SPICE
	Spectrometer/Telescope for Imaging X-rays	STIX

since, for the first time, the scientific community will have access to high cadence data from remote and in-situ instruments on board several spacecraft observing the Sun from different heliolongitudes, latitudes and radial distances (within 0.28 – 1.02 AU for the planned orbit for the launch date in February 2020). These data will be extremely helpful to test the current models, develop new tools and improve space weather forecasts (e.g., Rouillard et al., 2019). Particularly, related to the understanding of solar energetic particle events, in addition to disentangle where SEPs are accelerated, Solar Orbiter instruments will allow us to adress what are the seed particle populations and how SEPs are transported after being released from their sources.

The Energetic Particle Detector (EPD) suit on board Solar Orbiter (SolO) consists on four different in-situ particle instruments (Rodríguez-Pacheco et al., 2018, Gómez-Herrero et al., 2017), measuring energetic ions, protons and electrons within an energy range from few keV to 450 MeV, in overlaping intervals (see Fig. 2 in Gómez-Herrero et al., 2017). These are

i) SupraThermal Electrons and Protons (STEP),
ii) Sprathermal Ion Spectrograph (SIS),
iii) Electron Proton Telescope (EPT) and
iv) High Energy Telescope (HET).

We will focus our description on two of them, EPT and HET, which are based on similar instruments previously launched on board STEREO (the SEPT instrument) and Mars Science Laboratory (Radiation Assessment Detector - RAD), respectively (Gómez-Herrero et al., 2017).

SolO/EPD/EPT consists on two twin double ended telescopes providing four fields of view with a full conical aperture of 30° and a nominal geometric factor of 0.01 cm^2sr. It is designed to measure protons with energies from 20 keV to 7 MeV and electrons from 20 keV to 400 keV with up to 1 measurement per second. SolO/HET, analogously to EPT, is formed by two twin double-ended sensor heads, each sharing the electronic box with EPT sensor, providing four

TABLE 5.2: Pointing directions of the fields of view of the EPT and HET instruments on board Solar Orbiter.

Fields of view	**EPT/HET** $\hat{\mathbf{s}}$	
	φ [°]	θ [°]
HET-EPT1-forward (Sun)	-35.00	90.00
HET-EPT1-backward (Anti-Sun)	145.00	90.00
HET-EPT2-forward (South)	57.55	145.62
HET-EPT2-backward (North)	237.55	34.38

fields of view with a conical full aperture of 42.9° and a nominal geometric factor of 0.27 cm^2sr. HET will measure protons in the range from 10 MeV to 100 MeV, ions between 20 MeV/nuc to 450 MeV/nuc and electrons from 300 keV to 15 MeV. As well as for EPT, the maximum cadence of HET measurements is 1 s.

Table 5.2 summarises the coordinates of the four fields-of-view centre unit vectors $\hat{\mathbf{s}}$ of the EPT and HET instruments, in the spacecraft-centred spherical Spacecraft Solar Ecliptic (SSE) coordinates, where θ is the colatitude and φ is the azimuth. The Z axis corresponds to $\theta = 0°$ and it is perpendicular to the ecliptic plane. The azimuth origin is the spacecraft-to-Sun line. Note that EPT and HET share the same pointing vectors but differ on the aperture angle.

EPT and HET will measure electron events in an energy range that includes the modelled electron channels in Chapter 4 and Chapter 5, and HET will provide proton measurements for similar energies as those provided by the SEPEM RDSv2. Based on the solar energetic electron events modelled in the previous chapter, we studied how the peak intensity of these events vary within a heliocentric radial distance range similar to the distances that Solar Orbiter will cover as well as how EPT would observe the PADs of a few events in our sample. We present these studies in the next sections and finally, we used planned orbit missions for Solar Orbiter to show the impact of the updates to SOLPENCO2 produced in Chapter 2 in the results of the SEPEM statistical SEP fluence model for interplanetary missions.

5.2 Radial dependence of peak intensities and anisotropies

5.2.1 Introduction

Because of the interest of space agencies in correctly assessing SEP radiation environment in the inner heliosphere, there has been an extensive effort to understand the variation of the peak intensities of solar energetic proton events as a function of the heliocentric radial distance. A thorough summary of the early efforts is provided in the introduction of Lario et al. (2006). The observational study by Lario et al. (2006) shows that the radial dependence of protons may vary event to event and with the energy of the protons. Several studies have been devoted since then

to characterise this event to event variations: from models that consider the variations resulting from the contribution of the interplanetary shock as a particle accelerator (e.g., Aran et al., 2005, Ruzmaikin et al., 2005, Aran et al., 2006, Aran, 2007, Vainio et al., 2007, Aran et al., 2011b, Verkhoglyadova et al., 2012, Rodríguez-Gasén et al., 2014, Crosby et al., 2015, Aran et al., 2017a), to modelling studies that focus on the role of non-nominal solar winds (e.g., Kozarev et al., 2010, Dayeh et al., 2010) and on the role of different transport conditions describing the pitch-angle scattering (e.g., Lario et al., 2007, He et al., 2017).

Although >100 keV electrons, especially those trapped in the magnetosphere, may cause among other effects, damage to solar cells (Feynman and Gabriel, 2000), they are not usually considered a prime SEP radiation risk. However, solar energetic relativistic electrons are a perfect precursor signal for large SEP events. Posner (2007) showed that, for species coming from the same solar source, electron intensity and increase can be used to forecast the upcoming proton intensity within a time frame of one hour. The capability of electron measurements to forecast proton intensities for shorter heliocentric radial distances is more limited in time than at 1 AU. Nevertheless, in addition to the scientific interest *per se*, the study of the electron peak intensities that could be reach at distances close to the Sun is relevant from a practical point of view, for example, to estimate saturation and dead-time effects on particle detectors on board missions like BepiColombo, Parker Solar Probe or Solar Orbiter.

In this section, we recover the results obtained for the sample of the electron events modelled in Chapter 4 and study the variation of the peak intensity and anisotropy along an interplanetary magnetic field line by placing several virtual observers at different heliocentric radial distances. For obtaining the intensity and anisotropy time profiles for these virtual observers, we used the injection history, obtained from the modelling of the events, to convolute it with the Green's functions computed for the different radial distances extending from 0.31 AU to 0.94 AU.

5.2.2 Results

Due to data gaps in Helios observations, we found that injection profiles showed higher injections around a data gap than expected for a well-behaved injection function. These events showed a shift in the peak time that prevented us to consider the peak intensity reliable for the study. For that reason, we performed a 4-points smooth process on the injection profile for four events (b, c and d events on 1980 May 28, and event on 1981 June 10), in order to minimise the effects over the intensity profiles of convolving overestimated injections. This method worked partially for three of the events, but for the remainder event (event d on 1980 May 28) the smoothness was good enough to use it in the study of the peak intensities and the anisotropy values at the peak. As a result, we selected nine events from the full sample of fifteen, showing smooth enough injection profiles resulting in intensity-time profiles with no artefacts, once convoluted for the different Green's functions.

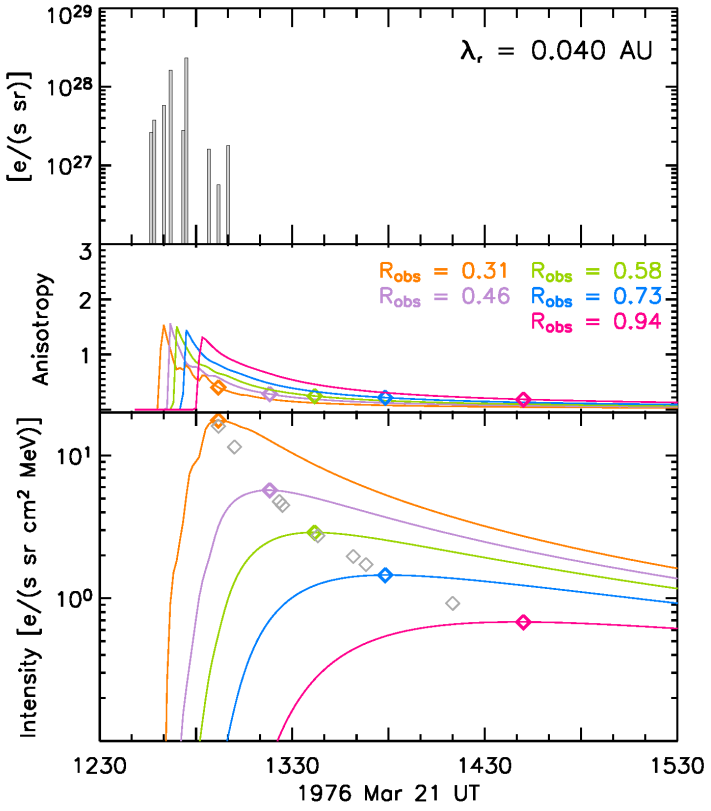

FIGURE 5.1: Event on 1976 Mar 21 modelled electron intensities at different radial distances, from 0.31 AU to 0.94 AU. The upper panel shows the inferred injection profile at the Sun and it is indicated the value of the mean free path. Middle panel shows in different colours, the anisotropy profiles corresponding to five different radial distances (0.31 AU, 0.46 AU, 0.58 AU, 0.73 AU and 0.94 AU). The lower panel shows the omni-directional modelled electron event at the above mentioned locations with the same colour code. Coloured diamonds depict the peak intensity for each mentioned location and grey diamonds correspond to the peak intensities at the remaining locations.

Figures 5.1, 5.2 and 5.3 show the synthetic profiles obtained for the nine events selected. The upper panels show the injection profile, where there is also indicated the inferred radial mean free path; middle panels show the anisotropy profile coloured according to the five selected radial distances (in AU units), with the anisotropy at the peak indicated by a coloured diamond. The bottom panels show the intensities at the same five radial distances, with coloured diamonds indicating the peak intensities for the depicted radial distances and grey diamonds for the peak intensities of the omitted distances. For event on 1980 May 28 d at ~23:30 UT, we also show in the upper panel the resulting curve of the smoothness performed on the injection profile. By looking at these figures we realise that impulsive injections with close to diffusive particle transport conditions yield to later occurrences of both peak and onset intensity times for the profiles observed at the larger distances (see Fig. 5.1 and the bottom right panel of Fig. 5.3). Note also that since electrons travel fast to the observer's position, a resolution of 15 minutes in data prevents the solving of the shape of intensity and anisotropy profiles, especially at the shorter radial distances, as shown for the 1980 April 5 event (top left panel of Fig. 5.2).

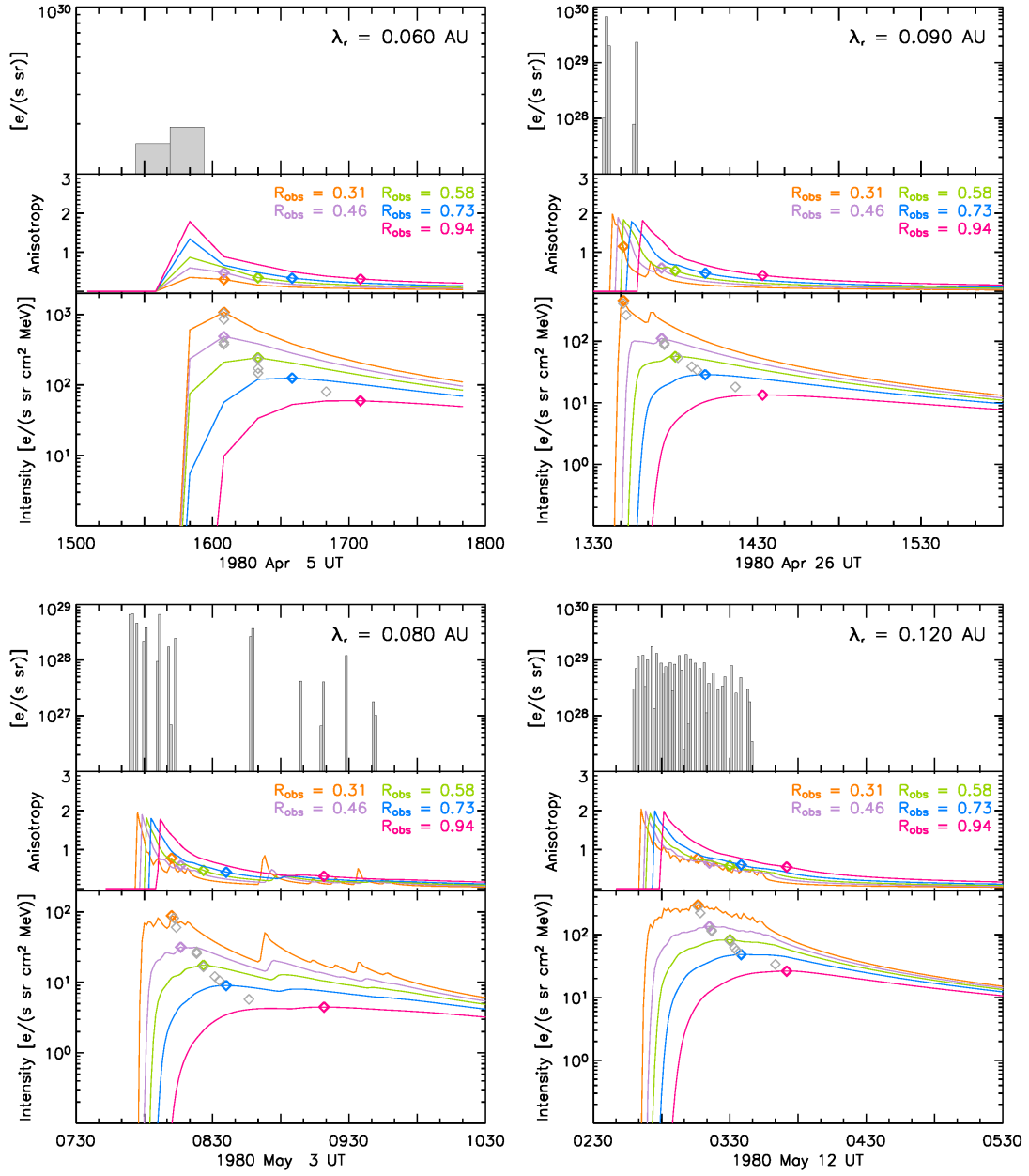

FIGURE 5.2: Same as in Figure 5.1 for events on 1980 April 5, 1980 April 26, 1980 May 3 and 1980 May 12.

Next, in order to quantify the variation of the peak intensity with the radial distance of the observer, we assumed a power-law functionality, $f(r) = b \cdot r^{-\alpha}$. Hence for the nine events shown in Figures 5.1, 5.2 and 5.3 we performed a linear regression fit of the logarithms of both quantities. For this we used the thirteen virtual modelled observers. We also used the same dependence to study the variation of the anisotropy at the time of the peak intensity. Figure 5.4 shows the obtained peak intensities (left panel) and anisotropy-at-peak (right panel) for each radial distance (empty triangles) and the results of the fittings (solid lines) with different colours for each event; it also shows in the left hand side of each fit, the resulting slope, the index α, and in the right hand side the date of the event. A summary of the results is presented in

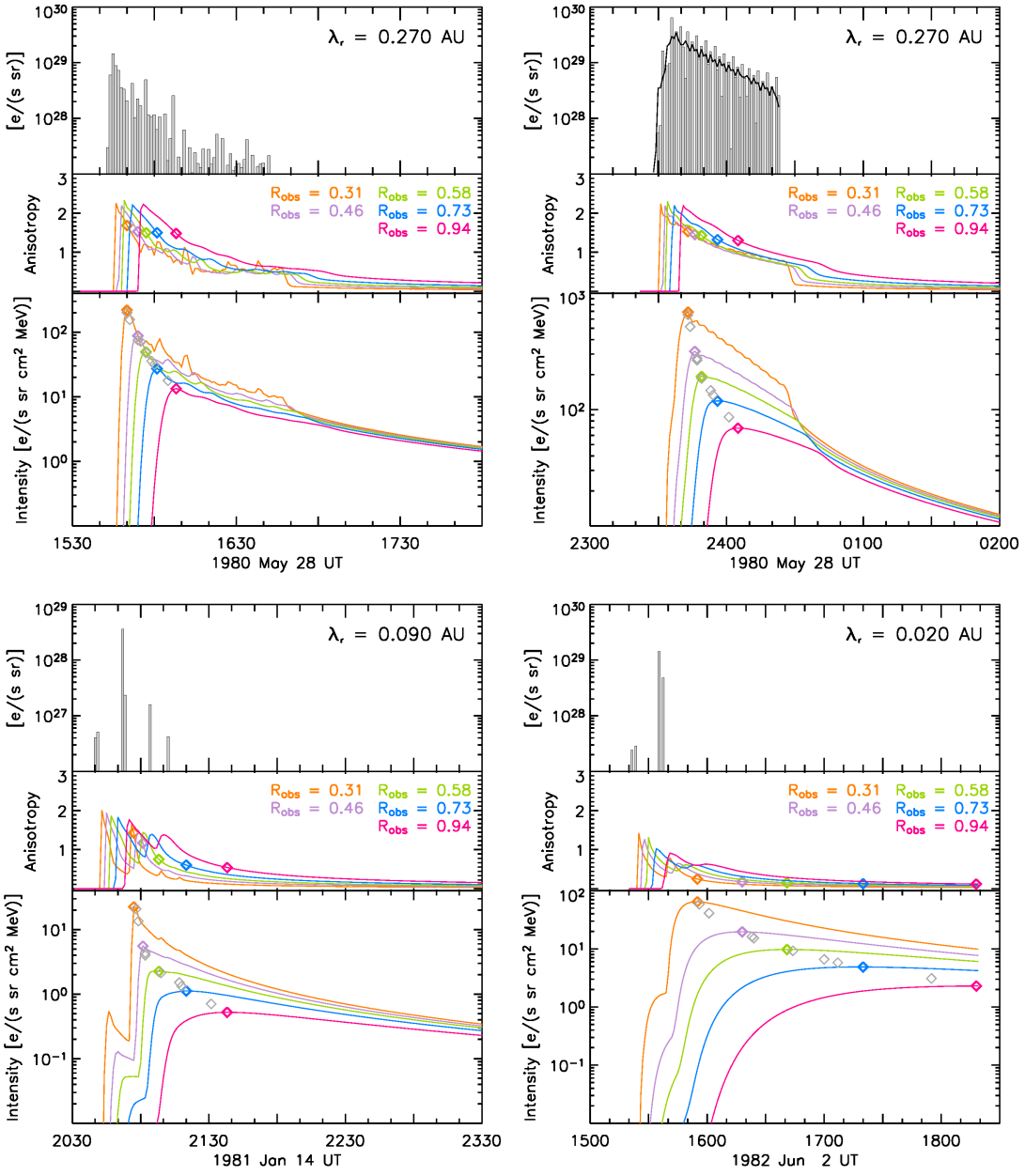

FIGURE 5.3: Same as in Figure 5.1 for events on 1980 May 28 a, 1980 May 28 d, 1981 January 14 and 1980 June 2.

Table 5.3, which lists, from left to right, the number associated to each event, the year and date of the event, the radial mean-free path previously inferred and the parameters obtained from the linear fittings, i.e., α indices, their associated errors and the correlation coefficients, for the peak intensities and for the anisotropies-at-peak. The values of the fitting parameters for the anisotropy-at-peak for event on 1980 April 5 are shown in red as we consider them not reliable, since the associated error is larger than the value of α and the correlation coefficient is very small (~0.008). Note also that the linear correlation found for the peak intensities is the worst amongst the events in the sample, due to the coarse temporal resolution of the data.

TABLE 5.3: Radial dependence parameters for the peak intensity and the anisotropy at the peak for the nine events in the sample.

Num	Year	Date	λ_r	Peak intensity			Anisotropy-at-peak		
			[AU]	α	$\delta\alpha$	r	α	$\delta\alpha$	r
1	1976	Mar 21	0.04	2.93	0.01	0.99992	0.69	0.03	0.990
2	1980	Apr 5	0.06	2.64	0.03	0.997	0.0	0.2	0.008
3	1980	Apr 26	0.09	3.17	0.03	0.9990	1.0	0.1	0.94
4	1980	May 3	0.08	2.69	0.07	0.9996	0.64	0.06	0.95
5	1980	May 12	0.12	2.16	0.05	0.9990	0.31	0.03	0.96
6	1980	May 28 a	0.27	2.50	0.02	0.9991	0.13	0.02	0.91
7	1980	May 28 d	0.27	2.08	0.03	0.99990	0.16	0.01	0.96
8	1981	Jan 14	0.09	3.47	0.03	0.9990	0.9	0.1	0.92
9	1982	Jun 2	0.02	3.01	0.01	0.999998	0.70	0.02	0.994

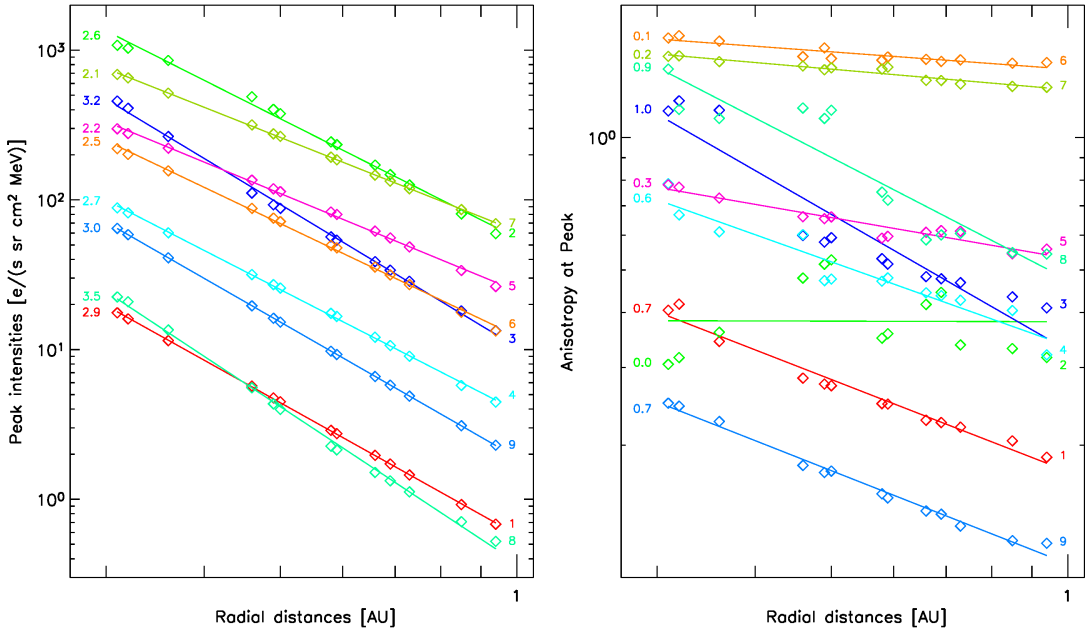

FIGURE 5.4: Fittings of the peak intensities (left panel) and the anisotropy at peak for the different radial distances of each event. The number of each event is shown at the right of each fit and the exponential index (α) at the left.

The values of the radial indices obtained, α, range from 2.08±0.03 to 3.47±0.03 in the case of peak intensities and from 0.13±0.06 to 1.0±0.1 for the anisotropy-at-peak, excluding the value corresponding to the event on 1980 April 5. With the exception of this event, we obtained good linear correlations for the peak intensity fits and fair correlations for the anisotropy-at-peak radial dependences. Therefore, we conclude that a power-law function may describe the behaviour of the peak intensity dependences and may also describe the anisotropy-at-peak dependence within the range of distances modelled, provided that the time resolution of the data is enough, i.e., $\lesssim$1 min.

Finally, we applied the radial dependences obtained in order to extrapolate the value of the

TABLE 5.4: Results for the extrapolation of the previous obtained trends for the minimum perihelion distance of Parker Solar Probe and Solar Orbiter for each event. Red values denote non-reliable results due to a large error.

Num	Year	Date	Parker Solar Probe min perihelion		Solar Orbiter min. perihelion	
			I_{Peak} [s sr cm^2 MeV]$^{-1}$	δI_{Peak} [s sr cm^2 MeV]$^{-1}$	I_{Peak} [s sr cm^2 MeV]$^{-1}$	δI_{Peak} [s sr cm^2 MeV]$^{-1}$
1	1976	Mar 21	7×10^3	1×10^4	2×10^1	4×10^1
2	1980	Apr 5	2.56×10^5	0.06×10^5	1.61×10^3	0.03×10^3
3	1980	Apr 26	2.52×10^5	0.3×10^5	5.9×10^2	0.6×10^2
4	1980	May 3	2.1×10^4	0.6×10^4	1.2×10^2	0.3×10^2
5	1980	May 12	2.44×10^4	0.1×10^4	3.9×10^2	0.2×10^2
6	1980	May 28 a	3.5×10^4	0.3×10^4	3.0×10^2	0.2×10^2
7	1980	May 28 d	4.7×10^4	0.08×10^4	8.7×10^2	0.1×10^2
8	1981	Jan 14	2×10^4	7×10^4	3×10^1	9×10^1
9	1982	Jun 2	2×10^4	1×10^4	9×10^1	5×10^1

peak intensity at the minimum perihelion radial distance for the Parker Solar Probe (0.041 AU) and the Solar Orbiter (0.28 AU) missions. For the nine events in the sample, we show in Table 5.4 from left to right, the number of the event, the year and date of the event, the peak intensity and its associated errors derived both for Parker Solar Probe and for Solar Orbiter. As in the previous table, red values denote events with intensity results equal to their associated errors. Note, that the uncertainties shown here are merely due to error propagation from the linear regression fits to the logarithm values of the peak intensities and distances. And hence, the small uncertainties obtained for the logarithm values translate to large linear errors, in some cases. Also, we considered all peak intensity values had no error associated. We obtain reliable results for all cases except the event on 1976 March 21 and 1981 January 14, for which δI_{Peak} is bigger than the peak value, because of to the large error in the b parameter ($b = 1 \pm 1$, for both cases).

On the other hand, for most of the events in the sample, the power law function was able to explain the anisotropy dependences for a wide range of distances in the inner heliosphere (0.3 – 1.0 AU). However, if values extrapolated towards smaller radial distances, some of the anisotropies would exceed the physical range (i.e., > 3). Thus, for the case of the anisotropy-at-peak fits, we can not apply the obtained parameters to perform an analogous extrapolation towards small radii such as done for the peak intensities.

5.2.3 Discussion

Theoretical models permit us to estimate the radial dependence of the peak intensity for impulsive (short-duration) solar injections, by assuming different particle transport conditions (Vainio et al., 2007). For diffusive transport conditions, the diffusion-advection model proposed by Parker (1965) can be applied. Vainio et al. (2007) obtained the analytical solutions of

the diffusion equation, finding that the spatial scaling law for the event maximum intensity is $I_{max}(r) \propto r^{-3}$. On the other hand, when applying the focused transport model of Roelof (1969), assuming that the mean free path of the particles is comparable to the heliocentric radial distance of the observer, it is not possible to find any analytical solution. Vainio et al. (2007) modelled the electron event on 2000 May 1 observed by the ACE spacecraft, using the focused transport model by (Agueda et al., 2008). They obtained a radial mean free path of 0.6 AU. Making use of the model results at other radial distances they inferred radial indices ranging from −2.60 for 45 – 62 keV electrons to −2.35 for 175 – 312 keV electrons. These values are similar to the radial indices we derive for the events in our sample with the larger mean free paths (i.e., 1980 May 28 a,d and 1980 May 12).

Lario et al. (2013) studied in detail five 71 – 112 keV electron multi-spacecraft events observed in the inner heliosphere by MESSENGER/EPS (Andrews et al., 2007) and by either STEREO-A/SEPT or STEREO-B/SEPT (Müller-Mellin et al., 2008), at ∼1 AU. They found that two events showed radial dependences steeper than r^{-3}, i.e., with values of α of 5.29 and 4.44. Lario et al. (2013) invoked the presence of complex magnetic structures (i.e., ICMEs) between MESSENGER and STEREO to explain extreme steep variation found. The other three events showed a dependence weaker than r^{-3}, with values of α of 1.39, 1.55 and 0.81. The authors remarked the limitations of MESSENGER/EPS on detecting electrons arriving from the Sunward hemisphere, which can prevent the observation of the real peak intensity and, as a result, provide a smoother scaling. In comparison, our study provides a narrower range for α (between ∼2.08 – ∼3.47), with most of the values below the upper limit for the diffusive model (r^{-3}), and only three events (1980 April 26, 1981 January 14, 1982 June 2) presenting values of α above this limit, corresponding to events for which we derived mid-range to small radial mean free path values (0.09 AU, 0.09 AU and 0.02 AU, respectively). On the other hand, we found also several examples of equally small values of the mean free path but with lower values of the α index. Hence, we can not claim that only the mean free path (as a measure of the degree of diffusiveness of the event) is playing a role shaping the peak intensity decay along the radial distance in our modelled events. Instead, we know that both interplanetary transport and the injection profile shape the event peak intensities at different radial distances.

We explore the possible correlation between α values and the mean free path values and we found not specially significant correlation (r ∼0.6), meaning that the injection profile might have an important contribution. We noticed that events with very short injection profiles tend to yield steeper α values. For the three events, mentioned above, showing the larger values of α, we inferred a short-duration injection profile. Motivated by this, we further investigated the correlation between the radial indices and the duration of the particle injection. Figure 5.5 shows the scatter plot of the α indices as a function of the total injection duration of the events (orange open diamonds). The event on 1980 May 3 has a duration more than 50 minutes larger than the rest of the events in the sample. Hence we have not taken this event in the study of this

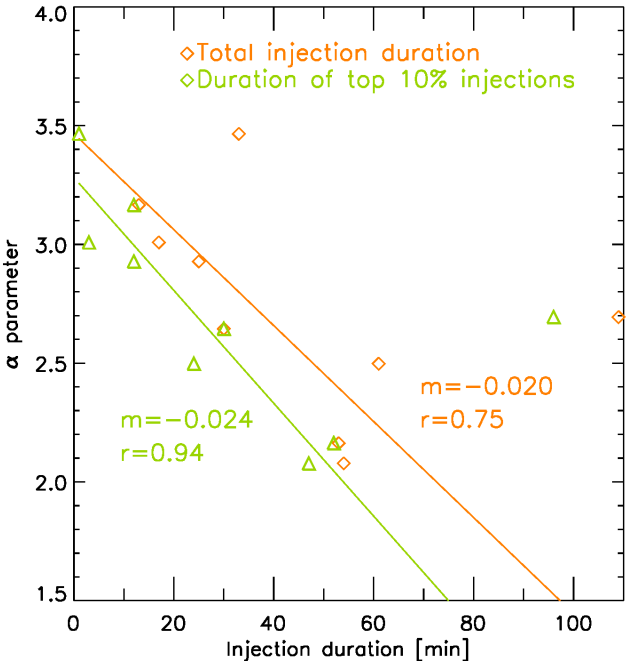

FIGURE 5.5: Alpha parameter value vs. injection duration. Orange: diamonds values and regression line taking the total injection duration of each profile. Olive green: triangles values and regression line computing the injection duration only regarding injections being at least 10% of the maximum injection. The values for the slope and the correlation coefficients are also shown with their correspondent colours.

correlation[2]. The solid orange line shown in Figure 5.5 corresponds to the linear regression fit performed. We found a weak correlation as determined by the values of the regression coefficient (r ~0.75). However, taking into account that several events in the sample show a main large injection episode and long injection tales with very little intensity that appear to play no role in the shape of the intensity profiles, specially at large radial distances, we computed the duration of the particle injection by including only those injections with injection-intensities within the 10% of the maximum injection, and checked for a possible correlation the radial index with the duration of these most intense injection episodes (indicated in Fig. 5.5 by olive green symbols and fitting parameters). Now, the correlation between both variables is much higher (r ~0.94). Hence, we can claim that injection duration plays an important role in the peak intensity decay with the radial distance. Our results and conclusion are in agreement with similar particle transport simulations performed by Lario et al. (2007) for short-duration injections of 4 – 13 MeV and 26 – 37 MeV protons within 0.3 – 1.6 AU.

[2]This outlier duration of the injection of the event on 1980 May 3 could be due to the long data gap shown in the observational profile, that prevented our model to match a sustained injection during that period, which will allow a good fitting at the observed distance but does not allow us to perform a reliable extrapolation of this injection profile to other distances as the lacking part could be important at longer radii.

5.3 Directional distributions. Comparison Helios/E6 vs. SolO/EPD/EPT

5.3.1 Angular response of SolO/EPD/EPT

We selected three SEP events of the fifteen modelled events seen by Helios (in Chapter 5) in order to study how SolO/EPD/EPT would observe the PADs of these events if it were at the same position as the Helios spacecraft.

For this purpose, we modelled EPD/EPT on board Solar Orbiter, following an analogous technique as presented in Section 4.3.2. In this case, unlike Helios, we needed to model Solar Orbiter as an spin-stabilised spacecraft taking into account the specifications explained in Section 5.1 regarding the pointing vectors and apertures of the four fields of view and the geometric factor of the instrument. Hence, we obtained a bi-directional matrix R_{jk} of 180x360 elements with 1° resolution, being (j,k) the indices of θ and φ angles where the normalised detection probability for each direction is recorded. Figure 5.6 shows the response function of the four fields of view of EPT defined in the SSE coordinate system, where the origin of the colatitude, $\theta = 0°$, corresponds to the Z axis perpendicular to the ecliptic plane (pointing northward), and the origin for the azimuth, $\varphi = 0°$ to the spacecraft-to-Sun line. Unlike Helios/E6, for EPT it is obvious that the instrument has only a partial coverage of particles coming over the ecliptic plane with only a very homogeneous detection range around $\varphi = 145°$ and $\varphi = 325°$ in this plane, corresponding to the Anti-sunward and Sunward directions along the nominal IMF (at 1 AU). On the other hand, the comparison with Figure 4.10 shows that, unlike E6, EPT covers a range of angles far from the ecliptic plane, at around $\theta \sim 34.38°$ (over the ecliptic) and $\theta \sim 145.62°$ (below the ecliptic), which may be interesting to measure particles at non-ideal configurations of the IMF, as for example, during the passing of CIRs or ICMEs.

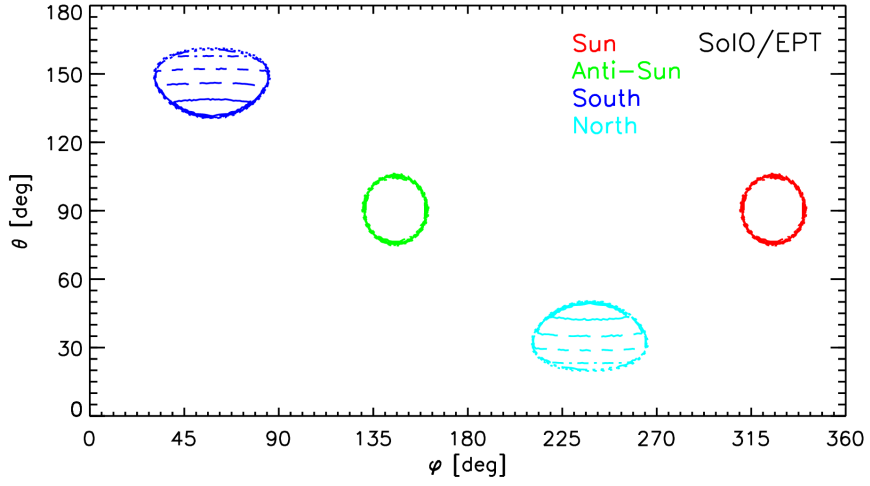

FIGURE 5.6: Angular response of the four fields of view of EPT defined in the SSE coordinate system of Solar Orbiter.

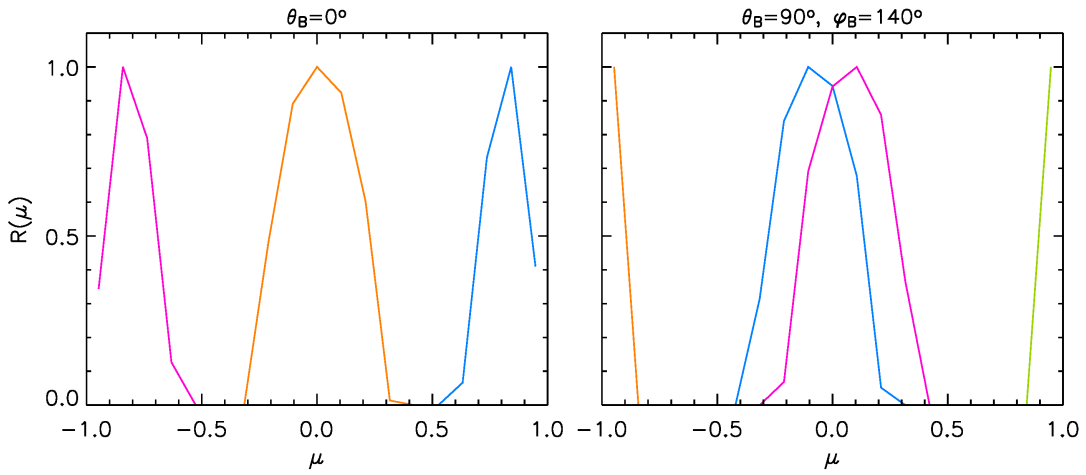

FIGURE 5.7: Normalised angular response of the fields of view of EPT assuming two magnetic field configurations: $\theta_B = 0°$(left panel), and $\theta_B = 90°$ and $\varphi_B = 140°$ (right panel). The fields of view are indicated by different colours: Sun (olive green), Anti-Sun (orange), South (blue) and North (magenta).

Next, we performed the same analysis as previously done for Helios/E6 regarding the pitch-angle cosine response and coverage as a function of the direction of the magnetic field, for SolO/EPD/EPT. For this purpose, we proceeded to determine the pitch-angle cosine range scanned by each field of view analogously as in Section 4.3.2. We defined the directions of the IMF as $\hat{B} = (1, \theta_B, \varphi_B)$ where θ_B is the colatitude angle and φ_B is the azimuth, in spherical coordinates. Then, we computed the values of the pitch-angle cosines corresponding to the grid of directions where the fields-of-view responses were evaluated, μ_{jk}, and obtained the pitch-angle response of each field of view for a given magnetic field configuration, R^s_{jk}.

Figure 5.7 shows the pitch-angle cosine response function for each field of view of EPT, assuming two different magnetic field configurations: $\theta_B = 0°$ (left panel), and ($\theta_B = 90°$,$\varphi_B = 140°$) (right panel). In the first case, the magnetic field is aligned with the spacecraft Z axis and the response function does not depend on the value of φ_B. Contrary to Helios/E6, for this configuration, SolO/EPD/EPT has a larger coverage of pitch angles. On the second case where the magnetic field is in the ecliptic plane, $\theta_B = 90°$ and $\varphi_B = 140°$, EPT is also covering, in addition to similar pitch-angle cosine range centred at $\mu = 0$ as for $\theta_B = 0°$, the Sun and Anti-Sun directions ($\mu = \pm 1$). In this latter case, the coverage is worse in comparison to what we found for Helios/E6, which showed full pitch-angle coverage.

Figure 5.8 shows the pitch-angle coverage as a function of the magnetic field colatitude for the four fields of view of EPT. The range of μ-values scanned by each field of view lies within lines of the same colour. Each panel shows the coverage for a different magnetic field configuration, from top to bottom and from left to right: $\varphi_B = 30°$; $\varphi_B = 90°$; $\varphi_B = 140°$ and $\varphi_B = 270°$. On the other hand, in an homologous layout, Figure 5.9 shows the pitch-angle coverage as a function of the magnetic field azimuth for the four fields of view of EPT. Each

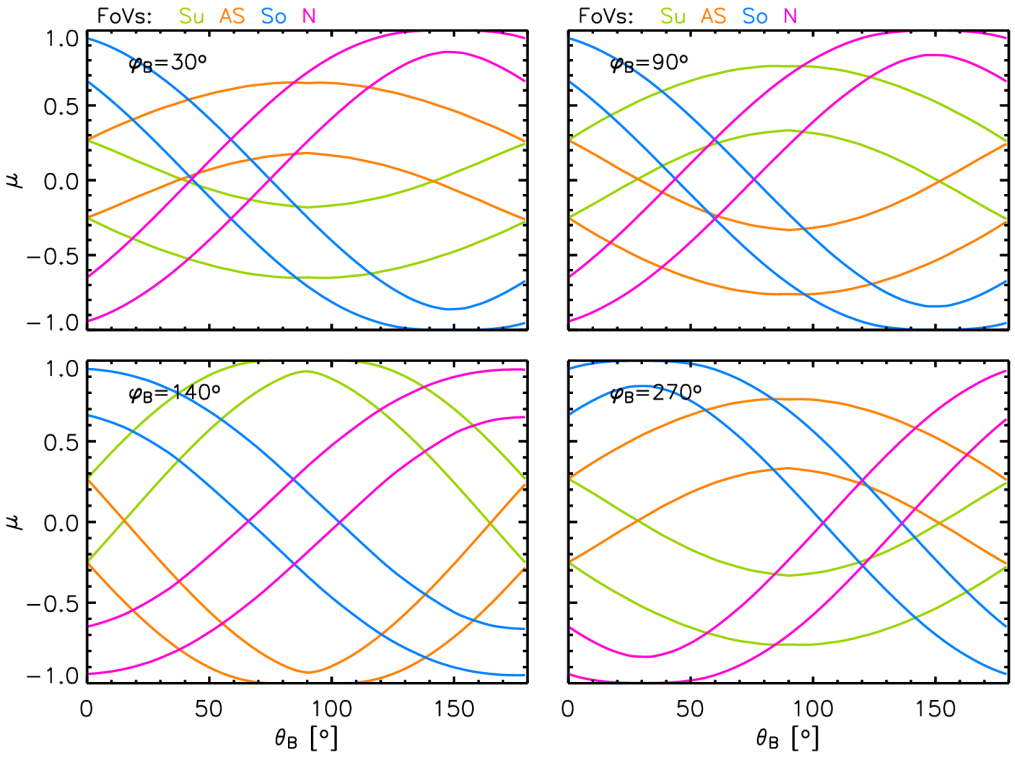

FIGURE 5.8: Pitch-angle coverage of EPT fields: maximum and minimum pitch-angle cosines detected by each field of view as a function of the magnetic field colatitude ($\theta_B = 90°$ means that the magnetic field is on the ecliptic plane) and for fixed values of the magnetic field azimuth angle, φ_B: 30° (top left), 90° (top right), 140° (bottom left) and 270° (bottom right).

panel shows the coverage for different values of the magnetic field colatitude, from top to bottom and from left to right: $\theta_B = 0°$; $\theta_B = 45°$; $\theta_B = 90°$ and $\theta_B = 135°$.

We note that the pitch-angle coverage is strongly dependent on the magnetic field configuration. The multiple configurations of μ-coverage drawn by the four fields of view can be described as follows: i) Only one μ-region covering a wide range of pitch angles, for instance, in the case of $\theta_B = 45°$ and $\varphi_B = 55°$, we found a μ-region defined by $\mu \in (-0.43, 0.43)$ (see top right panel of Fig. 5.9) and for $\theta_B = 105°$ and $\varphi_B = 270°$ we found $\mu \in (-0.77, 0.77)$ (see top right panel of Fig. 5.8). ii) Two μ-regions, where intermediate pitch-angle values are detected by two of the fields of view, as found, e.g., for $\theta_B = 140°$ and $\varphi_B = 140°$ we can see that the Sun and North field of views detect $\mu \in (0.45, 0.85)$ and the South and Anti-Sun, $\mu \in (-0.45, -0.85)$ (bottom left panel of Fig. 5.8). iii) A three μ-regions configuration, at around $\mu = 1$, $\mu = 0$ and $\mu = -1$, is also found for several cases, like $\theta_B = 45°$ and $\varphi_B = 240°$ (top right panel of Fig. 5.9). iv) And, four μ-regions, where the four fields of view scan different pitch-angles, like for $\theta_B = 135°$ and $\varphi_B = 90°$ (bottom right panel of Fig. 5.9), finding the coverage of the fields of view equally spread. This latter configuration seems to be given only in very specific scenarios, during transitions between the other three, as an intermediate situation when the magnetic field is not aligned with any of the telescopes.

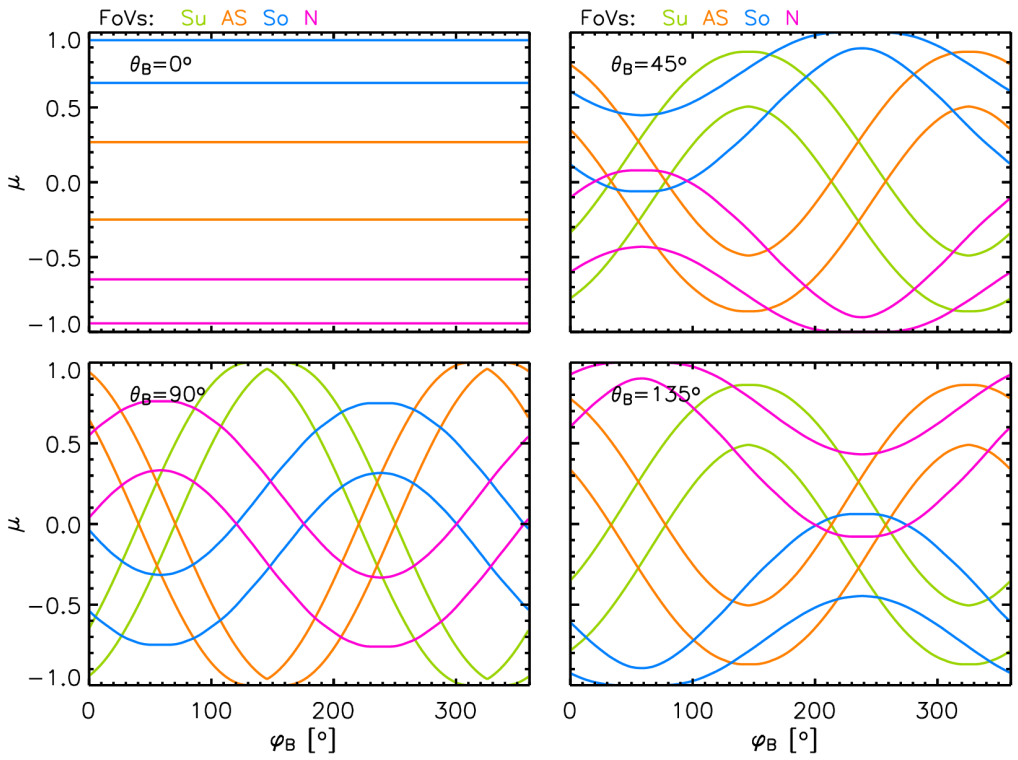

FIGURE 5.9: Same as Figure5.8 but as a function of the magnetic field azimuth ($\varphi_B = 0°$ means that IMF is pointing along the spacecraft-Sun line), and for fixed values of the magnetic field colatitude, θ_B: 0° (top left), 45° (top right), 90° (bottom left) and 135° (bottom right).

It is clear from these figures that, by construction, each pair of telescopes on the same axis scan pitch-angle cosine regions of opposite sign, in those instances where they do not coincide. We decided to continue studying how PADs would be observed by EPT by different configurations of the IMF, and leave for future work to determine the magnetic field directions yielding the larger coverage of μ. However, from Figures 5.8 and 5.9, we can see that the largest μ coverage is attained when the IMF points along the spacecraft-Sun line, $\theta_B = 90°$ and $\varphi_B = 0°$ (bottom left panel of Fig. 5.9).

5.3.2 Synthetic PADs observed by SolO/EPD/EPT

In this section, following the method developed in Chapter 4 (see Sect. 4.3.2.2), we study how a synthetic PAD would be observed by the four fields of view of EPT for different configurations of the local magnetic field vector. As explained in the previous chapter, we use the normalised PADs for three selected times (A, B and C; see Fig. 4.13) of the Green's functions of particle transport at 0.53 AU for two values of the radial mean free path, $\lambda_r = 0.25$ AU and $\lambda_r = 1.08$ AU, and a fourth case (D) to study the behaviour of the detector in front of bi-directional PADs.

Figure 5.10 and Figure 5.11 show the normalised synthetic PADs (black curves), the observations at the centre of each sector (coloured crosses) and the observed normalised intensity at the average pitch angle of each sector (coloured diamonds), assuming four different configurations

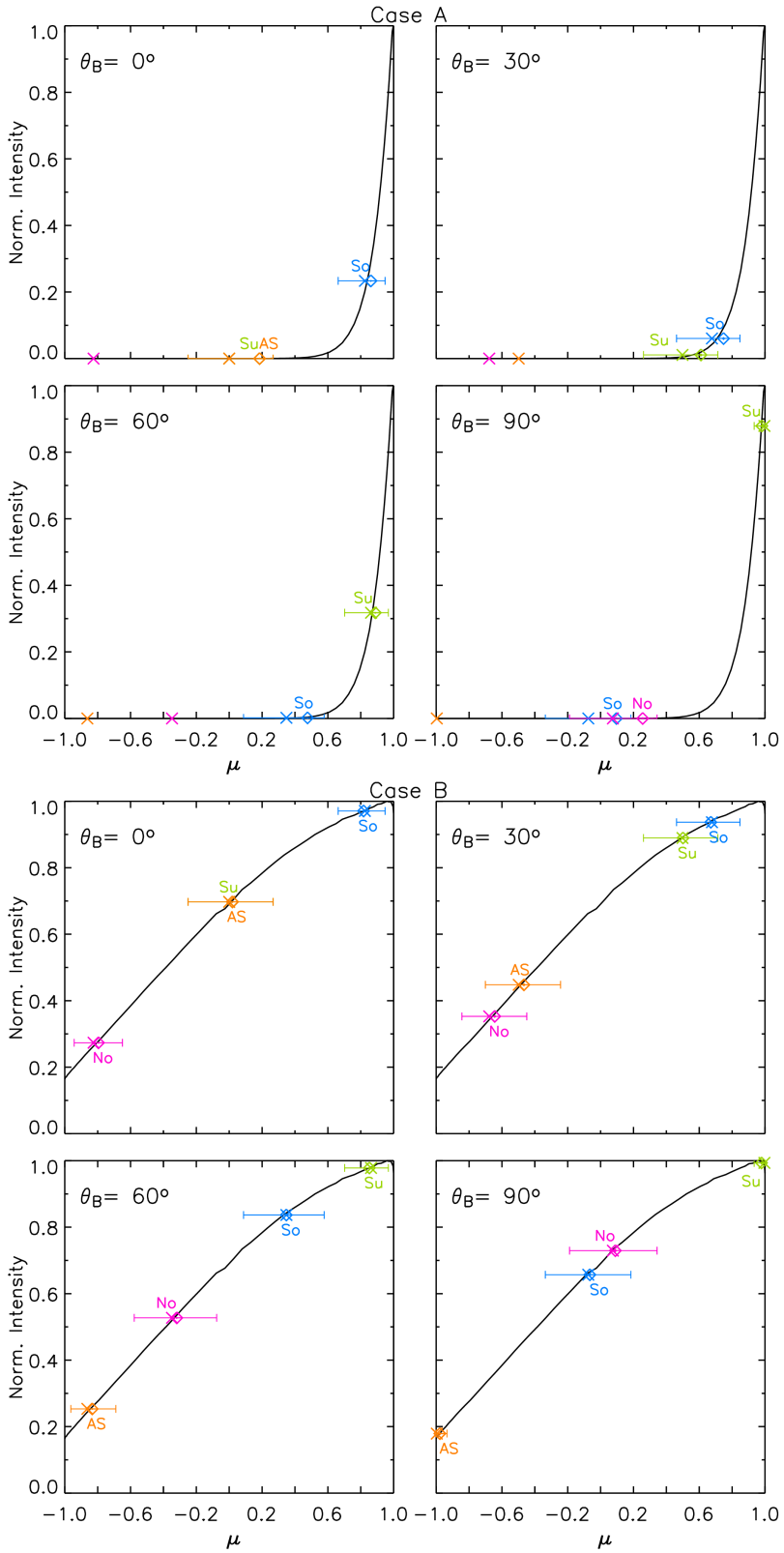

FIGURE 5.10: Intensities observed by the four EPT fields of view for two synthetic PADs (case A and case B, see Fig. 4.13) assuming different values of θ_B $0°, 30°, 60°, 90°$). Fields of view and the pitch angle range they observe (horizontal bars) are labelled in different colours (Su: Sun; AS: Anti-Sun; No: North; So: South). It is also indicated the pitch angle observed by the centre of each sector (crosses) and the average pitch angle measured within the range of each (diamonds).

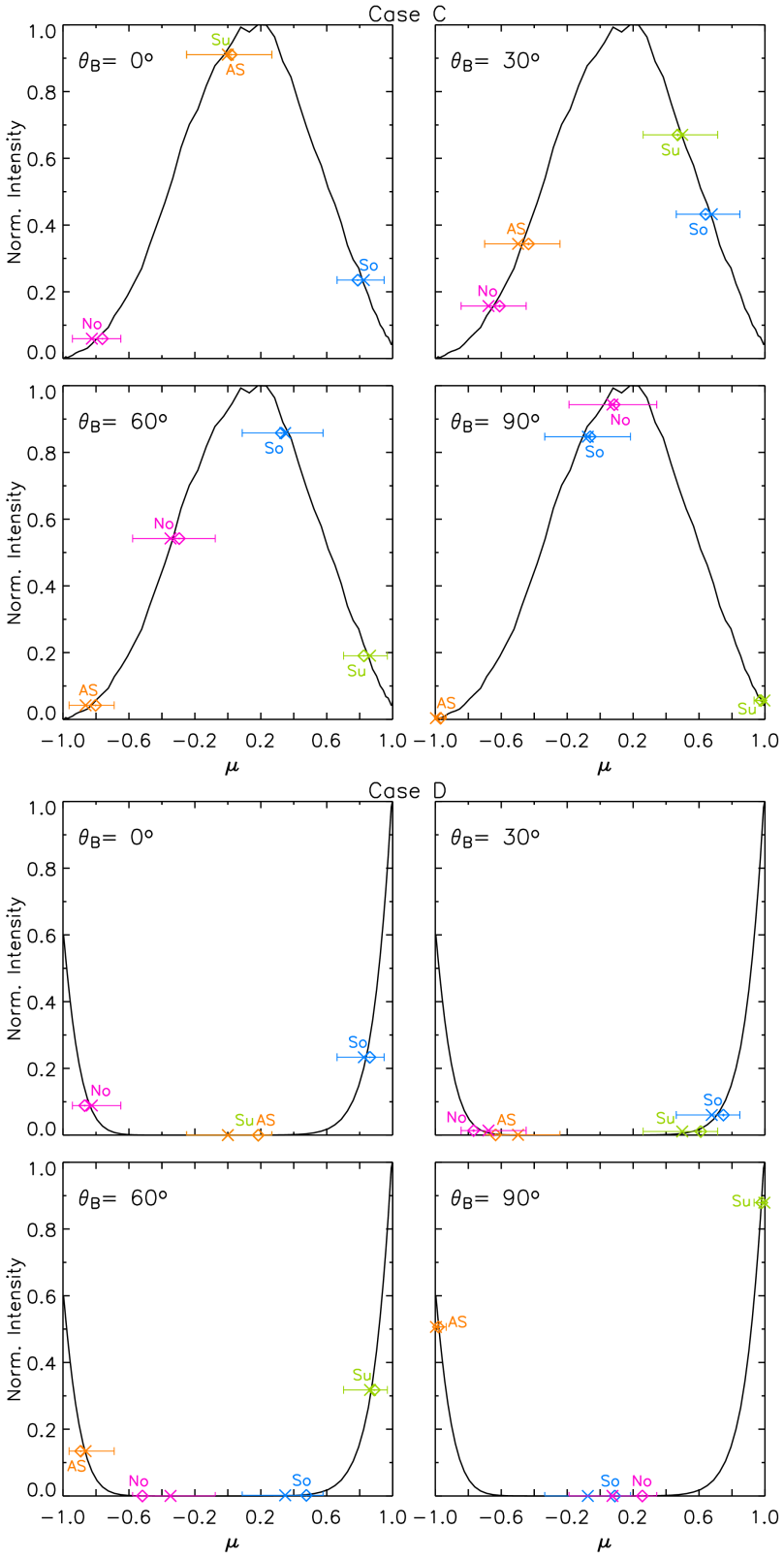

FIGURE 5.11: Same as in Figure 5.10 for case C, and D (see Fig. 4.13).

of the local magnetic field vector given by $\theta_B = 0°, 30°, 60°, 90°$. Figure 5.10 shows the PADs for case A (top) and case B (bottom). Figure 5.11 shows case C (top) and case D (bottom).

At a first glance, we can notice clear differences with the results we obtained for Helios/E6 (see Figs. 4.14 and 4.15). Firstly, we see that we are able to obtain PAD information for $\theta_B = 0°$ for every case, even better than for configurations of EPT with $\theta_B = 30°$ as we can recover a better reconstruction of the given PAD in the A, C and D cases; only for case B, where we have an smooth decay from 1 to -1, we would be able to reliably reconstruct the distribution for $\theta_B = 30°$. In case A, we obtain similar results as those yielded by Helios/E6 for $\theta_B = 60°$, slightly better for $\theta_B = 30°$ and for $\theta_B = 90°$, EPT better observes the PAD for $\mu \sim 1$, but it loses information about the decrease of the PAD. For case B, we can claim that all tested θ_B configurations, the distribution would be satisfactorily recovered, and in comparison to Helios/E6 performance, the configuration of EPT permits a better reconstruction of the PAD both for $\theta_B = 0°$ and $\theta_B = 30°$. In case C, EPT performs better than E6 for $\theta_B = 0°$ and $\theta_B = 90°$, where a closer value of the peak of the distribution is recovered. For $\theta_B = 60°$ slightly worse results are found but for $\theta_B = 30°$, Helios/E6 performs better. Finally, case D for EPT model gives, in general, slightly better results to those obtained for E6, being specially noticeable for $\theta_B = 0°$ where we recover part of the distribution, and for $\theta_B = 90°$, where the maximum of the distribution recovered is closer to the synthetic one.

We find that values of the pitch angle measured by the centre of the telescopes are very close to the actual values of the PADs, even if for some particular cases we can find a tiny underestimation of the anisotropy (case C). Further, the obtained values of the PADs as seen by SolO/EPD/EPT appear to be closer to the actual ones that those given by Helios/E6, with the only exception of the case C for $\theta_B = 30°$ and $\theta_B = 60°$, where EPT loses all the range around $\mu = 0$, and therefore, the peak of the distribution.

Hence, our conclusion is that SolO/EPD/EPT observations will provide a good coverage of the PADs in a majority of cases; thus, allowing the extraction of the PADs from its observations, despite that for several specific scenarios with high anisotropic PADs and magnetic field directions close to $\theta_B \sim 30°$ there is a clear risk of underestimating the anisotropy.

5.3.3 Modelling events as seen by SolO/EPD/EPT

We aim at studying the how SolO/EPD/EPT will measure PADs throughout the duration of actual SEP events. For this purpose, as mentioned at the beginning of Section 5.3, we selected three events seen by the Helios spacecraft that we modelled in the previous chapter, in order to simulate the PADs that SolO/EPD/EPT would have observed during those events at the position of the Helios spacecraft. Since pitch-angle information depends on the direction of the local magnetic field, we used the magnetic field observed by Helios/E2 to compute the pitch angles seen by Solar Orbiter.

Figure 5.12 shows the modelling results for the events on 1976 March 21 (left plot), 1980 May 28b (middle plot) and 1981 June 10 (right plot). For each case, the first panel shows the synthetic directional intensities seen by each field of view of SolO EPT (coloured curves) and the omnidirectional (black curve) intensities. The second panel shows the centre pitch-angle cosine (coloured dots) and range (yellow shadows) of the four fields of view. The third panel depicts the reconstructed synthetic intensity evolution for every pitch angle as modelled for EPT. Finally, the fourth and fifth panels show the magnetic field direction, colatitude and azimuth, in the RTN coordinate system measured by Helios/E2. Vertical lines across the panels mark for each event the times used for the study of the PAD found at the end of this section. Vertical blank spaces crossing the second and third panels are due to either magnetic field data gaps or to time steps longer than one minute in the original data which prevented to compute with higher frequency. Conversely, blank spaces that do not cross entirely both panels, and that often extend horizontally for periods longer than one minute, correspond to both μ-values (second panel) and pitch-angles (third panel) not observed by EPT. We can see that for these three cases, EPT has an overall good pitch-angle coverage during most of the duration of the events, even with different magnetic field configurations and sudden changes in the IMF direction, as seen in the event on 1976 March 21, where B_θ scans a wide range of values with several sharp changes. We qualify that the coverage is overall good for these events because the pitch-angle coverage for the peak intensity is good for the first two events, and for the last one, the pitch-angles observed permit to describe well the PADs (see discussion below). In addition, it is also interesting to notice that the four fields of view always allow us to recover at least two different pitch angle observations, and more commonly three or even four, when all of them are observing a different pitch angle. At the onset of the events, however, EPT would have missed the particles travelling more aligned with the IMF (i.e., $|\mu|$ 1) for the 1976 March 21 and 1980 May 28 b events.

Figure 5.13 shows the comparison between the previous results obtained for Helios/E6 in Chapter 4 and those obtained when modelling SolO/EPD/EPT for the same subset of events, given on 1976 March 21, 1980 May 28b and 1981 June 10. For each event and from top to bottom, the first panel shows the electron release at the Sun, showing (when needed) a smooth profile (black curve). Note that in these plots injections are not shifted +8 min (as those shown in Chapter 4), as there is no comparison with EM emissions at 1 AU. Second and third panels show, as modelled for Helios/E6, the intensity-time profiles, for sectored (coloured curves) and omnidirectional (black curve) intensities, and the intensity distribution (colour coded) as a function of the evolution of the pitch angle. Fourth and fifth panels show, as modelled for SolO/EPD/EPT, the directional intensity-time profiles for the four fields of view and omnidirectional (coloured and black curves as labelled) intensities, and the intensity intensity distribution (colour coded) as a function of the evolution of the pitch angle. Vertical lines across panels from second to fifth mark, for each event, the times used for the PAD study below. The sixth panel shows the computed anisotropy as given by the transport model (black curve), and as modelled using the

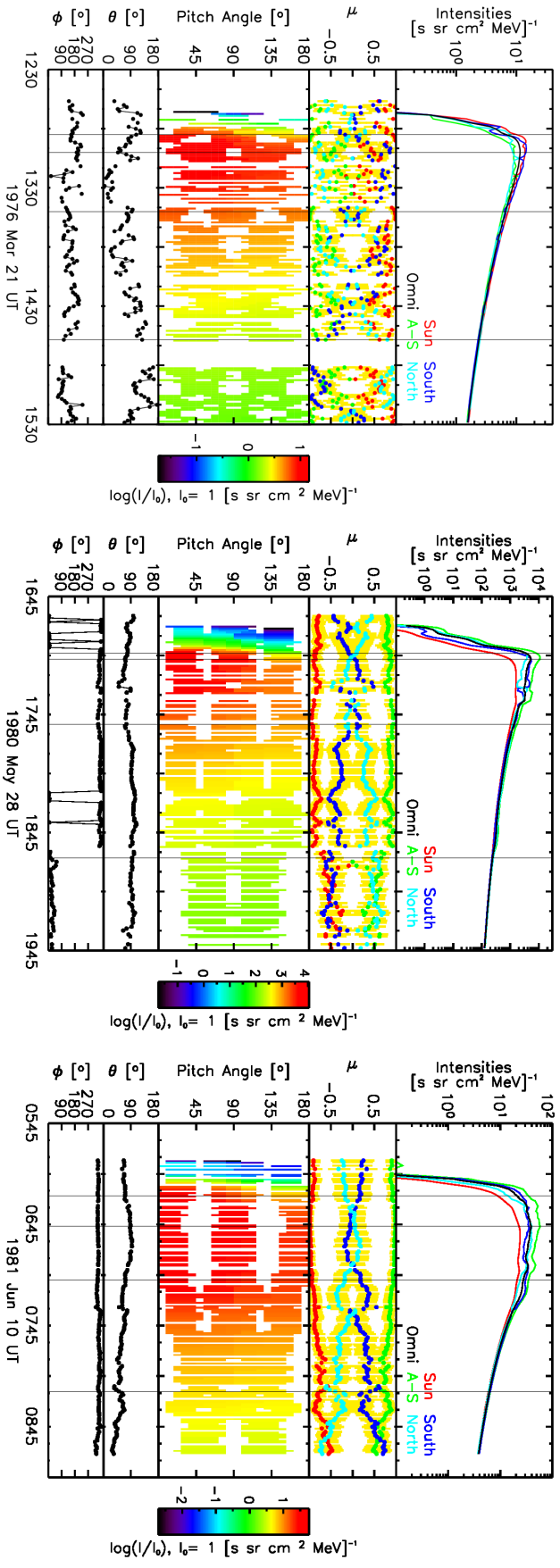

FIGURE 5.12: Results for three of the modelled events using SolO/EPD/EPT angular response: 1976 March 21, 1980 May 28b and 1981 June 10. From top to bottom panels: i) intensities as observed by each field of view (coloured curves) and omnidirectional intensity (black curve); ii) electron pitch-angle cosine as would be observed at the centre of each field of view (coloured dots) using the same colour code, and their ranges (yellow shadow); iii) pitch angle intensity-time diagram; iv) and v) magnetic field colatitude and azimuth angles in RTN spacecraft coordinate system. Vertical lines across panels denote the different times used for the PAD analysis.

angular response of SolO/EPD/EPT (red curve) and Helios/E6 (green curve). Finally, the seventh panel shows the magnetic field cartesian components of the magnetic field as measured by Helios/E2 in the SSE coordinate system.

From Figure 5.13, we can see that, with the method applied, we obtain for EPT similar intensity-time profiles as the profiles modelled for Helios/E6; the peak intensities attained for EPT show values comparable with those obtained for Helios/E6. Also, the pitch-angle coverage derived for EPT is good enough to trace properly the event and for the first event, the coverage is better than for Helios at the beginning of the decay phase, between 13:25 and 13:35 UT, where both detectors would observe around $\mu = 0$ but EPT shows a wider range even covering $\mu = \pm 1$ at some point. On the other hand, Helios/E6 shows better coverage most of the time, but EPT in fact is covering enough portion of the intensity distribution, in terms of different pitch-angles, to accurately describe the evolution of the event profile. Furthermore, regarding the anisotropy of the particle intensity distribution, both modelled instruments yield similar evolutions for the selected events, allowing us to claim that EPT observations will give reliable anisotropy data. Finally, we want to remark that these events where specially chosen during the study presented in Chapter 4 because they show good coverage for Helios/E6 instrument. This means that it is probable that many other events discarded from the E6 observations for not being good enough for the previous study, could have been used if observed by EPT, specially those where θ_B shows values far from the ecliptic plane, where Helios could no observe.

Finally, for each event, we started the analysis of the observed PADs by looking at the PADs obtained at the four times marked in Figures 5.12 and 5.13. Figure 5.14 shows the resulting PADs for the three events at the following times: close to the onset, that is, at the time when the half of the peak intensity is reached (indicated as 'Onset'), at the time of the peak intensity ('Peak'), at the early decay phase ('Decay') and late in decay phase ('End'). Normalised intensities are shown for Helios/E6 sectors (coloured crosses), SolO/EPD/EPT field of views (coloured diamonds) with the μ-range covered by each field of view (horizontal lines) and the PAD derived directly from the model (black dotted line). On top of each panel the maximum intensity observed by each detector is indicated, as used for the normalisation. For the inspected times, we can see that the four fields of view of EPT permit us to closely recover the modelled PAD (black curve), even for the more anisotropic distributions observed at the 'Onset' and at the 'Peak' times. The differences in the PADs observed by E6 and EPT at the peak intensity were due to the fact that Helios could not observe particles coming from 20° away of the ecliptic plane, so observed times (and intensities) of the peak intensity were different. When there was no time difference between peak intensity observations (as in event on 1980 May 28b), both PAD results were closer. Then, from the three events studied in this section we conclude that the four fields of view of EPT allow us to describe the observed PADs. In order to draw further conclusions on the reconstruction of PADs from EPT 'observations' we plan to extend the study to the other events in the sample and to other times in the intensity profiles.

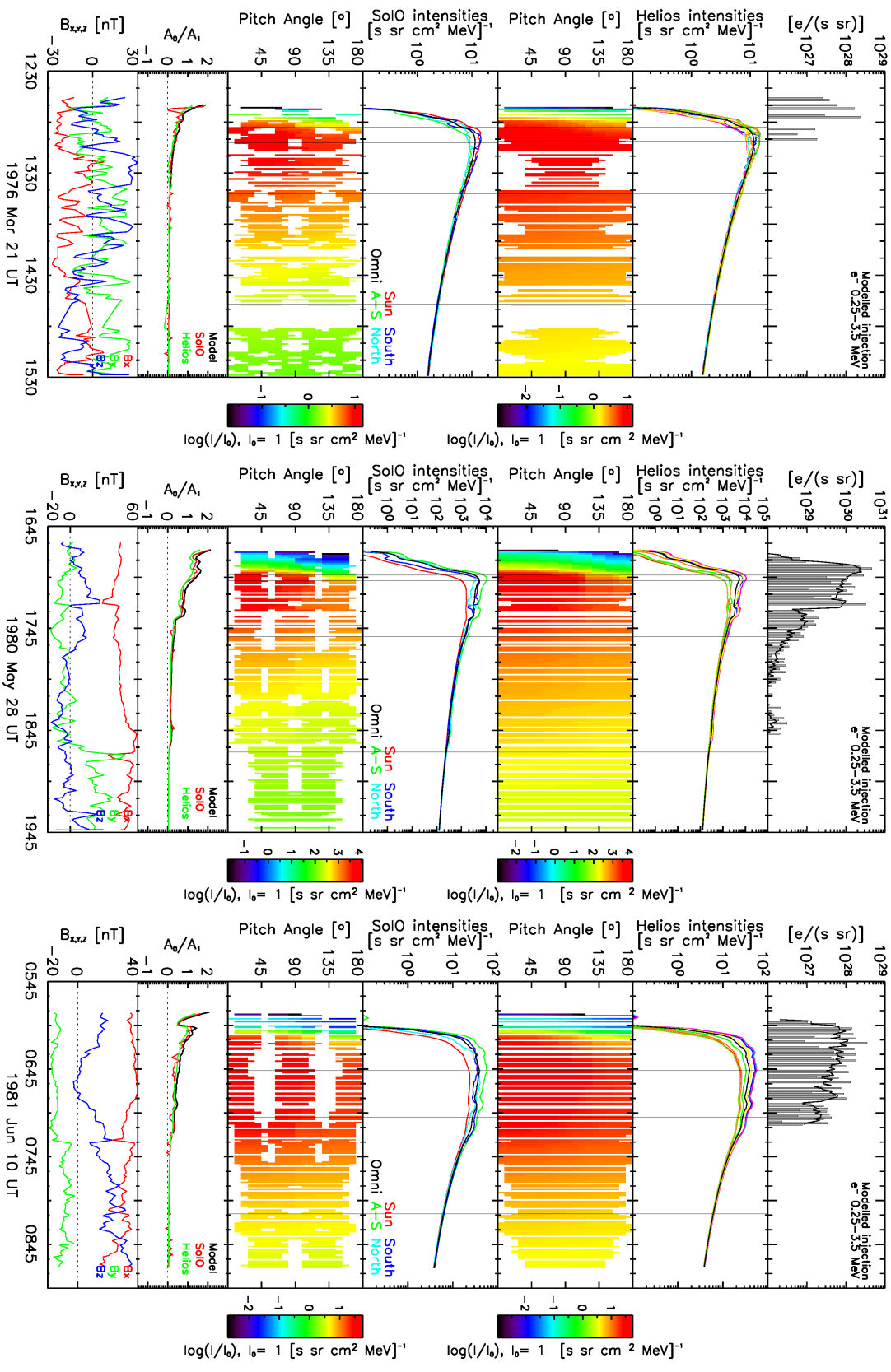

FIGURE 5.13: Comparison between results obtained for Helios/E6 and SolO/EPD/EPT for events on 1976 March 21, 1980 May 28b and 1981 June 10. Panels from top to bottom: i) histogram shows the inferred release time profile while black curve (when present) shows the result of the smoothness process; ii) electron intensity profiles modelled for E6, coloured curves indicate sectored profiles while black curve shows omnidirectional; iii) pitch-angle intensity evolution for E6 observations; iv) electron intensity profiles modelled for EPT, coloured curves indicate each field of view profile while black curve shows omnidirectional, as indicated in the labels; v) pitch-angle intensity evolution for EPT observations; vi) anisotropy as given by the model (black curve), as modelled for EPT (red curve) and as modelled for E6 (green curve); vii) magnetic field Cartesian components, Bx (red curve), By (green curve) and Bz (blue curve).

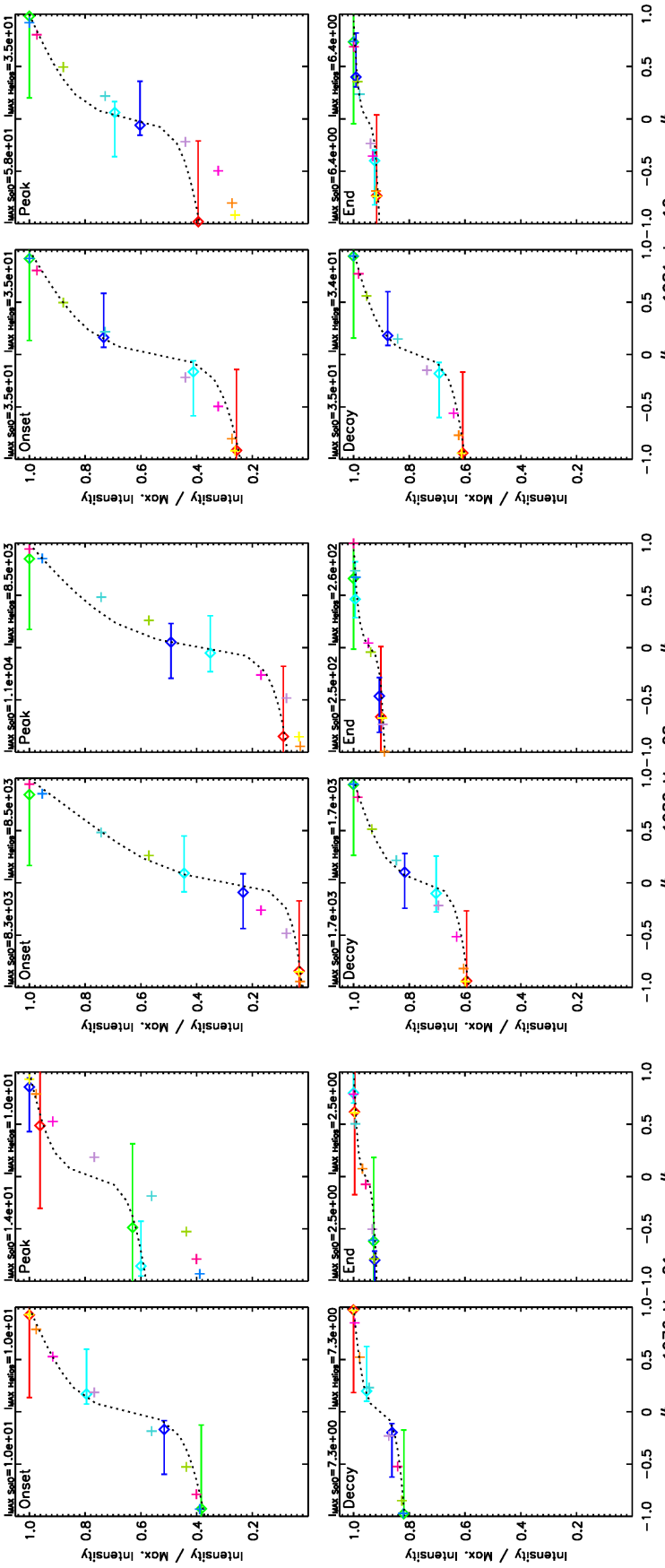

FIGURE 5.14: Normalised intensities vs. pitch-angle cosine observed by the four SolO/EPD/EPT fields of view (diamonds) and the eight Helios/E6 sectors (crosses) for the four times depicted at Figure 5.12 of each event. EPT fields of view also show the covered pitch-angle range (horizontal lines). Dotted black curve shows the Green's function modelled PAD from where both instrument measurements are extracted. On the top of each panel is shown the maximum intensity measured by each detector.

5.4 Solar Orbiter total mission fluence estimation

5.4.1 Introduction to the SEPEM interplanetary model

At the end of Chapter 2 we showed, for individual SEP events, that the method we developed to include the downstream fluence variation with the heliocentric radial distance introduces an event-to-event variation of the power-law dependences of the total fluence of the events with the radial distance (see also App. D). In this section, we made use of the SEPEM statistical SEP model for interplanetary missions to show the effect of the updates performed to the predictions of the SEPEM/SOLPENCO2 tool in the SOL2UP project, including the new treatment of the downstream fluence variation. During ESA's SOL2UP project, the SEP event categories were extended from six to ten and four new reference cases were modelled with SOLPENCO2. The modelling of these events was not part of this thesis work, but we mention here that the new cases modelled (see Type2c, Type3b and Type4a, in App. B), which include the largest events in the SREL list, provided new power-law radial dependences to the SEPEM statistical model both for the fluence and the peak intensities. However, as mentioned above, the method developed for the downstream fluence introduces more variability to the radial dependences on top of the variations provided by the ten reference cases. Hence, any changes observed in the results on the radial dependence of the SEPEM statistical model for interplanetary missions after applying the updates of SOL2UP are due to a combination of introducing more reference events and the new method for the downstream fluence contribution, being the latter more significant for the lower energies than for the high energies because of the larger values of the DTFRs for the lower proton energies found in Chapter 2. This effect can be appreciated in the radial dependences of the SEP events shown in Section 2.4.3 and in Appendix D.

The SEPEM statistical SEP model for interplanetary missions is available at the SEPEM application server[3] under the *'Away from 1 AU modelling'* menu, in the *'Creat models'* call. The model options are fully documented in (Crosby et al., 2015) and Jiggens et al. (2012) for the probability distribution functions options. Further information can be found in the SEPEM help pages at the right menu of the SEPEM server. For the simulations performed in this section we selected a cut-off power-law to describe the fluence probability distribution function and the Lévy distribution for both the waiting times and events duration (see Sect. 1.5). In the modelling performed in this section, we used two different mission orbits planned for Solar Orbiter: the orbit for the launch planned in October 2018 (CReMA 3.0 orbit from the Science Operations Centre of the mission, private communication R. Gómez-Herrero) and for the launch planned for February 2020 (CReMA 4.0 document referred in Sect. 5.1). From these mission orbit files, we used the daily heliocentric radial position of Solar Orbiter (date, time and distance in AU) as input to the SEPEM model. The relevant outputs provided by this SEPEM tool for the analysis presented in the next sections are the cumulative fluences for each of the SEPEM

[3] `http://www.sepem.eu/`

reference proton energy channels and for the whole mission durations at a 90% confidence level, and the cumulative fluence values over the different solar cycle phases encompassed by the mission orbits. The probability curves are generated for three different heliocentric radial distance scaling approaches:

i) 1 AU: no radial distance dependence is used, instead fluence computed at 1 AU for the events in the input event list are used;
ii) ECSS: the radial dependence recommended by the European Cooperations for Space Standardisation ECSS-E-ST-10-04C April 2008 Document is used, which means that there is no scaling applied for distances larger than 1 AU and a r^{-2} scaling law is used for distances < 1 AU. Therefore the fluences of all events in the list are scaled with the same radial dependence, and events observed closer to the Sun will substantially rise their fluence contribution to the mission total fluence in comparison to if they were observed at 1 AU;
iii) SEPEM: the radial dependences derived from SOLPENCO2 are used, whose new version includes the results of the study performed in Chapter 2. This scaling method entails an intermediate scaling, rising the fluence observed by the spacecraft at distances < 1 AU but with an overall weaker dependence than r^{-2}.

In the next sections, we present the comparison of the application of the SEPEM model results prior and after the updated radial dependences and the comparison of the results for the two mission orbits specified above.

5.4.2 Comparison of SEPEM model versions

For the simulations of this section we used the orbit planned for launch in October 2018 that encompassed three different solar cycle periods, two solar minima and one solar maximum, over more than nine years, finishing in 2028. This orbit was planned to have a large second aphelion over 1.4 AU, in order to conduct gravitational assistance manoeuvres using Mars gravitational attraction achieving a high-eccentricity orbit. On the other hand, the closest perihelion to the Sun was 0.28 AU. The simulations were performed using two different versions of the SEPEM RDSv2 due to the continuous update performed by ESA to the application server. The simulation with the radial dependences prior to the update done in this thesis and in the SOL2UP project uses the SEPEM RDSv2.0 with ten reference energy channels, covering the proton range from 5 – 200 MeV. In addition, the event list expands from January 1988 to December 2006 (both included), and for the 147 events in the list the fluence was calculated without subtracting the pre-event intensity levels. In contrast, the second simulation performed uses and extended version of the RDSv2.0, with eleven reference energy channels covering the proton energy range from 5 – 298 MeV. Also event list used as input to the statistical model, the SREL list (Table A.4), contains 172 events occurred between January 1998 and March 2013. For the events

in this list, a background subtraction was performed as described by Jiggens et al. (2018a). This data set without the background intensities is hereafter named, SEPEM RDSv2.2[4].

Figure 5.15 shows the cumulative fluence for the reference energy channel, 7.23 – 10.46 MeV, over the whole mission period for the 90% confidence level computed for the aforementioned mission orbit. In the top row are shown the results from the modelling using the old SEPEM/-SOLPENCO2 radial scaling laws prior to SOL2UP. In the bottom row the results for the updated radial dependences are displayed. Mission time is divided into the different solar cycle phases encompassed separated by black vertical lines: first solar minimum between the launch time and the beginning of 2020 (first blue column), solar maximum going from 2020 to the end of 2027 (red column) and a second solar minimum from 2027 to the end of the mission (second blue column). Furthermore, at each shows the heliocentric radial distance of the Solar Orbiter orbit (black curve), as indicated on the right vertical axis. Finally, the time-length for each period is depicted in years at the top inside part of each panel.

The comparison of the top with the bottom rows of Figure 5.15 for the 1 AU case (left column) and the ECSS case (right column) that has one fixed scaling law, allowed us to evaluate the effect of the different dataset used in the simulations. We can see that the fluence obtained for the RDSv2.2 data set (bottom row) is slightly smaller than the older version RDSv2.0 used (top row). Assuming that the events added in the event list (period 2010 – 2013) would not change significantly the cumulative fluence predicted by the model, we conclude that the smaller values obtained in the new version are due to the effect of the background subtraction (see also the discussion in Jiggens et al., 2018a), and to a lesser extend due to the further division of compound SEP events into individual enhancements in the SREL (Pacheco et al., 2017b). On the other hand, we noticed that for the SEPEM scaling method, the old version (top middle panel) yielded cumulative fluence values slightly smaller than for the 1 AU case (top left panel); however, for the updated radial distance scaling (SOL2UP version) the cumulative fluence values (bottom middle panel) are larger than the corresponding 1 AU value (bottom left panel). In addition, for the updated version, the cumulative fluence values found for the SEPEM scaling method are larger than for the previous version, meaning that the updated scaling SEPEM method provides a larger increase of the predicted fluences (with respect to 1 AU values) than the previous version. For the two simulations performed, the ECSS method predicts the larger values for the cumulative fluence. Hence, for this energy channel and with a 90% confidence level, we could conclude that with the SOL2UP updates, the SEPEM method for radial distance scaling of the SEP fluences predicts an overall radial dependence softer than the inverse squared law recommended by ECSS.

[4]Note that we applied another method for the background subtraction in order to compute the fluences, but the input values provided by us to the statistical model are the fluence values normalised to the values obtained at 1 AU, and hence we provided only the scaling factors to other radial distances; thus allowing the use of other methodologies for the treatment of data.

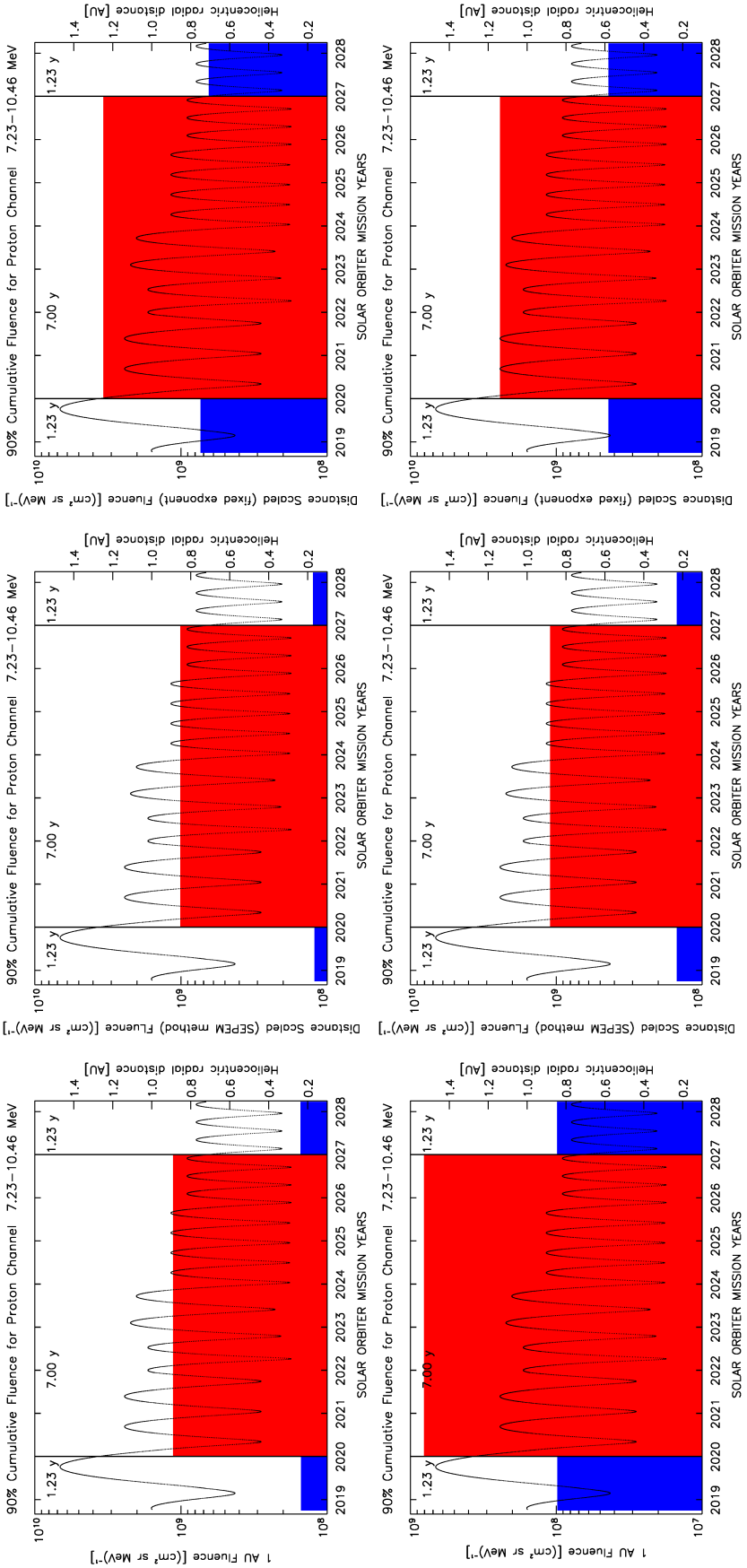

FIGURE 5.15: Mission total fluence for the Solar Orbiter planed orbit of 2018 modelled with the version of SEPEM prior to SOL2UP (upper row) and the updated approach (bottom row). Each column, from left to right, corresponds to different scaling approaches: 1 AU fluence model, SEPEM model and ECSS model.

Next we analysed the energy spectra of the cumulative fluence for the same confidence level (90%). For this, we extracted the corresponding values from the output files of the SEPEM tool, and fitted the energy spectra with a Weibull function, which is described by an exponential cut-off power law characterised as follows (Xapsos et al., 2000):

$$\frac{d\Phi}{dE} = \Phi_0 \, k \, \alpha \, E^{\alpha-1} \exp\left(-k \, E^{\alpha}\right), \tag{5.1}$$

where differential fluences, $\frac{d\Phi}{dE}$, are expressed in $\mathrm{cm}^{-2}\,\mathrm{MeV}^{-1}$ as a function of the energy, E, in MeV; the constants Φ_0, k and α are given by a non linear regression fit, where Φ_0 is indicating the event magnitude, expressed in cm^{-2}, and k and α give a measure of the spectrum hardness. The non-linear fittings are performed via a Levenberg-Marquardt least-squares fit method.

Figure 5.16 presents the cumulative proton fluence spectra results for the 90% confidence level for the ten energy channels of SEPEM RDSv2.0, computed using the non-updated version of the SEPEM server tool. Each panel displays the resulting energy spectra for each solar cycle period considered during the computed mission time: first solar minimum (top-left), solar maximum (top-right), second solar minimum (bottom-left) and the total mission length (bottom-right). For each period the fluence results for the three different radial distance scalings considered are shown: 1 AU (blue dots), ECSS (green dots) and SEPEM (orange dots). Furthermore, the resulting fittings to the energy spectra with the Weibull function (Eq. 5.1) are represented by solid lines following the same colour code. Figure 5.17 shows the same information but for the simulation performed with the SEPEM RDSv2.2 and the new updates done by SOL2UP project. In this case, the fitting of the energy spectra was performed for the ten first energy channels. We discarded the highest energy channel of SEPEM RDSv2.2 both for the sake of comparison with the previous RDSv2.0 and because this energy channel showed for some events intensity values below the background levels.

Table 5.5 shows the parameters of the fittings performed to the energy spectra of the total mission duration for the two simulations performed, prior ('Previous SEPEM model', see Fig. 5.16), and after the implementation of the SOL2UP updates ('Updated SEPEM model', see Fig. 5.17). For each radial dependence or scaling used, i.e., 1 AU, SEPEM method and ECSS, the results for the three fitted parameters (Φ_0, k and α) and the correlation coefficient (R^2) are listed. We can clearly see that as qualitatively shown in Figures 5.16 and 5.17, the performed fittings are accurate and give a very good result for the correlation coefficient.

We want to remark that the peculiar behaviour for the lower energies of the SEPEM radial scaling method, which provides fluences below those predicted by the 1 AU case in the simulation performed prior to the SOL2UP updates (see Fig. 5.16) is no longer found in the simulation including the SOL2UP radial dependence updates. The greater variation of radial dependences provided now by the SEPEM/SOLPENCO2 model, which are at the low-energies a result of the analysis performed in this thesis of the downstream fluence variation with the heliolongitude and

radial distance, yields predicted cumulative values within the 1 AU and ECSS radial distance approaches. Hence, by using the SEPEM method, the requirements for radiation protection for interplanetary missions could be softened. However, prior to this, the results that we find here should be validated with actual data covering the whole energy spectrum. Solar Orbiter itself will provide us with this opportunity.

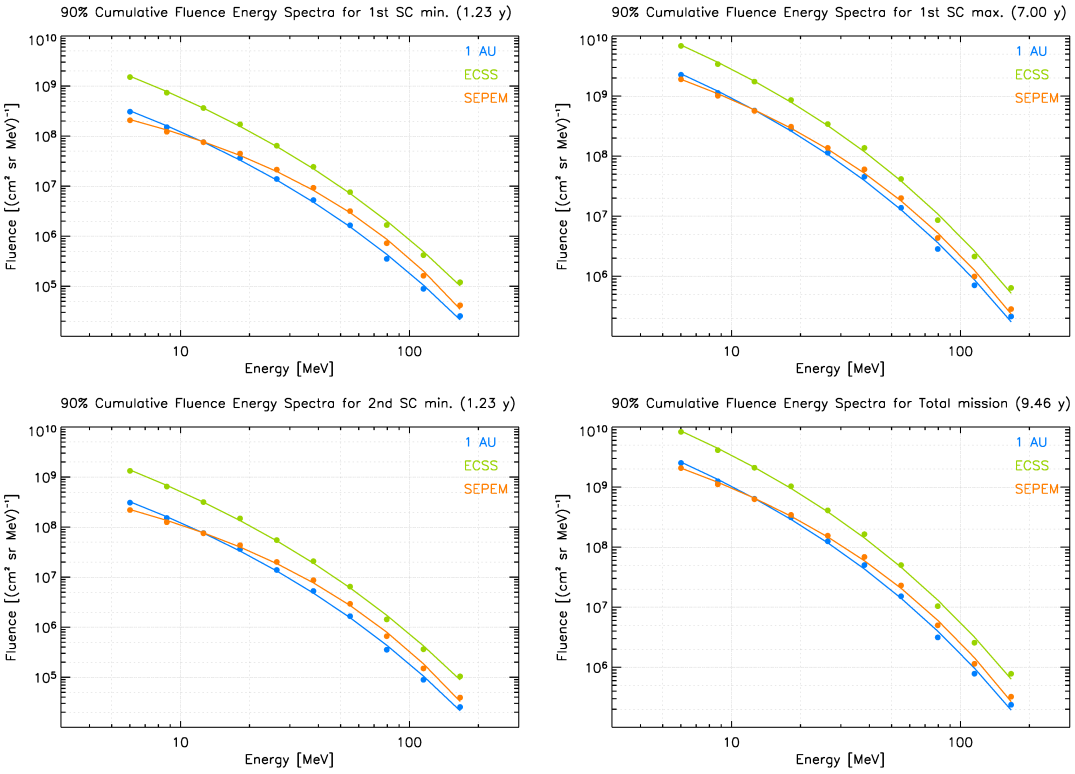

FIGURE 5.16: Mission cumulative fluence spectra for the Solar Orbiter planed orbit for October 2018 modelled with the non-updated version of SEPEM RDS 2.0. Each panel, from left to right and from up to bottom, shows the cumulative fluence spectra for different time periods: first solar minimum, first solar maximum, second solar minimum and the full mission length.

5.4.3 Mission orbit comparison

After using SEPEM server tools to compute cumulated fluence and the fluence energy spectra for the Solar Orbiter mission orbit planned for launch in October 2018, we applied the model to the current approved mission orbit planned for launch in February 2020. In contrast to the October 2018 orbit, the current orbit will manage to achieve similar orbital characteristics without needing Mars assistance, reason why Solar Orbiter will never go beyond the Earth's orbit distance. The shortest perihelion will also be at 0.28 AU. We provided the February 2020 orbit information as input to the SEPEM server tool *Away from 1 AU* and retrieved the cumulative fluence energy spectra for different confidence levels and periods. In this case we used only the version of the SEPEM statistical model for interplanetary missions updated with the SEPEM RDSv2.2 and the radial distance dependences from SOL2UP.

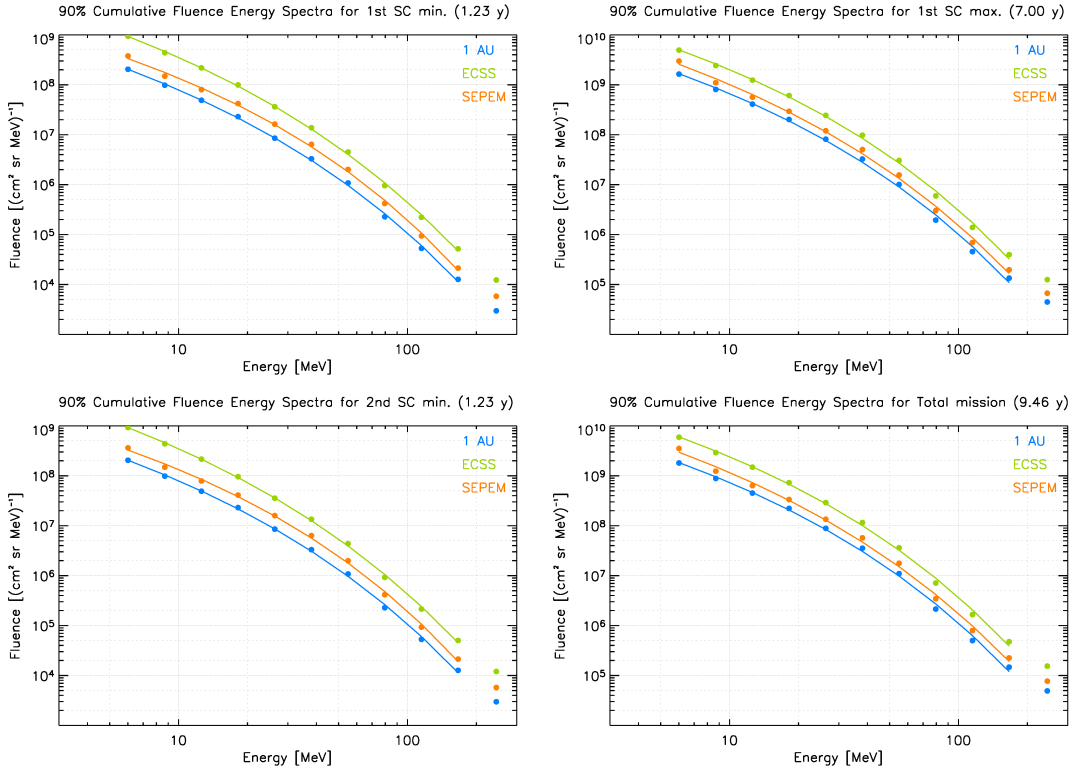

FIGURE 5.17: Same as in Figure 5.16 for the Solar Orbiter planed orbit for October 2018 modelled with the updated version of SEPEM, which provides fluences for 11 energy channels up to 289.2 MeV.

TABLE 5.5: Results of the spectra fittings for modelled cumulative fluences of ten energy channels of SEPEM for the orbit launch in October 2018 for the two simulations performed.

Solar Orbiter cumulated fluence for launch in October 2018 orbit				
Radial	**Previous SEPEM model**			
dependence	Φ_0 **[cm^{-2} sr^{-1}]**	**k [MeV$^{-\alpha}$]**	α	**R^2**
1 AU	2×10^{11}	1.4	0.39	0.998
SEPEM	8×10^{10}	0.7	0.49	0.998
ECSS (r^{-2})	8×10^{11}	1.4	0.39	0.9990
	Updated SEPEM model			
	Φ_0 **[cm^{-2} sr^{-1}]**	**k [MeV$^{-\alpha}$]**	α	**R^2**
1 AU	2×10^{11}	1.3	0.41	0.998
SEPEM	3×10^{11}	1.4	0.39	0.998
ECSS (r^{-2})	5×10^{11}	1.3	0.41	0.9990

Figure 5.18 shows the 90%-confidence cumulative fluence for the reference energy channel computed over the whole mission length, for the February 2020 orbit. Each panel follows the same structure as in Figure 5.15, but in this case the mission encompasses only two solar cycle phases: one solar maximum and one solar minimum. Among the three different radial distance scaling outputs, the lower fluences were attained by the 1 AU case and the highest by the ECSS

case. The SEPEM method showed intermediate values for the cumulative fluence. If we compare these results with the updated SEPEM version results for the orbit in October 2018 shown in Figure 5.15, we can see that the cumulative fluence for the solar cycle maximum periods are very similar for all radial scalings, even though the February 2020 orbit goes through a slightly shorter maximum period.

On the other hand, Figure 5.19 shows the 90%-confidence cumulative proton fluence spectra results, for the eleven energy channels of SEPEM RDSv2.2, following the same structure as in Figure 5.16, but for the February 2020 mission orbit. The energy spectra derived are shown for the solar maximum (left panel) and solar minimum (central panel) and for the full mission length (right panel). We find that the cumulative fluence values obtained for each radial scaling method both for the solar maximum phase and total mission length are similar to the corresponding values obtained for the October 2018 orbit. The values of the parameters of the fitting to the energy spectra for the February 2020 mission orbit are listed in Table 5.6. The comparison of the parameters obtained from the fitting of both orbits shows very similar values, which indicates that short stays in large radial distances as was planned for the October 2018 orbit, have little effect in the overall computed fluence. In addition, the comparison of the results for the worst case fluence spectra (not shown here) yielded also very similar values. This means that for missions with both similar total mission lengths and solar maximum phase durations, the probability of occurrence of the worst case event is very similar.

TABLE 5.6: Energy spectra fitting parameters for the February 2020 orbit.

Solar Orbiter cumulated fluence for the February 2020 orbit				
Radial	**Updated SEPEM model**			
dependence	$\mathbf{\Phi_0}$ **[cm^{-2} sr^{-1}]**	**k [MeV$^{-\alpha}$]**	α	$\mathbf{R^2}$
1 AU	2×10^{11}	1.3	0.4	0.998
SEPEM	3×10^{11}	1.4	0.39	0.998
ECSS (r^{-2})	5×10^{11}	1.3	0.41	0.9990

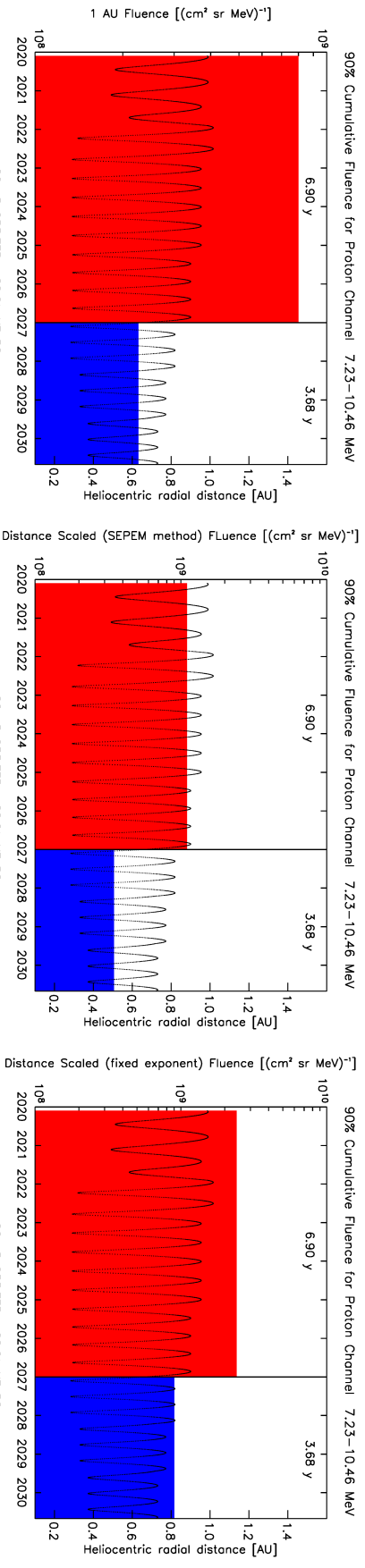

FIGURE 5.18: Same as in Figure 5.15 for the Solar Orbiter planed orbit for February 2020 modelled with the updated version of SEPEM. From left to right, each panel corresponds to: AU fluence model, SEPEM model and distance scaled as the ECSS model.

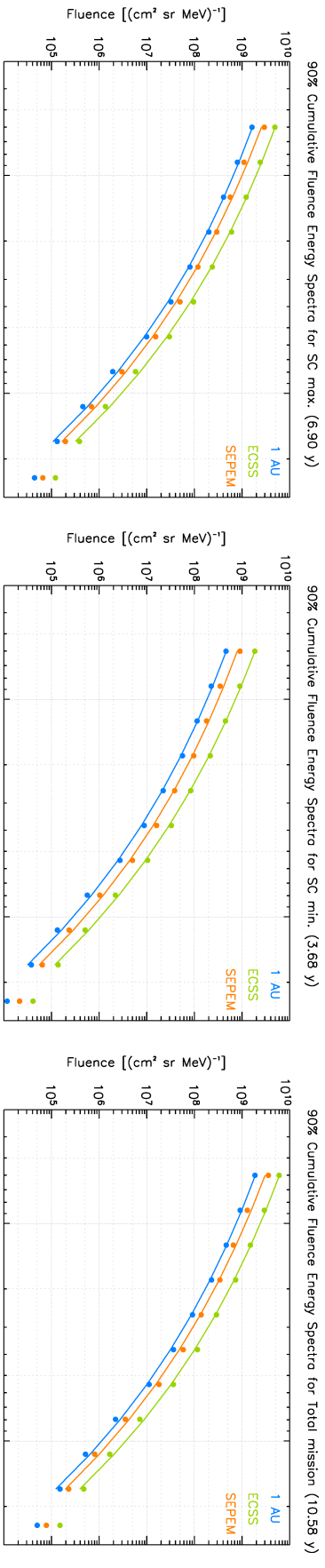

FIGURE 5.19: Same as in Figure 5.16 for the Solar Orbiter planed orbit for February 2020 modelled with the updated version of SEPEM. From left to right, each panel corresponds to: solar maximum, solar minimum, full mission length.

Chapter 6

Summary and future perspectives

6.1 Summary

Space weather is nowadays one of the main hazards for space missions and it is becoming an increasingly important field of study as manned missions flying out of the Earth's magnetosphere becomes a reality. Space weather effects over electronic devices have been proven to be an actual problem for space based observatories and probes travelling through the heliosphere. They are also the most restrictive factor to engage in interplanetary manned missions, as the high radiation doses typically found out of the protection of the Earth's magnetic field can easily cause severe health conditions.

The aim of this thesis was to improve the SEP prediction and modelling tools that will allow us to better comprehend the SEP radiation environment in the inner heliosphere. Through this work, we presented several improvements in pre-existing SEP events modelling tools. We performed a novel observational study of the contribution of the downstream fluence to the total fluence of large solar energetic proton events (Pacheco et al., 2017b), which improves the predictions of the heliocentric radial distance variation of the event fluence of the SEPEM/-SOLPENCO2 tool (Crosby et al., 2015, Aran et al., 2017a), and as a result it also improves the fluence estimates of the ESA's SEPEM statistical SEP model for interplanetary missions. We adapted SEPinversion (Agueda et al., 2012b) to study STEREO events (Pacheco et al., 2017a), as well as we developed a new methodology to take into account the energy and angular response of detectors on board Helios (Pacheco et al., 2019a) and the future Solar Orbiter. We obtained the angular response for the SolO/EPD/EPT telescope and performed, for the first time, a study on how EPT will observe the SEP pitch-angle distributions during actual SEP events (Pacheco et al., 2019b).

6.1.1 Analysis of the downstream fluence of gradual SEP events

- We analysed the post-shock fluence of gradual SEP events observed at the near-Earth space and those observed by STEREO mission during the period from 1988 to 2013 as well as the events detected by the Helios mission from 1975 to 1985, at heliocentric radial distances between 0.3 AU and 0.85 AU. For the 1 AU observations in the period from 2010-2013, we determined the solar source of the particles, that is, the parent solar eruptive phenomena (i.e., CME and flares) and the associated interplanetary shock passing by the spacecraft position, and hence, we updated the SEPEM radial dependent reference event list (SREL).

- We computed the downstream contribution to the total fluence for each of the selected events in the SREL list, the compiled STEREO event list and in the Helios event list. We determined the upstream (pre-shock), downstream (post-shock) and total fluences of the selected events, and created a software to automatically perform the necessary tasks, for the events in the SREL list.

- Afterwards, we performed a multi-spacecraft study of SEP events to determine whether there exists a variation of the downstream fluence of these SEP events with the heliolongitude of their parent solar source. From the eight pairs of events simultaneously detected by near-Earth spacecraft and by one of the STEREO spacecraft, we found that the downstream-to-total fluence ratios (DTFRs) do vary with the heliolongitude. Eastern events show higher DTFRs ratios than their western counterparts. Also, we found that the DTFRs decrease with the energy of the protons.

- The extension of the study to 168 events observed at 1 AU permitted us to quantify the variation of the DTFRs with the heliolongitude, by fitting polynomials to the moving mean values of these ratios. Moreover, the number of events observed by the Helios spacecraft at heliocentric radial distances between 0.3 AU and 0.85 AU that were suitable for the downstream fluence analysis is small, preventing any quantification of the DTFRs variation. However, the same trend is found as for the 1 AU data: eastern events tend to show higher DTFRs ratios than western events. On the other hand, we find that the mean DTFRs are roughly constant with the heliocentric radial distance (within errors). Consequently, we used the fits obtained from the better statistics gathered from 1 AU observations to determine the evolution of the downstream-to-total fluence ratios with the heliolongitude.

- Furthermore, since SOLPENCO2 provides predictions for spacecraft located at different radial distances but along the same IMF line, we could translate the variation in heliolongitude (provided by the curvature of the IMF line) of these spacecraft to a radial variation of the DFTRs. Therefore, we used the polynomial fits derived from 1 AU to characterise

the variation of the DTFRs for the virtual observers located at other radial distances. We assumed that the polynomial fits derived represent the "Average Variation" with heliolongitude, and applied the same tendency for all events in SREL, starting from the observed DTFR value at the observed heliolongitude.

- Finally, after the implementation of the DTFRs to the calculation of the total fluences of the events in SREL into the SEPEM/SOLPENCO2 tool, the resulting radial dependences of the total fluences vary from event to event thanks to the contribution of the downstream fluence modelled in this work. We have shown that strong positive radial dependences of the total fluence provided previously by SOLPENCO2 for eastern events are now softened. The same is true for the largest events in SREL.

6.1.2 Electron events observed over a narrow range of heliolongitudes

- We studied the characteristics of two impulsive near-relativistic events observed by the STEREO mission on 2014 August 1 with few hours of delay when both spacecraft presented a longitudinal separation of only 34°. We adapted the SEPinversion software to use SEPT data directly and we modelled the observations in order to explain the significant differences in the intensities measured by both spacecraft. STEREO B was better magnetically connected to the solar source of the particles but it observed lower electron intensities while STEREO A had a worse connection but it measured a factor ∼5 higher peak intensity (Klassen et al., 2016). We also compared the type III radio burst observed by the two spacecraft with the electron intensity onsets at the spacecraft and found that even though STEREO B was better connected and the type III bursts were detected at the same time by both spacecraft, STEREO A measured an earlier onset for the electron event. Furthermore, we found clear differences on the evolution of the PADs and the fact that STEREO A was inside a slow solar wind stream but STEREO B was in a fast solar wind stream.

- For each event, we inferred the electron injection-time profile at the Sun and the electron mean-free path that best fitted the data. The timing of the inferred injection profiles matched with the type III radio emission observed at the Sun. We found values of the mean free path for STEREO A of $\lambda_r = 0.31$ AU for Event I and $\lambda_r = 0.37$ AU for Event II, and STEREO B of $\lambda_r = 0.10$ AU for Event I and $\lambda_r = 0.06$ AU for Event II. These differences in the transport conditions of electrons as well as the difference in the injection profiles are enough to explain the onset delay as well as anisotropy and peak intensity differences between both observations. We conclude that interplanetary transport conditions can differ significantly changes even for very close heliolongitudes and specially for different solar wind streams.

6.1.3 Electron events observed by Helios in the inner (< 1 AU) heliosphere.

- We developed a full inversion method to study relativistic electron events observed by the Helios mission. For that purpose we modelled of the angular response of the E6 sectors and the energetic response of the E03 channel of the instrument. The method consisted on an inversion procedure of the original Helios electron data taking into account both responses, angular and energetic, to disentangle the release-time history at the Sun and the transport conditions of the particles along the IMF, characterised by the mean electron free path.

- We examined Helios data for the whole mission period and gathered a list of fifteen impulsive electron events which fulfilled the selection criteria. We scanned the literature to determine the events' solar sources and the associated EM emissions. We computed the Green's functions for the interplanetary transport of relativistic electrons, which do not suffer from adiabatic deceleration, taking into account the different transport scenarios and applied them to the energy response of E03 channel to build the Green's function of the channel for each specific case. This full inversion method allowed us to infer the release-time history and the mean free path for each event. We obtained the electron injection profile and the mean free path that best fitted the observations for each event on the list, with values of $\lambda_{\parallel}$ between 0.02 AU and 0.27 AU. These values suggest a predominance (ten cases out of fifteen) of weak-focused transport ($0.1 < \lambda_{\parallel}/L < 1$) for the studied events. Four events presented focused transport($\lambda_{\parallel}/L \geq 1$) while only one showed values of the mean free path in the diffusive transport regime ($\lambda_{\parallel}/L \leq 0.1$). These results were in agreement with those found in the literature (Kallenrode et al., 1992b, Kallenrode, 1993b, Agueda and Lario, 2016). With respect to the inferred injection profiles, we found two groups regarding the injection duration: for ten events the injection lasted more than 30 min and for five events it was shorter than that. The recovered injections matched with the duration of the EM observations for each event.

- We looked for an explanation for the long-lasting injection profiles and found that either coronal CME-driven shocks and magnetic structures in the corona trapping electrons and allowing a gradual leakage of particle could justify the observations (Klein et al., 2010, Dresing et al., 2018). We found no dependence of the radial mean free path with the helioradial distance of the observer. We found that strongly diffusive events observed by Helios at small radial distances would not be observable at 1 AU. These results point towards the necessity of having pitch-angle distribution data from multi-spacecraft observations at different radial distances to study in further detail the radial and longitudinal dependences of the particle transport.

6.1.4 Applications to Solar Orbiter

6.1.4.1 Radial dependences

- We studied the radial dependences of the electron peak intensities and anisotropies in the inner heliosphere, in the range from 0.31 AU to 0.94 AU, for nine of the fifteen events observed by Helios and modelled in the previous chapter. We used the inferred injection-time profiles and convoluted them with the Green's functions for each helioradial distance. We computed the peak intensities and the anisotropy at the peak for each distance and used the power law function $f(r) = b \cdot r^{-\alpha}$ to fit these values along the radial distance. We recovered fits with correlation coefficients close to 1 and small error values for the α parameter for all of the peak intensities and most of the fitted anisotropies, except for the event on 1980 April 5 which was studied with a resolution of only 15 min instead of 1 min. Hence, we claim that radial decay of electron peak intensities can be explained by a power law.

- We compared the obtained values of α with the corresponding mean free path of the events and found no correlation. Then we contrasted the α values with the duration of the most intense injection (all those values showing at least 10% intensity of the maximum injection) finding a significant correlation between both parameters. We also concluded that the duration of the injection was a key factor in order to explain the radial dependence of the peak intensity of the events. For most of the events in the sample, the power law function was able to explain the anisotropy dependences for a wide range of distances in the inner heliosphere (0.3 – 1.0 AU). However, if values extrapolated towards smaller radial distances, some of the anisotropies would exceed the physical range (i.e., > 3). Thus, a power-law cannot be used to extrapolate the values of the anisotropy at the peak intensity time for small radial distances such as the Solar Orbiter and Parker Solar Probe perihelia.

6.1.4.2 EPD PAD modelling

- We modelled the angular response of the EPT instrument that will fly on board Solar Orbiter and studied the pitch-angle coverage of the instrument during different synthetic observational scenarios regarding the local IMF.

- We applied the obtained response to three of the modelled events shown in Chapter 4 to get the measurements of the pitch-angle distributions that Solar Orbiter would have observed. We found that, in general, Solar Orbiter will will be able to provide comparable pitch-angle coverage to Helios for those events for which particles arrive through an IMF close to the ecliptic plane. For events occurring during periods when the IMF is out of that plane, Solar Orbiter is expected to provide significant better coverage.

6.1.4.3 Solar Orbiter total mission fluence estimation

- We used the SEPEM server tool *Away from 1 AU* to compute the expected fluence that Solar Orbiter will receive during its mission. For that purpose, we provided with the details of the planned orbit with launch date in October 2018 to compute the cumulated fluence for the whole mission. The tool returns the results of the cumulative fluence at different confidence levels for three different heliocentric radial distance scalings: 1 AU, ECSS and SEPEM method that includes the predictions from the SOLPENCO2 tool.

- We ran the computation for the version of SEPEM prior to the implementation of SOL2UP project results (explained in Chap. 2), and the updated version with the new radial dependences for the SEPEM method. We compared the results between them and found slightly higher cumulative fluence for the updated SEPEM method, but lower fluences for 1 AU and ECSS dependences. On the other hand, when analysing the energy spectra, we found that the results for the model before the update showed values for the SEPEM method below those produced by the 1 AU case for the lower energies. On contrary, the updated model presented consistent spectra for all energies, being the values of the SEPEM method between the fluences determined at 1 AU and ECSS dependence. We concluded that the standard inverse square-law assumption (ECSS model) overestimates the cumulative fluence and hence, the use of SEPEM method to compute the shielding needed for space missions will imply a reduction in the costs. However, a validation of these results should be performed to establish firm conclusions.

- We also provided SEPEM server tool with the current planned orbit with launch on 2020 February for Solar Orbiter. We compared the previous examined orbit results of 90% confident cumulative fluences and worst case scenario fluences with the results obtained for this orbit. We found almost equal results for the cumulative fluences and worst case scenario of both orbits as well as equivalent energy spectra, taking into account that the new orbit will only span over one maximum and one minimum period with a total of 10.56 years, instead of two minimums and one maximum as the orbit planned for launch on 2018 October with a total extent of 9.46 years.

6.2 Future perspectives

There are still many open issues in the field of SEP events we hope to address in a near future. Among these, we consider several interesting improvements we could already work on:

- To model the angular response of other Solar Orbiter particle instruments: HET, STEP and SIS. This would allow us to provide an analogue comparison of the pitch-angle coverage

of these instruments as already performed for EPT. We would then be ready for analysing the scientific data as soon as it is available.

- To model the angular response of the Parker Solar Probe particle instruments and compare the pitch-angle coverages of them with previous modelled instruments, in order to aid the analysis and interpretation of the scientific data.
- To extend the list of events observed by STEREO and Helios and model them with the developed inversion software, in order to gather an extensive list of results for the injection profiles and mean free paths.
- To implement a filtering algorithm, as a wavelet-based trend filtering, to de-noise the PADs and study the effect of noise on the modelling, comparing previous results of modelled events, specially injection profiles, with those obtained from the filtered data.
- To apply the transport model developed by Agueda (2008) to construct a grid of Green's functions of interplanetary transport of electrons for different radial distances and solar wind conditions that allow us to study the events observed by Solar Orbiter and Parker Solar Probe.
- To model the energy response of the particle instruments on board STEREO, Solar Orbiter, Parker Solar Probe and any other mission for which we could obtain data able to be used in the inversion software developed.
- To use the SEPEM tool *Away from 1 AU* to study the cumulative fluence and worst case scenario fluence for other interplanetary missions like for Helios, which we are currently working on, and current missions such as BepiColombo. Solar Orbiter will also provide us with a good opportunity to validate the model results.
- To apply the radial dependences modelled for SEPEM to new statistical models and compare the different results obtained.
- To enlarge the SEPEM RDS event list used to study the radial dependences with older events (1975 – 1988) and new ones up to now (2013 – 2019).

On the other hand, there are several possible studies that have not been possible so far, either because they demand longer time periods or because of the fact that the data needed to proceed with it is still unavailable, such as:

- To carry out more multi-spacecraft studies, using data from Parker Solar Probe, Solar Orbiter, STEREO and other available missions to study the radial and longitudinal dependences of the SEP transport characteristics.
- To improve the angular response modelling of the instruments using a new anisotropic approach for the incoming particle population.
- To improve the MHD model currently used on SEPEM server to describe interplanetary shocks.
- To develop a new 3-D transport model of SEPs taking into account other transport processes such as perpendicular diffusion.

Appendix A

SOL2UP event tables

A.1 Tables for events between 2010-2013

In this section we show the list of multi-spacecraft events observed by near Earth spacecraft (Table A.1), by STEREO-A (Table A.2) and by STEREO-B (Table A.3).

In each of these tables the following information is listed. The first column gives the event number starting from August 2010. When a event can be split into different SEP events (also called SEP enhancements), the individual events are differentiated with letters (a, b, c....). The second and third columns give the date and time of each SEP event enhancement. Next, the fourth, fifth and sixth columns give the latitude, longitude of the associated flare (as seen by the corresponding spacecraft) and the X-ray start date and time, respectively. The seventh column shows the time of the shock passage by the ACE spacecraft; in the cases where a shock was not identified this column has been left empty. The eight column shows the solar wind type ('fast' or 'slow'), or the solar wind speed for the STEREO spacecraft. The ninth column indicates if the event has been included in the analysis of the downstream fluence (see next section), and finally the tenth column gives the X-ray flare class. As mentioned in Chapter 2, we established the association of the SEP events with their solar eruptive source. We further checked these associations against the already published studies (Lario et al., 2013, Richardson et al., 2014, Rouillard et al., 2012, Baker et al., 2013, Gómez-Herrero et al., 2015). Authors in SOL2UP: D. Pacheco, A. Aran, N. Agueda.

TABLE A.1: SREL list for events between 2010 – 2013.

Near-Earth observations - SEPEM data									
Event	**Start time [UT]**	**End time [UT]**	**Lat. (N+/S-)**	**Lon. (W+/E-)**	**Flare time [UT]**	**Shock time [UT]**	**Solar wind type**	**Downst. analysis**	**Flare class**
1-a	14/08/2010 10:20	15/08/2010 11:50	12	56	14/08/2010 09:38		slow	N	C4.4
2-a	18/08/2010 06:00	19/08/2010 11:55	18	88	18/08/2010 04:45		slow	N	C4.5
3-a	07/03/2011 20:10	13/03/2011 18:00	30	48	07/03/2011 19:43	10/03/2011 05:45	slow	Y	M3.7
4-a	21/03/2011 02:30	23/03/2011 12:00	16	130	21/03/2011 02:15		slow	N	B3.5
5-a	05/06/2011 16:00	07/06/2011 06:15	-16	145	04/06/2011 21:45	07/06/2011 09:14	slow	N	B2.7
5-b	07/06/2011 06:15	14/06/2011 06:15	-22	53	07/06/2011 06:15	10/06/2011 08:11	slow	Y	M2.5
5-c	14/06/2011 06:15	19/06/2011 19:00	19	-76	14/06/2011 04:45	17/06/2011 02:05	fast	Y	Z0.0
6-a	04/08/2011 04:34	08/08/2011 16:00	16	38	04/08/2011 03:40	05/08/2011 18:40	slow	Y	M9.3
7-a	09/08/2011 07:59	11/08/2011 14:00	14	69	09/08/2011 07:47		fast	N	X6.9
8-a	06/09/2011 23:15	10/09/2011 14:00	14	18	06/09/2011 22:12	09/09/2011 11:48	slow	Y	X2.1
9-a	22/09/2011 10:32	25/09/2011 11:12	9	-89	22/09/2011 10:29	25/09/2011 10:46	slow	N	X1.4
9-b	25/09/2011 11:12	01/10/2011 18:00	10	-56	24/09/2011 12:33	26/09/2011 11:44	slow	N	M7.1
10-a	22/10/2011 10:30	26/10/2011 16:00	27	87	22/10/2011 10:00	24/10/2011 17:49	slow	Y	M1.3
11-a	03/11/2011 22:25	06/11/2011 16:00	3	-152	03/11/2011 22:16		slow	N	M4.7
12-a	26/11/2011 07:30	30/11/2011 15:00	11	47	26/11/2011 06:09	28/11/2011 21:00	slow	Y	C1.2
13-a	19/01/2012 14:39	23/01/2012 04:00	32	-27	19/01/2012 13:43	22/01/2012 05:33	slow	Y	M3.2
13-b	23/01/2012 04:00	27/01/2012 18:00	33	21	23/01/2012 03:38	24/01/2012 14:40	slow	Y	M8.7
13-c	27/01/2012 18:00	04/02/2012 00:00	33	85	27/01/2012 17:37	30/01/2012 15:43	slow	Y	X1.7
14-a	24/02/2012 19:00	29/02/2012 00:00	10	-88	24/02/2012 00:45	26/02/2012 21:07	slow	Y	B4.5
15-a	05/03/2012 03:00	06/03/2012 23:30	19	-58	05/03/2012 02:30	07/03/2012 03:28	slow	N	X1.1
15-b	06/03/2012 23:30	13/03/2012 16:30	18	-31	07/03/2012 00:02	08/03/2012 10:53	slow	Y	X5.4
15-c	13/03/2012 16:30	18/03/2012 03:00	17	66	13/03/2012 17:12	15/03/2012 12:42	fast	Y	M7.9
16-a	17/05/2012 02:05	21/05/2012 17:00	7	88	17/05/2012 01:25	20/05/2012 01:20	slow	Y	M5.1
17-a	26/05/2012 21:00	30/05/2012 20:00	16	122	26/05/2012 20:46		slow	N	B3.6
18-a	14/06/2012 14:19	18/06/2012 10:00	-19	-6	14/06/2012 12:51	16/06/2012 19:34	slow	Y	M1.9
19-a	06/07/2012 23:35	08/07/2012 16:59	-13	59	06/07/2012 23:01		slow	N	X1.1
19-b	08/07/2012 16:59	11/07/2012 14:00	-14	86	08/07/2012 16:23		slow	N	M6.9
20-a	12/07/2012 17:05	16/07/2012 15:00	-13	3	12/07/2012 15:36	14/07/2012 17:39	slow	Y	X1.4
21-a	17/07/2012 13:59	19/07/2012 04:30	-15	88	17/07/2012 12:02		slow	N	M1.7
21-b	19/07/2012 04:30	23/07/2012 02:30	-13	88	19/07/2012 04:16	20/07/2012 04:00	slow	Y	M7.7
21-c	23/07/2012 02:30	26/07/2012 18:00	2	125	23/07/2012 02:35		slow	N	
22-a	01/09/2012 00:00	06/09/2012 16:00	-19	-42	31/08/2012 19:59	03/09/2012 11:21	slow	Y	C8.4
23-a	28/09/2012 00:20	02/10/2012 08:00	9	32	27/09/2012 23:35	30/09/2012 22:18	slow	Y	C3.7
24-a	14/12/2012 12:20	17/12/2012 18:00				16/12/2012 16:50	slow	N	
25-a	15/03/2013 18:45	18/03/2013 19:59	9	-6	15/03/2013 05:46	17/03/2013 05:21	slow	Y	M1.1

TABLE A.2: Table for events observed by STEREO A between 2010 and 2013.

STEREO A									
Event	**Start time [UT]**	**End time [UT]**	**Lat. (N+/S-)**	**Long. (W+/E-)**	**Flare time ([UT]**	**Shock time [UT]**	**v_{sw} [km s^{-1}]**	**Downst. analysis**	**Flare class**
1-a	14/08/2010 10:14	17/08/2010 11:50	14	-24	14/08/2010 09:38		370	N	C4.4
2-a	18/08/2010 05:50	20/08/2010 23:35	21	8	18/08/2010 04:45	20/08/2010 16:12	333	Y	C4.5
3-a	07/03/2011 20:10	12/03/2011 07:20	23	-40	07/03/2011 19:43	09/03/2011 06:47	470	Y	M3.7
4-a	21/03/2011 03:00	24/03/2011 16:30	7	42	21/03/2011 02:15	22/03/2011 18:20	424	Y	B3.5
5-a	04/06/2011 22:09	14/06/2011 06:09	-24	51	04/06/2011 21:45	05/06/2011 18:58	637	Y	
5-b	04/06/2011 22:09	14/06/2011 06:09	-30	-42	07/06/2011 06:15		555	N	M2.5
5-c	14/06/2011 06:09	18/06/2011 15:09	13	-172	14/06/2011 04:45		394	N	
6-a	04/08/2011 04:34	09/08/2011 11:30	19	-63	04/08/2011 03:40	06/08/2011 12:42	403	Y	M9.3
7-a	09/08/2011 07:59	12/08/2011 20:19	18	-32	09/08/2011 07:47	11/08/2011 05:37	423	Y	X6.9
8-a	06/09/2011 23:15	10/09/2011 13:34	23	-85	06/09/2011 22:12		332	N	X2.1
9-a	21/09/2011 22:05	22/09/2011 10:32	29	11	21/09/2011 22:32		405	N	C2.1
9-b	22/09/2011 10:32	25/09/2011 06:00	19	167	22/09/2011 10:29	24/09/2011 08:03	353	Y	X1.4
10-a	22/10/2011 16:20	25/10/2011 18:45	39	-18	22/10/2011 10:00	25/10/2011 04:50	330	Y	M1.3
11-a	03/11/2011 22:25	09/11/2011 00:00	14	103	03/11/2011 22:16		342	N	M4.7
12-a	26/11/2011 07:30	30/11/2011 00:20	20	-59	26/11/2011 06:09	28/11/2011 14:50	453	Y	C1.2
13-a	19/01/2012 15:00	23/01/2012 04:00	31	-135	19/01/2012 13:43		353	N	M3.2
13-b	23/01/2012 04:00	27/01/2012 18:00	31	-87	23/01/2012 03:38		508	N	M8.7
13-c	27/01/2012 18:00	09/02/2012 07:59	30	-23	27/01/2012 17:37	29/01/2012 13:03	356	Y	X1.7
14-a	24/02/2012 19:00	27/02/2012 21:24	2	163	24/02/2012 00:45		419	N	B4.5
15-a	05/03/2012 03:00	06/03/2012 23:30	9	-167	05/03/2012 02:30		398	N	X1.1
15-b	06/03/2012 23:30	13/03/2012 16:30	8	-140	07/03/2012 00:02		402	N	X5.4
15-b	06/03/2012 23:30	13/03/2012 16:30	5	-106	09/03/2012 03:22		402	N	M6.3
15-c	13/03/2012 16:30	17/03/2012 02:24	6	-44	13/03/2012 17:12	15/03/2012 22:32	401	N	M7.9
16-a	17/05/2012 02:05	22/05/2012 15:15	-3	-27	17/05/2012 01:25	18/05/2012 12:42	618	Y	M5.1
17-a	26/05/2012 21:00	02/06/2012 00:00	4	2	26/05/2012 20:45	28/05/2012 02:48	337	Y	B3.6
18-a	14/06/2012 14:19	19/06/2012 04:00	-24	-124	14/06/2012 12:51		518	N	M1.9
19-a	06/07/2012 23:35	08/07/2012 16:59	-13	-61	06/07/2012 23:01		417	N	X1.1
19-b	08/07/2012 16:59	10/07/2012 22:05	-14	-34	08/07/2012 16:23	10/07/2012 18:54	507	N	M6.9
20-a	12/07/2012 17:05	15/07/2012 20:39	-12	-117	12/07/2012 15:36		424	N	X1.4
21-a	18/07/2012 05:30	20/07/2012 04:30	20	57	18/07/2012 06:04		386	N	C3.1
21-b	20/07/2012 04:30	23/07/2012 02:05	-10	-33	19/07/2012 04:16	20/07/2012 22:43	481	N	M7.7
21-c	23/07/2012 02:05	04/08/2012 07:59	5	4	23/07/2012 01:59	23/07/2012 20:55	445	Y	
22-a	31/08/2012 20:30	08/09/2012 07:39	-9	-166	31/08/2012 19:59		398	N	C8.4
23-a	27/09/2012 10:30	05/10/2012 00:00	-12	21	27/09/2012 09:54	29/09/2012 18:35	364	N	
24-a	14/12/2012 12:20	16/12/2012 03:45				17/12/2012 16:57	336	N	
25-a	15/03/2013 07:30	18/03/2013 04:00	-4	-138	15/03/2013 05:46		376	N	M1.1

TABLE A.3: Events observed by STEREO B between 2010 and 2013.

STEREO B									
Event	**Start time [UT]**	**End time [UT]**	**Lat. (N+/S-)**	**Long. (W+/E-)**	**Flare time [UT]**	**Shock time [UT]**	**v_{sw} [km s^{-1}]**	**Downst. analysis**	**Flare class**
1-a	14/08/2010 10:14	17/08/2010 11:50	20	128	14/08/2010 09:38		312	N	C4.4
2-a	18/08/2010 05:50	20/08/2010 23:35	26	160	18/08/2010 04:45		439	N	C4.5
3-a	07/03/2011 20:10	12/03/2011 07:20	22	143	07/03/2011 19:43		382	N	M3.7
4-a	21/03/2011 03:00	24/03/2011 16:30	10	-135	21/03/2011 02:15		476	N	B3.5
5-a	04/06/2011 22:09	14/06/2011 06:09	-9	-122	04/06/2011 21:45		455	N	
5-b	04/06/2011 22:09	14/06/2011 06:09	-15	146	07/06/2011 06:15		455	N	M2.5
5-c	14/06/2011 06:09	18/06/2011 15:09	27	17	14/06/2011 04:45		457	N	
6-a	04/08/2011 04:34	09/08/2011 11:30	27	131	04/08/2011 03:40		344	N	M9.3
7-a	09/08/2011 07:59	12/08/2011 20:19	25	162	09/08/2011 07:47		572	N	X6.9
8-a	06/09/2011 23:15	10/09/2011 13:34	23	113	06/09/2011 22:12		443	N	X2.1
9-a	22/09/2011 10:32	24/09/2011 12:45	16	7	22/09/2011 10:29	24/09/2011 03:58	475	N	X1.4
9-b	24/09/2011 12:45	03/10/2011 00:00	16	41	24/09/2011 12:33		488	N	M7.1
10-a	22/10/2011 16:20	25/10/2011 18:45	29	-172	22/10/2011 10:00		415	N	M1.3
11-a	03/11/2011 22:25	09/11/2011 00:00	3	-50	03/11/2011 22:16	06/11/2011 05:10	384	N	M4.7
12-a	26/11/2011 07:30	30/11/2011 00:20	6	153	26/11/2011 06:09		335	N	C1.2
13-a	19/01/2012 15:00	23/01/2012 04:00	20	86	19/01/2012 13:43		406	N	M3.2
13-b	23/01/2012 04:00	27/01/2012 18:00	21	134	23/01/2012 03:38		381	N	M8.7
13-c	27/01/2012 18:00	09/02/2012 07:59	21	-161	27/01/2012 17:37		399	N	X1.7
14-a	24/02/2012 19:00	27/02/2012 21:24	-2	29	24/02/2012 00:45		352	N	B4.5
15-a	05/03/2012 03:00	06/03/2012 23:30	8	60	05/03/2012 02:30		392	N	X1.1
15-b	06/03/2012 23:30	13/03/2012 16:30	7	87	07/03/2012 00:02		414	Y	X5.4
15-b	06/03/2012 23:30	13/03/2012 16:30	4	121	09/03/2012 03:22		414	N	M6.3
15-c	13/03/2012 16:30	17/03/2012 02:24	7	-176	13/03/2012 17:12		387	N	M7.9
16-a	17/05/2012 02:05	22/05/2012 15:15	9	-154	17/05/2012 01:25		398	N	M5.1
17-a	27/05/2012 04:41	01/06/2012 00:00	7	58	27/05/2012 04:41		656	N	C3.1
18-a	14/06/2012 14:19	19/06/2012 04:00	-11	110	14/06/2012 12:51		495	N	M1.9
19-a	06/07/2012 23:35	08/07/2012 16:59	-2	174	06/07/2012 23:01		433	N	X1.1
19-b	08/07/2012 16:59	10/07/2012 22:05	-3	-159	08/07/2012 16:23		373	N	M6.9
20-a	12/07/2012 17:05	15/07/2012 20:39	-2	118	12/07/2012 15:36		495	N	X1.4
21-a	18/07/2012 05:30	20/07/2012 04:30	30	-67	18/07/2012 06:04		441	N	C3.1
21-b	20/07/2012 04:30	23/07/2012 02:05	-1	-157	19/07/2012 04:16		374	N	M7.7
21-c	23/07/2012 02:05	04/08/2012 07:59	14	-120	23/07/2012 01:59	23/07/2012 21:20	335	N	
22-a	31/08/2012 20:30	08/09/2012 07:39	-8	74	31/08/2012 19:59	03/09/2012 07:11	331	Y	C8.4
23-a	27/09/2012 10:30	05/10/2012 00:00	17	150	27/09/2012 23:35		441	N	C3.7
24-a	14/12/2012 12:20	16/12/2012 03:45				18/12/2012 20:05	387	N	
25-a	15/03/2013 07:30	18/03/2013 04:00	-3	134	15/03/2013 05:46		302	N	M1.1

A.2 Event tables for the full range

Here we show the full lists of events contained in the SREL catalogue (Table A.4), and the lists used for deriving the radial dependences from Helios 1 (Table A.5) and Helios 2 (Table A.6).

In Table A.4 first column indicate the event number and each SEP event inside the event. The times comprising the whole the duration of the event including all the SEP events is depicted for each event, before detailing the SEP events. Then, SEP events comprising the event are indicated by a letter following the event number (a, b, c....). Second and third columns indicate the date and time of the start and end of each event and SEP event. Fourth and fifth give the parent flare latitude and longitude; when there is no associated source identified, it is signalled using "9999" value. Columns sixth and seventh show the flare date and time as observed in X-ray, the shock arrival date and time to the ACE spacecraft location. If there is no flare or shock identified related with the event, it is signalled using "99/99/9999 99:99" value. Column eight indicates if the event has been included in the analysis of the downstream fluence. Last two columns show the event type (see App. B, NC: 'not classified') and the solar wind type ('fast' or 'slow'; ND: 'not determined'). Authors in SEPEM: B. Sanahuja, A. Aran, N. Crosby, T. Falkenberg, G. Michalareas. Authors in SOL2UP: D. Pacheco, A. Aran, N. Agueda.

TABLE A.4: Complete SOL2UP Radial dependent Event List (SREL).

Event	Start time [UT]	End time [UT]	Lat. (N+/S-)	Long. (W+/E-)	Flare time [UT]	Shock time [UT]	Downst. analysis	Event type	Solar wind type
	1988								
Event 001	02/01/1988 23:00	06/01/1988 13:50							
1-a	02/01/1988 23:00	06/01/1988 13:50	-34	18	02/01/1988 21:11	04/01/1988 20:12	Y	3b	slow
Event 002	25/08/1988 13:55	31/08/1988 11:00							
2-a	24/08/1988 01:00	26/08/1988 10:58	24	-88	23/08/1988 17:57	25/08/1988 09:32	N	2c	ND
2-b	26/08/1988 10:58	29/08/1988 15:54	-20	-66	26/08/1988 10:58	99/99/9999 99:99	N	1b	ND
2-c	29/08/1988 15:44	01/09/1988 18:00	-21	-54	29/08/1988 15:44	31/08/1988 16:16	N	2c	ND
Event 003	08/11/1988 15:45	10/11/1988 11:40							
3-a	08/11/1988 12:40	12/11/1988 19:00	16	7	08/11/1988 12:28	11/11/1988 07:53	Y	3b	slow
Event 004	14/12/1988 15:30	19/12/1988 20:10							
4-a	14/12/1988 12:00	16/12/1988 08:41	30	-60	14/12/1988 13:37	99/99/9999 99:99	N	1b	fast
4-b	16/12/1988 08:41	20/12/1988 15:30	26	-37	16/12/1988 08:41	18/12/1988 18:24	Y	3b	fast
	1989								
Event 005	04/01/1989 21:20	06/01/1989 03:20							
5-a	04/01/1989 19:30	06/01/1989 20:00	-20	60	04/01/1989 17:53	06/01/1989 23:54	N	2a	slow
Event 006	08/03/1989 03:30	21/03/1989 12:15							
6-a	07/03/1989 08:00	10/03/1989 22:30	35	-69	06/03/1989 13:50	08/03/1989 18:00	Y	2c	slow
6-b	10/03/1989 22:30	17/03/1989 17:43	31	-22	10/03/1989 19:00	13/03/1989 01:00	Y	4b	fast
6-c	17/03/1989 17:43	21/03/1989 16:00	33	60	17/03/1989 17:44	19/03/1989 04:23	Y	4b	fast
Event 007	23/03/1989 20:15	24/03/1989 21:30							
7-a	23/03/1989 20:15	28/03/1989 00:00	18	28	23/03/1989 19:39	26/03/1989 12:00	Y	3b	slow
Event 008	10/04/1989 21:15	18/04/1989 01:45							
8-a	10/04/1989 06:00	18/04/1989 20:00	35	-29	09/04/1989 00:44	11/04/1989 14:35	Y	2b	slow
Event 009	02/05/1989 16:50	08/05/1989 21:15							
9-a	03/05/1989 03:26	09/05/1989 18:00	27	-30	03/05/1989 03:26	05/05/1989 00:10	Y	2b	ND
Event 010	22/05/1989 18:30	29/05/1989 10:00							
10-a	20/05/1989 09:57	28/05/1989 12:08	20	-16	22/05/1989 00:24	23/05/1989 13:46	Y	3b	ND
10-b	28/05/1989 12:08	30/05/1989 22:00	-19	75	28/05/1989 12:09	99/99/9999 99:99	N	1b	ND
Event 011	30/06/1989 20:35	02/07/1989 05:55							
11-a	30/06/1989 20:35	02/07/1989 05:55	26	60	29/06/1989 21:17	01/07/1989 15:46	N	NC	ND

Table continues on the next page

Event	Start time [UT]	End time [UT]	Lat. (N+/S-)	Long. (W+/E-)	Flare time [UT]	Shock time [UT]	Downst. analysis	Event type	Solar wind type
Event 012	25/07/1989 09:05	26/07/1989 17:45							
12-a	25/07/1989 09:05	26/07/1989 19:45	25	84	25/07/1989 08:39	99/99/9999 99:99	N	1b	slow
Event 013	12/08/1989 15:45	06/09/1989 03:15							
13-a	12/08/1989 15:45	16/08/1989 01:08	-16	37	12/08/1989 14:27	14/08/1989 06:13	Y	4a	slow
13-b	16/08/1989 01:08	01/09/1989 08:10	18	84	16/08/1989 01:08	17/08/1989 15:41	Y	4b	fast
13-c	01/09/1989 08:10	06/09/1989 20:00	-20	-61	01/09/1989 08:10	04/09/1989 00:27	Y	2c	slow
Event 014	12/09/1989 13:30	16/09/1989 01:30							
14-a	12/09/1989 13:30	16/09/1989 01:30	-18	79	12/09/1989 04:59	15/09/1989 00:47	Y	2a	slow
Event 015	29/09/1989 11:55	10/10/1989 05:20							
15-a	29/09/1989 11:55	10/10/1989 05:20	-26	105	29/09/1989 11:33	02/10/1989 03:39	Y	4b	slow
Event 016	19/10/1989 13:10	09/11/1989 16:50							
16-a	19/10/1989 13:10	22/10/1989 17:05	-27	-10	19/10/1989 12:55	20/10/1989 16:50	Y	4a	fast
16-b	22/10/1989 17:05	24/10/1989 18:20	-27	32	22/10/1989 17:55	24/10/1989 02:15	N	4a	fast
16-c	24/10/1989 18:20	29/10/1989 04:50	-29	57	24/10/1989 18:31	26/10/1989 14:27	Y	4b	fast
16-d	29/10/1989 04:50	01/11/1989 16:30	9999	90	29/10/1989 04:51	99/99/9999 99:99	N	1a	fast
16-e	01/11/1989 16:30	06/11/1989 13:40	17	-51	01/11/1989 15:14	02/11/1989 20:14	N	2c	ND
16-f	06/11/1989 13:40	09/11/1989 16:50	20	-19	06/11/1989 13:43	09/11/1989 00:54	N	2b	ND
Event 017	15/11/1989 07:25	17/11/1989 16:05							
17-a	15/11/1989 07:10	18/11/1989 10:30	11	26	15/11/1989 06:38	17/11/1989 09:25	Y	3b	slow
Event 018	27/11/1989 06:25	05/12/1989 09:05							
18-a	26/11/1989 17:00	30/11/1989 11:45	30	-5	25/11/1989 22:55	27/11/1989 21:39	Y	2b	slow
18-b	30/11/1989 11:45	05/12/1989 09:05	24	52	30/11/1989 12:29	01/12/1989 17:49	Y	4b	fast
	1990								
Event 019	19/03/1990 06:30	22/03/1990 01:40							
19-a	19/03/1990 05:00	22/03/1990 12:00	31	43	19/03/1990 04:38	20/03/1990 22:43	Y	4b	slow
Event 020	28/03/1990 17:00	30/03/1990 12:10							
20-a	28/03/1990 14:30	31/03/1990 06:00	-4	37	28/03/1990 07:51	30/03/1990 07:20	Y	2a	ND
Event 021	07/04/1990 06:45	12/04/1990 08:15							
21-a	07/04/1990 06:45	10/04/1990 13:38	32	-62	07/04/1990 15:11	09/04/1990 08:43	Y	2c	ND
21-b	10/04/1990 13:38	13/04/1990 14:00	22	-72	10/04/1990 13:38	12/04/1990 03:26	Y	2c	ND
Event 022	16/04/1990 06:05	23/04/1990 07:15							
22-a	16/04/1990 00:00	24/04/1990 00:00	32	-57	15/04/1990 03:02	17/04/1990 07:19	Y	2c	ND
Event 023	28/04/1990 05:30	29/04/1990 16:40							
23-a	28/04/1990 05:30	29/04/1990 16:40	2	19	27/04/1990 08:50	99/99/9999 99:99		NC	ND
Event 024	10/05/1990 21:05	12/05/1990 11:55							
24-a	10/05/1990 21:05	12/05/1990 11:55	9999	-90	10/05/1990 19:48	99/99/9999 99:99		NC	ND
Event 025	17/05/1990 21:30	31/05/1990 16:35							
25-a	15/05/1990 13:00	21/05/1990 22:19	42	-38	15/05/1990 12:46	18/05/1990 07:43	Y	2b	ND
25-b	21/05/1990 22:19	24/05/1990 21:00	35	36	21/05/1990 22:19	23/05/1990 08:00	Y	4b	ND
25-c	24/05/1990 21:00	26/05/1990 20:45	33	78	24/05/1990 20:46	26/05/1990 20:37	N	3a	ND
25-d	26/05/1990 20:45	28/05/1990 04:28	9999	90	26/05/1990 20:45	99/99/9999 99:99	N	1b	ND
25-e	28/05/1990 04:28	01/06/1990 15:00	18	-39	28/05/1990 04:28	30/05/1990 09:04	Y	3b	ND
Event 026	12/06/1990 02:45	14/06/1990 12:15							
26-a	12/06/1990 05:41	15/06/1990 07:30	10	33	12/06/1990 05:41	14/06/1990 03:10	Y	2a	ND
Event 027	13/07/1990 18:00	15/07/1990 01:05							
27-a	13/07/1990 16:00	15/07/1990 14:15	19	108	13/07/1990 09:59	15/07/1990 02:00	Y	2a	ND
Event 028	26/07/1990 04:20	30/07/1990 01:35							
28-a	26/07/1990 00:00	30/07/1990 16:30	-15	-55	25/07/1990 22:23	28/07/1990 03:31	Y	3b	slow
Event 029	31/07/1990 15:25	06/08/1990 12:05							
29-a	31/07/1990 00:00	07/08/1990 11:30	20	-45	30/07/1990 06:33	01/08/1990 07:41	Y	2b	ND
Event 030	12/08/1990 23:30	16/08/1990 08:55							
30-a	11/08/1990 17:00	18/08/1990 00:00	20	-72	10/08/1990 18:09	13/08/1990 10:27	Y	2c	ND
	1991								
Event 031	27/01/1991 14:45	02/02/1991 19:30							
31-a	31/01/1991 02:30	03/02/1991 15:30	-17	33	31/01/1991 02:30	01/02/1991 18:42	Y	4b	fast
Event 032	08/02/1991 09:55	09/02/1991 17:05							
32-a	08/02/1991 09:55	09/02/1991 17:05	-13	80	08/02/1991 02:44	99/99/9999 99:99	N	1b	slow
Event 033	25/02/1991 10:40	27/02/1991 01:55							
33-a	25/02/1991 08:40	28/02/1991 17:00	-16	80	25/02/1991 08:19	27/02/1991 08:27	Y	2a	ND
Event 034	12/03/1991 18:50	15/03/1991 02:00							
34-a	12/03/1991 18:50	15/03/1991 02:00	-7	-59	12/03/1991 12:28	99/99/9999 99:99	N	NC	slow
Event 035	16/03/1991 15:15	17/03/1991 19:05							
35-a	16/03/1991 15:15	19/03/1991 19:05	-14	-5	16/03/1991 10:52	19/03/1991 14:00	N	2b	slow
Event 036	23/03/1991 06:40	31/03/1991 14:30							
36-a	23/03/1991 02:40	31/03/1991 16:30	-26	-28	22/03/1991 22:43	24/03/1991 03:41	Y	4a	slow
Event 037	02/04/1991 06:45	10/04/1991 01:15							
37-a	02/04/1991 23:27	11/04/1991 01:00	14	0	02/04/1991 23:27	04/04/1991 11:22	Y	2b	fast
Event 038	22/04/1991 12:00	24/04/1991 15:00							
38-a	22/04/1991 12:00	24/04/1991 15:00	9999	9999	99/99/9999 99:99	99/99/9999 99:99	N	NC	ND
Event 039	10/05/1991 15:05	15/05/1991 10:50							
39-a	10/05/1991 15:05	13/05/1991 01:45	9999	9999	99/99/9999 99:99	13/05/1991 08:57	N	NC	slow
39-b	13/05/1991 01:45	15/05/1991 12:50	-9	90	13/05/1991 01:03	99/99/9999 99:99	N	1a	ND

Table continues on the next page

Event	Start time [UT]	End time [UT]	Lat. (N+/S-)	Long. (W+/E-)	Flare time [UT]	Shock time [UT]	Downst. analysis	Event type	Solar wind type
Event 040	18/05/1991 12:00	29/05/1991 12:00							
40-a	18/05/1991 12:00	19/05/1991 13:44	32	85	18/05/1991 05:06	99/99/9999 99:99	N	1b	slow
40-b	19/05/1991 13:44	22/05/1991 00:39	-11	-17	19/05/1991 13:44	22/05/1991 00:18	N	2b	slow
40-c	22/05/1991 00:39	25/05/1991 14:05	-29	3	22/05/1991 00:39	24/05/1991 02:30	N	2a	fast
40-d	25/05/1991 14:05	29/05/1991 12:00	22	-35	25/05/1991 14:05	99/99/9999 99:99	N	1b	fast
Event 041	30/05/1991 04:00	20/06/1991 14:00							
41-a	30/05/1991 04:00	01/06/1991 15:09	5	-38	29/05/1991 22:14	31/05/1991 10:39	N	2b	fast
41-b	01/06/1991 15:09	06/06/1991 00:54	25	-90	01/06/1991 15:09	04/06/1991 15:36	N	2c	fast
41-c	06/06/1991 00:54	09/06/1991 01:37	33	-44	06/06/1991 00:54	07/06/1991 22:28	N	4b	fast
41-d	09/06/1991 01:37	11/06/1991 02:05	34	-4	09/06/1991 01:37	10/06/1991 17:16	N	4b	fast
41-e	11/06/1991 02:05	15/06/1991 06:33	31	17	11/06/1991 02:05	12/06/1991 10:12	Y	4b	fast
41-f	15/06/1991 06:33	20/06/1991 14:00	33	69	15/06/1991 06:33	17/06/1991 10:19	Y	4b	fast
Event 042	29/06/1991 21:25	13/07/1991 05:40							
42-a	28/06/1991 20:00	30/06/1991 04:43	28	-85	28/06/1991 06:26	30/06/1991 01:16	N	2c	slow
42-b	30/06/1991 04:43	07/07/1991 01:20	-6	19	30/06/1991 02:43	02/07/1991 08:11	Y	3b	ND
42-c	07/07/1991 01:20	10/07/1991 12:28	26	-3	07/07/1991 01:20	08/07/1991 16:36	Y	4b	slow
42-d	10/07/1991 12:28	14/07/1991 00:30	-22	-34	10/07/1991 12:28	12/07/1991 09:24	Y	2b	fast
Event 043	25/08/1991 21:10	30/08/1991 22:30							
43-a	25/08/1991 10:00	01/09/1991 12:00	24	-77	25/08/1991 00:31	27/08/1991 15:15	Y	2c	slow
Event 044	06/09/1991 15:25	07/09/1991 21:45							
44-a	06/09/1991 08:00	08/09/1991 18:00	19	37	05/09/1991 21:21	99/99/9999 99:99	N	1b	ND
Event 045	30/09/1991 09:40	03/10/1991 15:40							
45-a	30/09/1991 07:40	04/10/1991 00:30	-21	-32	29/09/1991 15:33	01/10/1991 17:40	Y	2b	slow
Event 046	28/10/1991 05:50	29/10/1991 06:00							
46-a	28/10/1991 05:50	29/10/1991 13:30	-13	-15	27/10/1991 05:48	28/10/1991 10:54	N	2b	ND
Event 047	30/10/1991 07:30	31/10/1991 20:05							
47-a	30/10/1991 06:23	01/11/1991 18:00	-8	25	30/10/1991 06:11	31/10/1991 17:12	Y	3b	fast
Event 048	21/12/1991 21:40	23/12/1991 06:50							
48-a	21/12/1991 14:00	24/12/1991 22:00	9999	90	21/12/1991 11:45	23/12/1991 18:02	Y	2a	ND
Event 049	29/12/1991 05:40	30/12/1991 08:30							
49-a	29/12/1991 02:00	31/12/1991 01:00	-16	47	28/12/1991 21:08	99/99/9999 99	N	1b	ND
	1992								
Event 050	06/02/1992 22:45	10/02/1992 00:30							
50-a	06/02/1992 16:30	11/02/1992 00:00	-13	10	06/02/1992 10:48	08/02/1992 14:28	Y	2a	slow
Event 051	27/02/1992 11:40	28/02/1992 15:05							
51-a	27/02/1992 10:40	02/03/1992 00:00	6	2	27/02/1992 09:22	29/02/1992 09:20	Y	2a	ND
Event 052	16/03/1992 04:30	17/03/1992 14:10							
52-a	15/03/1992 05:00	18/03/1992 12:00	-14	-29	15/03/1992 01:21	17/03/1992 09:51	N	3b	slow
Event 053	09/05/1992 06:15	13/05/1992 20:15							
53-a	08/05/1992 17:30	14/05/1992 16:00	-26	-8	08/05/1992 15:37	09/05/1992 19:57	Y	4b	fast
Event 054	25/06/1992 20:30	01/07/1992 23:25							
54-a	25/06/1992 20:30	02/07/1992 17:00	9	67	25/06/1992 19:47	27/06/1992 20:35	Y	3a	fast
Event 055	05/08/1992 20:35	08/08/1992 09:05							
55-a	04/08/1992 12:00	09/08/1992 17:00	-9	-68	03/08/1992 07:06	06/08/1992 11:45	Y	2c	slow
Event 056	30/10/1992 18:45	08/11/1992 05:15							
56-a	30/10/1992 18:45	02/11/1992 02:31	-22	61	30/10/1992 18:16	01/11/1992 21:47	N	4b	ND
56-b	02/11/1992 02:31	10/11/1992 00:00	-23	90	02/11/1992 02:31	03/11/1992 08:00	Y	4b	ND
	1993								
Event 057	04/03/1993 13:20	05/03/1993 22:30							
57-a	04/03/1993 12:35	06/03/1993 17:00	-14	56	04/03/1993 12:17	99/99/9999 99:99	N	1b	slow
Event 058	06/03/1993 23:05	09/03/1993 20:10							
58-a	06/03/1993 21:05	10/03/1993 20:10	-4	-29	06/03/1993 20:14	09/03/1993 21:00	Y	2b	slow
Event 059	12/03/1993 18:50	14/03/1993 15:05							
59-a	12/03/1993 18:00	16/03/1993 12:00	0	51	12/03/1993 17:03	15/03/1993 05:26	Y	3a	fast
	1994								
Event 060	20/02/1994 02:20	22/02/1994 21:20							
60-a	20/02/1994 01:50	24/02/1994 00:00	9	2	20/02/1994 01:38	21/02/1994 09:01	Y	4b	fast
Event 061	19/10/1994 22:35	21/10/1994 12:05							
61-a	19/10/1994 21:39	23/10/1994 00:00	12	24	19/10/1994 21:27	22/10/1994 08:49	Y	3b	slow
	1995								
Event 062	20/10/1995 07:35	22/10/1995 04:15							
62-a	20/10/1995 06:35	23/10/1995 10:00	-9	55	20/10/1995 05:54	22/10/1995 21:05	Y	3a	slow
	1997								
Event 063	04/11/1997 06:50	10/11/1997 19:40							
63-a	04/11/1997 06:10	06/11/1997 11:49	-14	33	04/11/1997 05:52	06/11/1997 22:02	N	3a	ND
63-b	06/11/1997 11:49	12/11/1997 12:00	-18	63	06/11/1997 11:49	09/11/1997 09:52	Y	4b	ND
	1998								
Event 064	20/04/1998 12:55	26/04/1998 15:05							
64-a	20/04/1998 10:19	27/04/1998 00:00	-44	90	20/04/1998 10:07	23/04/1998 17:28	Y	4b	slow
Event 065	29/04/1998 23:15	01/05/1998 06:20							
65-a	29/04/1998 22:00	02/05/1998 10:30	-18	-20	29/04/1998 16:37	01/05/1998 21:22	Y	2b	slow

Table continues on the next page

Event	Start time [UT]	End time [UT]	Lat. (N+/S-)	Long. (W+/E-)	Flare time [UT]	Shock time [UT]	Downst. analysis	Event type	Solar wind type
Event 066	02/05/1998 13:55	04/05/1998 23:05							
66-a	02/05/1998 13:55	05/05/1998 23:30	-15	15	02/05/1998 13:31	04/05/1998 02:15	Y	3b	fast
Event 067	06/05/1998 08:25	08/05/1998 00:20							
67-a	06/05/1998 08:25	08/05/1998 16:00	-11	65	06/05/1998 07:58	08/05/1998 09:52	Y	3a	fast
Event 068	09/05/1998 06:50	11/05/1998 04:10							
68-a	09/05/1998 03:16	12/05/1998 00:00	-15	86	09/05/1998 03:04	99/99/9999 99:99	N	1b	slow
Event 069	17/06/1998 16:00	18/06/1998 23:55							
69-a	16/06/1998 20:00	19/06/1998 18:00	-17	103	16/06/1998 18:03	99/99/9999 99:99	N	1b	slow
Event 070	22/08/1998 17:25	31/08/1998 20:00							
70-a	24/08/1998 22:02	01/09/1998 10:00	35	-9	24/08/1998 21:50	26/08/1998 06:15	Y	4b	slow
Event 071	24/09/1998 17:25	25/09/1998 21:15							
71-a	23/09/1998 13:45	26/09/1998 10:00	18	-9	23/09/1998 06:40	24/09/1998 23:13	Y	3b	slow
Event 072	30/09/1998 14:25	04/10/1998 04:20							
72-a	30/09/1998 13:16	04/10/1998 19:15	23	81	30/09/1998 13:04	02/10/1998 06:53	Y	4b	fast
Event 073	19/10/1998 04:10	20/10/1998 04:30							
73-a	18/10/1998 23:00	20/10/1998 21:00	9999	120	99/99/9999 99:99	99/99/9999 99:99	N	NC	slow
Event 074	06/11/1998 03:45	08/11/1998 18:30							
74-a	05/11/1998 20:00	09/11/1998 18:00	26	18	05/11/1998 19:00	08/11/1998 04:21	Y	2a	slow
Event 075	14/11/1998 06:30	17/11/1998 15:55							
75-a	14/11/1998 06:30	18/11/1998 18:00	28	120	14/11/1998 05:15	99/99/9999 99:99	N	1a	slow
	1999								
Event 076	21/01/1999 00:30	26/01/1999 02:40							
76-a	20/01/1999 20:00	27/01/1999 13:00	27	-90	20/01/1999 19:06	22/01/1999 19:45	Y	3b	fast
Event 077	24/04/1999 16:15	26/04/1999 12:35							
77-a	24/04/1999 14:00	27/04/1999 12:00	9999	120	24/04/1999 13:00	27/04/1999 06:00	Y	3a	slow
Event 078	04/05/1999 14:45	08/05/1999 12:00							
78-a	03/05/1999 21:00	09/05/1999 17:00	15	-32	03/05/1999 05:36	05/05/1999 14:57	Y	2b	slow
Event 079	27/05/1999 12:15	28/05/1999 14:40							
79-a	27/05/1999 11:18	29/05/1999 04:00	9999	90	27/05/1999 11:06	99/99/9999 99:99	N	1b	slow
Event 080	01/06/1999 22:10	07/06/1999 15:05							
80-a	01/06/1999 20:10	04/06/1999 09:11	9999	90	01/06/1999 16:27	02/06/1999 21:57	Y	3a	slow
80-b	04/06/1999 08:00	08/06/1999 18:00	17	69	04/06/1999 06:52	99/99/9999 99:99	N	1a	slow
	2000								
Event 081	18/02/2000 08:45	19/02/2000 11:55							
81-a	17/02/2000 20:29	18/02/2000 09:21	-29	-7	17/02/2000 20:17	99/99/9999 99:99	N	1b	slow
81-b	18/02/2000 09:21	22/02/2000 00:00	-16	78	18/02/2000 09:21	20/02/2000 20:45	Y	3a	slow
Event 082	04/04/2000 17:40	06/04/2000 23:45							
82-a	04/04/2000 15:44	08/04/2000 00:00	16	66	04/04/2000 15:12	06/04/2000 16:00	Y	2a	slow
Event 083	16/05/2000 08:05	17/05/2000 08:20							
83-a	15/05/2000 18:00	19/05/2000 12:00	-24	67	15/05/2000 15:46	17/05/2000 21:39	Y	2a	fast
Event 084	07/06/2000 04:00	12/06/2000 21:10							
84-a	06/06/2000 20:00	10/06/2000 16:52	21	-18	06/06/2000 14:58	08/06/2000 08:41	Y	2b	fast
84-b	10/06/2000 16:52	13/06/2000 19:00	22	38	10/06/2000 16:40	99/99/9999 99:99	N	1b	fast
Event 085	25/06/2000 16:40	26/06/2000 20:50							
85-a	25/06/2000 11:00	27/06/2000 12:00	14	56	25/06/2000 07:17	99/99/99999 99:99	N	1b	slow
Event 086	13/07/2000 00:30	23/07/2000 19:20							
86-a	11/07/2000 03:00	14/07/2000 10:03	18	-49	10/07/2000 21:05	13/07/2000 09:18	Y	2c	fast
86-b	14/07/2000 10:03	22/07/2000 11:35	22	7	14/07/2000 10:03	15/07/2000 14:15	Y	4a	fast
86-c	22/07/2000 11:35	24/07/2000 16:00	14	56	22/07/2000 11:17	99/99/99999 99:99	N	1b	fast
Event 087	28/07/2000 02:55	30/07/2000 09:05							
87-a	28/07/2000 02:00	01/08/2000 01:00	9999	120	27/07/2000 19:30	31/07/2000 18:16	Y	2a	ND
Event 088	13/08/2000 00:45	15/08/2000 03:30							
88-a	12/08/2000 18:00	16/08/2000 18:00	13	46	12/08/2000 13:48	14/08/2000 21:36	Y	2a	fast
Event 089	12/09/2000 14:50	18/09/2000 01:25							
89-a	12/09/2000 11:43	18/09/2000 12:00	-17	9	12/09/2000 11:31	15/09/2000 03:59	Y	4b	fast
Event 090	16/10/2000 08:55	18/10/2000 21:40							
90-a	16/10/2000 06:52	19/10/2000 23:00	4	90	16/10/2000 06:40	99/99/9999 99:99	N	1b	fast
Event 091	25/10/2000 15:15	27/10/2000 19:10							
91-a	25/10/2000 13:00	29/10/2000 00:00	10	66	25/10/2000 08:45	28/10/2000 09:08	Y	2a	slow
Event 092	31/10/2000 06:20	02/11/2000 12:50							
92-a	31/10/2000 06:20	02/11/2000 12:50	18	-7	31/10/2000 02:51	99/99/9999 99:99	N	NC	slow
Event 093	08/11/2000 23:45	15/11/2000 17:00							
93-a	08/11/2000 22:54	18/11/2000 00:00	10	77	08/11/2000 22:42	10/11/2000 06:04	Y	4a	fast
Event 094	24/11/2000 07:00	04/12/2000 11:40							
94-a	24/11/2000 05:07	05/12/2000 18:00	22	3	24/11/2000 04:55	26/11/2000 11:24	Y	4b	slow
	2001								
Event 095	22/01/2001 01:15	25/01/2001 00:10							
95-a	21/01/2001 20:00	25/01/2001 00:10	-7	-46	20/01/2001 21:06	23/01/2001 10:06	Y	2c	slow
Event 096	28/01/2001 19:30	31/01/2001 14:25							
96-a	28/01/2001 15:52	01/02/2001 04:00	-4	59	28/01/2001 15:40	31/01/2001 07:22	Y	3a	slow
Event 097	26/03/2001 18:45	27/03/2001 23:50							
97-a	25/03/2001 21:00	28/03/2001 08:00	16	-25	25/03/2001 16:25	27/03/2001 17:15	Y	2b	slow

Table continues on the next page

Event	Start time [UT]	End time [UT]	Lat. (N+/S-)	Long. (W+/E-)	Flare time [UT]	Shock time [UT]	Downst. analysis	Event type	Solar wind type
Event 098	29/03/2001 13:50	01/04/2001 10:25							
98-a	29/03/2001 10:09	01/04/2001 10:25	20	19	29/03/2001 09:57	31/03/2001 01:14	Y	3b	slow
Event 099	02/04/2001 11:20	21/04/2001 23:25							
99-a	02/04/2001 11:20	09/04/2001 16:20	17	78	02/04/2001 21:32	04/04/2001 14:22	Y	4b	fast
99-b	09/04/2001 16:20	12/04/2001 09:40	-23	9	10/04/2001 05:26	11/04/2001 15:28	Y	4b	fast
99-c	12/04/2001 09:40	15/04/2001 13:20	-19	43	12/04/2001 09:39	14/04/2001 01:45	Y	3a	fast
99-d	15/04/2001 13:20	18/04/2001 02:45	-20	85	15/04/2001 13:19	18/04/2001 00:05	N	4b	ND
99-e	18/04/2001 02:45	22/04/2001 23:30	9999	120	18/04/2001 02:14	21/04/2011 15:08	Y	3a	slow
Event 100	27/04/2001 04:55	28/04/2001 20:15							
100-a	26/04/2001 22:00	29/04/2001 16:00	20	5	26/04/2001 12:12	28/04/2001 04:31	Y	2a	slow
Event 101	07/05/2001 15:00	09/05/2001 19:10							
101-a	07/05/2001 13:00	09/05/2001 23:15	25	35	07/05/2001 11:36	99/99/99 99:99	N	1b	slow
Event 102	20/05/2001 08:45	21/05/2001 14:25							
102-a	20/05/2001 06:15	23/05/2001 12:00	999	90	20/05/2001 06:03	99/99/9999 99:99	N	1b	slow
Event 103	15/06/2001 16:05	18/06/2001 04:00							
103-a	15/06/2001 16:05	19/06/2001 03:00	9999	100	15/06/2001 15:30	18/06/2001 01:54	Y	3a	slow
Event 104	09/08/2001 20:10	11/08/2001 15:50							
104-a	09/08/2001 18:10	13/08/2001 00:00	10	10	09/08/2001 10:20	12/08/2001 10:50	N	2a	slow
Event 105	16/08/2001 00:55	29/08/2001 23:59							
105-a	16/08/2001 00:07	21/08/2001 12:06	-20	140	15/08/2001 23:55	17/08/2001 10:16	Y	3a	slow
105-b	21/08/2001 12:06	25/08/2001 16:23	-9	59	21/08/2001 12:06	99/99/9999 99:99	N	1b	slow
105-c	25/08/2001 16:23	29/08/2001 23:59	-17	-34	25/08/2001 16:23	27/08/2001 19:19	N	2b	slow
Event 106	24/09/2001 12:00	12/10/2001 03:05							
106-a	24/09/2001 10:00	01/10/2001 04:41	-16	-23	24/09/2001 09:32	25/09/2001 20:05	Y	4a	fast
106-b	01/10/2001 04:41	09/10/2001 10:37	-22	91	01/10/2001 04:41	11/10/2001 07:55	N	4b	fast
106-c	09/10/2001 10:37	13/10/2001 14:00	-25	-10	09/10/2001 10:46	11/10/2001 16:20	Y	2b	slow
Event 107	19/10/2001 04:55	28/10/2001 16:10							
107-a	19/10/2001 01:55	22/10/2001 14:27	15	29	19/10/2001 16:13	21/10/2001 16:12	Y	3b	slow
107-b	22/10/2001 14:27	25/10/2001 14:42	-21	-18	22/10/2001 14:27	25/10/2001 08:01	N	3b	slow
107-c	25/10/2001 14:42	28/10/2001 16:10	-16	21	25/10/2001 14:42	28/10/2001 02:42	N	2a	slow
Event 108	04/11/2001 16:55	12/11/2001 20:05							
108-a	04/11/2001 16:55	14/11/2001 12:00	6	18	04/11/2001 16:03	06/11/2001 01:25	Y	4a	slow
Event 109	17/11/2001 19:55	30/11/2001 13:00							
109-a	17/11/2001 08:00	22/11/2001 20:28	-13	-42	17/11/2001 04:49	19/11/2001 17:35	Y	2b	fast
109-b	22/11/2001 20:30	01/12/2001 18:00	-17	24	22/11/2001 20:18	24/11/2001 05:38	Y	4b	slow
Event 110	12/12/2001 01:00	13/12/2001 08:00							
110-a	11/12/2001 16:00	14/12/2001 20:00	9999	120	11/12/2001 14:50	99/99/9999 99:99	N	NC	slow
Event 111	26/12/2001 05:55	09/01/2002 07:00							
111-a	26/12/2001 04:44	28/12/2001 20:04	8	54	26/12/2001 04:32	29/12/2001 04:47	N	4b	slow
111-b	28/12/2001 20:04	09/01/2002 16:00	-26	-90	28/12/2001 20:02	30/12/2001 19:32	Y	2c	slow
	2002								
Event 112	10/01/2002 09:55	18/01/2002 18:35							
112-a	09/01/2002 23:00	14/01/2002 05:29	9999	-90	08/01/2002 20:25	10/01/2002 15:44	Y	2c	slow
112-b	14/01/2002 05:29	18/01/2002 18:35	9999	90	14/01/2002 05:29	99/99/9999 99:99	N	1b	slow
Event 113	16/03/2002 08:05	24/03/2002 18:05							
113-a	16/03/2002 01:00	20/03/2002 12:00	-8	3	15/03/2002 22:09	18/03/2002 12:36	N	2a	slow
113-b	20/03/2002 12:00	22/03/2002 12:00	-9	46	18/03/2002 02:31	20/03/2002 13:05	N	2a	ND
113-c	22/03/2002 12:00	25/03/2002 14:00	-10	90	22/03/2002 10:12	25/03/2002 00:58	Y	2a	slow
Event 114	17/04/2002 11:30	28/04/2002 13:35							
114-a	17/04/2002 11:30	21/04/2002 00:43	-14	34	17/04/2002 07:46	19/04/2002 08:02	Y	2a	ND
114-b	21/04/2002 00:43	29/04/2002 04:00	-14	84	21/04/2002 00:43	23/04/2002 04:15	Y	4b	slow
Event 115	22/05/2002 07:50	25/05/2002 00:15							
115-a	22/05/2002 07:20	26/05/2002 15:00	-19	56	21/05/2002 21:29	23/05/2002 10:15	Y	4b	fast
Event 116	07/07/2002 14:00	09/07/2002 13:55							
116-a	07/07/2002 11:27	09/07/2002 21:00	9999	90	07/07/2002 11:15	99/99/9999 99:99	N	1b	ND
Event 117	16/07/2002 13:20	30/07/2002 16:30							
117-a	16/07/2002 12:30	20/07/2002 18:20	16	1	15/07/2002 19:58	17/07/2002 15:26	Y	4b	fast
117-b	20/07/2002 18:20	24/07/2002 04:00	-13	-90	20/07/2002 21:04	22/07/2002 04:51	Y	2c	fast
117-c	24/07/2002 04:00	26/07/2002 20:51	-13	-72	23/07/2002 00:18	25/07/2002 12:59	N	2c	ND
117-d	26/07/2002 20:51	31/07/2002 12:00	-19	-26	26/07/2002 20:51	29/07/2002 12:40	N	2b	ND
Event 118	14/08/2002 03:35	15/08/2002 20:40							
118-a	14/08/2002 03:35	16/08/2002 10:00	9	54	14/08/2002 01:47	15/08/2002 18:30	Y	2a	fast
Event 119	16/08/2002 22:10	20/08/2002 05:10							
119-a	16/08/2002 13:00	18/08/2002 23:30	-6	-17	16/08/2002 11:36	18/08/2002 18:10	N	2b	slow
119-b	18/08/2002 23:30	20/08/2002 08:22	-12	19	18/08/2002 21:12	99/99/9999 99:99	N	1b	fast
119-c	20/08/2002 08:22	21/08/2002 16:00	-10	38	20/08/2002 08:22	99/99/9999 99:99	N	1b	slow
Event 120	22/08/2002 03:10	27/08/2002 23:10							
120-a	22/08/2002 02:00	24/08/2002 00:50	-7	62	22/08/2002 01:47	99/99/9999 99:99	N	1b	slow
120-b	24/08/2002 00:50	28/08/2002 14:00	-2	80	24/08/2002 00:49	26/08/2002 10:41	Y	3a	slow
Event 121	06/09/2002 06:25	09/09/2002 17:35							
121-a	06/09/2002 00:00	11/09/2002 12:00	9	-28	05/09/2002 16:18	07/09/2002 16:10	Y	2b	slow

Table continues on the next page

Event	Start time [UT]	End time [UT]	Lat. (N+/S-)	Long. (W+/E-)	Flare time [UT]	Shock time [UT]	Downst. analysis	Event type	Solar wind type
Event 122	01/11/2002 18:40	03/11/2002 00:50							
122-a	01/11/2002 18:40	03/11/2002 00:50	9999	9999	99/99/9999 99:99	99/99/9999 99:99	N	NC	ND
Event 123	09/11/2002 17:10	11/11/2002 21:15							
123-a	09/11/2002 15:00	13/11/2002 00:00	-12	29	09/11/2002 13:08	11/11/2002 11:52	Y	4b	fast
Event 124	25/11/2002 18:35	26/11/2002 19:10							
124-a	25/11/2002 06:00	28/11/2002 12:00	17	-34	24/11/2002 20:14	26/11/2002 21:10	Y	2b	ND
Event 125	28/05/2003 07:55	01/06/2003 08:35							
125-a	28/05/2003 02:00	31/05/2003 02:13	-6	20	28/05/2003 00:17	29/05/2003 18:25	Y	3b	fast
125-b	31/05/2003 02:13	01/06/2003 22:01	-7	65	31/05/2003 02:13	99/99/9999 99:99	N	1b	fast
Event 126	18/06/2003 09:20	22/06/2003 14:05							
126-a	18/06/2003 09:20	23/06/2003 20:00	-8	-61	17/06/2003 22:25	20/06/2003 07:56	Y	2c	fast
Event 127	23/10/2003 00:45	24/10/2003 23:05							
127-a	22/10/2003 22:00	24/10/2003 14:47	-18	-78	22/10/2003 20:06	24/10/2003 14:47	N	2c	
127-b	24/10/2003 14:47	26/10/2003 17:03	-17	-84	23/10/2003 19:50	26/10/2003 07:49	N	2c	slow
Event 128	26/10/2003 18:05	09/11/2003 21:05							
128-a	26/10/2003 17:15	28/10/2003 09:52	2	38	26/10/2003 17:03	28/10/2003 01:31	N	4b	fast
128-b	28/10/2003 09:52	29/10/2003 20:39	-16	-8	28/10/2003 11:00	29/10/2003 05:58	Y	4a	fast
128-c	29/10/2003 20:39	02/11/2003 17:04	-15	2	29/10/2003 20:37	30/10/2003 16:19	Y	4a	fast
128-d	02/11/2003 17:04	04/11/2003 19:29	-14	56	02/11/2003 17:03	04/11/2003 05:59	Y	4b	fast
128-e	04/11/2003 19:29	12/11/2003 00:00	-19	83	04/11/2003 19:29	06/11/2003 21:15	Y	4b	fast
Event 129	20/11/2003 07:15	25/11/2003 07:05							
129-a	20/11/2003 07:15	26/11/2003 14:00	2	17	20/11/2003 23:53	99/99/9999 99:99	N	NC	fast
Event 130	02/12/2003 12:50	06/12/2003 06:05							
130-a	02/12/2003 12:00	07/12/2003 00:00	-14	90	02/12/2003 10:00	05/12/2003 03:21	Y	2a	ND
	2004								
Event 131	11/04/2004 06:45	12/04/2004 23:05							
131-a	11/04/2004 05:00	13/04/2004 21:00	-14	47	11/04/2004 03:54	12/04/2004 17:45	Y	2a	slow
Event 132	23/07/2004 15:05	28/07/2004 18:10							
132-a	22/07/2004 14:00	25/07/2004 14:19	4	-10	22/07/2004 07:41	24/07/2004 05:45	Y	2b	fast
132-b	25/07/2004 14:19	30/07/2004 00:00	4	33	25/07/2004 14:19	26/07/2004 22:30	Y	4b	fast
Event 133	31/07/2004 20:55	02/08/2004 14:45							
133-a	31/07/2004 20:55	02/08/2004 14:45	9999	95	31/07/2004 05:16	99/99/9999 99:99	N	NC	fast
Event 134	13/09/2004 19:55	17/09/2004 18:15							
134-a	12/09/2004 23:00	18/09/2004 18:00	4	-42	12/09/2004 00:56	13/09/2004 19:40	Y	2b	slow
Event 135	19/09/2004 18:05	21/09/2004 15:10							
135-a	19/09/2004 17:24	23/09/2004 00:00	3	58	19/09/2004 17:12	22/09/2004 06:00	Y	3a	slow
Event 136	01/11/2004 06:10	02/11/2004 20:15							
136-a	01/11/2004 06:10	02/11/2004 20:15	9999	90	01/11/2004 05:55	99/99/9999 99:99	N	1a	slow
Event 137	07/11/2004 02:50	15/11/2004 02:45							
137-a	06/11/2004 20:00	07/11/2004 15:54	10	-6	06/11/2004 02:06	99/99/9999 99:99	N	1b	ND
137-b	07/11/2004 15:54	09/11/2004 16:59	9	17	07/11/2004 15:42	09/11/2004 09:10	N	4b	fast
137-c	09/11/2004 16:59	10/11/2004 01:59	7	51	09/11/2004 16:59	99/99/9999 99:99	N	1a	fast
137-d	10/11/2004 01:59	17/11/2004 12:00	9	49	10/11/2004 01:59	11/11/2004 17:00	Y	4b	ND
Event 138	05/12/2004 07:35	06/12/2004 15:45							
138-a	03/12/2004 08:00	07/12/2004 18:00	8	2	03/12/2004 00:06	05/12/2004 07:00	Y	2a	ND
	2005								
Event 139	15/01/2005 08:25	23/01/2005 17:35							
139-a	15/01/2005 06:42	15/01/2005 22:37	16	-4	15/01/2005 06:30	99/99/9999 99:99	N	1b	ND
139-b	15/01/2005 22:37	17/01/2005 09:52	15	5	15/01/2005 22:25	17/01/2005 08:00	N	4b	fast
139-c	17/01/2005 09:52	20/01/2005 06:30	15	25	17/01/2005 09:52	18/01/2005 14:00	Y	4b	fast
139-d	20/01/2005 06:30	26/01/2005 00:00	14	61	20/01/2005 06:39	21/01/2005 16:45	Y	4b	fast
Event 140	06/05/2005 06:55	08/05/2005 20:35							
140-a	06/05/2005 06:55	08/05/2005 20:35	9999	9999	99/99/9999 99:99	99/99/9999 99:99	N	NC	ND
Event 141	13/05/2005 21:00	17/05/2005 12:30							
141-a	13/05/2005 18:00	18/05/2005 22:30	12	-11	13/05/2005 16:13	15/05/2005 02:05	Y	4b	fast
Event 142	16/06/2005 20:50	18/06/2005 05:55							
142-a	16/06/2005 20:50	19/06/2005 00:00	9	85	16/06/2005 20:01	99/99/9999 99:99	N	1b	fast
Event 143	13/07/2005 18:10	20/07/2005 01:55							
143-a	13/07/2005 16:30	14/07/2005 10:16	11	90	13/07/2005 14:01	99/99/9999 99:99	N	1b	fast
143-b	14/07/2005 10:16	17/07/2005 11:29	8	89	14/07/2005 10:16	16/07/2005 01:50	Y	3a	slow
143-c	17/07/2005 11:29	21/07/2005 11:00	9999	100	17/07/2005 11:29	99/99/9999 99:99	N	1b	slow
Event 144	26/07/2005 23:20	04/08/2005 21:40							
144-a	25/07/2005 00:00	30/07/2005 06:17	11	-90	24/07/2005 13:45	27/07/2005 18:48	Y	3b	slow
144-b	30/07/2005 06:17	07/08/2005 00:00	12	-60	30/07/2005 06:17	01/08/2005 06:05	N	3b	fast
Event 145	22/08/2005 03:35	22/08/2005 03:35							
145-a	22/08/2005 00:42	22/08/2005 16:58	-11	54	22/08/2005 00:44	99/99/9999 99:99	N	1b	ND
145-b	22/08/2005 16:58	27/08/2005 23:00	12	60	22/08/2005 16:46	24/08/2005 05:45	Y	4b	slow
Event 146	07/09/2005 23:25	16/09/2005 22:55							
146-a	07/09/2005 20:00	13/09/2005 19:20	-6	-89	07/09/2005 17:17	09/09/2005 13:25	Y	4b	ND
146-b	13/09/2005 19:20	16/09/2005 22:55	-9	-10	13/09/2005 19:19	15/09/2005 08:30	Y	4b	ND

Table continues on the next page

Event	Start time [UT]	End time [UT]	Lat. (N+/S-)	Long. (W+/E-)	Flare time [UT]	Shock time [UT]	Downst. analysis	Event type	Solar wind type
	2006								
Event 147	05/12/2006 17:35	16/12/2006 22:50							
147-a	05/12/2006 10:00	06/12/2006 18:42	-7	-79	05/12/2006 02:18	99/99/9999 99:99	N	1b	slow
147-b	06/12/2006 18:42	13/12/2006 02:15	-7	-68	06/12/2006 18:29	08/12/2006 04:20	Y	4b	fast
147-c	13/12/2006 02:15	14/12/2006 21:18	-6	23	13/12/2006 02:14	14/12/2006 13:52	Y	4b	fast
147-d	14/12/2006 21:18	16/12/2006 22:50	-6	44	14/12/2006 21:07	99/99/9999 99:99	N	1a	fast
	2010								
Event 148	14/08/2010 10:20	15/08/2010 11:50							
148-a	14/08/2010 10:20	15/08/2010 11:50	12	56	14/08/2010 09:38	99/99/9999 99:99	N	1b	slow
Event 149	18/08/2010 06:00	19/08/2010 11:55							
149-a	18/08/2010 06:00	19/08/2010 11:55	18	88	18/08/2010 04:45	99/99/9999 99:99	N	1b	slow
	2011								
Event 150	07/03/2011 20:10	12/03/2011 07:20							
150-a	07/03/2011 20:10	13/03/2011 18:00	30	48	07/03/2011 19:43	10/03/2011 05:45	Y	3a	slow
Event 151	21/03/2011 02:30	22/03/2011 16:30							
151-a	21/03/2011 02:30	23/03/2011 12:00	16	130	21/03/2011 02:15	99/99/9999 99:99	N	1b	slow
Event 152	05/06/2011 16:00	18/06/2011 15:09							
152-a	05/06/2011 16:00	07/06/2011 06:15	-16	145	04/06/2011 21:45	07/06/2011 09:14	N	3a	slow
152-b	07/06/2011 06:15	14/06/2011 06:15	-22	53	07/06/2011 06:15	10/06/2011 08:11	Y	3a	slow
152-c	14/06/2011 06:15	19/06/2011 19:00	19	-76	14/06/2011 04:45	17/06/2011 02:05	Y	2c	fast
Event 153	04/08/2011 04:34	08/08/2011 08:30							
153-a	04/08/2011 04:34	08/08/2011 16:00	16	38	04/08/2011 03:40	05/08/2011 18:40	Y	3a	slow
Event 154	09/08/2011 07:59	10/08/2011 23:19							
154-a	09/08/2011 07:59	11/08/2011 14:00	14	69	09/08/2011 07:47	99/99/9999 99:99	N	1b	fast
Event 155	06/09/2011 23:15	09/09/2011 11:35							
155-a	06/09/2011 23:15	10/09/2011 14:00	14	18	06/09/2011 22:12	09/09/2011 11:48	Y	3b	slow
Event 156	22/09/2011 10:32	30/09/2011 06:04							
156-a	22/09/2011 10:32	25/09/2011 11:12	9	-89	22/09/2011 10:29	25/09/2011 10:46	N	3b	slow
156-b	25/09/2011 11:12	01/10/2011 18:00	10	-56	24/09/2011 12:33	26/09/2011 11:44	N	3b	slow
Event 157	22/10/2011 10:30	25/10/2011 18:45							
157-a	22/10/2011 10:30	26/10/2011 16:00	27	87	22/10/2011 10:00	24/10/2011 17:49	Y	2a	slow
Event 158	03/11/2011 22:25	06/11/2011 16:00							
158-a	03/11/2011 22:25	06/11/2011 16:00	3	-152	03/11/2011 22:16	99/99/9999 99:99	N	1b	slow
Event 159	26/11/2011 07:30	30/11/2011 00:20							
159-a	26/11/2011 07:30	30/11/2011 15:00	11	47	26/11/2011 06:09	28/11/2011 21:00	Y	3a	slow
	2012								
Event 160	19/01/2012 14:39	03/02/2012 03:54							
160-a	19/01/2012 14:39	23/01/2012 04:00	32	-27	19/01/2012 13:43	22/01/2012 05:33	Y	2b	slow
160-b	23/01/2012 04:00	27/01/2012 18:00	33	21	23/01/2012 03:38	24/01/2012 14:40	Y	4b	slow
160-c	27/01/2012 18:00	04/02/2012 00:00	33	85	27/01/2012 17:37	30/01/2012 15:43	Y	4b	slow
Event 161	24/02/2012 19:00	27/02/2012 21:24							
161-a	24/02/2012 19:00	29/02/2012 00:00	10	-88	24/02/2012 00:45	26/02/2012 21:07	Y	2c	slow
Event 162	05/03/2012 03:00	17/03/2012 02:24							
162-a	05/03/2012 03:00	06/03/2012 23:30	19	-58	05/03/2012 02:30	07/03/2012 03:28	N	2c	slow
162-b	06/03/2012 23:30	13/03/2012 16:30	18	-31	07/03/2012 00:02	08/03/2012 10:53	Y	4a	slow
162-c	13/03/2012 16:30	18/03/2012 03:00	17	66	13/03/2012 17:12	15/03/2012 12:42	Y	3a	fast
Event 163	17/05/2012 02:05	20/05/2012 15:15							
163-a	17/05/2012 02:05	21/05/2012 17:00	7	88	17/05/2012 01:25	20/05/2012 01:20	Y	3a	slow
Event 164	26/05/2012 21:00	29/05/2012 04:54							
164-a	26/05/2012 21:00	30/05/2012 20:00	16	122	26/05/2012 20:46	99/99/9999 99:99	N	1b	slow
Event 165	14/06/2012 14:19	18/06/2012 10:00							
165-a	14/06/2012 14:19	18/06/2012 10:00	-19	-6	14/06/2012 12:51	16/06/2012 19:34	Y	2b	slow
Event 166	06/07/2012 23:35	10/07/2012 22:05							
166-a	06/07/2012 23:35	08/07/2012 16:59	-13	59	06/07/2012 23:01	99/99/9999 99:99	N	1b	slow
166-b	08/07/2012 16:59	11/07/2012 14:00	-14	86	08/07/2012 16:23	99/99/9999 99:99	N	1a	slow
Event 167	12/07/2012 17:05	16/07/2012 15:00							
167-a	12/07/2012 17:05	16/07/2012 15:00	-13	3	12/07/2012 15:36	14/07/2012 17:39	Y	3b	slow
Event 168	17/07/2012 13:59	26/07/2012 18:00							
168-a	17/07/2012 13:59	19/07/2012 04:30	-15	88	17/07/2012 12:02	99/99/9999 99:99	N	1a	slow
168-b	19/07/2012 04:30	23/07/2012 02:30	-13	88	19/07/2012 04:16	20/07/2012 04:00	Y	3a	slow
168-c	23/07/2012 02:30	26/07/2012 18:00	2	125	23/07/2012 02:35	99/99/9999 99:99	N	1b	slow
Event 169	01/09/2012 01:59	05/09/2012 07:39							
169-a	01/09/2012 00:00	06/09/2012 16:00	-19	-42	31/08/2012 19:59	03/09/2012 11:21	Y	2b	slow
Event 170	28/09/2012 00:20	01/10/2012 18:00							
170-a	28/09/2012 00:20	02/10/2012 08:00	9	32	27/09/2012 23:35	30/09/2012 22:18	Y	3a	slow
Event 171	14/12/2012 12:20	17/12/2012 18:00							
171-a	14/12/2012 12:20	17/12/2012 18:00	9999	9999	99/99/9999 99:99	16/12/2012 16:50	N	NC	slow
	2013								
Event 172	15/03/2013 18:45	18/03/2013 19:59							
172-a	15/03/2013 18:45	18/03/2013 19:59	9	-6	15/03/2013 05:46	17/03/2013 05:21	Y	2b	slow

In Tables A.5 and A.6 are shown the full lists of Helios events gathered by our group. Both lists have identical structure. First column indicate the event number. Second and third columns indicate the date and time of the solar flare (X-ray) and flare longitude as seen from Earth. Fourth and fifth give the particle onset time and end time at the spacecraft. Sixth column shows the shock time at the spacecraft. In case of more that one shock detected, they are listed vertically in order; this column is left empty if no shock was detected. Seventh and eighth columns give the helioradial distance of the spacecraft at the event time and the longitudinal separation to the solar source. Ninth and tenth columns lists if the events were included in the analysis of the downstream fluence, and the associated references checked (see table's footnotes).

TABLE A.5: Helios 1 event list.

			Helios 1						
Event	**Flare time [UT]**	**Source long.**	**Start time [UT]**	**End time [UT]**	**Shock time [UT]**	**S/C radial dist. [AU]**	**Relative source long.**	**Downst. analysis**	**Refs.**
	1975								
1	21/08/1975 15:19	W74	21/08/1975 15:19	22/08/1975 15:19		0.63	E96	N	1
2	22/08/1975 01:16	W81	22/08/1975 01:16	23/08/1975 01:16		0.63	E90	N	1
	1976								
3	21/03/1976 00:00	W33	21/03/1976 00:00	22/03/1976 00:00		0.36	W08	N	2
4	23/03/1976 00:00	E90	23/03/1976 08:00	28/03/1976 00:00		0.34	E124	N	2
5	28/03/1976 19:38	E28	28/03/1976 19:20	31/03/1976 09:59		0.31	E89	N	3
6	30/04/1976 20:48	W46	30/04/1976 20:48	04/05/1976 12:00		0.66	E113	N	4
	1977								
7	04/04/1977 00:00	E77	04/04/1977 12:59	07/04/1977 08:00		0.37	E81	N	2
8	07/09/1977 22:43	E90	07/09/1977 22:43	11/09/1977 12:00		0.76	W134	N	1
9	12/09/1977 10:14	E42	12/09/1977 10:14	13/09/1977 10:14		0.72	E179	N	3
10	19/09/1977 10:53	W57	19/09/1977 10:53	23/09/1977 12:00	20/09/1977 19:07 20/09/1977 20:37	0.65	E83	Y	3
11	24/09/1977 05:49	W120	24/09/1977 05:49	30/09/1977 00:00	25/09/1977 02:40	0.59	E24	Y	4
12	12/10/1977 01:52	W02	12/10/1977 01:52	13/10/1977 01:52		0.36	W178	N	3
13	07/11/1977 00:00	E64	07/11/1977 00:00	10/11/1977 12:00	07/11/1977 18:14	0.47	E06	N	2
14	22/11/1977 10:06	W40	22/11/1977 10:06	26/11/1977 12:00	24/11/1977 22:27	0.65	W80	Y	3
15	06/12/1977 19:37	W18	06/12/1977 19:37	09/12/1977 14:00		0.8	W53	N	5
	1978								
16	06/03/1978 12:12	E20	06/03/1978 12:12	12/03/1978 12:00	08/03/1978 08:44	0.84	W36	Y	3
17	08/04/1978 02:39	W11	08/04/1978 02:00	10/04/1978 03:59	09/04/1978 07:18	0.52	W51	Y	3
18	11/04/1978 14:17	W56	11/04/1978 14:17	13/04/1978 02:00		0.47	W91	N	3
19	28/04/1978 13:34	E38	28/04/1978 13:34	06/05/1978 18:00	29/04/1978 03:48 30/04/1978 11:15 02/05/1978 13:30	0.31	E71	Y	3
20	07/05/1978 03:36	W68	07/05/1978 03:36	08/05/1978 03:35	07/05/1978 20:05	0.36	E15	Y	3
21	31/05/1978 10:47	W43	31/05/1978 10:47	03/06/1978 16:00	02/06/1978 08:18	0.65	E88	N	3
22	22/06/1978 17:09	E18	22/06/1978 17:09	27/06/1978 12:00	26/06/1978 11:40	0.85	E154	N	6
23	23/09/1978 10:20	W50	23/09/1978 10:20	01/10/1978 07:19	25/09/1978 02:29	0.76	E71	Y	3
24	01/10/1978 07:19	E57	01/10/1978 07:19	02/10/1978 07:19		0.68	W180	N	1
25	09/10/1978 19:51	W61	09/10/1978 19:51	12/10/1978 03:59		0.58	E68	N	1
26	13/10/1978 12:38	W01	13/10/1978 12:38	15/10/1978 21:59	13/10/1978 13:41 13/10/1978 20:41 14/10/1978 13:49	0.53	E132	N	1
27	05/11/1978 09:18	W36	05/11/1978 09:18	06/11/1978 09:18		0.31	E178	N	7
28	10/11/1978 01:22	E01	10/11/1978 00:59	12/11/1978 15:59		0.33	W116	N	3
29	28/11/1978 05:50	E47	28/11/1978 05:45	29/11/1978 04:15	29/11/1978 03:17	0.54	W16	N	3
30	11/12/1978 19:44	E14	11/12/1978 19:44	17/12/1978 00:00		0.7	W39	N	3
31	14/12/1978 00:05	W78	14/12/1978 00:05	19/12/1978 00:00		0.72	W130	N	8
	1979								
32	03/04/1979 02:13	W14	03/04/1979 01:15	08/04/1979 00:00	03/04/1979 19:44	0.75	W84	Y	3
33	14/04/1979 14:43	E08	14/04/1979 14:43	15/04/1979 16:42	15/04/1979 04:04	0.62	W57	Y	9
34	22/04/1979 23:25	E10	22/04/1979 23:25	23/04/1979 23:25		0.52	W47	N	10
35	27/04/1979 06:51	E17	27/04/1979 06:51	02/05/1979 00:00	28/04/1979 04:27	0.47	W31	Y	9

Table continues on the next page

Event	Flare time [UT]	Source long.	Helios 1						Refs.
			Start time [UT]	End time [UT]	Shock time [UT]	S/C radial dist. [AU]	Relative source long.	Downst. analysis	
36	04/05/1979 17:01	W55	04/05/1979 17:01	05/05/1979 17:01		0.37	W83	N	9
37	24/05/1979 16:55	E95	24/05/1979 16:55	27/05/1979 18:00		0.38	E170	N	11
38	27/05/1979 06:50	W65	28/05/1979 00:00	01/06/1979 00:00	28/05/1979 18:41	0.41	E21	N	7
39	05/06/1979 05:13	E14	05/06/1979 05:13	13/06/1979 00:00	11/06/1979 20:54	0.52	E119	N	1
40	04/07/1979 19:02	E35	04/07/1979 19:02	05/07/1979 19:02	05/07/1979 11:30	0.83	E157	N	8
41	15/11/1979 21:39	W35	15/11/1979 21:39	20/11/1979 00:00		0.33	E133	N	3
42	27/11/1979 06:19	W03	27/11/1979 06:19	30/11/1979 23:00		0.34	W127	N	7
43	12/12/1979 17:13	W79	12/12/1979 17:13	13/12/1979 17:13	13/12/1979 08:53	0.54	W160	N	12
44	13/12/1979 08:18	E16	13/12/1979 08:18	14/12/1979 08:18	13/12/1979 08:53	0.54	W63	N	13
45	19/12/1979 22:15	E36	19/12/1979 22:15	25/12/1979 12:00	23/12/1979 13:02	0.62	W37	Y	3
	1980								
46	10/01/1980 05:15	E09	10/01/1980 05:15	15/01/1980 22:59	10/01/1980 23:09 13/01/1980 07:29	0.82	W57	Y	9
47	12/01/1980 20:20	W55	12/01/1980 20:20	13/01/1980 20:20	13/01/1980 07:29	0.84	W121	N	5
48	04/04/1980 15:10	W34	04/04/1980 15:10	05/04/1980 15:10		0.85	W120	N	3
49	29/04/1980 12:57	W71	29/04/1980 12:57	01/05/1980 15:59	01/05/1980 06:19 01/05/1980 13:46	0.61	W151	N	9
50	01/05/1980 16:31	E63	01/05/1980 16:31	03/05/1980 15:59		0.58	W15	N	3
51	03/05/1980 12:39	E43	03/05/1980 12:39	07/05/1980 00:00	04/05/1980 18:27	0.56	W33	Y	8
52	11/05/1980 15:00	E16	11/05/1980 15:00	14/05/1980 18:00		0.46	W48	N	9
53	21/05/1980 21:07	W15	21/05/1980 20:44	24/05/1980 10:59	22/05/1980 20:56	0.34	W47	Y	9
54	28/05/1980 15:52	W28	28/05/1980 15:52	30/05/1980 15:00	29/05/1980 11:05	0.31	W23	N	14
55	28/05/1980 17:05	W35	28/05/1980 17:05	29/05/1980 17:05	29/05/1980 11:05	0.31	W30	N	14
56	28/05/1980 19:24	W33	28/05/1980 19:24	29/05/1980 19:24	29/05/1980 11:05	0.31	W28	Y	14
57	28/05/1980 23:42	W39	28/05/1980 23:42	29/05/1980 23:42	29/05/1980 11:05	0.31	W34	N	14
58	02/06/1980 09:00	W93	02/06/1980 09:00	05/06/1980 10:00	03/06/1980 09:13	0.32	W58	Y	3
59	07/06/1980 03:13	W74	07/06/1980 03:13	08/06/1980 07:59		0.37	W15	N	9
60	08/06/1980 10:37	W87	08/06/1980 10:37	09/06/1980 07:00		0.38	W24	N	3
61	21/06/1980 01:14	W88	21/06/1980 01:14	23/06/1980 13:59	22/06/1980 20:34	0.55	E06	Y	3
62	27/06/1980 16:12	W67	27/06/1980 16:12	28/06/1980 16:12		0.63	E33	N	12
63	29/06/1980 10:41	W90	29/06/1980 10:41	30/06/1980 10:41		0.64	E11	N	12
64	05/07/1980 22:35	W28	05/07/1980 22:35	10/07/1980 00:00	07/07/1980 11:26	0.72	E77	N	12
65	17/07/1980 05:38	E06	17/07/1980 05:38	24/07/1980 00:00	21/07/1980 01:20	0.81	E113	Y	12
66	15/10/1980 05:42	E55	15/10/1980 05:42	29/10/1980 00:00		0.83	E145	N	9
67	23/10/1980 10:32	W75	23/10/1980 10:32	24/10/1980 10:32		0.76	E16	N	12
68	25/10/1980 09:37	W60	25/10/1980 09:37	26/10/1980 09:37		0.74	E31	N	12
69	10/11/1980 11:40	W54	10/11/1980 11:40	11/11/1980 17:28		0.57	E47	N	15
70	11/11/1980 17:29	W69	11/11/1980 17:29	14/11/1980 06:19	13/11/1980 01:31	0.54	E33	N	15
71	14/11/1980 06:19	W116	14/11/1980 06:19	21/11/1980 00:00	14/11/1980 10:32 14/11/1980 21:10 18/11/1980 13:48	0.52	W10	Y	3
72	23/11/1980 17:54	W23	23/11/1980 17:54	29/11/1980 02:00	25/11/1980 09:03	0.39	E104	N	3
73	29/11/1980 23:48	E26	29/11/1980 23:48	30/11/1980 23:48		0.33	E177	N	3
74	09/12/1980 07:03	W40	09/12/1980 07:03	10/12/1980 07:03		0.32	E168	N	7
	1981								
75	14/01/1981 21:05	E02	14/01/1981 21:00	15/01/1981 12:00		0.74	W80	N	9
76	25/01/1981 09:08	E90	25/01/1981 09:08	31/01/1981 00:00	27/01/1981 00:08 27/01/1981 17:48 28/01/1981 15:35	0.83	E09	N	3
77	24/04/1981 14:11	W50	24/04/1981 14:11	25/04/1981 14:11	25/04/1981 11:04	0.81	W151	N	3
78	28/04/1981 22:13	W90	28/04/1981 22:13	29/04/1981 22:13		0.78	E170	N	3
79	30/04/1981 03:07	W90	30/04/1981 03:07	08/05/1981 22:00	02/05/1981 10:47 06/05/1981 17:25	0.77	E170	N	12
80	08/05/1981 22:51	E37	08/05/1981 22:51	10/05/1981 12:29	10/05/1981 03:11	0.68	W61	Y	9
81	10/05/1981 12:07	E90	10/05/1981 12:19	13/05/1981 02:44	11/05/1981 07:08	0.66	W07	Y	3
82	13/05/1981 04:24	E55	13/05/1981 04:24	14/05/1981 06:29	13/05/1981 21:23	0.64	W40	Y	3
83	14/05/1981 08:05	E35	14/05/1981 08:05	16/05/1981 07:59	15/05/1981 16:35	0.63	W59	Y	16
84	16/05/1981 08:58	E14	16/05/1981 08:50	22/05/1981 00:00	17/05/1981 00:00	0.61	W79	Y	3
85	04/06/1981 19:28	W16	04/06/1981 19:28	09/06/1981 22:59		0.36	W69	N	3
86	10/06/1981 06:27	E24	10/06/1981 06:27	10/06/1981 22:00		0.32	E01	N	9
87	17/06/1981 09:50	W47	17/06/1981 09:50	18/06/1981 09:09		0.32	W28	N	9
88	18/06/1981 09:09	W29	18/06/1981 09:09	19/06/1981 09:09	19/06/1981 01:04	0.33	W05	Y	16
89	20/07/1981 13:28	W75	20/07/1981 13:28	22/07/1981 22:00	21/07/1981 23:44	0.71	E15	Y	3
90	24/07/1981 07:53	E55	24/07/1981 07:53	25/07/1981 07:53	24/07/1981 15:33	0.74	E147	N	3
91	07/11/1981 03:54	W39	07/11/1981 03:54	08/11/1981 03:54		0.76	E37	N	12
92	14/11/1981 21:52	W49	14/11/1981 21:52	18/11/1981 21:59	16/11/1981 15:18	0.69	E29	Y	13

Table continues on the next page

Event	Flare time [UT]	Source long.	Helios 1						Refs.
			Start time [UT]	End time [UT]	Shock time [UT]	S/C radial dist. [AU]	Relative source long.	Downst. analysis	
93	19/11/1981 02:29	W100	19/11/1981 02:29	20/11/1981 12:00	20/11/1981 00:54	0.64	W20	Y	13
94	22/11/1981 03:23	W74	22/11/1981 03:23	27/11/1981 12:00	22/11/1981 23:28	0.61	E09	N	9
95	05/12/1981 14:40	W40	05/12/1981 14:40	09/12/1981 06:59		0.43	E62	N	3
96	09/12/1981 19:11	W16	09/12/1981 19:11	14/12/1981 00:00	11/12/1981 21:15	0.38	E98	Y	3
	1982								
97	04/01/1982 06:10	W88	04/01/1982 06:10	05/01/1982 06:10		0.43	E148	N	12
98	10/01/1982 05:32	E90	10/01/1982 05:32	11/01/1982 05:32		0.51	W22	N	17
99	28/01/1982 07:17	E42	28/01/1982 07:17	30/01/1982 08:00		0.72	W56	N	9
100	30/01/1982 23:58	E19	30/01/1982 23:58	05/02/1982 00:00	04/02/1982 06:22	0.75	W78	N	3
101	08/02/1982 12:49	W88	08/02/1982 12:49	09/02/1982 06:00		0.82	E176	N	15
102	09/02/1982 04:07	W90	09/02/1982 06:00	09/02/1982 22:00		0.82	E174	N	12
103	10/02/1982 01:01	E54	10/02/1982 01:01	15/02/1982 00:00	11/02/1982 11:31	0.83	W43	Y	9
104	02/06/1982 15:54	E81	02/06/1982 15:54	03/06/1982 02:30		0.57	W25	N	9
105	03/06/1982 11:40	E72	03/06/1982 11:40	04/06/1982 13:12	04/06/1982 10:00	0.57	W33	N	3
106	06/06/1982 16:30	E26	06/06/1982 16:30	13/06/1982 00:00	08/06/1982 19:10 09/06/1982 10:57 10/06/1982 07:04 12/06/1982 08:46 12/06/1982 12:31 12/06/1982 13:02 12/06/1982 18:29	0.52	W75	N	6
107	27/06/1982 18:09	W90	27/06/1982 18:09	03/07/1982 00:00		0.31	W118	N	12
108	09/07/1982 07:35	E76	09/07/1982 07:35	11/07/1982 01:00	10/07/1982 13:06	0.38	E111	Y	12
109	12/07/1982 09:05	E36	12/07/1982 09:05	14/07/1982 13:12	13/07/1982 03:09	0.42	E81	Y	12
110	17/07/1982 23:09	W36	17/07/1982 23:09	18/07/1982 23:09		0.5	E21	N	12
111	19/07/1982 00:52	W45	19/07/1982 00:52	20/07/1982 00:52		0.51	E16	N	12
112	22/07/1982 17:34	W86	22/07/1982 17:34	28/07/1982 12:00	23/07/1982 07:59	0.56	W21	Y	3
113	08/08/1982 02:05	W65	08/08/1982 02:05	09/08/1982 19:59		0.74	E12	N	9
114	22/11/1982 18:29	W36	22/11/1982 18:29	23/11/1982 20:29	23/11/1982 12:02	0.76	E25	Y	9
115	26/11/1982 02:36	W87	26/11/1982 02:15	03/12/1982 00:00	26/11/1982 17:53	0.73	W26	Y	3
116	07/12/1982 23:40	W89	07/12/1982 23:40	13/12/1982 00:00	08/12/1982 12:59	0.6	W22	Y	3
117	15/12/1982 01:57	E24	15/12/1982 01:57	17/12/1982 15:59		0.51	E100	N	12
118	17/12/1982 18:45	W20	17/12/1982 18:45	19/12/1982 15:00	19/12/1982 03:59	0.47	E60	Y	12
119	19/12/1982 16:32	W75	19/12/1982 16:32	25/12/1982 00:00	20/12/1982 11:08	0.45	E09	Y	3
120	26/12/1982 09:09	E14	26/12/1982 09:51	29/12/1982 15:59	26/12/1982 20:29	0.37	E118	Y	18
	1983								
121	05/01/1983 13:21	W90	05/01/1983 13:21	06/01/1983 13:21		0.31	E66	N	12
122	03/02/1983 06:10	W07	03/02/1983 06:10	06/02/1983 00:00		0.62	W125	N	9
123	03/08/1983 15:15	W02	03/08/1983 15:15	04/08/1983 01:59		0.52	E44	N	9
124	04/08/1983 03:41	W24	04/08/1983 03:41	05/08/1983 10:00		0.52	E23	N	12
	1985								
125	22/01/1985 00:03	W40	22/01/1985 00:03	25/01/1985 21:59	22/01/1985 17:10 23/01/1985 12:04 24/01/1985 11:35	0.41	E24	N	9
121	05/01/1983 13:21	W90	05/01/1983 13:21	06/01/1983 13:21		0.31	E66	N	12
122	03/02/1983 06:10	W07	03/02/1983 06:10	06/02/1983 00:00		0.62	W125	N	9
123	03/08/1983 15:15	W02	03/08/1983 15:15	04/08/1983 01:59		0.52	E44	N	9
124	04/08/1983 03:41	W24	04/08/1983 03:41	05/08/1983 10:00		0.52	E23	N	12
	1985								
125	22/01/1985 00:03	W40	22/01/1985 00:03	25/01/1985 21:59	22/01/1985 17:10	0.41	E24	N	9

[1] Kahler (1982) [2] Gardini et al. (2011) [3] Lario et al. (2006) [4] Cliver et al. (1982) [5] Kallenrode (1993a)
[6] NOAA SEP event list: `http://umbra.nascom.nasa.gov/SEP/`. [7] Heras et al. (1994)
[8] Solar Geophysical Data: `http://www.ngdc.noaa.gov/stp/space-weather/online-publications/stp_sgd/`
[9] Kallenrode et al. (1992a) [10] Sanahuja et al. (1983) [11] Sanahuja and Domingo (1987)
[12] Cane et al. (1986) [13] Reames et al. (1997) [14] Kallenrode and Wibberenz (1991) [15] Kahler et al. (1984) [16] Sanahuja (1988)
[17] Reames et al. (1996) [18] SGD8301.

TABLE A.6: Helios 2 event list.

Event	Flare time [UT]	Source long.	Helios 2						Refs.
			Start time [UT]	End time [UT]	Shock time [UT]	S/C radial dist. [AU]	Relative source long.	Downst. analysis	
	1975								
1	21/08/1975 15:19	W74						N	1
2	22/08/1975 01:16	W81						N	1
	1976								
3	21/03/1976 00:00	W33	21/03/1976 00:00	22/03/1976 00:00		0.59	W36	N	2
4	23/03/1976 00:00	E90	23/03/1976 08:00	28/03/1976 00:00		0.57	E89	N	2
5	28/03/1976 19:38	E28	28/03/1976 19:20	31/03/1976 09:59	30/03/1976 04:31 30/03/1976 17:44	0.49	E34	Y	3
6	30/04/1976 20:48	W46	30/04/1976 20:48	04/05/1976 12:00		0.43	E109	N	4
	1977								
7	04/04/1977 00:00	E77	04/04/1977 12:59	07/04/1977 08:00		0.5	E77	N	2
8	07/09/1977 22:43	E90	07/09/1977 22:43	11/09/1977 12:00		0.81	W107	N	1
9	12/09/1977 10:14	E42	12/09/1977 10:14	13/09/1977 10:00		0.78	W154	N	3
10	19/09/1977 10:53	W57	19/09/1977 10:53	23/09/1977 12:00		0.71	E108	N	3
11	24/09/1977 05:49	W120	24/09/1977 05:49	30/09/1977 00:00	25/09/1977 12:51 26/09/1977 12:06	0.66	E47	Y	4
12	12/10/1977 01:52	W02	12/10/1977 01:52	13/10/1977 01:04		0.43	W171	N	3
13	07/11/1977 00:00	E64	07/11/1977 00:00	11/11/1977 12:00	07/11/1977 18:54	0.39	E27	N	2
14	22/11/1977 10:06	W40	22/11/1977 10:06	26/11/1977 12:00	23/11/1977 16:08 24/11/1977 06:10	0.59	W49	Y	3
15	06/12/1977 19:37	W18	06/12/1977 19:37	09/12/1977 14:00		0.76	W20	N	5
	1978								
16	06/03/1978 12:12	E20	06/03/1978 12:12	12/03/1978 12:00	07/03/1978 23:54 11/03/1978 13:39	0.86	W03	Y	3
17	08/04/1978 02:39	W11	08/04/1978 02:00	10/04/1978 03:59	09/04/1978 07:16	0.54	W22	Y	3
18	11/04/1978 14:17	W56	11/04/1978 14:17	12/04/1978 16:00	12/04/1978 14:14	0.48	W62	Y	3
19	28/04/1978 13:34	E38	28/04/1978 13:34	06/05/1978 18:00	29/04/1978 02:56	0.29	E97	N	3
20	07/05/1978 03:36	W68	07/05/1978 03:36	08/05/1978 03:03	07/05/1978 22:22	0.33	E48	N	3
21	31/05/1978 10:47	W43	31/05/1978 10:47	03/06/1978 16:00		0.64	E126	N	3
22	22/06/1978 17:09	E18	22/06/1978 17:09	27/06/1978 12:00		0.85	W168	N	6
23	23/09/1978 10:20	W50	23/09/1978 10:20	01/10/1978 07:02	25/09/1978 01:26	0.74	E108	Y	3
24	01/10/1978 07:19	E57	01/10/1978 07:19	02/10/1978 07:02		0.66	W142	N	1
25	09/10/1978 19:51	W61	09/10/1978 19:51	12/10/1978 03:59		0.55	E106	N	1
26	13/10/1978 12:38	W01	13/10/1978 12:38	15/10/1978 21:59		0.49	E172	N	1
27	05/11/1978 09:18	W36	05/11/1978 09:18	06/11/1978 09:01		0.3	W123	N	7
28	10/11/1978 01:22	E01	10/11/1978 00:59	15/11/1978 00:00		0.34	W57	N	3
29	28/11/1978 05:50	E47	28/11/1978 05:45	29/11/1978 04:00		0.58	E31	N	3
30	11/12/1978 19:44	E14	11/12/1978 19:44	14/12/1978 00:00	13/12/1978 02:46 13/12/1978 12:45	0.74	E05	Y	3
31	14/12/1978 00:05	W78	14/12/1978 00:05	19/12/1978 00:00		0.76	W87	N	8
	1979								
32	03/04/1979 02:13	W14	03/04/1979 01:15	08/04/1979 00:00	04/04/1979 13:30 05/04/1979 15:28	0.68	W41	Y	3
33	14/04/1979 14:43	E08	14/04/1979 14:43	15/04/1979 16:03		0.53	W10	N	9
34	22/04/1979 23:25	E10	22/04/1979 23:25	23/04/1979 23:02	23/04/1979 15:15	0.42	E06	N	10
35	27/04/1979 06:51	E17	27/04/1979 06:51	02/05/1979 00:00		0.37	E29	N	9
36	04/05/1979 17:01	W55	04/05/1979 17:01	05/05/1979 17:00		0.29	W07	N	9
37	24/05/1979 16:55	E95	24/05/1979 16:55	27/05/1979 18:00		0.48	W120	N	11
38	27/05/1979 06:50	W65	28/05/1979 00:00	01/06/1979 00:00	28/05/1979 07:57 28/05/1979 10:28 30/05/1979 04:41	0.5	E86	N	7
39	05/06/1979 05:13	E14	05/06/1979 05:13	13/06/1979 00:00	11/06/1979 06:15 11/06/1979 19:04	0.62	E175	N	1
40	04/07/1979 19:02	E35	04/07/1979 19:02	05/07/1979 19:00		0.89	W158	N	8
41	15/11/1979 21:39	W35	15/11/1979 21:39	20/11/1979 00:00		0.33	W109	N	3
42	27/11/1979 06:19	W03	27/11/1979 06:19	30/11/1979 23:00	28/11/1979 15:59	0.48	W36	Y	7
43	12/12/1979 17:13	W79	12/12/1979 17:13	13/12/1979 17:00	13/12/1979 12:23	0.68	W97	N	12
44	13/12/1979 08:18	E16	13/12/1979 08:18	14/12/1979 08:00	13/12/1979 12:23	0.68	W01	N	13
45	19/12/1979 22:15	E36	19/12/1979 22:15	19/12/1979 06:59		0.75	E20	N	3
	1980								
46	10/01/1980 05:15	E09	10/01/1980 05:15	15/01/1980 22:59	10/01/1980 20:48	0.9	W08	N	9
47	12/01/1980 20:20	W55	12/01/1980 20:20	13/01/1980 20:02		0.92	W72	N	5

[1] Kahler (1982) [2] Gardini et al. (2011) [3] Lario et al. (2006) [4] Cliver et al. (1982) [5] Kallenrode (1993a)
[6] NOAA SEP event list: `http://umbra.nascom.nasa.gov/SEP/`. [7] Heras et al. (1994)
[8] Solar Geophysical Data: `http://www.ngdc.noaa.gov/stp/space-weather/online-publications/stp_sgd/`
[9] Kallenrode et al. (1992a) [10] Sanahuja et al. (1983) [11] Sanahuja and Domingo (1987) [12] Cane et al. (1986)
[13] Reames et al. (1997)

Appendix B

SOL2UP event types

B.1 Classification of SEP events in SOL2UP

The SEP events in the SREL (Table A.4) are classified into ten categories or event types as discussed in Aran et al. (2017a). Specifically, 249 out of 263 SEP enhancements were classified and 14 could not be distributed into any of the categories. Figure B.1 shows the number of events per each event-type. The event types and the corresponding reference SEP events are the following:

- **Type 1.** – Events without observed shock
  - **Type 1a.** Peak Intensity > 10 $[\mathrm{cm^2\,sr\,s\,MeV}]^{-1}$ [$E = 8.7$ MeV] $\Rightarrow$ December 14, 2006 SEP event.
  - **Type 1b.** Peak Intensity < 10 $[\mathrm{cm^2\,sr\,s\,MeV}]^{-1}$ [$E = 8.7$ MeV] $\Rightarrow$ June 10, 2000 SEP event.
- **Type 2** – Gradual, Low-Energy Cases [No SEP enhancement for $E > 66$ MeV protons in the upstream region of the events]
  - **Type 2a.** Solar origin between W120 and W00 $\Rightarrow$ April 4, 2000 SEP event.
  - **Type 2b.** Solar origin between W00 and E45 (both included) $\Rightarrow$ June 6, 2000 SEP event.
  - **Type 2c.** Solar origin between E45 and E90 $\Rightarrow$ March 6, 1989 SEP event.
- **Type 3** – Gradual, High-Energy Cases
  - **Type 3a** Peak Intensity < 50 $[\mathrm{cm^2\,sr\,s\,MeV}]^{-1}$ [$E = 8.7$ MeV] and solar origin at or westward from W30$\Rightarrow$ March 13, 2012 SEP event.
  - **Type 3b** Peak Intensity < 50 $[\mathrm{cm^2\,sr\,s\,MeV}]^{-1}$ [$E = 8.7$ MeV] and solar origin eastward from W30 $\Rightarrow$ March 29, 2001 SEP event.

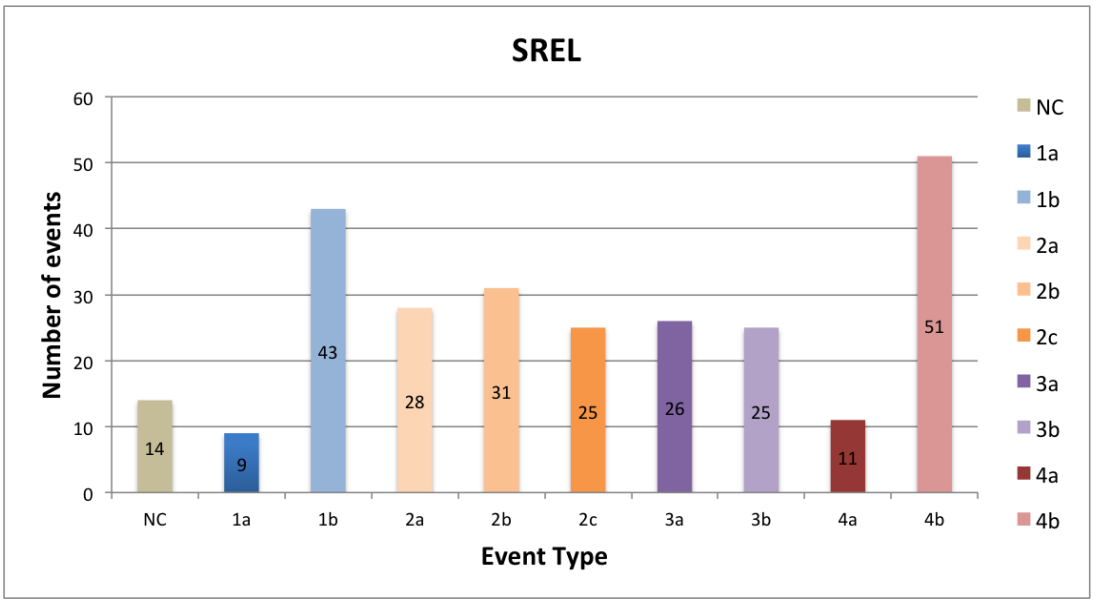

FIGURE B.1: Number of events per event type

► **Type 4** – Large Gradual, High-Energy Cases

- **Type 4a-np** Peak Intensity > 500 [cm^2 sr s MeV]$^{-1}$ [E = 8.7 MeV] and > 1 [cm^2 s sr MeV]$^{-1}$ at [E = 79.5 MeV] and intensity profiles do not show a prompt component ⇒ September 24, 2001 SEP event.
- **Type 4a-p** Peak Intensity > 500 [cm^2 sr s MeV]$^{-1}$ [E = 8.7 MeV] and > 1 [cm^2 s sr MeV]$^{-1}$ at [E = 79.5 MeV] and intensity profiles show a prompt component ⇒ October 29, 2003 SEP event.
- **Type 4b.** Peak Intensity ≥ 50 [cm^2 sr s MeV]$^{-1}$ [E = 8.7 MeV] ⇒ December 13, 2006 SEP event.

B.2 Radial dependences

Tables B.1 and B.2 show the radial indices derived from the modelling of the reference events with SOLPENCO2. These indices correspond to the fitting of a power-law with the heliocentric radial distance of the peak intensities and upstream fluences of the SOLPENCO2 synthetic proton intensity-time profiles, for each SEPEM reference energy channel.

TABLE B.1: Peak Intensities: radial indices for the ten event Types.

Energy [MeV]	1a	1b	2a	2b	2c	3a	3b	4a-np	4a-p	4b
6.01	−2.34	−1.77	−1.82	0.81	1.10	−2.08	−1.55	−0.94	−1.14	−0.50
8.70	−2.21	−1.72	−1.86	1.06	1.11	−2.04	−1.74	−0.94	−1.52	−0.99
12.58	−2.09	−1.66	−1.77	1.31	1.12	−1.95	−1.71	−0.87	−1.90	−1.36
18.18	−1.99	−1.61	−1.69	1.53	1.27	−1.86	−1.63	−0.78	−2.71	−1.72
26.30	−1.89	−1.57	−1.62	1.74	1.27	−1.76	−1.57	−0.69	−2.44	−1.78
38.03	−1.80	−1.53	−1.56	1.72	1.27	−1.64	−1.51	−0.59	−2.41	−1.67
54.99	−1.72	−1.50	−1.51	1.72	1.26	−1.59	−1.46	−0.50	−2.37	−1.75
79.53	−1.65	−1.48	−1.47	1.72	1.26	−1.61	−1.42	−0.37	−2.31	−1.75
115.01	−1.59	−1.46	−1.43	1.73	1.25	−1.60	−1.38	−0.23	−2.24	−1.67
166.31	−1.51	−1.43	−1.35	1.74	1.25	−1.58	−1.31	−0.14	−2.18	−1.59
244.22	−1.43	−1.40	−1.31	1.73	1.25	−1.55	−1.27	−0.04	−2.10	−1.59

TABLE B.2: Upstream fluences: radial indices for the ten event Types.

Energy [MeV]	1a	1b	2a	2b	2c	3a	3b	4a-np	4a-p	4b
6.01	−1.47	−1.20	−0.29	2.11	1.21	−0.96	0.25	0.31	−0.34	0.58
8.70	−1.39	−1.16	−0.50	2.40	1.26	−0.99	0.02	0.33	−0.41	0.26
12.58	−1.32	−1.12	−0.53	2.70	1.33	−0.98	−0.19	0.44	−0.51	−0.06
18.18	−1.25	−1.09	−0.55	2.96	1.85	−0.98	−0.27	0.56	−0.71	−0.35
26.30	−1.19	−1.06	−0.55	3.21	1.87	−0.98	−0.33	0.69	−0.73	−0.63
38.03	−1.14	−1.04	−0.55	3.22	1.90	−0.99	−0.37	0.82	−0.83	−0.80
54.99	−1.09	−1.02	−0.54	3.24	1.91	−1.00	−0.40	0.95	−0.88	−0.94
79.53	−1.04	−1.00	−0.51	3.26	1.93	−1.00	−0.42	1.18	−0.90	−1.03
115.01	−0.99	−0.97	−0.47	3.28	1.94	−1.00	−0.42	1.21	−0.91	−0.94
166.31	−0.86	−0.89	−0.33	3.33	1.96	−0.98	−0.33	1.33	−0.90	−0.84
244.22	−0.83	−0.89	−0.33	3.34	1.99	−0.88	−0.38	1.47	−0.82	−1.07

Appendix C

Downstream-to-total fluence ratios

This appendix compiles the plots showing the longitudinal dependences of the DTFRs for the different energies and radial distances. We can clearly see that the number of measurements available to compute the dependences is lower towards high energies and also at smaller radial distances.

In Section C.1 we show the DTFR dependences at 1 AU as a function of the heliolongitude. Figures shows the resulting mean DTFR values (red open circles) and standard deviations (red error bars) for 6.01 MeV, 18.18 MeV, 54.99 MeV and 115.01 MeV proton fluences. Figures show the same structure as explained for Figure 2.16. The black lines correspond to polynomials fits to the mean DTFR values obtained by adding the 3rd, 4th and 5th polynomial fits and the grey lines correspond to the addition of 3rd and 8th order polynomial fits.

Section C.1.1 shows the DTFR dependences in the range from 0.6 AU to 0.85 AU and Section C.1.1 in the range from 0.3 AU to 0.6 AU, compared to the tendency lines derived at 1 AU, for the same energies previously detailed. The black thick line corresponds to the polynomial fit applied to the mean DTFR values, obtained by adding the 3rd, 4th and 5th polynomial fits. Mauve lines correspond to tendencies derived from the fast solar wind case, violet lines to the intermediate solar wind speed and purple lines to the slow solar wind case.

C.1 Heliolongitude dependences of the DTFRs for 1 AU data

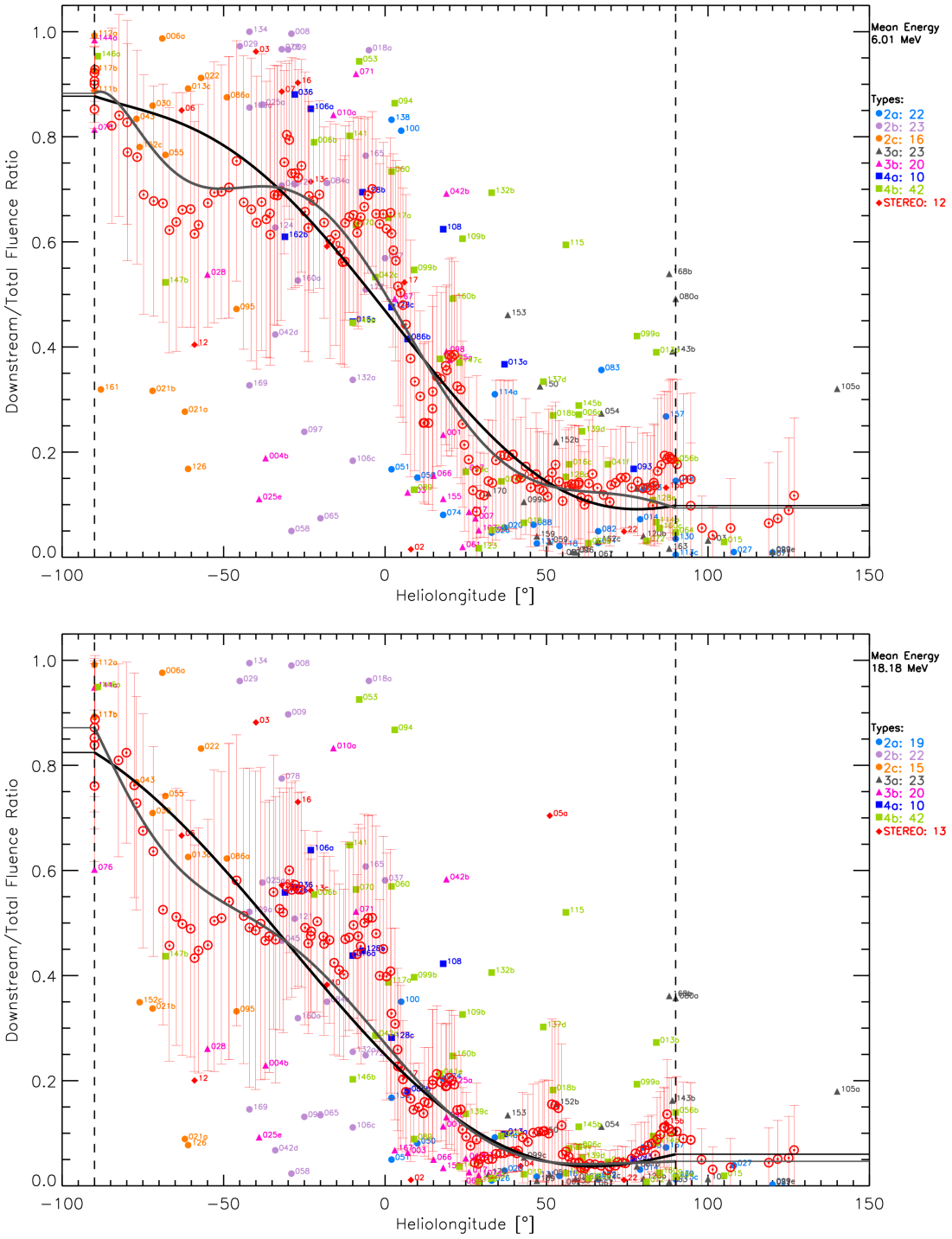

FIGURE C.1: DTFRs (coloured symbols) of the events analysed at 1 AU (labels indicate the event number) as a function of the heliolongitude. Red open circles and error bars correspond to the moving mean values and standard deviations. Upper panel: 6.01 MeV. Bottom panel: 18.18 MeV.

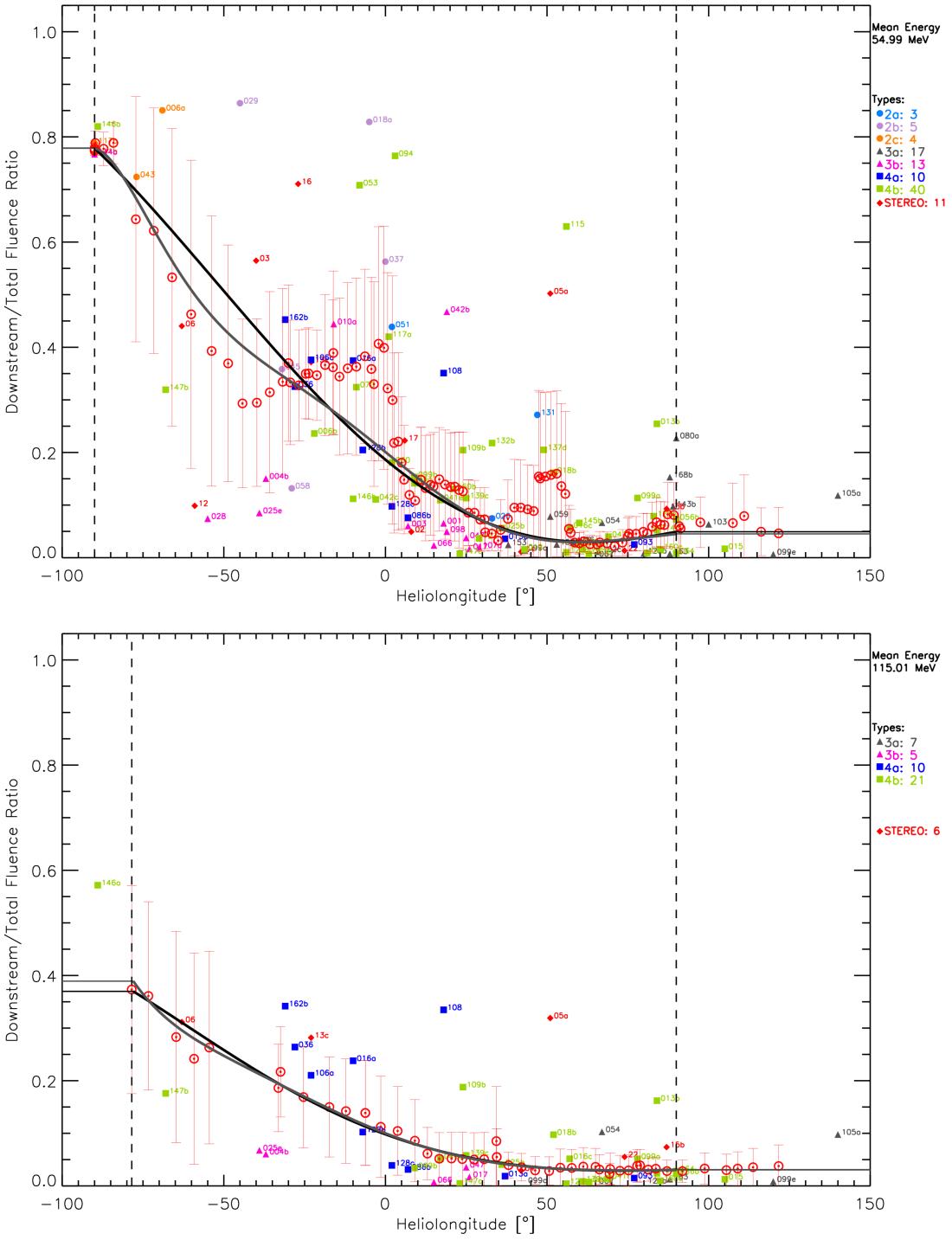

FIGURE C.2: DTFRs (coloured symbols) of the events analysed at 1 AU (labels indicate the event number) as a function of the heliolongitude. Red open circles and error bars correspond to the moving mean values and standard deviations. Upper panel: 54.99 MeV. Bottom panel: 115.01 MeV.

C.1.1 Comparison of 1 AU results with the DTFRs for 0.6 – 0.85 AU Helios data

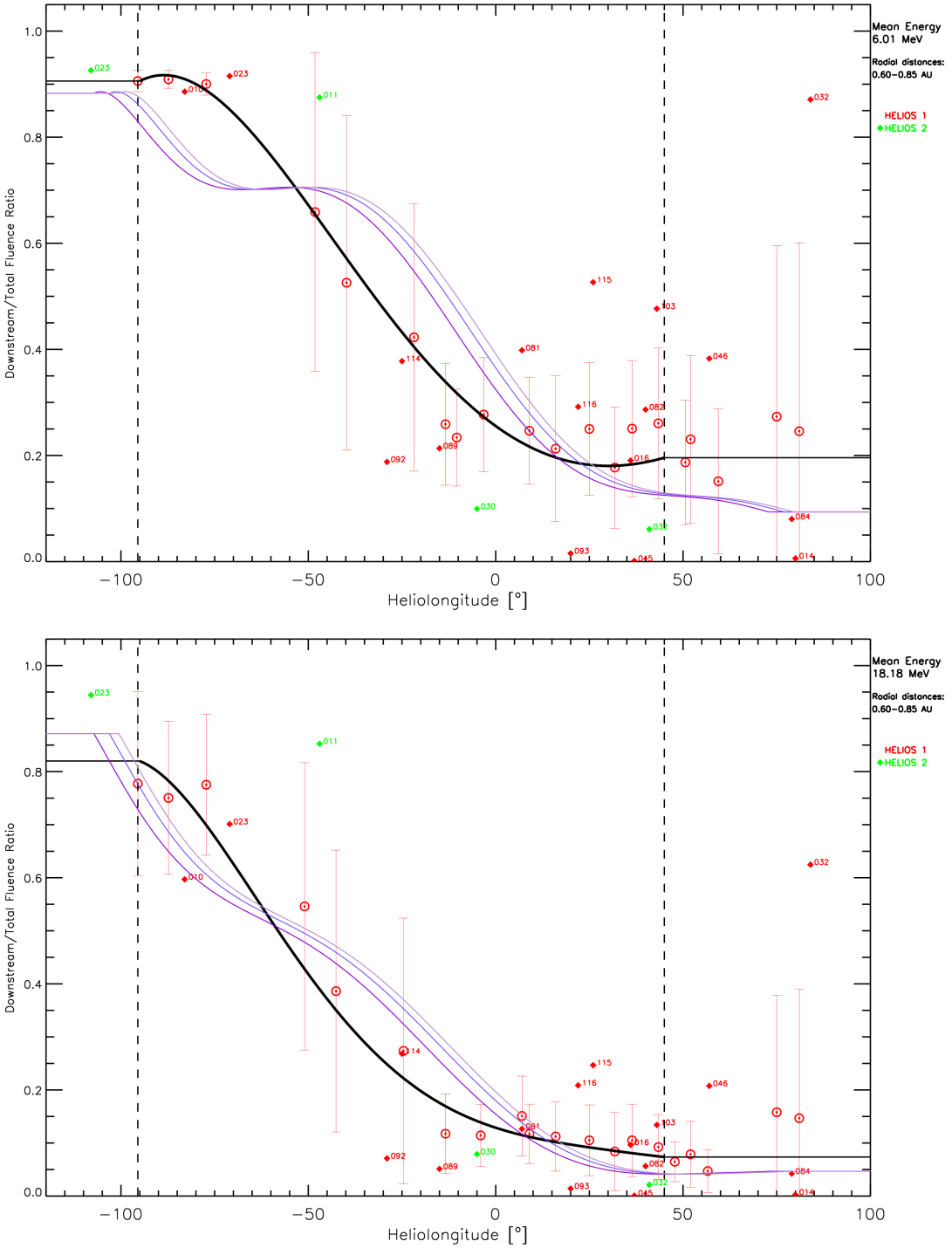

FIGURE C.3: Heliolongitude dependence of the DTFRs for 0.6 – 0.85 AU. Comparison of results derived from 1 AU data for the fast solar wind (mauve line), for the intermediate case (violet line) and for the slow wind (purple line) with those from Helios data (black line). Upper panel: 6.01 MeV. Bottom panel: 18.18 MeV.

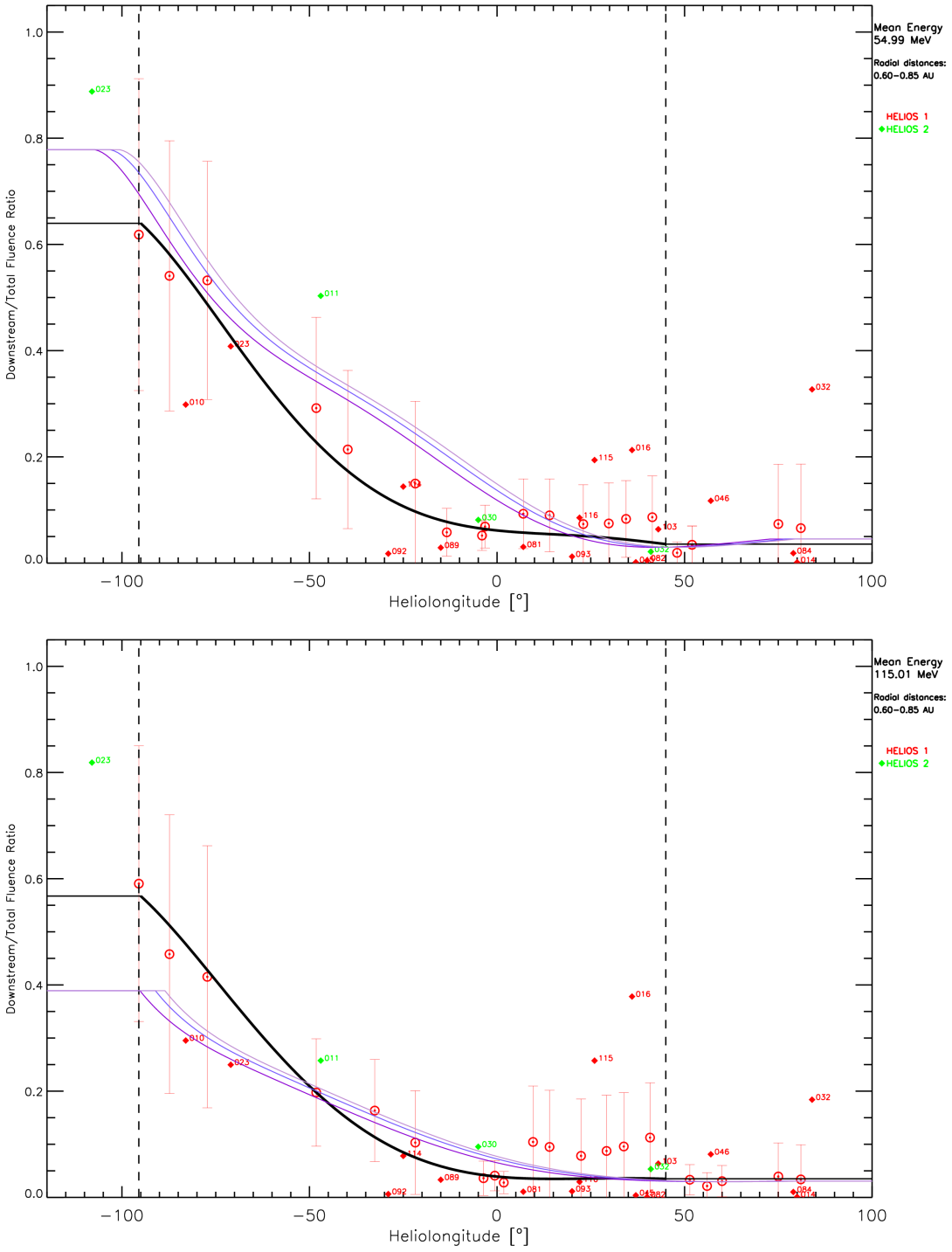

FIGURE C.4: Heliolongitude dependence of the DTFRs for 0.6 – 0.85 AU data. Comparison of results derived from 1 AU data for the fast solar wind (mauve line), for the intermediate case (violet line) and for the slow wind (purple line) with those from Helios data (black line). Upper panel: 54.99 MeV. Bottom panel: 115.01 MeV.

C.1.2 Comparison of 1 AU results with the DTFRs for 0.3 – 0.6 AU Helios data

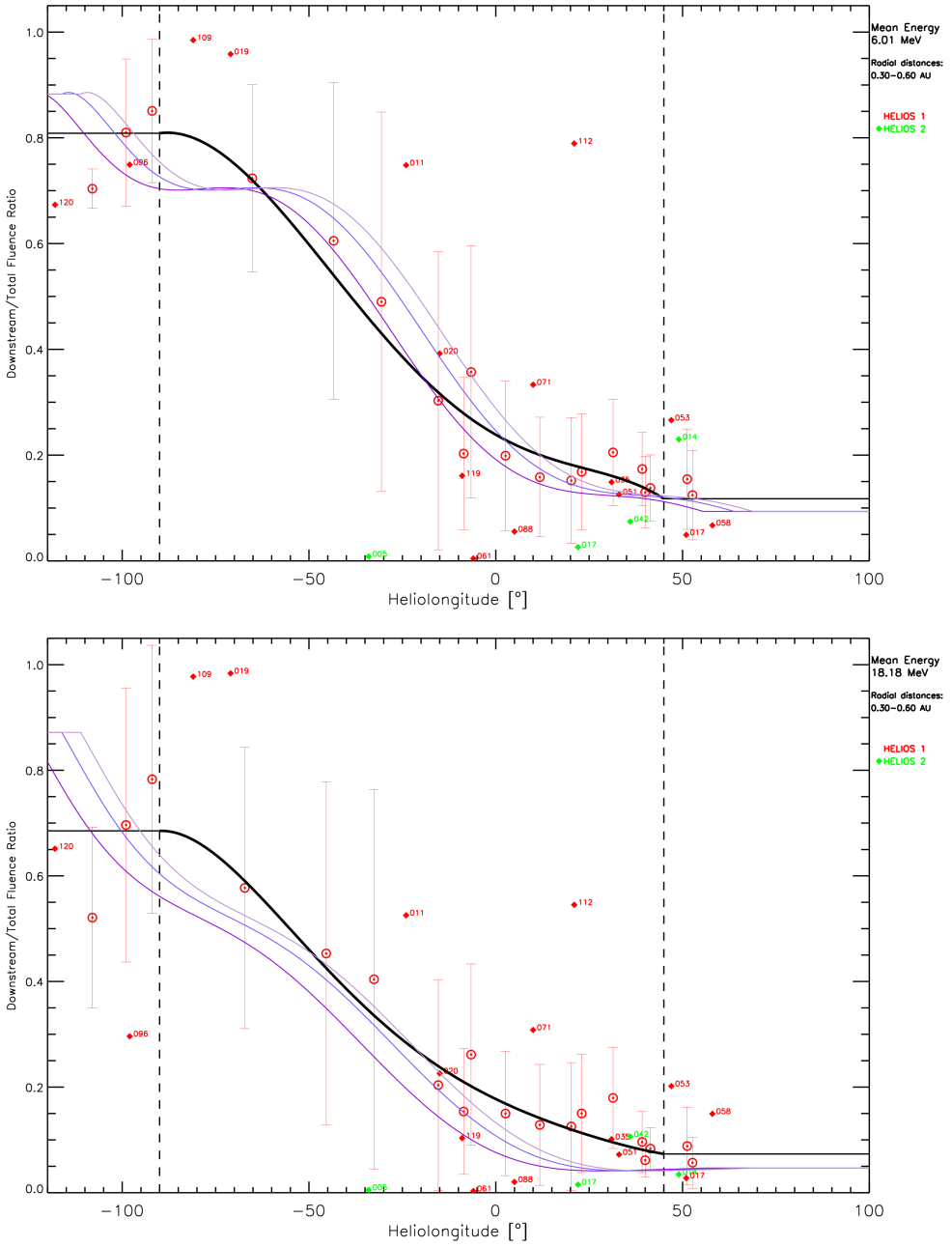

FIGURE C.5: Heliolongitude dependence of the DTFRs for 0.3 – 0.6 AU. Comparison of results derived from 1 AU data for the fast solar wind (mauve line), for the intermediate case (violet line) and for the slow wind (purple line) with those from Helios data (black line).Upper panel: 6.01 MeV. Bottom panel: 18.18 MeV.

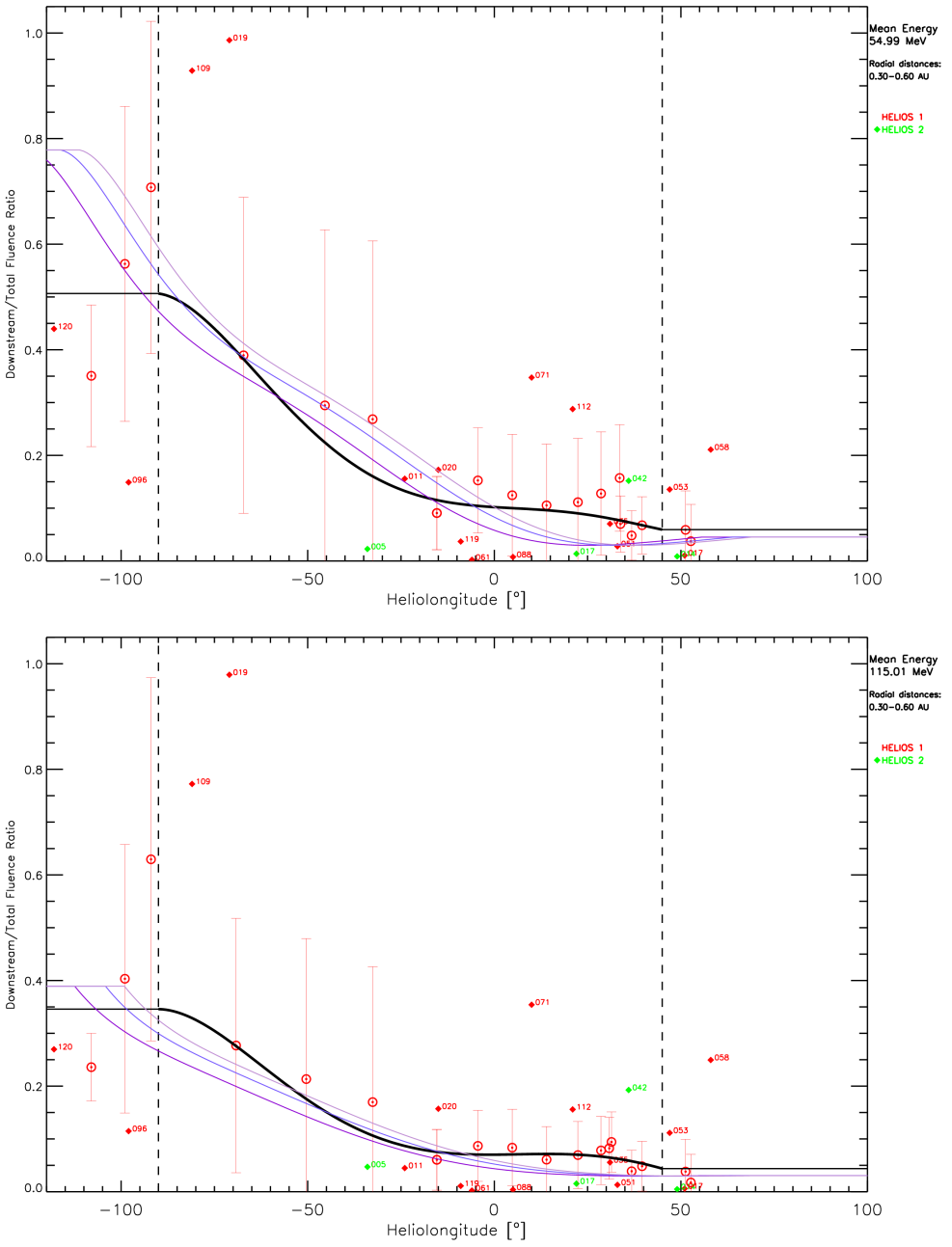

FIGURE C.6: Heliolongitude dependence of the DTFRs for 0.3 – 0.6 AU data. Comparison of results derived from 1 AU data for the fast solar wind (mauve line), for the intermediate case (violet line) and for the slow wind (purple line) with those from Helios data (black line). Upper panel: 54.99 MeV. Bottom panel: 115.01 MeV.

Appendix D

Radial dependence of the fluence for the largest SEP events in SREL

As examples of the impact of the Downstream-to-Total Fluence Ratios (DTFRs) obtained in Chapter 2 to the total fluence of the SEP events measured in the near-Earth space, we show the radial dependences obtained in the SOL2UP project for the largest events in SREL (see Table A.4). In Chapter 2 we show the results for the Event Type 4a-np, whereas in this appendix the same results but for events of Type 4a-p are presented. In the left panels of the next figures we show the variation of the upstream fluence with the radial distance as obtained from the SOLPENCO2 model, for each reference case. Note that for the events belonging to the same event type, the UF radial dependences are the same. The assumption made for the DTFRs in the previous results obtained during the SEPEM project (Aran et al., 2011b), translated into radial dependences for the TF equal to those of the UF for the same event. In contrast, now, after the analysis of the downstream fluence of SEP events performed in Chapter 2, different radial dependences of the TF are obtained for each event, as shown in the right panels of the figures below.

For each event shown, the comparison between the left and the right panels highlights the variation of the radial dependences found for the total fluence of the events with respect to the previous results obtained during the SEPEM project. The format of the figures is the same as in Figure 2.19, in Chapter 2.

The Type 4a-p category includes the seven largest events in SREL showing a prompt component. For the reference case, the DTFRs applied make the TF dependence with the radial distance steeper than the dependence derived from the modelling with SOLPENCO2 (particularly, for low energies). For the remaining six events the radial dependencies vary as shown in the following figures:

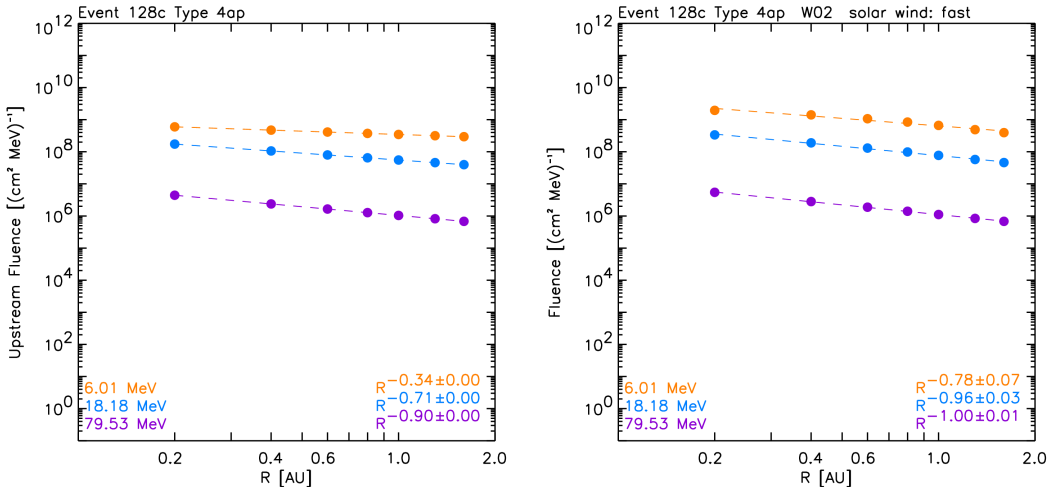

FIGURE D.1: Type 4a-p. 2003 October 29 SEP event. Radial dependence of the upstream fluence (left) and total fluence (right) for three different proton energies, 6.01 MeV (orange), 18.18 MeV (blue) and 79.53 MeV (purple).

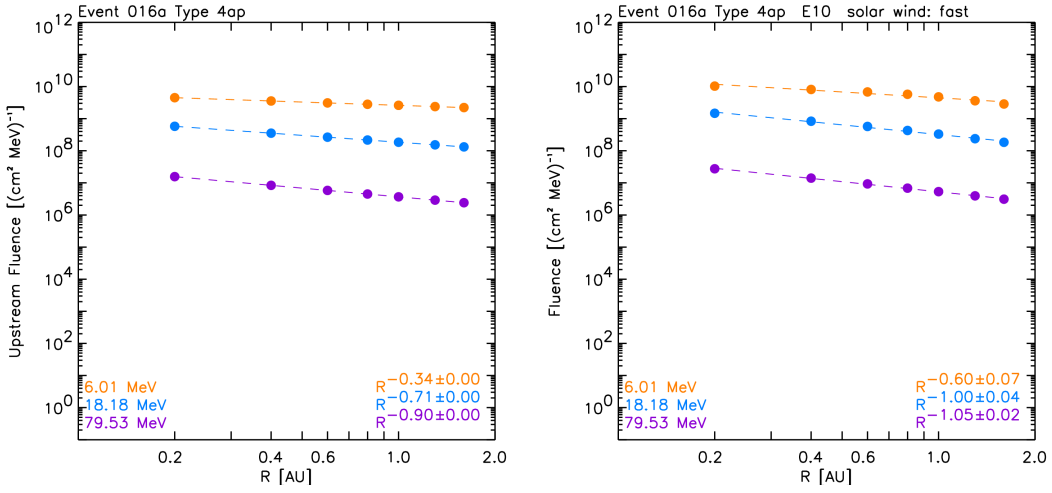

FIGURE D.2: 1989 October 19 SEP event. Radial dependence of the upstream fluence (left) and total fluence (right) for three different proton energies, 6.01 MeV (orange), 18.18 MeV (blue) and 79.53 MeV (purple).

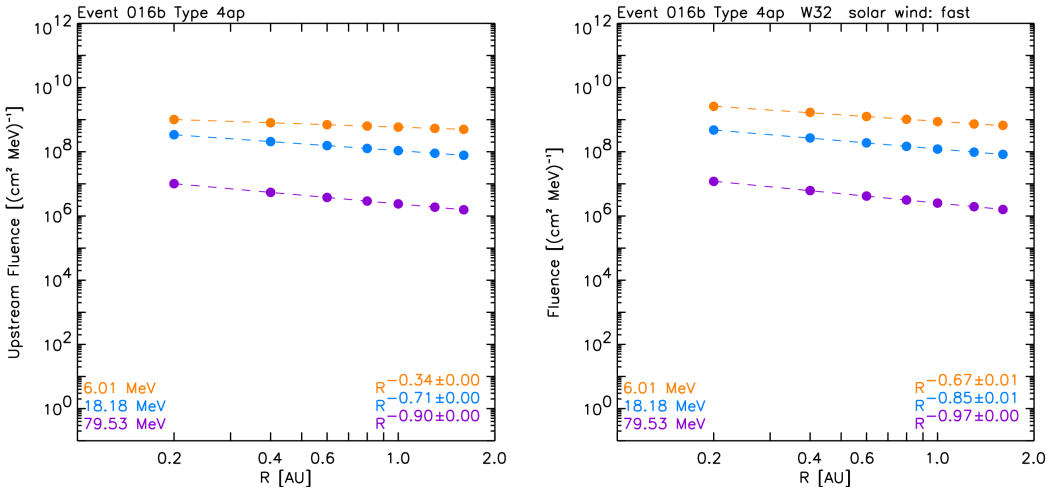

FIGURE D.3: 1989 October 22 SEP event. Radial dependence of the upstream fluence (left) and total fluence (right) for three different proton energies, 6.01 MeV (orange), 18.18 MeV (blue) and 79.53 MeV (purple).

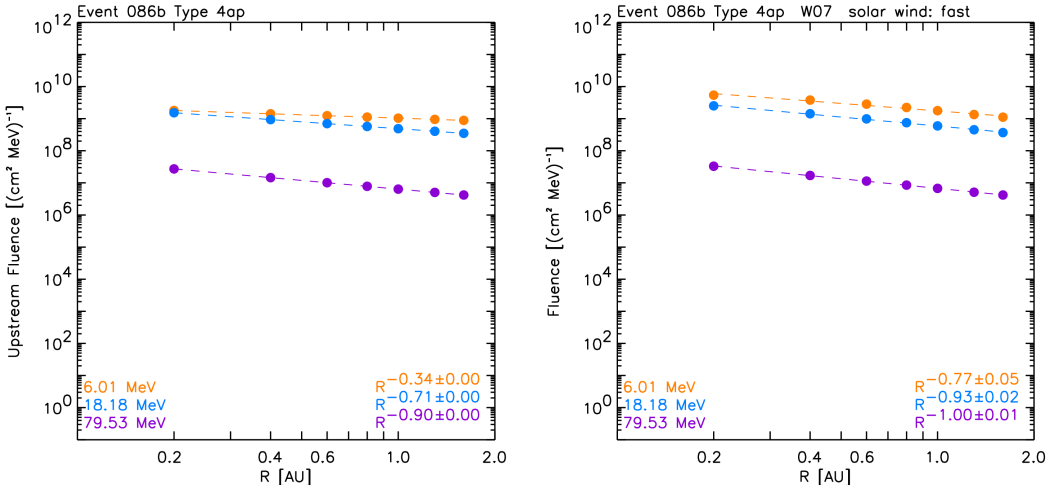

FIGURE D.4: 2000 July 14 SEP event. Radial dependence of the upstream fluence (left) and total fluence (right) for three different proton energies, 6.01 MeV (orange), 18.18 MeV (blue) and 79.53 MeV (purple).

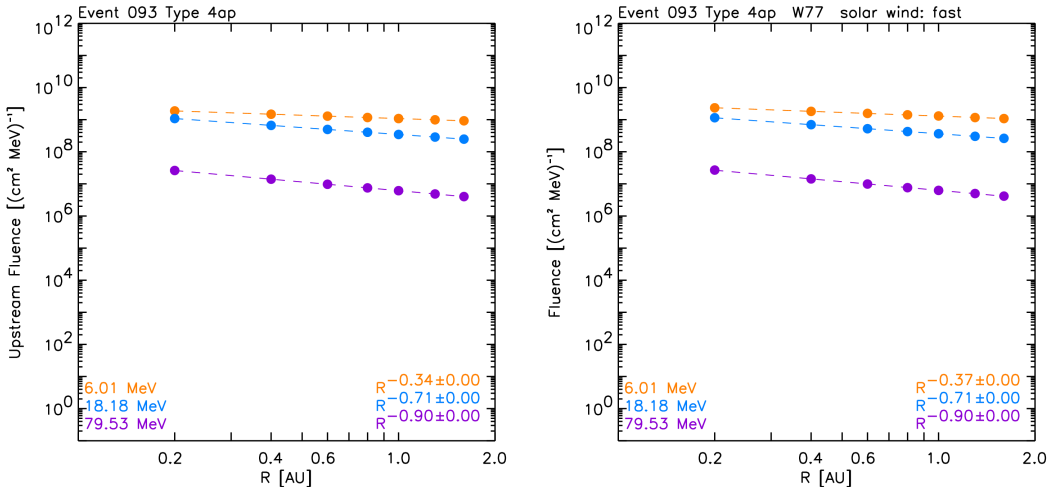

FIGURE D.5: 2000 November 8 SEP event. Radial dependence of the upstream fluence (left) and total fluence (right) for three different proton energies, 6.01 MeV (orange), 18.18 MeV (blue) and 79.53 MeV (purple).

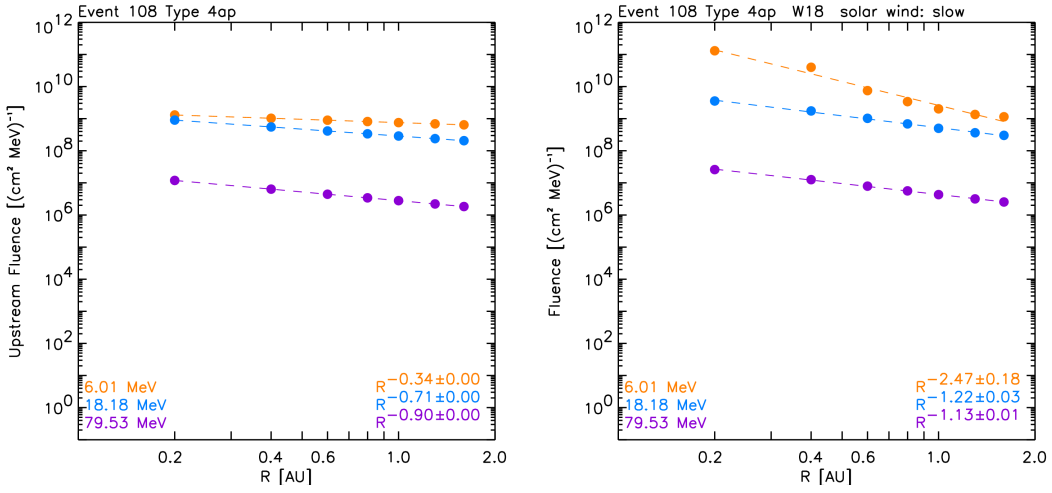

FIGURE D.6: 2001 November 4 SEP event. Radial dependence of the upstream fluence (left) and total fluence (right) for three different proton energies, 6.01 MeV (orange), 18.18 MeV (blue) and 79.53 MeV (purple).

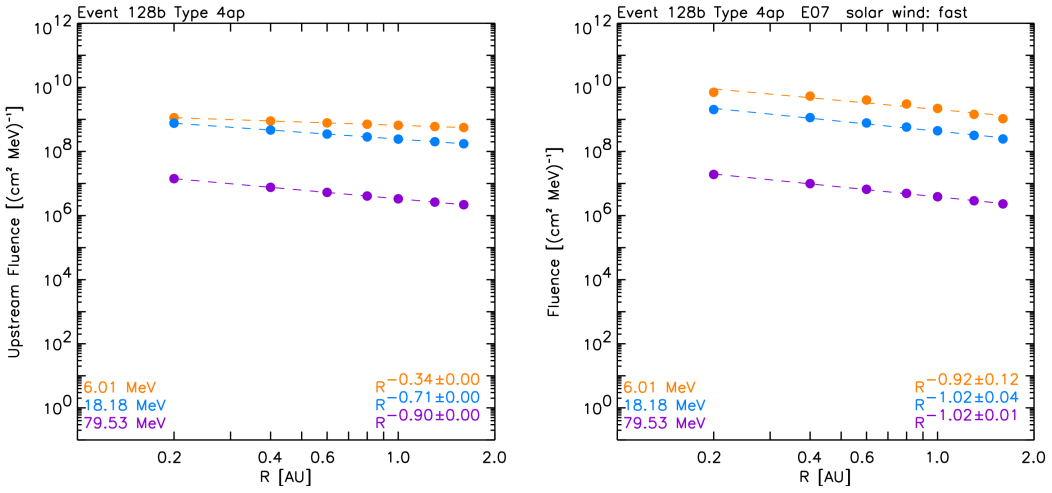

FIGURE D.7: 2003 October 28 SEP event. Radial dependence of the upstream fluence (left) and total fluence (right) for three different proton energies, 6.01 MeV (orange), 18.18 MeV (blue) and 79.53 MeV (purple).

Bibliography

Acuña, M. H., D. Curtis, J. L. Scheifele, C. T. Russell, P. Schroeder, A. Szabo, and J. G. Luhmann. The STEREO/IMPACT Magnetic Field Experiment. *Space Sci. Rev.*, **136**, 203–226, 2008. 10.1007/s11214-007-9259-2. 23, 62

Agueda, N. Near-relativistic electron events. Monte Carlo simulations of solar injection and interplanetary transport. Ph.D. thesis, Dep. Astronomia i Meteorologia University of Barcelona Martí i Franquès 1 08028 Barcelona, Spain, 2008. 88, 93, 157

Agueda, N., K.-L. Klein, N. Vilmer, R. Rodríguez-Gasén, O. E. Malandraki, et al. Release timescales of solar energetic particles in the low corona. *Astron. Astrophys.*, **570**, A5, 2014. 10.1051/0004-6361/201423549. 91, 101, 113

Agueda, N., and D. Lario. Release history and transport parameters of relativistic solar electrons inferred from near-the-Sun in situ observations. *Astrophys. J.*, **829**(2), 1–11, 2016. 10.3847/0004-637X/829/2/131, URL `http://dx.doi.org/10.3847/0004-637X/829/2/131`. 10, 82, 109, 111, 112, 115, 117, 154

Agueda, N., D. Lario, V. Ontiveros, E. Kilpua, B. Sanahuja, and R. Vainio. Multi-spacecraft Study of the 8 November 2000 SEP Event: Electron Injection Histories 100deg Apart. *Sol. Phys.*, **281**, 319–331, 2012a. 10.1007/s11207-012-9959-y. 9, 113

Agueda, N., D. Lario, R. Vainio, B. Sanahuja, E. Kilpua, and S. Pohjolainen. Modeling solar near-relativistic electron events. Insights into solar injection and interplanetary transport conditions. *Astron. Astrophys.*, **507**, 981–993, 2009. 10.1051/0004-6361/200912224. 68, 113

Agueda, N., and R. Vainio. On the parametrization of the energetic-particle pitch-angle diffusion coefficient. *J. Space Weather Space Clim.*, **3**(27), A10, 2013. 10.1051/swsc/2013034. 66, 100

Agueda, N., R. Vainio, S. Dalla, D. Lario, and B. Sanahuja. Current Sheet Regulation of Solar Near-Relativistic Electron Injection Histories. *Astrophys. J.*, **765**(2), 83, 2013. 10.1088/0004-637X/765/2/83. 11, 113

Agueda, N., R. Vainio, D. Lario, and B. Sanahuja. Injection and Interplanetary Transport of Near-Relativistic Electrons: Modeling the Impulsive Event on 2000 May 1. *Astrophys. J.*, **675**, 1601–1613, 2008. 10.1086/527527. 65, 66, 68, 93, 97, 100, 111, 128

Agueda, N., R. Vainio, and B. Sanahuja. A Database of >20 keV Electron Green's Functions of Interplanetary Transport at 1 AU. *Astrophys. J. Suppl. Ser.*, **202**, 18, 2012b. 10.1088/0067-0049/202/2/18. 65, 67, 68, 100, 151

Al-Haddad, N., S. Poedts, I. Roussev, C. J. Farrugia, W. Yu, and N. Lugaz. The Magnetic Morphology of Magnetic Clouds: Multi-spacecraft Investigation of Twisted and Writhed Coronal Mass Ejections. *Astrophys. J.*, **870**, 100, 2019. 10.3847/1538-4357/aaf38d. 9

Aminalragia-Giamini, S., I. Sandberg, C. Papadimitriou, I. A. Daglis, and P. Jiggens. The virtual enhancements - solar proton event radiation (VESPER) model. *Journal of Space Weather and Space Climate*, **8**(27), A06, 2018. 10.1051/swsc/2017040. 12

Andrews, G. B., T. H. Zurbuchen, B. H. Mauk, H. Malcom, L. A. Fisk, et al. The Energetic Particle and Plasma Spectrometer Instrument on the MESSENGER Spacecraft. *Space Sci. Rev.*, **131**, 523–556, 2007. 10.1007/s11214-007-9272-5. 128

Aran, A. Synthesis of proton flux profiles of SEP events associated with interplanetary shocks. The tool SOLPENCO. Ph.D. thesis, Universitat de Barcelona, Barcelona, Spain, 2007. URL `http://www.am.ub.edu/~blai/articles/Aran{_}thesis.pdf`. 122

Aran, A., N. Agueda, A. Afanasiev, and B. Sanahuja. Charged Particle Transport in the Interplanetary Medium, 63–78. Springer International Publishing, 2018. ISBN 978-3-319-60051-2. 10.1007/978-3-319-60051-2_4, URL `https://doi.org/10.1007/978-3-319-60051-2{_}4`. 5, 10

Aran, A., C. Jacobs, R. Rodríguez-Gasén, B. Sanahuja, and S. Poedts. WP410: Initial and boundary conditions for the shock-and- particle model. *SEPEM Technical Report, ESA/ESTEC Contract 20162/06/NL/JD, available at http://www.am.ub.es/ blai/publications.html*, 1–58, 2011a. 14, 19, 43, 47, 52

Aran, A., P. Jiggens, and B. Sanahuja. WP470: Inclusion of SOLPENCO2 into SAT model. Events list out of 1AU. *SEPEM Technical Report, ESA/ESTEC Contract 20162/06/NL/JD*, 1–56, 2011b. 14, 15, 19, 20, 122, 187

Aran, A., and D. Pacheco. SOL2UP WP2000: Selection of new reference SEP events for the SEPEM radial dependent statistical model. *SOL2UP Technical Report TN2-a, ESA/ESTEC Contract 4000114116/15/NL/HK*, 1–41, 2017. 15

Aran, A., D. Pacheco, N. Agueda, and B. Sanahuja. Updating SOLPENCO2 and New Analysis on Downstream FLuence (SOL2UP) Project. *Final Report, ESA/ESTEC Contract 4000114116/15/NL/HK*, 1–90, 2017a. 15, 21, 24, 28, 45, 54, 55, 122, 151, 175

Aran, A., D. Pacheco, and B. Sanahuja. SOL2UP WP2000: Radial dependencies of the reference SEP events. *SOL2UP Technical Report TN2-b, ESA/ESTEC Contract 4000114116/15/NL/HK*, 1–49, 2017b. 15

Aran, A., B. Sanahuja, and D. Lario. Fluxes and fluences of SEP events derived from SOLPENCO. *Annales Geophisicae*, **23**, 3047–3053, 2005. 122

Aran, A., B. Sanahuja, and D. Lario. SOLPENCO: A solar particle engineering code. *Advances in Space Research*, **37**, 1240–1246, 2006. 122

Aran, A., and R. Vainio. WP2100: Review of State of the Art Models and Tools XXX Interplanetary models. *IPRAM, Technical Note 1-A, ESA/ESTEC Contract 4000106133/12/NL/AF*, 1–48, 2013. 12

Baker, D. N., X. Li, A. Pulkkinen, C. M. Ngwira, M. L. Mays, A. B. Galvin, and K. D. C. Simunac. A major solar eruptive event in July 2012: Defining extreme space weather scenarios. *Space Weather*, **11**(10), 585–591, 2013. 10.1002/swe.20097. 159

Beeck, J., G. M. Mason, D. C. Hamilton, G. Wibberenz, H. Kunow, D. Hovestadt, and B. Klecker. A multispacecraft study of the injection and transport of solar energetic particles. *Astrophys. J.*, **322**, 1052–1072, 1987. 10.1086/165800. 9

Beeck, J., and G. Wibberenz. Pitch angle distributions of solar energetic particles and the local scattering properties of the interplanetary medium. *Astrophys. J.*, **311**, 437–450, 1986. 10.1086/164784. 100

Bialk, M., W. Dröge, and B. Heber. Determination of the Response Function of the University of Kiel Helios Cosmic Ray Instrument by Monte-Carlo Simulation. *International Cosmic Ray Conference*, **3**, 764, 1991. 77, 78, 89, 90, 91, 100, 111

Bougeret, J. L., K. Goetz, M. L. Kaiser, S. D. Bale, P. J. Kellogg, et al. S/WAVES: The Radio and Plasma Wave Investigation on the STEREO Mission. *Space Sci. Rev.*, **136**, 487–528, 2008. 10.1007/s11214-007-9298-8. 62

Brueckner, G. E., R. A. Howard, M. J. Koomen, C. M. Korendyke, D. J. Michels, et al. The Large Angle Spectroscopic Coronagraph (LASCO). *Sol. Phys.*, **162**, 357–402, 1995. 10.1007/BF00733434. 3

Cane, H. V., and D. Lario. An Introduction to CMEs and Energetic Particles. *Space Sci. Rev.*, **123**, 45–56, 2006. 10.1007/s11214-006-9011-3. 20

Cane, H. V., R. E. McGuire, and T. T. von Rosenvinge. Two classes of solar energetic particle events associated with impulsive and long-duration soft X-ray flares. *Astrophys. J.*, **301**, 448–459, 1986. 10.1086/163913. 172, 173

Cane, H. V., D. V. Reames, and T. T. von Rosenvinge. The role of interplanetary shocks in the longitude distribution of solar energetic particles. *J. Geophys. Res.*, **93**, 9555–9567, 1988. 10.1029/JA093iA09p09555. 4, 20

Cliver, E. W., S. W. Kahler, M. A. Shea, and D. F. Smart. Injection onsets of 2 GeV protons, 1 MeV electrons, and 100 keV electrons in solar cosmic ray flares. *Astrophys. J.*, **260**, 362–370, 1982. 10.1086/160261. 172, 173

Crosby, N., D. Heynderickx, P. Jiggens, A. Aran, B. Sanahuja, et al. SEPEM: A tool for statistical modeling the solar energetic particle environment. *Space Weather*, **13**(7), 406–426, 2015. 2013SW001008, 10.1002/2013SW001008, URL `http://dx.doi.org/10.1002/2013SW001008`. 14, 15, 19, 20, 21, 22, 122, 142, 151

Cucinotta, F. A., K. To, and E. Cacao. Predictions of space radiation fatality risk for exploration missions. *Life Sciences and Space Research*, **13**, 1–11, 2017. 10.1016/j.lssr.2017.01.005. 12

Dalla, S., M. S. Marsh, P. Zelina, and T. Laitinen. Time dependence of Fe/O ratio within a 3D solar energetic particle propagation model including drift. *Astron. Astrophys.*, **598**, A73, 2017. 10.1051/0004-6361/201628618, `1606.05612`. 11

Daly, E. J., G. Drolshagen, A. Hilgers, and H. D. R. Evans. Space Environment Analysis: Experience and Trends. In T.-D. Guyenne and A. Hilgers, eds., Environment Modeling for Space-Based Applications, vol. 392 of *ESA Special Publication*, 15, 1996. 12

Daly, E. J., P. Nieminen, A. Hilgers, and et al. Radiation Environment models and in-orbit monitoring. *Technical Note, TEC-EES/2005.265/ED, ESA*, 2005. 14

Dayeh, M. A., M. I. Desai, K. Kozarev, N. A. Schwadron, L. W. Townsend, M. PourArsalan, C. Zeitlin, and R. B. Hatcher. Modeling proton intensity gradients and radiation dose equivalents in the inner heliosphere using EMMREM: May 2003 solar events. *Space Weather*, **8**, S00E07, 2010. 10.1029/2009SW000566. 122

de Lucas, A., A. Dal Lago, R. Schwenn, and A. L. Clúa de Gonzalez. Multi-spacecraft observed magnetic clouds as seen by Helios mission. *Journal of Atmospheric and Solar-Terrestrial Physics*, **73**, 1361–1371, 2011a. 10.1016/j.jastp.2011.02.007. 25

de Lucas, A., R. Schwenn, A. dal Lago, E. Marsch, and A. L. Clúa de Gonzalez. Interplanetary shock wave extent in the inner heliosphere as observed by multiple spacecraft. *Journal of Atmospheric and Solar-Terrestrial Physics*, **73**, 1281–1292, 2011b. 10.1016/j.jastp.2010.12.011. 25

Domingo, V., B. Fleck, and A. I. Poland. The SOHO Mission: an Overview. *Sol. Phys.*, **162**, 1–37, 1995. 10.1007/BF00733425. 9

Dresing, N., R. Gómez-Herrero, B. Heber, A. Klassen, O. Malandraki, W. Dröge, and Y. Kartavykh. Statistical survey of widely spread out solar electron events observed with STEREO and ACE with special attention to anisotropies. *Astron. Astrophys.*, **567**, A27, 2014. 10.1051/0004-6361/201423789. 61

Dresing, N., R. Gómez-Herrero, B. Heber, A. Klassen, M. Temmer, and A. Veronig. Long-lasting injection of solar energetic electrons into the heliosphere. *Astron. Astrophys.*, **613**, A21, 2018. 10.1051/0004-6361/201731573, 1802.04722. 114, 117, 154

Dresing, N., R. Gómez-Herrero, B. Heber, R. Müller-Mellin, R. Wimmer-Schweingruber, and A. Klassen. Multi-spacecraft Observations of CIR-Associated Ion Increases During the Ulysses 2007 Ecliptic Crossing. *Sol. Phys.*, **256**, 409–425, 2009. 10.1007/s11207-009-9356-3. 9

Dresing, N., R. Gómez-Herrero, A. Klassen, B. Heber, Y. Kartavykh, and W. Dröge. The Large Longitudinal Spread of Solar Energetic Particles During the 17 January 2010 Solar Event. *Sol. Phys.*, **281**(1), 281–300, 2012. 10.1007/s11207-012-0049-y. 9

Dröge, W. Solar Particle Transport in a Dynamical Quasi-linear Theory. *Astrophys. J.*, **589**, 1027–1039, 2003. 10.1086/374812. 65

Dröge, W., Y. Kartavykh, A. Klassen, N. Dresing, and D. Lario. Multi-spacecraft observations and transport modeling of energetic electrons for a series of solar particle events in August 2010. *Astrophys. J.*, **30-July-20**(2), 1–17, 2016. 10.3847/0004-637X/826/2/134, URL http://dx.doi.org/10.3847/0004-637X/826/2/134. 5, 9, 11

Dröge, W., Y. Y. Kartavykh, B. Klecker, and G. A. Kovaltsov. Anisotropic Three-Dimensional Focused Transport of Solar Energetic Particles in the Inner Heliosphere. *Astrophys. J.*, **709**, 912–919, 2010. 10.1088/0004-637X/709/2/912. 11, 61

Feynman, J., and S. B. Gabriel. On space weather consequences and predictions. *J. Geophys. Res.*, **105**, 10,543–10,564, 2000. 10.1029/1999JA000141. 12, 122

Feynman, J., A. Ruzmaikin, and V. Berdichevsky. The JPL proton fluence model: an update. *Journal of Atmospheric and Solar-Terrestrial Physics*, **64**, 1679–1686, 2002. 10.1016/S1364-6826(02)00118-9. 13

Feynman, J., G. Spitale, J. Wang, and S. Gabriel. Interplanetary proton fluence model - JPL 1991. *J. Geophys. Res.*, **98**, 13, 1993. 10.1029/92JA02670. 13

Fränz, M., and D. Harper. Heliospheric coordinate systems. *Planet. Space Sci.*, **50**, 217–233, 2002. 10.1016/S0032-0633(01)00119-2. 77

Galvin, A. B., L. M. Kistler, M. A. Popecki, C. J. Farrugia, K. D. C. Simunac, et al. The Plasma and Suprathermal Ion Composition (PLASTIC) Investigation on the STEREO Observatories. *Space Sci. Rev.*, **136**, 437–486, 2008. 10.1007/s11214-007-9296-x. 23, 62

Gardini, A., M. Laurenza, and M. Storini. SEP events and multi-spacecraft observations: Constraints on theory. *Advances in Space Research*, **47**(12), 2127–2139, 2011. 10.1016/j.asr.2011.01.025. 82, 172, 173

Glover, A., A. Hilgers, L. Rosenqvist, and S. Bourdarie. Interplanetary proton cumulated fluence model update. *Advances in Space Research*, **42**, 1564–1568, 2008. 10.1016/j.asr.2007.08.023. 22

Gold, R. E., S. M. Krimigis, S. E. Hawkins, III, D. K. Haggerty, D. A. Lohr, E. Fiore, T. P. Armstrong, G. Holland, and L. J. Lanzerotti. Electron, Proton, and Alpha Monitor on the Advanced Composition Explorer spacecraft. *Space Sci. Rev.*, **86**, 541–562, 1998. 10.1023/A:1005088115759. 8, 22

Gómez-Herrero, R., N. Dresing, A. Klassen, B. Heber, D. Lario, N. Agueda, O. E. Malandraki, J. J. Blanco, J. Rodríguez-Pacheco, and S. Banjac. Circumsolar Energetic Particle Distribution on 2011 November 3. *Astrophys. J.*, **799**, 55, 2015. 10.1088/0004-637X/799/1/55. 9, 11, 24, 61, 113, 159

Gómez-Herrero, R., J. Rodríguez-Pacheco, R. F. Wimmer-Schweingruber, G. M. Mason, S. Sánchez-Prieto, et al. The Solar Orbiter Mission: an Energetic Particle Perspective. *ArXiv e-prints*, 2017. 1701.04057. 120

Goodwin, P. S., M. R. Traxler, W. G. Meeks, and F. M. Flanagan. Technical Memorandum 33-752: Tracking and Data Systems Support for the Helios Project. National Aeronautics and Space Administration, Washington, D.C. 20546, USA, 1976. URL https://ntrs.nasa.gov/archive/nasa/casi.ntrs.nasa.gov/19760019169.pdf. 75

Gopalswamy, N., H. Xie, S. Yashiro, and I. Usoskin. Coronal Mass Ejections and Ground Level Enhancements. *International Cosmic Ray Conference*, **1**, 169, 2005. 3

Hasselmann, K., and G. Wibberenz. Scattering of charged particles by random electromagnetic fields, vol. 34 of *Bericht, Institut für Schiffbau, 1953, 218*. Zeitschrift Für Geophysik, Hamburg, 3 edn., 1968. 66

Hasselmann, K., and G. Wibberenz. A Note on the Parallel Diffusion Coefficient. *Astrophys. J.*, **162**, 1049, 1970. 10.1086/150736. 66

He, H.-Q., G. Zhou, and W. Wan. Propagation of Solar Energetic Particles in Three-dimensional Interplanetary Magnetic Fields: Radial Dependence of Peak Intensities. *Astrophys. J.*, **842**, 71, 2017. 10.3847/1538-4357/aa7574, 1706.05443. 122

Heber, B., N. Agueda, R. Bütikofer, D. Galsdorf, K. Herbst, P. Kühl, J. Labrenz, and R. Vainio. Inversion Methodology of Ground Level Enhancements. In O. E. Malandraki and N. B. Crosby, eds., Solar Particle Radiation Storms Forecasting and Analysis, vol. 444 of *Astrophysics and Space Science Library*, 179–199, 2018. 10.1007/978-3-319-60051-2_10. 88

Heras, A. M., B. Sanahuja, D. Lario, Z. K. Smith, T. Detman, and M. Dryer. Three low-energy particle events: Modeling the influence of the parent interplanetary shock. *Astrophys. J.*, **445**, 497–508, 1995. 10.1086/175714. 6, 19

Heras, A. M., B. Sanahuja, T. R. Sanderson, R. G. Marsden, and K.-P. Wenzel. Observational signatures of the influence of the interplanetary shocks on the associated low-energy particle events. *J. Geophys. Res.*, **99**, 43–51, 1994. 172, 173

Heynderickx, D., A. Aran, F. Lei, B. Sanahuja, P. Turscott, and R. Vainio. Interplanetary and Planetary Radiation Model for Human Spaceflight (IPRAM). *Final Report, ESA/ESTEC Contract 4000106133/12/NL/AF*, 1–180, 2014. 12

Heynderickx, D., I. Sandberg, and P. Jiggens. SEPEM Reference Data Set v2.0. *http://sepem.eu/help/SEPEM_RDS_v2-00.zip*, 2017. 19, 22

Howard, R. A., J. D. Moses, A. Vourlidas, J. S. Newmark, D. G. Socker, et al. Sun Earth Connection Coronal and Heliospheric Investigation (SECCHI). *Space Sci. Rev.*, **136**, 67–115, 2008. 10.1007/s11214-008-9341-4. 36

Hu, J., G. Li, X. Ao, G. P. Zank, and O. Verkhoglyadova. Modeling Particle Acceleration and Transport at a 2-D CME-Driven Shock. *Journal of Geophysical Research (Space Physics)*, **122**(A11), 10, 2017. 10.1002/2017JA024077. 20

Hu, J., G. Li, S. Fu, G. Zank, and X. Ao. Modeling a Single SEP Event from Multiple Vantage Points Using the iPATH Model. *Astrophys. J. Lett.*, **854**, L19, 2018. 10.3847/2041-8213/aaabc1. 20

Jiggens, P., M.-A. Chavy-Macdonald, G. Santin, A. Menicucci, H. Evans, and A. Hilgers. The magnitude and effects of extreme solar particle events. *Journal of Space Weather and Space Climate*, **4**(27), A20, 2014a. 10.1051/swsc/2014017. 12

Jiggens, P., H. Evans, P. Truscott, D. Heynderickx, F. Lei, and E. DeDonder. Long-Term Destructive SEE Risk and Calculations Using Multiple "Worst-Case" Events Versus Modelling. *IEEE Transactions on Nuclear Science*, **61**, 1695–1702, 2014b. 10.1109/TNS.2014.2302994. 12

Jiggens, P., D. Heynderickx, I. Sandberg, P. Truscott, O. Raukunen, and R. Vainio. Updated Model of the Solar Energetic Proton Environment in Space. *Journal of Space Weather and Space Climate*, **8**(27), A31, 2018a. 10.1051/swsc/2018010, 1801.05422. 12, 13, 22, 144

Jiggens, P., A. Varotsou, P. Truscott, D. Heynderickx, F. Lei, H. Evans, and E. Daly. The Solar Accumulated and Peak Proton and Heavy Ion Radiation Environment (SAPPHIRE) Model. *IEEE Transactions on Nuclear Science*, **65**, 698–711, 2018b. 10.1109/TNS.2017.2786581. 13

Jiggens, P. T. A., and S. B. Gabriel. Time distributions of solar energetic particle events: Are SEPEs really random? *J. Geophys. Res.(Space Physics)*, **114**(A13), A10105, 2009. 10.1029/2009JA014291. 12, 13

Jiggens, P. T. A., S. B. Gabriel, D. Heynderickx, N. Crosby, A. Glover, and A. Hilgers. ESA SEPEM Project: Peak Flux and Fluence Model. *IEEE Transactions on Nuclear Science*, **59**, 1066–1077, 2012. 10.1109/TNS.2012.2198242. 13, 14, 15, 21, 22, 142

Jokipii, J. R. Cosmic-Ray Propagation. I. Charged Particles in a Random Magnetic Field. *Astrophys. J.*, **146**, 480, 1966. 65

Jun, I., R. T. Swimm, A. Ruzmaikin, J. Feynman, A. J. Tylka, and W. F. Dietrich. Statistics of solar energetic particle events: Fluences, durations, and time intervals. *Advances in Space Research*, **40**, 304–312, 2007. 10.1016/j.asr.2006.12.019. 14

Kahler, S. W. The role of the big flare syndrome in correlations of solar energetic proton fluxes and associated microwave burst parameters. *J. Geophys. Res.*, **87**, 3439–3448, 1982. 10.1029/JA087iA05p03439. 172, 173

Kahler, S. W., N. R. Sheeley, Jr., R. A. Howard, D. J. Michels, M. J. Koomen, R. E. McGuire, T. T. von Rosenvinge, and D. V. Reames. Associations between coronal mass ejections and solar energetic proton events. *J. Geophys. Res.*, **89**, 9683–9693, 1984. 10.1029/JA089iA11p09683. 172

Kallenrode, M.-B. Neutral lines and azimuthal 'transport' of solar energetic particles. *J. Geophys. Res.*, **98**, 5573–5591, 1993a. 10.1029/92JA02778. 172, 173

Kallenrode, M.-B. Particle propagation in the inner heliosphere. *J. Geophys. Res.*, **98**, 19,037–19,047, 1993b. 10.1029/93JA02079. 108, 109, 115, 116, 117, 154

Kallenrode, M.-B. Space physics : an introduction to plasmas and particles in the heliosphere and magnetospheres. Springer-Verlag Berlin Heidelberg, 1998. ISBN 978-3-662-09959-9. 10.1007/978-3-662-04443-8. 1

Kallenrode, M.-B., E. W. Cliver, and G. Wibberenz. Composition and azimuthal spread of solar energetic particles from impulsive and gradual flares. *Astrophys. J.*, **391**, 370–379, 1992a. 10.1086/171352. 82, 172, 173

Kallenrode, M.-B., and G. Wibberenz. Particle injection following solar flares on 1980 May 28 and June 8 - Evidence for different injection time histories in impulsive and gradual events? *Astrophys. J.*, **376**, 787–796, 1991. 10.1086/170327. 172

Kallenrode, M.-B., G. Wibberenz, and S. Hucke. Propagation conditions of relativistic electrons in the inner heliosphere. *Astrophys. J.*, **394**, 351–356, 1992b. 10.1086/171587. 82, 105, 108, 109, 112, 115, 117, 154

Klassen, A., N. Dresing, R. Gómez-Herrero, and B. Heber. First simultaneous observations of a near-relativistic electron spike event by both STEREO spacecraft. *Astron. Astrophys.*, **580**, A115, 2015. 10.1051/0004-6361/201525700. 9, 62

Klassen, A., N. Dresing, R. Gómez-Herrero, B. Heber, and M. R. Unexpected spatial intensity distributions and onset timing of solar electron events observed by closely spaced STEREO spacecraft. *Astron. Astrophys.*, **593**, A31, 2016. 10.1051/0004-6361/201628734, URL `http://dx.doi.org/10.1051/0004-6361/201628734`. 9, 61, 62, 63, 64, 65, 71, 72, 153

Klein, K.-L. Eruptive Activity Related to Solar Energetic Particle Events. In O. E. Malandraki and N. B. Crosby, eds., Solar Particle Radiation Storms Forecasting and Analysis, vol. 444 of *Astrophysics and Space Science Library*, 27–43, 2018. 10.1007/978-3-319-60051-2_2. 3

Klein, K.-L., and S. Dalla. Acceleration and Propagation of Solar Energetic Particles. *Space Sci. Rev.*, **212**, 1107–1136, 2017. 10.1007/s11214-017-0382-4. 4

Klein, K.-L., S. Krucker, G. Lointier, and A. Kerdraon. Open magnetic flux tubes in the corona and the transport of solar energetic particles. *Astron. Astrophys.*, **486**, 589–596, 2008. 10.1051/0004-6361:20079228. 104

Klein, K.-L., G. Trottet, and A. Klassen. Energetic Particle Acceleration and Propagation in Strong CME-Less Flares. *Sol. Phys.*, **263**, 185–208, 2010. 10.1007/s11207-010-9540-5. 114, 117, 154

Kocharov, L., and J. Torsti. Hybrid Solar Energetic Particle Events Observed on Board Soho. *Sol. Phys.*, **207**, 149–157, 2002. 10.1023/A:1015540311183. 5

Kocharov, L., R. Vainio, G. A. Kovaltsov, and J. Torsti. Adiabatic Deceleration of Solar Energetic Particles as Deduced from Monte Carlo Simulations of Interplanetary Transport. *Sol. Phys.*, **182**, 195–215, 1998. 10.1023/A:1005040118200. 65

Kozarev, K., N. A. Schwadron, M. A. Dayeh, L. W. Townsend, M. I. Desai, and M. PourArsalan. Modeling the 2003 Halloween events with EMMREM: Energetic particles, radial gradients, and coupling to MHD. *Space Weather*, **8**, S00E08, 2010. 10.1029/2009SW000550. 122

Krucker, S., G. J. Hurford, A. L. MacKinnon, A. Y. Shih, and R. P. Lin. Coronal γ-Ray Bremsstrahlung from Solar Flare-accelerated Electrons. *Astrophys. J. Lett.*, **678**, L63, 2008. 10.1086/588381. 4

Kunow, H. Angular distributions of energetic charged particles observed with HELIOS-1 and -2 between 0.3 and 1 AU and their relevance to manned interplanetary space missions. *Advances in Space Research*, **14**(10), 599–610, 1994. 10.1016/0273-1177(94)90515-0. 12

Kunow, H., G. Wibberenz, G. Green, R. Müller-Mellin, M. Witte, and H. Hempe. Das Kieler Experiment zur Messung der kosmischen Strahlung zwischen 1,0 und 0,3 AE (E6). *Raumfahrtforschung*, **19**(5), 253–258, 1975. 24, 76

Kunow, H., M. Witte, G. Wibberenz, H. Hempe, R. Mueller-Mellin, G. Green, B. Iwers, and J. Fuckner. Cosmic ray measurements on board HELIOS 1 from December 1974 to September 1975 Quiet time spectra, radial gradients, and solar events. *Journal of Geophysics Zeitschrift Geophysik*, **42**, 615–631, 1977. 76

Lario, D. PROPAGATION OF LOW-ENERGY PARTICLES THROUGH THE INTERPLANETARY MEDIUM: MODELING THEIR INJECTION FROM INTERPLANETARY SHOCKS. Ph.D. thesis, University of Barcelona, 1997. 10.1017/CBO9781107415324.004, `arXiv:1011.1669v3`. 20

Lario, D., A. Aran, N. Agueda, and B. Sanahuja. Radial dependence of proton peak intensities and fluences in SEP events: Influence of the energetic particle transport parameters. *Advances in Space Research*, **40**, 289–294, 2007. 10.1016/j.asr.2007.01.057. 122, 129

Lario, D., A. Aran, and R. B. Decker. Major solar energetic particle events of solar cycles 22 and 23: Intensities above the streaming limit. *Space Weather*, **6**, S12001, 2008. 10.1029/2008SW000403. 3

Lario, D., A. Aran, R. Gómez-Herrero, N. Dresing, B. Heber, G. C. Ho, R. B. Decker, and E. C. Roelof. Longitudinal and Radial Dependence of Solar Energetic Particle Peak Intensities: STEREO, ACE, SOHO, GOES, and MESSENGER Observations. *Astrophys. J.*, **767**, 41, 2013. 10.1088/0004-637X/767/1/41. 9, 11, 20, 24, 61, 128, 159

Lario, D., and R. B. Decker. Correction to 'Estimation of solar energetic proton mission-integrated fluences and peak intensities for missions traveling close to the Sun'. *Space Weather*, **9**, S12002, 2011a. 10.1029/2011SW000749. 14

Lario, D., and R. B. Decker. Estimation of solar energetic proton mission-integrated fluences and peak intensities for missions traveling close to the Sun. *Space Weather*, **9**, S11003, 2011b. 10.1029/2011SW000708. 14

Lario, D., R. B. Decker, E. C. Roelof, D. B. Reisenfeld, and T. R. Sanderson. Low-energy particle response to CMEs during the Ulysses solar maximum northern polar passage. *J. Geophys. Res.(Space Physics)*, **109**(A18), A01,107, 2004. 10.1029/2003JA010071. 9

Lario, D., M.-B. Kallenrode, R. B. Decker, E. C. Roelof, S. M. Krimigis, A. Aran, and B. Sanahuja. Radial and longitudinal dependence of solar 4-13 MeV and 27-37 MeV proton peak intensities and fluences: Helios and IMP-8 observations. *Astrophys. J.*, **653**, 1531–1544, 2006. 10.1086/508982. 11, 14, 61, 76, 82, 121, 172, 173

Lario, D., R.-Y. Kwon, A. Vourlidas, N. E. Raouafi, D. K. Haggerty, et al. Longitudinal Properties of a Widespread Solar Energetic Particle Event on 2014 February 25: Evolution of the Associated CME Shock. *Astrophys. J.*, **819**, 72, 2016. 10.3847/0004-637X/819/1/72. 64

Lario, D., N. E. Raouafi, R.-Y. Kwon, J. Zhang, R. Gómez-Herrero, N. Dresing, and P. Riley. The Solar Energetic Particle Event on 2013 April 11: An Investigation of its Solar Origin and Longitudinal Spread. *Astrophys. J.*, **797**, 8, 2014. 10.1088/0004-637X/797/1/8. 64

Lario, D., B. Sanahuja, and A. M. Heras. Energetic Particle Events: Efficiency of Interplanetary Shocks as 50 keV < E < 100 MeV Proton Accelerators. *Astrophys. J.*, **509**, 415–434, 1998. 10.1086/306461. 6, 7, 19

Lario, D., and G. M. Simnett. Solar Energetic Particle Variations. In J. M. Pap, P. Fox, C. Frohlich, H. S. Hudson, J. Kuhn, J. McCormack, G. North, W. Sprigg, and S. T. Wu, eds., Solar Variability and its Effects on Climate. Geophysical Monograph 141, vol. 141 of *Washington DC American Geophysical Union Geophysical Monograph Series*, 195, 2004. 10.1029/141GM14. 8, 20

Lawson, C. L., and R. J. Hanson. Solving least squares problems, 1974. 100

Lee, M. A., R. A. Mewaldt, and J. Giacalone. Shock Acceleration of Ions in the Heliosphere. *Space Sci. Rev.*, **173**, 247–281, 2012. 10.1007/s11214-012-9932-y. 2

Luhmann, J. G., D. W. Curtis, P. Schroeder, J. McCauley, R. P. Lin, et al. STEREO IMPACT Investigation Goals, Measurements, and Data Products Overview. *Space Sci. Rev.*, **136**(1), 117–184, 2008. 10.1007/s11214-007-9170-x, URL `https://doi.org/10.1007/s11214-007-9170-x`. 23

Marsden, R. G., K.-P. Wenzel, and E. J. Smith. The Ulysses Mission. In R. G. Marsden and L. A. Fisk, eds., The Sun and the Heliosphere in Three Dimensions, Proceedings of the Nineteenth ESLAB Symposium, Les Diablerets, Switzerland, June 4-6, 1985 Edited by R. G. Marsden. Dordrecht, D. Reidel Publishing Co. Astrophysics and Space Science Library. Volume 123, 1986, p.477, 477, 1986. 9

Mason, G. M., G. Li, C. M. S. Cohen, M. I. Desai, D. K. Haggerty, R. A. Leske, R. A. Mewaldt, and G. P. Zank. Interplanetary Propagation of Solar Energetic Particle Heavy Ions Observed at 1 AU and the Role of Energy Scaling. *Astrophys. J.*, **761**, 104, 2012. 10.1088/0004-637X/761/2/104. 10

McComas, D. J., S. J. Bame, P. Barker, W. C. Feldman, J. L. Phillips, P. Riley, and J. W. Griffee. Solar Wind Electron Proton Alpha Monitor (SWEPAM) for the Advanced Composition Explorer. *Space Sci. Rev.*, **86**, 563–612, 1998. 10.1023/A:1005040232597. 22

McGuire, R. E., T. T. von Rosenvinge, and F. B. McDonald. The composition of solar energetic particles. *Astrophys. J.*, **301**, 938–961, 1986. 10.1086/163958. 22

McKenna-Lawlor, S., A. Bhardwaj, F. Ferrari, N. Kuznetsov, A. K. Lal, et al. Recommendations to mitigate against human health risks incurred due to energetic particle irradiation beyond low earth orbit/BLEO. *Acta Astronautica*, **109**, 182–193, 2015. 10.1016/j.actaastro.2014.11.009. 12

Mewaldt, R. A., C. M. S. Cohen, W. R. Cook, A. C. Cummings, A. J. Davis, et al. The Low-Energy Telescope (LET) and SEP Central Electronics for the STEREO Mission. *Space Sci. Rev.*, **136**, 285–362, 2008. 10.1007/s11214-007-9288-x. 23

Mishev, A., and P. Jiggens. Preface to measurement, specification and forecasting of the Solar Energetic Particle (SEP) environment and Ground Level Enhancements (GLEs). *Journal of Space Weather and Space Climate*, **9**, E1, 2019. 10.1051/swsc/2019003. 12

Müller, D., R. G. Marsden, O. C. St. Cyr, and H. R. Gilbert. Solar Orbiter . Exploring the Sun-Heliosphere Connection. *Sol. Phys.*, **285**, 25–70, 2013. 10.1007/s11207-012-0085-7, 1207.4579. 119

Müller-Mellin, R., S. Böttcher, J. Falenski, E. Rode, L. Duvet, T. Sanderson, B. Butler, B. Johlander, and H. Smit. The Solar Electron and Proton Telescope for the STEREO Mission. *Space Sci. Rev.*, **136**, 363–389, 2008. 10.1007/s11214-007-9204-4. 61, 128

Musmann, G., F. M. Neubauer, A. Maier, and L. E. Das Förstersonden-Magnetfeldexperiment (E2) . *Raumfahrtforschung*, **19**(5), 232–236, 1975. 25, 79

Nolte, J. T., and E. C. Roelof. Large-Scale Structure of the Interplanetary Medium, I: High Coronal Source Longitude of the Quiet-Time Solar Wind. *Sol. Phys.*, **33**, 241–257, 1973a. 10.1007/BF00152395. 64

Nolte, J. T., and E. C. Roelof. Large-Scale Structure of the Interplanetary Medium. II: Evolving Magnetic Configurations Deduced from Multi-Spacecraft Observations. *Sol. Phys.*, **33**, 483–504, 1973b. 10.1007/BF00152435. 64

Nymmik, R. Extremely large solar high-energy particle events: Occurrence probability and characteristics. *Advances in Space Research*, **40**, 326–330, 2007. 10.1016/j.asr.2007.05.005. 13

Nymmik, R. A. Some problems with developing a standard for determining solar energetic particle fluxes. *Advances in Space Research*, **47**, 622–628, 2011. 10.1016/j.asr.2010.11.004. 13

Onsager, T., R. Grubb, J. Kunches, L. Matheson, D. Speich, R. W. Zwickl, and H. Sauer. Operational uses of the GOES energetic particle detectors. *Proc.SPIE*, **2812**, 2812 – 2812 – 10, 1996. 10.1117/12.254075, URL http://dx.doi.org/10.1117/12.254075. 22

Ontiveros, V., and A. Vourlidas. Quantitative Measurements of Coronal Mass Ejection-Driven Shocks from LASCO Observations. *Astrophys. J.*, **693**, 267–275, 2009. 10.1088/0004-637X/693/1/267, 0811.3743. 20

Pacheco, D., N. Agueda, A. Aran, B. Heber, and D. Lario. Full inversion of solar relativistic electron events measured by the Helios spacecraft. *Accepted for publication in Astron. Astrophys.*, –, 2019a. 10, 151

Pacheco, D., N. Agueda, R. Gómez-Herrero, and A. Aran. Interplanetary transport of solar near-relativistic electrons on 2014 August 1 over a narrow range of heliolongitudes. *J. Space Weather Space Clim.*, **7**(27), A30, 2017a. 10.1051/swsc/2017029. 9, 11, 62, 113, 151

Pacheco, D., A. Aran, N. Agueda, R. Gómez-Herrero, and D. Lario. Modelling electron pitch-angle distributions for EPT detector on-board Solar Orbiter. *In preparation for publication in Astron. Astrophys.*, –, 2019b. 151

Pacheco, D., A. Aran, N. Agueda, and B. Sanahuja. SOL2UP WP1200: Evaluation of the downstream contribution to total fluence. *Technical Note TN1 v2.1, SOL2UP Project, ESA/ESTEC Contract 4000114116/15/NL/HK*, 1–134, 2017b. 21, 28, 49, 52, 144, 151

Parker, E. N. The passage of energetic charged particles through interplanetary space. *Planet. Space Sci.*, **13**, 9–49, 1965. 10.1016/0032-0633(65)90131-5. 127

Pomoell, J., A. Aran, C. Jacobs, R. Rodríguez-Gasén, S. Poedts, and B. Sanahuja. Modelling large solar proton events with the shock-and-particle model. *J. Space Weather Space Clim.*, **5**, A12, 2015. 10.1051/swsc/2015015, URL http://www.swsc-journal.org/10.1051/swsc/2015015. 14, 19

Porsche, H. Die Helios-Sonde als Experimenten-Träger. *Raumfahrtforschung*, **19**, 223–225, 1975. 21, 24, 75

Posner, A. Up to 1-hour forecasting of radiation hazards from solar energetic ion events with relativistic electrons. *Space Weather*, **5**, 05001, 2007. 10.1029/2006SW000268. 122

Quinn, P. R., N. A. Schwadron, L. W. Townsend, R. F. Wimmer-Schweingruber, A. W. Case, H. E. Spence, J. K. Wilson, and C. J. Joyce. Modeling the effectiveness of shielding in the earth-moon-mars radiation environment using PREDICCS: five solar events in 2012. *Journal of Space Weather and Space Climate*, **7**(27), A16, 2017. 10.1051/swsc/2017014. 12

Reames, D. V. Particle acceleration at the Sun and in the heliosphere. *Space Sci. Rev.*, **90**, 413–491, 1999. 4

Reames, D. V. The Two Sources of Solar Energetic Particles. *Space Sci. Rev.*, **175**, 53–92, 2013. 10.1007/s11214-013-9958-9. 4, 6

Reames, D. V., L. M. Barbier, and C. K. Ng. The Spatial Distribution of Particles Accelerated by Coronal Mass Ejection–driven Shocks. *Astrophys. J.*, **466**, 473–486, 1996. 10.1086/177525. 20, 76, 172

Reames, D. V., S. W. Kahler, and C. K. Ng. Spatial and Temporal Invariance in the Spectra of Energetic Particles in Gradual Solar Events. *Astrophys. J.*, **491**, 414–420, 1997. 10.1086/304939. 172, 173

Richardson, I. G., T. T. von Rosenvinge, H. V. Cane, E. R. Christian, C. M. S. Cohen, A. W. Labrador, R. A. Leske, R. A. Mewaldt, M. E. Wiedenbeck, and E. C. Stone. >25 MeV Proton Events Observed by the High Energy Telescopes on the STEREO A and B Spacecraft and/or at Earth During the First ~ Seven Years of the STEREO Mission. *Sol. Phys.*, **289**, 3059–3107, 2014. 10.1007/s11207-014-0524-8. 9, 20, 24, 36, 61, 159

Rodriguez, J. V., J. C. Krosschell, and J. C. Green. Intercalibration of GOES 8–15 solar proton detectors. *Space Weather*, **12**(1), 92–109, 2014. 10.1002/2013SW000996, URL `http://dx.doi.org/10.1002/2013SW000996`. 22

Rodríguez-Gasén, R., A. Aran, B. Sanahuja, C. Jacobs, and S. Poedts. Variation of Proton Flux Profiles with the Observer's Latitude in Simulated Gradual SEP Events. *Sol. Phys.*, **289**, 1745–1762, 2014. 10.1007/s11207-013-0442-1. 122

Rodríguez-Pacheco, J., R. F. Wimmer-Schweingruber, G. M. Mason, and G. C. Ho. The Energetic Particle Detector (EPD). *To be submitted to Astron. Astrophys.*, 2018. 118, 120

Roelof, E. C. Propagation of Solar Cosmic Rays in the Interplanetary Magnetic Field. In Ögelman, H. and Wayland, J. R., ed., Lectures in High-Energy Astrophysics, 111, 1969. 65, 66, 88, 128

Rosenqvist, L., and A. Hilgers. Sensitivity of a statistical solar proton fluence model to the size of the event data set. *Geophys. Res. Lett.*, **30**, 1865, 2003. 10.1029/2003GL017038. 22

Rosenqvist, L., A. Hilgers, H. Evans, E. Daly, M. Hapgood, R. Stamper, R. Zwickl, S. Bourdarie, and D. Boscher. Toolkit for Updating Interplanetary Proton Cumulated Fluence Models. *Journal of Spacecraft and Rockets*, **42**, 1077–1090, 2005. 10.2514/1.8211. 22

Rouillard, A. P., R. F. Pinto, A. Vourlidas, and W. T. Thompson. Models and Tools for the Solar Orbiter mission. *To be submitted to Astron. Astrophys.*, 2019. 120

Rouillard, A. P., N. R. Sheeley, A. Tylka, A. Vourlidas, C. K. Ng, et al. The Longitudinal Properties of a Solar Energetic Particle Event Investigated Using Modern Solar Imaging. *Astrophys. J.*, **752**, 44, 2012. 10.1088/0004-637X/752/1/44. 24, 159

Ruffolo, D. Effect of adiabatic deceleration on the focused transport of solar cosmic rays. *Astrophys. J.*, **442**, 861–874, 1995. 10.1086/175489, arXiv:astro-ph/9408056. 65

Russell, C. T. The STEREO Mission. *Space Sci. Rev.*, **136**, 2008. 10.1007/s11214-008-9344-1. 21

Ruzmaikin, A., G. Li, G. P. Zank, J. Feynmann, and I. Jun. The Radial Dependence of Solar Energetic Particle Fluxes. In ESA SP-592: Solar Wind 11/SOHO 16, Connecting Sun and Heliosphere, 441–444, 2005. 122

Sanahuja, B. Energetic particle events during STIP interval XII. In STIP symposium on retrospective intervals, 265. Eds Shea and Smart, Book Crafters Publ. Co. Chelsea, Michigan, 1988. 172

Sanahuja, B., and V. Domingo. Low-energy protons associated with interplanetary shocks as an independent population in the solar wind. *J. Geophys. Res.*, **92**, 7280–7288, 1987. 10.1016/0273-1177(84)90327-2. 172, 173

Sanahuja, B., V. Domingo, K.-P. Wenzel, J. A. Joselyn, and E. Keppler. A large proton event associated with solar filament activity. *Sol. Phys.*, **84**, 321–337, 1983. 10.1007/BF00157465. 172, 173

Sandberg, I. Implementation of a New Calibration for SEP Datasets on SEPEM. *SEPCALIB Final Report*, 1–40, 2014. 19, 22

Sandberg, I., P. Jiggens, D. Heynderickx, and I. A. Daglis. Cross calibration of NOAA GOES solar proton detectors using corrected NASA IMP-8/GME data. *Geophys. Res. Lett.*, **41**, 4435–4441, 2014. 10.1002/2014GL060469. 19, 22

Sarris, E. T., S. M. Krimigis, and T. P. Armstrong. Observations of magnetospheric bursts of high-energy protons and electrons at approximately 35 earth radii with Imp 7. *J. Geophys. Res.*, **81**, 2341–2355, 1976. 10.1029/JA081i013p02341. 8

Schwenn, R., and E. Marsch. Physics of the Inner Heliosphere I. Large-Scale Phenomena. Springer-Verlag, Berlin, Heidelberg, 1990. 76

Schwenn, R., and E. Marsch. Physics of the Inner Heliosphere II. Particles, Waves and Turbulence. Springer, Berlin, Heidelberg, 1991. 76

Schwenn, R., H. Rosenbauer, and H. Miggenrieder. Das Plasmaxperiment auf HELIOS (E1). *Raumfahrtforschung*, **19**(5), 226–232, 1975. 25, 79

Schwer, K., R. B. Lilly, B. J. Thompson, and D. A. Brewer. The SDO Mission. *AGU Fall Meeting Abstracts*, SH21C-01, 2002. 9

Sellers, F., and F. Hanser. Design and calibration of the GOES-8 particle sensors: the EPS and HEPAD. *Proc.SPIE*, **2812**, 2812 – 2812 – 12, 1996. 10.1117/12.254083, URL `http://dx.doi.org/10.1117/12.254083`. 22

Smart, D. F., M. A. Shea, H. E. Spence, and L. Kepko. Two groups of extremely large >30 MeV solar proton fluence events. *Advances in Space Research*, **37**, 1734–1740, 2006. 10.1016/j.asr.2005.09.008. 13

Smith, C. W., J. L'Heureux, N. F. Ness, M. H. Acuña, L. F. Burlaga, and J. Scheifele. The ACE Magnetic Fields Experiment. *Space Sci. Rev.*, **86**, 613–632, 1998. 10.1023/A:1005092216668. 22

Space-Systems-Loral, ed. GOES I-M Databook, Revision 1, 1996. URL `https://goes.gsfc.nasa.gov/text/databook/databook.pdf`. 9

Strauss, R. D., and H. Fichtner. On Aspects Pertaining to the Perpendicular Diffusion of Solar Energetic Particles. *Astrophys. J.*, **801**, 29, 2015. 10.1088/0004-637X/801/1/29. 61

Strauss, R. D., O. Ogunjobi, H. Moraal, K. G. McCracken, and R. A. Caballero-Lopez. On the Pulse Shape of Ground-Level Enhancements. *Sol. Phys.*, **292**, 29, 2017. 10.1007/s11207-017-1086-3. 11, 67

Vainio, R., N. Agueda, A. Aran, and D. Lario. Modeling of Solar Energetic Particles in Interplanetary Space. In J. Lilensten, ed., Space Weather: Research Towards Applications in Europe, vol. 344 of *Astrophysics and Space Science Library*, 27–37. Springer Netherlands, 2007. ISBN 978-1-4020-5446-4. 10.1007/1-4020-5446-7_4. 4, 122, 127, 128

Verkhoglyadova, O. P., G. Li, X. Ao, and G. P. Zank. Radial Dependence of Peak Proton and Iron Ion Fluxes in Solar Energetic Particle Events: Application of the PATH Code. *Astrophys. J.*, **757**, 75, 2012. 10.1088/0004-637X/757/1/75. 122

Vogt, A., B. Heber, A. Kopp, M. S. Potgieter, and R. D. Strauss. Jovian electrons in the inner heliosphere. Proposing a new source spectrum based on 30 years of measurements. *Astron. Astrophys.*, **613**, A28, 2018. 10.1051/0004-6361/201731736. 12

von Rosenvinge, T. T., D. V. Reames, R. Baker, J. Hawk, J. T. Nolan, et al. The High Energy Telescope for STEREO. *Space Sci. Rev.*, **136**, 391–435, 2008. 10.1007/s11214-007-9300-5. 23

Wibberenz, G., and H. V. Cane. Multi-Spacecraft Observations of Solar Flare Particles in the Inner Heliosphere. *Astrophys. J.*, **650**, 1199–1207, 2006. 10.1086/506598. 10, 61, 111, 115

Wibberenz, G., K. Kecskeméty, H. Kunow, A. Somogyi, B. Iwers, Y. I. Logachev, and V. G. Stolpovskii. Coronal and interplanetary transport of solar energetic protons and electrons. *Sol. Phys.*, **124**, 353–392, 1989. 10.1007/BF00156275. 77

Wiedenbeck, M. E., G. M. Mason, C. M. S. Cohen, N. V. Nitta, R. Gómez-Herrero, and D. K. Haggerty. Observations of solar energetic particles from ³ He-rich events over a wide range of heliographic longitude. *Astrophys. J.*, **762**(1), 54, 2013. 10.1088/0004-637X/762/1/54, URL `http://stacks.iop.org/0004-637X/762/i=1/a=54?key=crossref.48ceaf9e4a92f4e43fb335e03c6f7d9f`. 9

Wijsen, N., A. Aran, J. Pomoell, and S. Poedts. Modelling three-dimensional transport of solar energetic protons in a corotating interaction region generated with EUHFORIA. *Astron. Astrophys.*, **622**, A28, 2019. 10.1051/0004-6361/201833958. 4, 11

Xapsos, M. A., J. L. Barth, E. G. Stassinopoulos, E. A. Burke, and G. B. Gee. Model for Solar Proton Risk Assesment. *IEEE Tans. Nucl. Sci.*, **51**(6), 3394–3398, 2004. 13

Xapsos, M. A., J. L. Barth, E. G. Stassinopoulos, S. R. Messenger, R. J. Walters, G. P. Summers, and E. A. Burke. Characterizing solar proton energy spectra for radiation effects applications. *IEEE Transactions on Nuclear Science*, **47**(6 III), 2218–2223, 2000. 10.1109/23.903756. 146

Xapsos, M. A., C. Stauffer, T. Jordan, J. L. Barth, and R. A. Mewaldt. Model for Cumulative Solar Heavy Ion Energy and Linear Energy Transfer Spectra. *IEEE Transactions on Nuclear Science*, **54**, 1985–1989, 2007. 10.1109/TNS.2007.910850. 13

Xapsos, M. A., G. Summers, J. L. Barth, E. G. Stassinopoulos, and E. A. Burke. Probability Model for Cumulative Solar Proton Event Fluences. *IEEE Transactions on Nuclear Science*, **47**, 486–490, 2000. 13

Xapsos, M. A., G. P. Summers, J. L. Barth, E. G. Stassinopoulos, and E. A. Burke. Probability model for worst case solar proton event fluences. *IEEE Transactions on Nuclear Science*, **46**, 1481–1485, 1999. 10.1109/23.819111. 13

Xapsos, M. A., G. P. Summers, and E. A. Burke. Probability model for peak fluxes of solar proton events. *IEEE Transactions on Nuclear Science*, **45**, 2948–2953, 1998. 10.1109/23.736551. 13

Zeitlin, C., D. M. Hassler, F. A. Cucinotta, B. Ehresmann, R. F. Wimmer-Schweingruber, et al. Measurements of Energetic Particle Radiation in Transit to Mars on the Mars Science Laboratory. *Science*, **340**, 1080–1084, 2013. 10.1126/science.1235989. 12